Modelling of plasmonic systems:
Advanced numerical methods and applications

THÈSE N^O 6951 (2016)

PRÉSENTÉE LE 19 FÉVRIER 2016
À LA FACULTÉ DES SCIENCES ET TECHNIQUES DE L'INGÉNIEUR
LABORATOIRE DE NANOPHOTONIQUE ET MÉTROLOGIE
PROGRAMME DOCTORAL EN PHOTONIQUE

ÉCOLE POLYTECHNIQUE FÉDÉRALE DE LAUSANNE

POUR L'OBTENTION DU GRADE DE DOCTEUR ÈS SCIENCES

PAR

Raziman THOTTUNGAL VALAPU

EPFL

ÉCOLE POLYTECHNIQUE
FÉDÉRALE DE LAUSANNE

Suisse
2016

Abstract

Metallic nanostructures interact in complex ways with light, forming the subject of plasmonics and bringing novel physical phenomena and practical applications. The fundamental and practical importance of plasmonics necessitates the development of a multitude of simulation techniques. Surface integral equation (SIE) is a numerical method which is particularly suited for simulating many plasmonic systems. In this thesis, we develop SIE-based numerical methods for plasmonics and use them to study plasmonic systems of interest.

Electric and magnetic surface currents are the basic quantities calculated in SIE, and it is appealing to directly compute various physical quantities directly using them. We develop a formalism to compute optical forces and torques, polarisation charges and multipole moments using the surface currents for better accuracy and efficiency.

Numerical simulation is all about finding the right balance between accuracy and computational cost. SIE allows to choose this tradeoff in computing the integrals for the simulation matrix. We study the effect of the integration routine on the accuracy of the matrix and propose an optimised recipe for evaluating the integrals. Although this recipe incurs an overhead, we show how it becomes necessary in computing some physical quantities and simulating some systems, and how it allows simulations using a coarser discretisation.

One drawback of SIE is that it can only simulate domains for which the response of each domain can be expressed in terms of the Green's function for the domain. Only homogeneous and periodic domains could be dealt with till now, limiting its applicability. We extend SIE to simulate nanostructures embedded in the layers of a stratified medium to partly overcome this restriction, paving the way for further improvements.

SIE has the ability to model complex and realistic geometries. We exploit this feature to study the effect of fabrication-induced rounding on nanorods and gap antennae. We show how rounding results in blue shift of resonances, migration of charges from corners to edges to faces, and reduced coupling between nanostructures.

The surface current-based formalism to calculate optical forces and torques permits their computation for particles in close proximity. We use this to study the internal forces in compound plasmonic systems, and show the presence of strong internal forces between their components. We also demonstrate surprising features such as force and torque reversal, and circular polarisation-dependent behaviour in achiral systems. We then numerically investigate the possibility of using optical torques to orient and rotate plasmonic nanostructures, relying on surface plasmon resonance, retardation effects and circular polarisation.

Polarisation charges contain useful information about the behaviour of plasmonic systems, but

Abstract

there are difficulties in understanding and visualising them. We discuss the complex nature of polarisation charges and suggest various techniques to visualise them in complicated systems in a manner which is easy to understand without loss of information.

Finally, we utilise the ability of SIE to compute accurate near fields to study the Raman enhancement in multi-walled carbon nanotubes on coating with metal, and the analogous quenching of Raman signal from silicon substrates.

ii

Résumé

La plasmonique étudie les interactions complexes de la lumière avec des nanostructures métalliques ainsi que les phénomènes physiques associés et les applications pratiques qui en résultent. Pour tirer profit de la plasmonique, il a été nécessaire de développer une grande variété de méthodes de simulation numérique. Parmi celles-ci, la méthode des équations intégrales de surface (en anglais surface integral equation, SIE) est particulièrement bien adaptée à la simulation de systèmes plasmoniques. Dans cette thèse, je développe de nouvelles méthodes numériques basées sur la SIE et les utilise pour étudier différents systèmes plasmoniques expérimentaux.

Les courants de surface électriques et magnétiques représentent les quantités de base calculées avec SIE et il est intéressant de déduire des grandeurs physiques directement de ces courants. Ainsi, je développe un formalisme permettant de calculer les forces et moments optiques, les charges de polarisation et les moments multipolaires directement des courants de surface.

L'art de la simulation numérique consiste à trouver le bon équilibre entre précision et coût de calcul. SIE permet d'ajuster cet équilibre avec le calcul des intégrales qui composent la matrice du système. Ainsi, j'étudie l'influence des routines d'intégration sur la précision de la matrice du système d'équations et je développe une recette optimisée pour évaluer ces intégrales. Bien que cette nouvelle recette ait un coût calcul, je montre que son utilisation est nécessaire pour obtenir certaines grandeurs physiques ou simuler des systèmes particuliers ; elle offre cependant aussi la possibilité d'utiliser une maille de discrétisation plus grossière pour une précision donnée.

Une limitation de SIE est le fait qu'elle ne peut simuler que des domaines dont la réponse peut s'exprimer en termes de fonction de Green. Ainsi, jusqu'à présent, seuls des domaines homogènes ou périodiques pouvaient être simulés avec SIE, limitant l'utilité de la méthode. Dans cette thèse, j'augmente son champ d'applications en montrant comment simuler aussi des nanostructures incluses dans des milieux stratifiés.

SIE peut modéliser des géométries complexes et réalistes. J'exploite ceci pour étudier les effets d'arrondis sur les arrêtes induits par la fabrication des nanostructures. Je montre en particulier que pour des nano-bâtonnets et des antennes dipolaires, ces arrondis produisent un décalage des résonances vers le bleu et une migration des charges depuis les arrêtes vers les faces, résultant en une diminution du couplage entre les particules.

La méthode développée pour calculer les forces et moments optiques à partir des courants de surface permet d'étudier des particules en interaction très proche. Je l'utilise pour étudier

Abstract

les forces internes dans des systèmes plasmoniques et démontre l'existence de forces très importantes entre différentes parties d'un même système. Des effets surprenants, tels que l'inversion de la force et du moment, ainsi que l'apparition d'effets liés à la polarisation circulaire dans des géométries non-chirales, sont mis en évidence. Finalement, j'étudie la possibilité d'orienter et de faire tourner des nanostructures en utilisant leurs résonances plasmons, des effets de retard ainsi qu'une polarisation incidente circulaire.

Les charges de polarisation contiennent des informations utiles pour le comportement des systèmes plasmoniques, bien qu'elles soient difficiles à visualiser. Je discute leur nature complexe et suggère différentes manières originales et efficaces de les visualiser et de les rendre intelligibles.

Finalement, j'utilise les performances de SIE pour calculer le champ proche afin de déterminer d'une part l'exaltation du signal Raman provenant de nanotubes de carbone recouverts de métal et d'autre part la diminution du signal Raman provenant du substrat sur lequel ces nanotubes sont déposés.

Contents

Contents

1 Introduction

Metals show a very rich behaviour in their interaction with light. Shine of coinage metals has been the source of their high value, and arises from their electronic properties. Electromagnetic fields at optical frequencies can excite propagating waves confined to metal-dielectric interfaces (surface plasmon polaritons), as well as non-propagating electromagnetic modes in metallic nanostructures (localised surface plasmons) [1, 2]. Plasmonics is the study of plasmons – or more simply, the study of the interaction between coinage metals and light. Modern interest in the optical response of metals can be traced back to the experiments of Faraday on gold and other metals [3]. The field of plasmonics has grown considerably in the recent years due to advances in nanoscale fabrication, uncovering novel physical phenomena and giving rise to practical applications in the process [4–11].

The interest in nanoscale plasmonics is primarily due to two features it provides: extreme localisation of the electromagnetic fields resulting in large field intensities and gradients; and the versatile tunability of the plasmonic resonances. Large local intensities and extreme sensitivity to local changes provide plasmonic systems with the ability to detect minute changes in refractive index caused by the presence of chemicals. Chemical and biological sensing is hence an area where plasmonics has found widespread application [12–23]. Strong near fields also help to enhance fluorescence [24–33], Raman scattering [34–40], infrared absorption [41–48] and nonlinear effects [49–55]. Strong field gradients and extreme localisation enable optical trapping and manipulation with high accuracy [56–61]. Plasmonics has also found applications in improving the design of solar cells [62–67] and photodetectors [68–71].

With the plethora of effects and applications arises the requirement to study, design and optimise plasmonic systems theoretically. Designing plasmonic structures with desired optical properties has become a field of active pursuit, and the ability to accurately simulate the optical response of these structures is of paramount importance. The search for analytical descriptions of plasmonic effects is more than a century old [72], but the initial methods were restricted to ideal systems due to the requirement of mathematical solutions involving computations to be performed by humans. The advent of computers enabled the creation of more calculation-intensive methods which could deal with more general and realistic physical

systems. The development of simulation tools continues to be an active area of research, especially in plasmonics where the discovery of new phenomena places novel requirements on the simulation methods. We present an overview of the commonly used numerical methods in plasmonics in Section 1.1.

In this thesis, we develop and improve simulation tools for plasmonic systems. They are then used to perform numerical experiments on plasmonic systems with experimental relevance. We achieve a better understanding of various plasmonic phenomena by this, and discover novel and promising physical effects. The thesis content is outlined in Section 1.3.

1.1 Numerical methods in plasmonics

Various numerical methods are used to simulate the optical response of plasmonic nanostructures both in the time domain and in the frequency domain. A comprehensive review of the computational techniques was recently published in Ref. [73]. We provide a basic description of the common simulation methods here.

Though the goal of all these numerical methods is to solve Maxwell's equations to obtain the electromagnetic response [74], the solution can be performed by treating these equations in an integral form or in a differential form. The different methods have specific strengths and weaknesses, and the best matching numerical technique should be chosen for each problem. The most commonly used methods in plasmonics include finite difference time domain (FDTD), finite element method (FEM), volume integral equation (VIE) and surface integral equation (SIE).

Finite difference time domain (FDTD) solves Maxwell's equations in the differential form in the time domain by discretising space and time into a structured grid [75–78]. The various fields are evaluated at its points, and the derivatives in Maxwell's equations are approximated by finite differences on the grid. The time evolution of the electromagnetic field can be traced, starting from an initial condition. FDTD is a popular numerical method thanks to the simplicity of its description and because it allows the simulation of time-domain phenomena. However, being a time domain method, simulating frequency-dependent effects in dispersive materials is not straightforward [79–81]. Also, the typical implementation of FDTD using a uniform grid can be problematic while dealing with complex surfaces and regions of high field gradients, and non-uniform grids have to be introduced [82, 83]. Finally, since it is only possible to discretise a finite region of space, the discretisation lattice must be terminated carefully by introducing absorbing or perfectly matched layer boundary conditions [84–86].

Finite element method (FEM) also solves Maxwell's equations in the differential form, but in general it is formulated in the frequency domain [87, 88]. In this method, a finite volume of space is discretised into elements and the field in each element is expanded over a set of basis functions. The solution of the system is found using the Galerkin approach. Choosing triangular and tetrahedral elements allows describing complicated geometries faithfully, making the

method superior to FDTD in this aspect, though it is more computationally expensive. Using continuity-enforcing basis functions of high enough order allows matching the variation of fields within an element well, providing good accuracy and convergence [89, 90]. Since FEM is a frequency domain method, it can easily include dispersive effects and study frequency-dependent phenomena. However, the issue of having to discretise a finite region of space and requiring special boundary conditions remains. Hybrid methods such as the discontinuous Galerkin method are used to combine the advantages of FDTD and FEM and to obtain time domain solutions [91–95].

Solving Maxwell's equations in the integral form can overcome some of the above issues. The volume integral equation (VIE) method provides the integral form solution in the frequency domain using the Green's function [96, 97]. This approach can be used for scatterers placed in backgrounds for which the Green's function can be computed, such as homogeneous and stratified media [97–101]. The rest of the domains can be arbitrary, allowing the simulation of structures with inhomogeneous optical properties. One important consideration in VIE is the proper treatment of singularities at source points. The most attractive feature of the method is that it requires only the discretisation of the scatterers, and the automatic treatment of the background means that artificial truncation of space is not required. However, unlike FDTD and FEM, the matrices involved in VIE are dense, requiring higher costs in storing and solving the matrices for the same number of discretised elements. Discrete dipole approximation (DDA) is a very similar technique in which the singularity at the source is not considered and the polarisabilities of the discretised elements are computed from the lattice dispersion relation [102–104]. An added advantage of DDA is that fast Fourier transforms can be used to speed up its implementation significantly [102].

Surface integral equation (SIE) can be considered a combination of finite element and volume integral methods. The surfaces of the scatterers are discretised and the fields on each surface element are expanded over a set of basis functions. Maxwell's equations are then solved in the surface integral form, and the solution of the system is found using the Galerkin approach [105–108]. SIE is the primary simulation method used in this thesis, therefore we provide a description of the formulation used in Section 1.2. Apart from the general advantages of the frequency domain methods and VIE, the most attractive feature of SIE is that it requires the discretisation of only the boundaries of scatterers, reducing computational overhead and allowing a more faithful representation of surfaces. However, the resultant matrix is still dense, and SIE can only be used with domains for which the Green's function can be computed [109–111]. A closely related method is the boundary element method (BEM) which uses scalar and vector potentials instead of fields and specifies the elements on the boundary to have constant values instead of using basis functions. The solution of the system is hence performed by point matching instead of the Galerkin approach [112–117]. Hybrid methods combining SIE to deal with the background domain and FEM to treat inner domains also exist [118].

In addition to the accuracy of the numerical methods, it is also important to get a correct

description of the physics of the modelled systems. Plasmonic computations usually treat domains as linear and local while describing the constitutive relations for various media. In systems where this approximation breaks down, the computation has to be modified to incorporate nonlinear [119–124] and nonlocal [125–127] effects. At very short length scales, Maxwell's equations might be inadequate to describe the electromagnetic response and a quantum mechanical treatment might be required [128–134]. In this thesis, we will not concern ourselves with such effects and restrict our attention to linear, homogeneous, isotropic domains and follow the SIE treatment in Ref. [105].

1.2 Surface integral equation formulation

There exist different formulations to solve surface integral equations numerically, with varying numerical accuracy [107, 108]. We will be following the formulation in Ref. [105], where surface currents are expanded in terms of the Rao-Wilton-Glisson (RWG) basis functions [135]. The tangential boundary values of the surface integral equations are used, and the Poggio-Miller-Chang-Harrington-Wu-Tsai (PMCHWT) formulation [136–138] is chosen to combine the integral equations over domains. We will now discuss the basics of the theoretical and implementational aspects of the SIE formulation based on Ref. [105]. Further details can be found there.

We describe space as a union of homogeneous isotropic domains $\{\Omega_i\}$, as depicted in Fig. 1.1(a). For a domain Ω_i with constant electric permittivity ε_i and magnetic permeability μ_i, the wave equation for the electric field at the frequency ω has the following form, assuming harmonic dependence ($e^{-i\omega t}$) for all fields

$$\nabla \times \nabla \times \mathbf{E}_i(\mathbf{r}) - k_i^2 \mathbf{E}_i(\mathbf{r}) = i\omega\mu_i\mathbf{j}_i(\mathbf{r}) \,, \tag{1.1}$$

where k_i is the wavenumber in the medium, and $\mathbf{E}_i$ and $\mathbf{j}_i$ are the electric field and free current density, respectively. This equation can be solved with the help of the dyadic Green's function
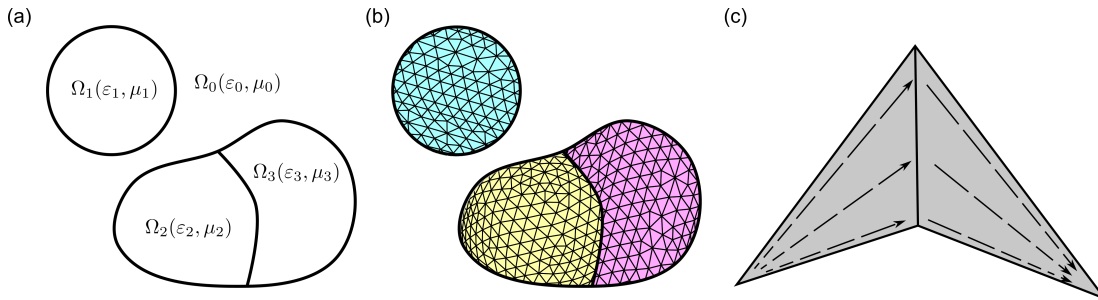

Figure 1.1 – Schematic of the SIE formulation. (a) Space is described as a union of homogeneous domains with constant material properties. (b) Surfaces of the domains are discretised by a triangular mesh. (c) The surface currents are expressed in terms of RWG basis functions, which are linear functions defined over adjacent triangles.

$\overline{\mathbf{G}}$ which is defined using [139],

$$\nabla \times \nabla \times \overline{\mathbf{G}}_i(\mathbf{r},\mathbf{r}') = k_i^2 \overline{\mathbf{G}}_i(\mathbf{r},\mathbf{r}') - \overline{\mathbf{I}}\delta(\mathbf{r}-\mathbf{r}')\,. \tag{1.2}$$

In a homogeneous domain, the dyadic Green's function has the form

$$\begin{aligned}
\overline{\mathbf{G}}_i(\mathbf{r},\mathbf{r}') &= \left(\overline{\mathbf{I}} + \frac{\nabla\nabla}{k_i^2}\right)\frac{e^{ik_i|\mathbf{r}-\mathbf{r}'|}}{4\pi|\mathbf{r}-\mathbf{r}'|} \\
&= \left(\overline{\mathbf{I}} + \frac{\nabla\nabla}{k_i^2}\right)G_i(\mathbf{r},\mathbf{r}')\,,
\end{aligned} \tag{1.3}$$

where $G_i(\mathbf{r},\mathbf{r}') = G_i(R = |\mathbf{r}-\mathbf{r}'|)$ is the scalar Green's function which depends only on the distance between the source and observation points.

Using the dyadic Green's function, we can obtain the surface integral equation for the electric field, known as the electric field integral equation (EFIE),

$$\left(i\omega\mu_i \int\limits_{\partial\Omega_i} \mathrm{d}S'\overline{\mathbf{G}}_{\mathrm{i}}(\mathbf{r},\mathbf{r}')\cdot\mathbf{J}_{\mathrm{i}}(\mathbf{r}') + \int\limits_{\partial\Omega_{\mathrm{i}}} \mathrm{d}S'[\nabla'\times\overline{\mathbf{G}}_{\mathrm{i}}(\mathbf{r},\mathbf{r}')]\cdot\mathbf{M}_{\mathrm{i}}(\mathbf{r}')\right)_{\mathrm{tan}} = (\mathbf{E}_i^{\mathrm{inc}}(\mathbf{r}))_{\mathrm{tan}}\,, \tag{1.4}$$

where $\partial\Omega_i$ is the boundary of the domain Ω_i with $\hat{\mathbf{n}}_i$ as the outward normal. $\mathbf{E}_i^{\mathrm{inc}}$ is the incident electric field, and $\mathbf{J}_i$ and $\mathbf{M}_i$ are the electric and magnetic surface currents, defined in terms of the surface magnetic and electric fields as

$$\mathbf{J}_i(\mathbf{r}) = \hat{\mathbf{n}}_i \times \mathbf{H}_i(\mathbf{r})\,, \tag{1.5a}$$
$$\mathbf{M}_i(\mathbf{r}) = -\hat{\mathbf{n}}_i \times \mathbf{E}_i(\mathbf{r})\,. \tag{1.5b}$$

Note that the subscript tan in Eq. (1.4) corresponds to taking the tangential boundary value of the integral.

Since the wave equation for the magnetic field

$$\nabla \times \nabla \times \mathbf{H}_i(\mathbf{r}) - k_i^2 \mathbf{H}_i(\mathbf{r}) = \nabla \times \mathbf{j}_i(\mathbf{r}) \tag{1.6}$$

has a similar form as for the electric field in Eq. (1.1), the dyadic Green's function for the magnetic field is the same as Eq. (1.3). Using it, we can derive the magnetic field integral equation (MFIE),

$$\left(i\omega\varepsilon_i \int\limits_{\partial\Omega_i} \mathrm{d}S'\overline{\mathbf{G}}_{\mathrm{i}}(\mathbf{r},\mathbf{r}')\cdot\mathbf{M}_{\mathrm{i}}(\mathbf{r}') - \int\limits_{\partial\Omega_{\mathrm{i}}} \mathrm{d}S'[\nabla'\times\overline{\mathbf{G}}_{\mathrm{i}}(\mathbf{r},\mathbf{r}')]\cdot\mathbf{J}_{\mathrm{i}}(\mathbf{r}')\right)_{\mathrm{tan}} = (\mathbf{H}_i^{\mathrm{inc}}(\mathbf{r}))_{\mathrm{tan}}\,. \tag{1.7}$$

We have to solve Eqs. (1.4) and (1.7) for the surface currents $\mathbf{J}$ and $\mathbf{M}$. For this, we discretise the boundary of the domain into triangles, as shown in Fig. 1.1(b). RWG functions as used as basis

functions to expand the currents,

$$\mathbf{J}_i(\mathbf{r}) = \sum_{n=1}^{M} \alpha_{in} \mathbf{f}_{in}(\mathbf{r}) \,, \tag{1.8a}$$

$$\mathbf{M}_i(\mathbf{r}) = \sum_{n=1}^{M} \beta_{in} \mathbf{f}_{in}(\mathbf{r}) \,, \tag{1.8b}$$

where $\mathbf{f}_{in}$ are the RWG basis functions, which are linear functions defined on triangle pairs joined by an edge, as shown in Fig. 1.1(c) [135]. The form of the RWG functions is shown in Using the Galerkin approach, we can use the same basis functions as testing functions and convert Eqs. (1.4) and (1.7) to the matrix equations

$$\left[i\omega\mu_i \mathbf{D}_i \quad \mathbf{K}_i \right] \cdot \psi_i = \mathbf{q}_i^E \,, \tag{1.9a}$$

$$\left[-\mathbf{K}_i \quad i\omega\varepsilon_i \mathbf{D}_i \right] \cdot \psi_i = \mathbf{q}_i^H \,, \tag{1.9b}$$

where the elements of the system matrices $\mathbf{D}$ and $\mathbf{K}$ are given by

$$(\mathbf{D}_i)_{nk} = \int_{\partial\Omega_i} \mathrm{d}S \mathbf{f}_{in}(\mathbf{r}) \cdot \int_{\partial\Omega_i} \mathrm{d}S' \overline{\mathbf{G}}_i(\mathbf{r},\mathbf{r}') \cdot \mathbf{f}_{ik}(\mathbf{r}') \,, \tag{1.10a}$$

$$(\mathbf{K}_i)_{nk} = \int_{\partial\Omega_i} \mathrm{d}S \mathbf{f}_{in}(\mathbf{r}) \cdot \int_{\partial\Omega_i} dS' \left[\nabla' \times \overline{\mathbf{G}}_i(\mathbf{r},\mathbf{r}') \right] \cdot \mathbf{f}_{ik}(\mathbf{r}') \,, \tag{1.10b}$$

the incidence vectors $\mathbf{q}^E$ and $\mathbf{q}^H$ have components

$$\left(\mathbf{q}_i^E \right)_n = \int_{\partial\Omega_i} \mathrm{d}S \mathbf{f}_{in}(\mathbf{r}) \cdot \mathbf{E}_i^{\mathrm{inc}}(\mathbf{r}) \,, \tag{1.11a}$$

$$\left(\mathbf{q}_i^H \right)_n = \int_{\partial\Omega_i} \mathrm{d}S \mathbf{f}_{in}(\mathbf{r}) \cdot \mathbf{H}_i^{\mathrm{inc}}(\mathbf{r}) \,, \tag{1.11b}$$

and the solution vector $\psi_i = [\alpha_{i\{1\cdots M\}} \quad \beta_{i\{1\cdots M\}}]^T$. The expressions for $\mathbf{D}$ and $\mathbf{K}$ containing the dyadic Green's function and its curl in Eqs. (1.10a) and (1.10b) can be converted to the following method of moments-friendly form involving the scalar Green's function and its gradient:

$$(\mathbf{D}_i)_{nk} = -\frac{1}{k_i^2} \int_{S_n} \mathrm{d}S \nabla \cdot \mathbf{f}_{in}(\mathbf{r}) \int_{S_k} \mathrm{d}S' G_i(\mathbf{r},\mathbf{r}') \nabla' \cdot \mathbf{f}_{ik}(\mathbf{r}') + \int_{S_n} \mathrm{d}S \mathbf{f}_{in}(\mathbf{r}) \cdot \int_{S_k} \mathrm{d}S' G_i(\mathbf{r},\mathbf{r}') \mathbf{f}_{ik}(\mathbf{r}') \,,$$

$$\tag{1.12a}$$

$$(\mathbf{K}_i)_{nk} = \int_{S_n} \mathrm{d}S \mathbf{f}_{in}(\mathbf{r}) \cdot \int_{S_k} dS' \left[\nabla' G_i(\mathbf{r},\mathbf{r}') \right] \times \mathbf{f}_{ik}(\mathbf{r}') \,, \tag{1.12b}$$

where S_n (S_k) is the surface of the pair of triangles over which $\mathbf{f}_n$ ($\mathbf{f}_k$) is defined. Note that these integrals are 4D and can be carried out as two successive 2D integrations on the source ($\mathbf{r}'$)

and test (**r**) triangle pairs.

In practice, the singular nature of the Green's function at $\mathbf{r} = \mathbf{r}'$ can be problematic for the numerical evaluation of these integrals when the triangles are close to each other or overlapping. This problem can be mitigated by singularity subtraction. The scalar Green's function $G_i(R)$ is separated into a smooth and a singular part,

$$G_i(R) = G_i^{\text{sing}}(R) + G_i^{\text{smooth}}(R) \tag{1.13}$$

$$\text{with } G_i^{\text{sing}}(R) = \frac{1}{4\pi}\left(\frac{1}{R} - \frac{k_i^2 R}{2}\right). \tag{1.14}$$

The first term is trivially singular at $R = 0$, while the second results in a singularity for ∇G_i. The singular part can be integrated analytically over $\mathbf{r}'$ [140], while the smooth part is integrated numerically without accuracy issues. In both cases, the integral over **r** must still be integrated numerically.

The surface currents switch sign across a boundary since the sign of the normal gets reversed and the tangential fields are continuous. Thus the coefficients of the RWG functions over neighbouring domains differ only in their sign. The matrix equations for different domains in Eq. (1.9) have common unknowns, and are combined using the PMCHWT formulation to obtain accurate solutions [136–138],

$$\sum_i \begin{bmatrix} i\omega\mu_i\mathbf{D}_i & \mathbf{K}_i \\ -\mathbf{K}_i & i\omega\varepsilon_i\mathbf{D}_i \end{bmatrix} \cdot \psi = \sum_i \begin{bmatrix} \mathbf{q}_i^E \\ \mathbf{q}_i^H \end{bmatrix}. \tag{1.15}$$

The resultant matrix equation can be solved using methods such as Gaussian elimination, conjugate gradient and *LU* decomposition [141, 142] to find the coefficients $\{\alpha, \beta\}$ of the surface currents. Once these are found, the fields anywhere in the domains can be found using the following surface integral equations

$$\mathbf{E}_i(\mathbf{r}) = \mathbf{E}_i^{\text{inc}}(\mathbf{r}) - i\omega\mu_i \int\limits_{\partial\Omega_i} \mathrm{d}S' \overline{\mathbf{G}}_{\text{i}}(\mathbf{r},\mathbf{r}') \cdot \mathbf{J}_{\text{i}}(\mathbf{r}') - \int\limits_{\partial\Omega_i} \mathrm{d}S'[\nabla' \times \overline{\mathbf{G}}_{\text{i}}(\mathbf{r},\mathbf{r}')] \cdot \mathbf{M}_{\text{i}}(\mathbf{r}'), \tag{1.16a}$$

$$\mathbf{H}_i(\mathbf{r}) = \mathbf{H}_i^{\text{inc}}(\mathbf{r}) - i\omega\varepsilon_i \int\limits_{\partial\Omega_i} \mathrm{d}S' \overline{\mathbf{G}}_{\text{i}}(\mathbf{r},\mathbf{r}') \cdot \mathbf{M}_{\text{i}}(\mathbf{r}') + \int\limits_{\partial\Omega_i} \mathrm{d}S'[\nabla' \times \overline{\mathbf{G}}_{\text{i}}(\mathbf{r},\mathbf{r}')] \cdot \mathbf{J}_{\text{i}}(\mathbf{r}'). \tag{1.16b}$$

1.3 Outline

The contents of this thesis have been divided into two parts. Part I is dedicated to developing advanced simulation tools based on the SIE formulation. Chapter 2 describes how to compute useful physical quantities such as optical forces and torques, polarisation charges and electric and magnetic moments directly from the SIE surface currents without intermediate computation of the fields for improved efficiency. In Chapter 3, we analyse how the integration

routine used for the computation of the SIE matrix affects the accuracy of the matrix elements and in turn, that of the physical quantities computed using SIE such as optical cross sections, fields and forces. We present an optimised integration recipe for the homogeneous SIE matrix computation and extend it for periodic SIE. Chapter 4 presents an extension of SIE to simulate nanostructures embedded in layers of stratified media.

SIE and the various tools developed in Part I are used to study some important systems and effects in plasmonics in Part II. In Chapter 5, we study how the far-field scattering from plasmonic nanostructures and the polarisation charges induced on them are affected by fabrication-induced rounding of the edges and corners. Chapter 6 presents a detailed analysis of internal forces and torques in compound plasmonic systems consisting of multiple parts. We uncover many interesting and potentially useful effects such as strong lateral forces, wavelength-dependent force and torque switching, and response of achiral systems to circular polarisation. We present a numerical investigation in Chapter 7 of the possibility of achieving three dimensional orientation of plasmonic nanostructures using optical torques. A conceptual treatment of polarisation charges in plasmonic systems is presented in Chapter 8. We discuss the meaning of complex polarisation charges and describe how to understand, visualise and extract relevant information from charges in systems of increasing complexity. Finally, we present a numerical study of Raman enhancement in metal-coated multiwalled carbon nanotubes in Chapter 9. We will then end the thesis by summarising the results and presenting an outlook on future research in Chapter 10.

Improvements to SIE Part I

2 Efficient computation of secondary quantities from SIE surface currents

Different numerical methods in electrodynamics compute a few basic quantities, and other relevant physical quantities are calculated using them. In the case of SIE, the surface electric and magnetic currents are the fundamental output. In this chapter, we develop a formalism to calculate optical forces and torques, polarisation charges, and electric and magnetic moments directly from the surface currents efficiently without intermediate calculation of the fields. Parts of this chapter were published in peer-reviewed journal articles [61, 143].

2.1 Introduction

The basic quantities computed by SIE are the electric and magnetic surface currents at the domain boundaries, defined using Eqs. (1.5a) and (1.5b). The parallel components of the fields ($\mathbf{E}_\parallel$ and $\mathbf{H}_\parallel$) can be expressed directly in terms of surface currents $\mathbf{J}$ and $\mathbf{M}$ (we drop the subscript referring to the domain):

$$\mathbf{H}_\parallel = \mathbf{J} \times \hat{\mathbf{n}}, \tag{2.1a}$$

$$\mathbf{E}_\parallel = \hat{\mathbf{n}} \times \mathbf{M}. \tag{2.1b}$$

We can now use Maxwell's equations to derive the perpendicular components of the fields ($\mathbf{E}_\perp$ and $\mathbf{H}_\perp$):

$$\mathbf{E}_\perp = -\frac{i}{\omega \varepsilon_0 \varepsilon_r} (\nabla \cdot \mathbf{J}) \hat{\mathbf{n}}, \tag{2.2a}$$

$$\mathbf{H}_\perp = -\frac{i}{\omega \mu_0 \mu_r} (\nabla \cdot \mathbf{M}) \hat{\mathbf{n}}, \tag{2.2b}$$

where ω is the angular frequency of light and ε_r and μ_r are the relative permittivity and relative permeability of the domain. Combining these results, we obtain the surface fields entirely in

terms of the surface currents:

$$\mathbf{E} = -\frac{i}{\omega\varepsilon_0\varepsilon_r}(\nabla\cdot\mathbf{J})\hat{\mathbf{n}} + \hat{\mathbf{n}}\times\mathbf{M}, \tag{2.3a}$$

$$\mathbf{H} = -\frac{i}{\omega\mu_0\mu_r}(\nabla\cdot\mathbf{M})\hat{\mathbf{n}} + \mathbf{J}\times\hat{\mathbf{n}}. \tag{2.3b}$$

SIE expands the surface currents over each triangle in terms of RWG basis functions [135], and the surface currents have the following forms

$$\mathbf{J} = \gamma_1(\mathbf{r}-\mathbf{r_1}) + \gamma_2(\mathbf{r}-\mathbf{r_2}) + \gamma_3(\mathbf{r}-\mathbf{r_3}), \tag{2.4a}$$

$$\mathbf{M} = \delta_1(\mathbf{r}-\mathbf{r_1}) + \delta_2(\mathbf{r}-\mathbf{r_2}) + \delta_3(\mathbf{r}-\mathbf{r_3}), \tag{2.4b}$$

where $\mathbf{r}_i$ are the vertices of the triangle, and γ_i and δ_i are the coefficients associated with each vertex. The currents, and thus the surface fields, are linear functions of position over each triangle. The physical quantities required to be computed are typically polynomial functions over the fields, as will be seen later in this chapter. They can be reduced to polynomials over the surface currents using Eqs. (2.3a) and (2.3b) and integrated over the triangles in the surface mesh analytically. The following identities are used to evaluate the various required integrals analytically:

$$\int_T c\,\mathrm{dS_T} = cA, \tag{2.5a}$$

$$\int_T \mathbf{r}\,\mathrm{dS_T} = \mathbf{r}_C A, \tag{2.5b}$$

$$\int_T \mathbf{r}\cdot\mathbf{r}\,\mathrm{dS_T} = \left[9\,\mathbf{r}_c\cdot\mathbf{r}_c + \sum_i \mathbf{r}_i\cdot\mathbf{r}_i\right]\frac{A}{12}, \tag{2.5c}$$

$$\int_T (\mathbf{a}\cdot\mathbf{r})\mathbf{r}\,\mathrm{dS_T} = \left[9\,(\mathbf{a}\cdot\mathbf{r}_c)\mathbf{r}_c + \sum_i (\mathbf{a}\cdot\mathbf{r}_i)\mathbf{r}_i\right]\frac{A}{12}, \tag{2.5d}$$

for arbitrary constant scalar c and constant vector $\mathbf{a}$, where $\mathbf{r}_c$ is the centroid and A is the area of the triangle T.

2.2 Optical forces and torques

Propagating light waves contain momentum, which they can impart to particles [144, 145]. The more common and intuitive scenario is that of light pushing the particles in the direction of propagation, the so-called scattering force [146]. However, it is also possible to pull particles by certain optical beams [147]. In addition, inhomogeneities in the electric field intensity intrinsic to the incident beam or created due to the presence of other structures interacting with the incident field can result in a gradient force on the particle as well [146]. Such optical forces have been used for trapping and manipulating particles since the pioneering work of

Ashkin [148], and have found practical applications in areas of physical and life sciences [56, 149–152]. Recently, the utilisation of complex optical landscapes, such as those produced by nanostructures – in particular plasmonic nanostructures – has opened new possibilities for trapping and manipulating structures at the nanoscale using near–field optical forces [58–60, 153–164].

In the light of present and forthcoming opportunities to exploit optical forces, there is a need for versatile numerical techniques with the ability to simulate optical forces and torques on complicated systems with intricate geometries. Different approaches can be used to compute optical forces, including interacting dipoles [165–168], analytical two spheres model [169], generalised Mie theory [170] and numerical approaches using finite difference time domain [171], to cite a few. To analyse optical forces on realistically shaped structures, the use of numerical techniques is essential since no analytical methods are available for such general calculations [172].

The optical force on an object placed in vacuum can be obtained by integrating the Maxwell's stress tensor σ on a surface S enclosing it. The conservation of momentum can be expressed as [144]:

$$\frac{\partial (\mathbf{P}_{\text{mech}} + \mathbf{P}_{\text{field}})_i}{\partial t} = \oint_S \sum_j \sigma_{ij} n_j \mathrm{d}S, \tag{2.6}$$

where $\mathbf{P}_{\text{mech}}$ and $\mathbf{P}_{\text{field}}$ are the mechanical and electromagnetic momenta, respectively. The vector $\hat{\mathbf{n}}$ is the outward normal to the closed surface S, and σ is the Maxwell's stress tensor with components given by:

$$\sigma_{ij} = \varepsilon_0 E_i E_j + \mu_0 H_i H_j - \frac{1}{2}(\varepsilon_0 E_k E_k + \mu_0 \ H_k H_k)\delta_{ij}. \tag{2.7}$$

If the fields have harmonic dependence ($e^{-i\omega t}$), the time average of the stress tensor over a cycle can be written as

$$\langle \sigma_{ij} \rangle = \frac{1}{2} \text{Re} \left[\varepsilon_0 E_i E_j^* + \mu_0 H_i H_j^* - \frac{1}{2}(\varepsilon_0 E_k E_k^* + \mu_0 \ H_k H_k^*)\delta_{ij} \right], \tag{2.8}$$

where the instantaneous fields have now been replaced by their complex amplitudes. The time average of $\mathbf{P}_{\text{field}}$ over an entire period is a constant. Hence its derivative vanishes and the left hand side of Eq. (2.6) reduces to the total force on the volume enclosed by S. Thus the time averaged optical force acting on the material is given by [173]:

$$\langle F_i \rangle = \oint_S \langle \sigma_{ij} \rangle \ n_j \ \mathrm{d}S. \tag{2.9}$$

The commonly used method to calculate optical forces from Eq. (2.9), illustrated in Fig. 2.1 (a), is to choose a large number of points on a surface S enclosing the particle and perform
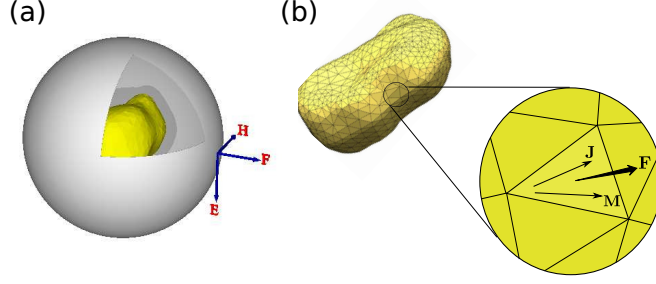
Figure 2.1 – (a) The traditional approach used to calculate forces on nanostructures requires integrating Maxwell's stress tensor as a function of electric (**E**) and magnetic (**H**) fields over a fictitious surface (e.g. a sphere) surrounding the structure; (b) we show that Maxwell's stress tensor can be obtained as a function of surface electric (**J**) and magnetic (**M**) currents directly over the surface mesh elements.

numerical integration of the Maxwell's stress tensor over these points. This method has a few drawbacks. First of all, achieving sufficient numerical accuracy requires the evaluation of fields at a large number of points on the surface, which is computationally expensive. In addition, it is not always easy to generate points over a surface enclosing only the particle when the particle is placed in the vicinity of some other nanostructure [174].

To overcome these difficulties, we notice that the surface of integration S can be shrunk to just enclose the particle, so that it coincides with the outer boundary of the particle itself. We can thus evaluate the Maxwell's stress tensor and hence the force directly over the surface mesh as illustrated in Fig. 2.1 (b), directly from the surface currents. There is no intermediate computation of electric and magnetic fields using surface integrals, thereby improving both the accuracy and the speed of calculation. Furthermore, no imaginary surface needs to be generated around the particle and the method is able to deal with particles placed very close to each other as well. The total optical force acting on the object will be

$$\langle F_i \rangle = \sum_T \int_T \langle \sigma_{ij} \rangle \, n_j \, \mathrm{d}S_T, \tag{2.10}$$

where T are the triangles on the surface of the object. Substituting the forms for the surface fields from Eqs. (2.3a) and (2.3b) in Eq. (2.10), we obtain the surface integral equation for the optical force as:

$$\mathbf{F} = \sum_T \int_T \mathrm{d}S_T \left\{ \frac{(\nabla \cdot \mathbf{M})(\nabla \cdot \mathbf{M}^*)}{2\omega^2 \mu_0} \hat{\mathbf{n}} + \frac{(\nabla \cdot \mathbf{J})(\nabla \cdot \mathbf{J}^*)}{2\omega^2 \varepsilon_0} \hat{\mathbf{n}} - \frac{1}{2}(\varepsilon_0 \mathbf{M} \cdot \mathbf{M}^* + \mu_0 \mathbf{J} \cdot \mathbf{J}^*) \hat{\mathbf{n}} \right.$$

$$\left. + \frac{i}{\omega} \left[(\mathbf{J} \times \hat{\mathbf{n}})(\nabla \cdot \mathbf{M}^*) + (\hat{\mathbf{n}} \times \mathbf{M})(\nabla \cdot \mathbf{J}^*) \right] \right\}. \tag{2.11}$$

From the forms of the surface currents in Eqs. (2.4a) and (2.4b), it can be seen that Eq. (2.11) can be evaluated as a sum of quantities which can be computed analytically over the triangles
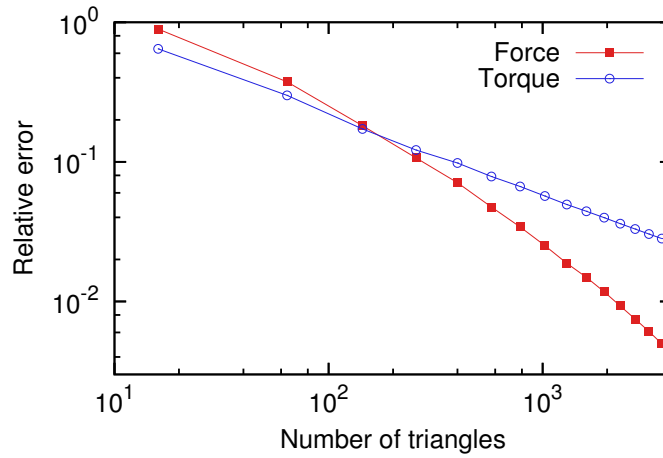
Figure 2.2 – Relative error in force (**F**) and torque (**T**) as a function of the number of triangles the surface is discretised into for a sphere of 30 nm radius illuminated at 390 nm.

using Eqs. (2.5a) to (2.5c). Hence, once the currents are known, the force calculation takes $O(N)$ time only, where N is the number of triangles the surface is discretised into. In comparison, had we created an imaginary surface surrounding the structure and evaluated fields on K points on it, the field evaluation step would have had a time complexity of $O(NK)$. Note that there is also a factor associated with the computation of Green's tensor in the latter case, which can become quite significant if the background is complex and the Green's tensor evaluation is costly.

2.2.1 Results

To demonstrate the validity of the technique, we compare our numerical results with the exact solution given by Mie theory. The force on a silver sphere of 30 nm radius when illuminated by a linearly polarised plane wave at 390 nm is computed. Since we obtain the force on every mesh describing the surface of the object, we can also compute the torque. This is done for the same geometry, but the sphere is now illuminated with a circularly polarised plane wave at the same wavelength. The dielectric constant of the sphere is taken from Johnson and Christy [175]. The variation of the error with the discretisation of the spherical surface is shown in Fig. 2.2. It is evident from the results that the error can be sufficiently minimised with suitable discretisation of the structure.

After having demonstrated the accuracy of the method, we investigate a compound plasmonic system consisting of two spheres separated by a distance d [169, 176, 177]. For the simulation, we consider two silver spheres of 30 nm radius separated by a centre to centre distance of $d = 70$ nm and 80 nm. The wavelength dependence of the force for both separations is plotted in Fig. 2.3. The force between the particles is attractive for the entire wavelength range. We clearly see the signature of plasmonic resonance in the present system. The resonance blue shifts as the gap between the spheres is increased. The z–component of the force F_z shows
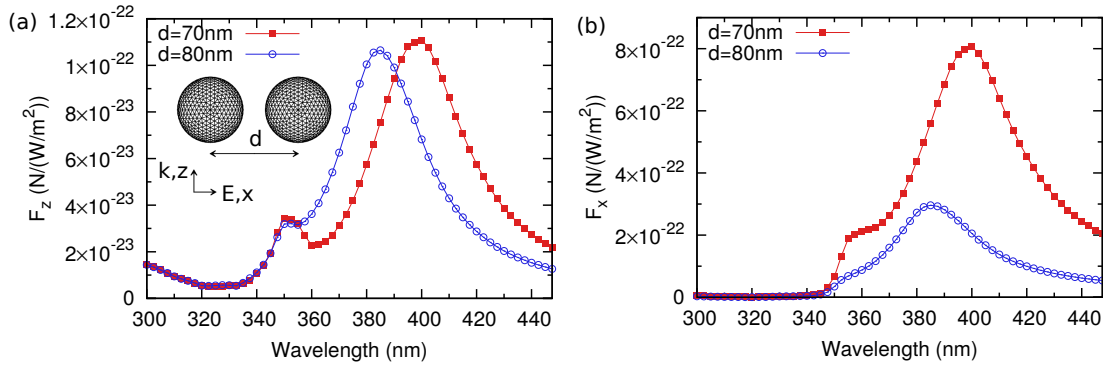
Figure 2.3 – Wavelength dependence of (a) z–component, and (b) x–component of optical force on one sphere of a two-sphere system composed of two silver spheres of 30 nm radius separated by a centre to centre distance of d. The system is illuminated by a plane wave incident along z and polarised along x, as illustrated in the inset of panel (a), and the force is computed for the sphere shown on the left.

similar magnitudes at the plasmon resonances for both separations since z is the direction of the incident wave. Hence the force in the z–direction is primarily the radiation force and is not affected significantly by the interaction with the other sphere, Fig. 2.3(a). However, the x–component of the force is the internal force between the two spheres arising from the electromagnetic interaction between them. Therefore increasing the distance between the spheres reduces the x–component of the force F_x, as expected.

We now examine the effect of distance between the spheres more thoroughly. Figure 2.4 shows the variation of the force between the nanoparticles for a given incident wavelength 370 nm as the separation is varied from 100 nm to 900 nm. The z–component of the force F_z saturates to a constant value as the distance between them is increased. As explained earlier, this is the
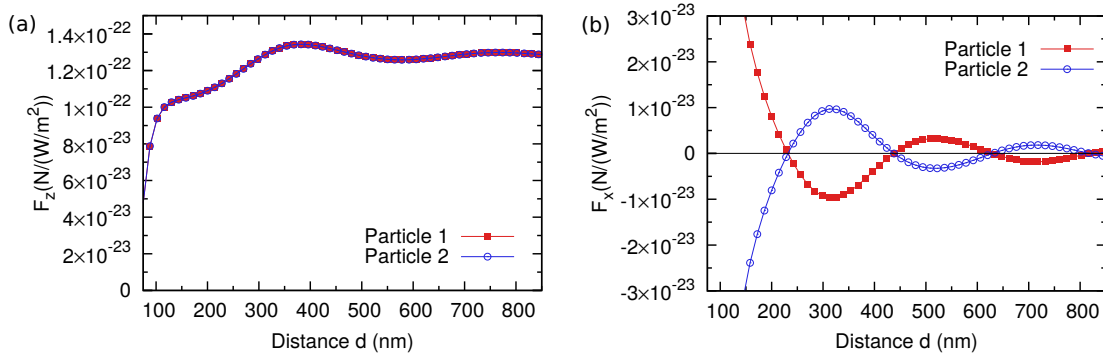

Figure 2.4 – Distance dependence of (a) z–component, and (b) x–component of optical force on each sphere of a two-sphere system composed of two silver spheres of 30 nm radius separated by a centre to centre distance of d. The illumination geometry is same as that in the inset of Fig. 2.3(a), and the wavelength of the incident light is 370 nm. Particle 1 is the sphere on the left.
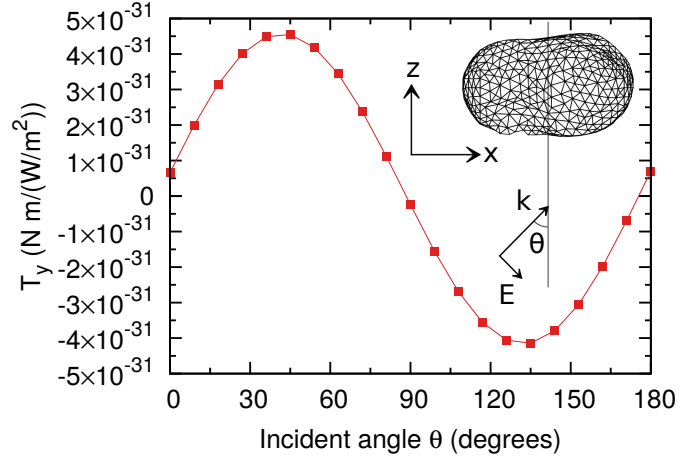
Figure 2.5 – Dependence of the y-component of torque (T_y) on the angle of incidence (θ) for the realistic structure shown in the inset for TM polarised plane wave illumination at 500 nm.

expected behaviour since this is the radiation force. On the other hand, the x–component of the force F_x oscillates in magnitude. This can be understood as follows. The incident field induces dipole moments in both spheres which are very similar in magnitude and phase. The force between two identical dipoles oscillates between attractive and repulsive depending on the separation between them due to retardation effects [178]. Moreover, the forces on the two spheres are equal and opposite due to the symmetry of the system, which again confirms the numerical validity and accuracy of our formalism, Fig. 2.4(b).

We extend our formalism to calculate the torque on a realistic structure with a very complex surface geometry shown in the inset of Fig. 2.5 [179]. The structure has approximate dimensions of 50 nm × 30 nm × 30 nm, and is illuminated by a TM polarised plane wave in the xz–plane, incident at an angle θ with the z–axis. The y–component of torque is plotted as a function of the angle of incidence in Fig. 2.5 and shows significant changes. When the incident wave is normal to the principal axes of the system, the torque is small in magnitude. The magnitude increases for oblique incidence. Such torque calculation as done here can be used for understanding the motion of asymmetric particles in a optical tweezer.

Finally, we compare the force computed using our approach with an approximate formula based on the gradient force [167, 180],

$$\mathbf{F} = \frac{1}{4} \operatorname{Re}\{\alpha\} \nabla |\mathbf{E}|^2 , \tag{2.12}$$

where α is the polarisability of the particle. The system under consideration is a gap antenna with arms of dimensions 100 nm × 40 nm × 40 nm made of gold. The antenna is placed along x-axis and illuminated by a planewave propagating along z and polarised along x, as illustrated in the inset of Fig. 2.6. A sphere is placed at the centre of the gap and displaced by 5 nm along y, and we look at the restoring force.
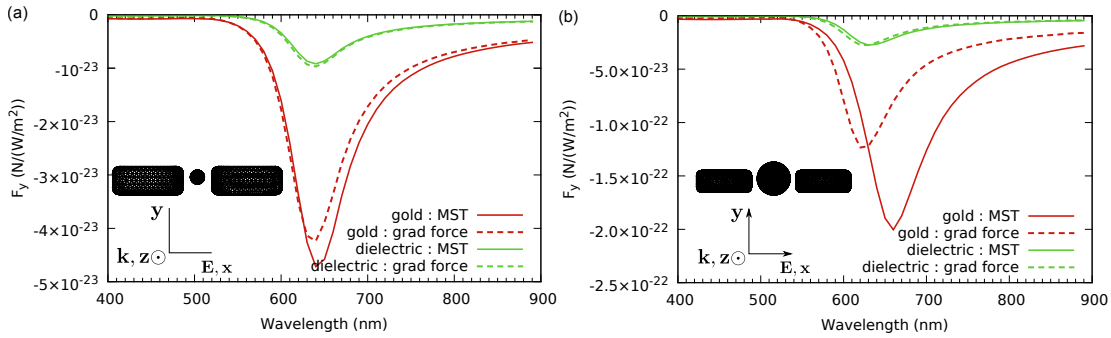
Figure 2.6 – Restoring forces on a nanoparticle displaced from the centre of a plasmonic gap antenna, computed using the Maxwell's stress tensor method and using the gradient force approximation. In (a), the gap size is 40 nm and the particle radius is 10 nm and in (b), they are 80 nm and 30 nm respectively. Glass and gold spheres are considered.

Figure 2.6 (a) shows the comparison between the forces calculated using the gradient force method and the Maxwell's stress tensor method for a gap of 40 nm and the displaced particle of radius 10 nm. We see that the gradient force approach is quite good for both the metallic (gold) particle and the dielectric (glass) particle, though the quantitative agreement is better for the latter. However, the situation is very different for the case of 80 nm gap and 30 nm radius shown in Fig. 2.6. Here, though the two methods show very similar results for the glass sphere, the mismatch is too high for the gold sphere. This shows that even when particles are much smaller than the wavelength of light, the full Maxwell stress tensor integral is required for accurate computation of the force.

2.2.2 Forces in dielectric media : The Abraham-Minkowski debate

Till now, we have been working with vacuum as the background medium while computing the forces. When we move to a dielectric background such as water where experiments are usually performed, there is confusion about the expression for the force. Fundamentally, this confusion arises from the two commonly used definitions for the momentum of light: the Abraham form $\mathbf{E} \times \mathbf{H}$ [181, 182] and the Minkowski form $\mathbf{D} \times \mathbf{B}$ [183].

In fact, there is a similar ambiguity in the definition of Poynting vector as well, and this can change the computed radiative power [184]. However, this is not an issue in practice since the scattering and absorption are usually computed normalised to the incident power, and using the same expression for all Poynting vectors takes care of the problem. However, the case of optical forces and torques is not that simple. Different forms of the stress tensor can result in different values of the force if computed by direct integration. The "correct" expression for stress tensor in dielectric media has thus been a topic of long standing controversy [145, 185, 186].
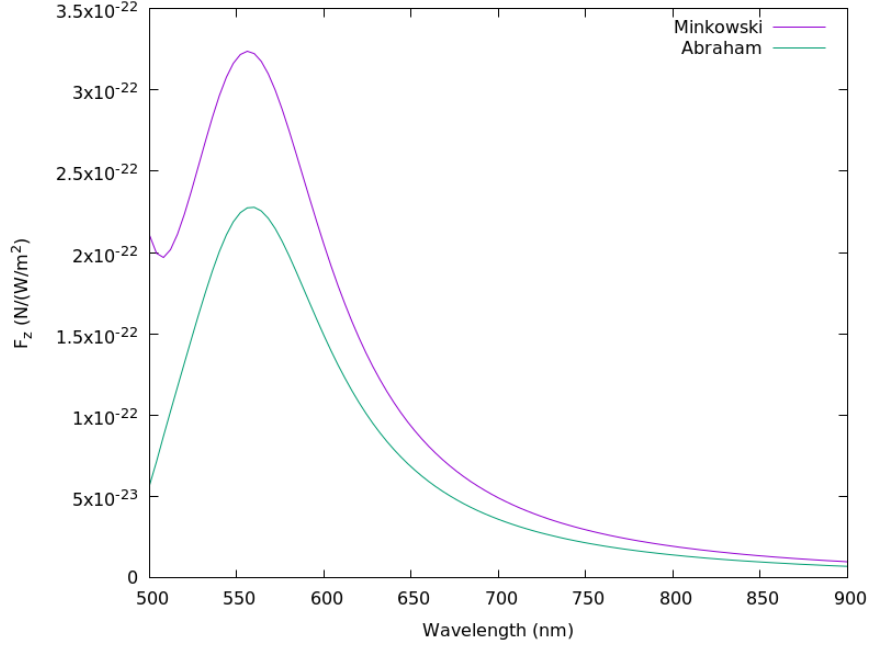
Figure 2.7 – Scattering force on a 50 nm radius gold sphere in water computed by integrating the Abraham and Minkowski stress tensors using the surface currents.

The expressions for the stress tensor under Abraham and Minkowski formulations are [187],

$$\sigma_{ij}^A = \varepsilon_0 E_i E_j + \frac{1}{\mu_0} B_i B_j - \frac{1}{2}\left(\varepsilon_0 |\mathbf{E}|^2 + \frac{1}{\mu_0}|\mathbf{B}|^2\right), \tag{2.13}$$

$$\sigma_{ij}^M = E_i D_j + H_i B_j - \frac{1}{2}\left(\mathbf{E}\cdot\mathbf{D} + \mathbf{H}\cdot\mathbf{B}\right). \tag{2.14}$$

Note that they both reduce to Eq. (2.7) in vacuum.

Since both stress tensors have similar forms except for constant multiplicative factors, they can both be integrated from the surface currents in similar fashion. The scattering force computed using the two methods for a gold sphere of 50 nm radius immersed in water and illuminated by a planewave is shown in Fig. 2.7. Not only do the Abraham and Minkowski forces differ in magnitude, there is a difference in the qualitative features of the force plot at lower wavelengths as well.

The reason for this difference is that stress tensors themselves do not contain the full picture. They might omit the momentum contributions from the material medium as well as from the interactions between light and the medium. Different stress tensors incorporate different aspects of the interaction, and neither of them can be used naively in all circumstances [185]. Care should hence be taken to include the material contributions correctly in addition to the stress tensor contribution while performing simulations in dielectric backgrounds, and the correct expression of the stress tensor should be used for the situation. Once this choice has been made, the integral of the stress tensor can be performed using the surface currents.

2.3   Polarisation charges

Applying an electric field on an object placed in a background of a different dielectric constant induces polarisation charges at the surfaces where permittivity changes abruptly. Numerical evaluation of polarisation charges at nanostructure surfaces provides insights into various aspects of the electromagnetic response of the nanostructures such as scattering, forces, coupling, second harmonic generation and Fano resonances [188–195].

From Maxwell's equations, the surface charge density at an interface can be expressed in terms of the discontinuity in the normal component of the electric field at the interface,

$$\sigma_p = \varepsilon_0 (\mathbf{E}_{\text{out}} - \mathbf{E}_{\text{in}}) \cdot \hat{\mathbf{n}}. \tag{2.15}$$

Using the normal component of the electric field found in Eq. (2.2a), this reduces to

$$\sigma_p = -\frac{i}{\omega} \left(\frac{1}{\varepsilon_{r,\text{out}}} - \frac{1}{\varepsilon_{r,\text{in}}} \right) \nabla \cdot \mathbf{J}. \tag{2.16}$$

Linearity of the RWG basis functions implies that the surface charge is constant over each triangle. Care should be thus taken to refine the SIE surface mesh around regions where the surface charge has large variations.

2.3.1   Results

As an example to show the usefulness of polarisation charge plots, we will look at the charges on the gap antennae we analysed in the previous section. The polarisation charges on the gap antennae with and without the gold sphere in the gap at the peak force wavelength are presented in Fig. 2.8. The charge distribution on the 40 nm gap antenna in Fig. 2.8 (a) is not
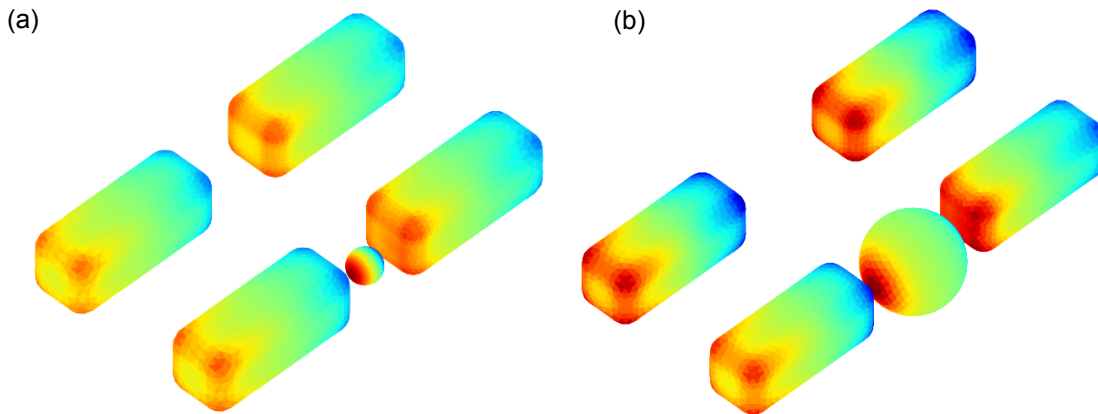

Figure 2.8 – Polarisation charges on the gap antennae in Fig. 2.6 at the peak force wavelength, with and without the gold nanoparticle in the gap. In (a), the gap size is 40 nm and the particle radius is 10 nm and in (b), they are 80 nm and 30 nm respectively.

modified significantly by the introduction of the sphere. However, there is visible change when the 60 nm gold sphere is introduced in the gap of the 80 nm gap antenna, shown in Fig. 2.8 (b). The polarisation charges on the antenna arms move closer towards the gap faces. The sphere is thus not just a passive element being influenced by the scattered fields from the gap antenna, but affects the antenna in return as well. This explains the failure of the gradient force approximation seen in Fig. 2.6.

2.4 Multipole moments

Though polarisation charges provide a good visualisation of the optical response of nanostructures, multipole analysis of induced charges and currents provides a more quantitative and physical understanding of the system [196–199]. Two different approaches are typically employed to obtain the multipolar decomposition of the optical response. One method involves decomposing the scattered field into the sum of orthogonal vector spherical harmonics, and retrieving the moments from the coefficients of the basis functions [144, 200–203]. In the second method, a series expansion is performed over the source currents, and the coefficients of the terms in the expansion give the multipole moments [144, 197, 202–205]. We follow the latter approach and attempt to express the multipole moments in terms of the surface currents. The derivation will be along the same lines as [144], but using the volume integral equations for electric field instead of the vector potential so that dielectric backgrounds can be dealt with easily. Also, since we are interested in optical frequencies, only non-magnetic ($\mu_r = 1$) media will be considered.

Using the volume integral equation for electric field [97], the scattered field due to an object in a volume V can be expressed in terms of the electric field within the scatterer as

$$\mathbf{E}^{sc}(\mathbf{r}) = k_0^2 \int_V \Delta\varepsilon(\mathbf{r}') \, \mathbf{G}^B(\mathbf{r}, \mathbf{r}') \, \mathbf{E}(\mathbf{r}') \, d\mathbf{r}' \,, \tag{2.17}$$

where k_0 is the vacuum wavenumber, $\Delta\varepsilon = \varepsilon_r - \varepsilon_B$ is the difference between the relative permittivities of the scatterer and the background (the dielectric contrast), and $\mathbf{G}^B$ is the dyadic Green's function of the background medium given by

$$\begin{aligned} \mathbf{G}^B(\mathbf{r}, \mathbf{r}') &= \left(\mathbf{1} + \frac{\nabla\nabla}{k_B^2}\right) g^B(\mathbf{r}, \mathbf{r}') \\ &= \left(\mathbf{1} + \frac{\nabla\nabla}{k_B^2}\right) \frac{\exp(ik_B s)}{4\pi s} \,, \end{aligned} \tag{2.18}$$

where k_B is the wavenumber in the background medium, and $s = |\mathbf{r} - \mathbf{r}'|$ is the distance between the source and observation points. We immediately see that the source of the scattered field is localised within the object since the dielectric contrast is zero outside. It should also be noted that this volume integral does not show any discontinuity across the interface since the electric field remains finite, and we can thus work with our integration volume entirely inside

the scatterer. Since the gradient operates on the observation coordinate $\mathbf{r}$ and the integral is over the source coordinate $\mathbf{r}'$, we can take the gradient operators outside the integral. We are interested in homogeneous domains with a constant dielectric contrast for each domain, and we can drop the explicit coordinate dependence to obtain,

$$
\begin{aligned}
\mathbf{E}^{sc}(\mathbf{r}) &= \left(\mathbf{1} + \frac{\nabla\nabla}{k_B^2}\right)\mathbf{e}^{sc}(\mathbf{r}) \\
&= \left(\mathbf{1} + \frac{\nabla\nabla}{k_B^2}\right)k_0^2 \int_V \Delta\varepsilon \, \frac{\exp(ik_B s)}{4\pi s}\mathbf{E}(\mathbf{r}')\,d\mathbf{r}'\,.
\end{aligned}
\tag{2.19}
$$

We will attempt to obtain a multipole expansion over $\mathbf{e}^{sc}$. Using Maxwell's equations, the electric field can be expressed in terms of the volume current density $\mathbf{j}$ as

$$
\mathbf{E}(\mathbf{r}') = \frac{i}{\omega\varepsilon_0(\varepsilon_r - 1)}\mathbf{j}(\mathbf{r}')\,.
\tag{2.20}
$$

Plugging this in the previous equation and using the vacuum dispersion relation $\omega = k_0 c$, we have

$$
\mathbf{e}^{sc}(\mathbf{r}) = i\omega\mu_0 \int_V \frac{\exp(ik_B s)}{4\pi s}\frac{\varepsilon_r - \varepsilon_B}{\varepsilon_r - 1}\mathbf{j}(\mathbf{r}')\,d\mathbf{r}'\,.
\tag{2.21}
$$

We now define the contrast current density,

$$
\mathbf{j}_c(\mathbf{r}') = \frac{\varepsilon_r - \varepsilon_B}{\varepsilon_r - 1}\mathbf{j}(\mathbf{r}')\,.
\tag{2.22}
$$

Note that the contrast current density would have been equal to the volume current density if the background was vacuum. Thus the dielectric background has been taken into consideration in a very natural fashion. We finally obtain,

$$
\mathbf{e}^{sc}(\mathbf{r}) = i\omega\frac{\mu_0}{4\pi}\int_V \frac{\exp(ik_B s)}{s}\mathbf{j}_c(\mathbf{r}')\,d\mathbf{r}'\,.
\tag{2.23}
$$

The integrand is now identical to the one in Eq. (9.3) of [144], the quantity over which the series expansion is performed - with the only difference that the current density has been replaced by the contrast current density. Under the far-field approximation, we have

$$
s \approx r - \hat{\mathbf{r}}\cdot\mathbf{r}'\,,
\tag{2.24}
$$

where $\mathbf{r} = r\hat{\mathbf{r}}$. Under this approximation, the scattered field reduces to

$$
\mathbf{e}^{sc}(\mathbf{r}) = i\omega\frac{\mu_0}{4\pi}\frac{\exp(ik_B r)}{r}\int_V \mathbf{j}_c(\mathbf{r}')\exp\!\left(-ik_B\hat{\mathbf{r}}\cdot\mathbf{r}'\right)d\mathbf{r}'\,.
\tag{2.25}
$$

Finally, we will perform a series expansion over the oscillating exponential term inside the

integral to obtain,

$$\mathbf{e}^{sc}(\mathbf{r}) = i\omega \frac{\mu_0}{4\pi} \frac{\exp(ik_B r)}{r} \sum_n \frac{(-ik)^n}{n!} \int_V \mathbf{j}_c(\mathbf{r}')(\hat{\mathbf{r}} \cdot \mathbf{r}')^n \, d\mathbf{r}' . \tag{2.26}$$

The $n = 0$ term gives the electric dipole,

$$\mathbf{p} = \frac{i}{\omega} \int_V \mathbf{j}_c(\mathbf{r}') \, d\mathbf{r}' , \tag{2.27}$$

where the prefactor has been added to match convention, so that we obtain the electric field due to the dipole as

$$\mathbf{E}(\mathbf{r}) = \omega^2 \mu_0 \mathbf{G}^B(\mathbf{r}, \mathbf{r}') \cdot \mathbf{p}(\mathbf{r}'), \tag{2.28}$$

and the scattered power as

$$P = \frac{\mu_0 \omega^4 \sqrt{\varepsilon_B}}{12\pi c} |\mathbf{p}|^2. \tag{2.29}$$

We will now convert the volume integral in Eq. (2.27) into a surface integral.

$$\begin{aligned}
\mathbf{p} &= \frac{i}{\omega} \int_V \mathbf{j}_c(\mathbf{r}') \, d\mathbf{r}' \\
&= \frac{i}{\omega} \frac{\varepsilon_r - \varepsilon_B}{\varepsilon_r - 1} \int_V \mathbf{j}(\mathbf{r}') \, d\mathbf{r}' \\
&= \frac{i}{\omega} \frac{\varepsilon_r - \varepsilon_B}{\varepsilon_r} \int_V \nabla' \times \mathbf{H}(\mathbf{r}') \, d\mathbf{r}' \\
&= \frac{i}{\omega} \frac{\varepsilon_r - \varepsilon_B}{\varepsilon_r} \oint_{\partial V^-} \hat{\mathbf{n}} \times \mathbf{H}(\mathbf{r}') \, dS' \\
&= \frac{i}{\omega} \frac{\varepsilon_r - \varepsilon_B}{\varepsilon_r} \oint_{\partial V^-} \mathbf{J}(\mathbf{r}') \, dS' .
\end{aligned} \tag{2.30}$$

The dipole moment can thus be found by integrating the surface electric current over the domain boundary. Note that the integration surface lies just inside the volume (∂V^-) since **J** switches sign on crossing the interface. Next, we will find an alternate expression for the dipole moment from the polarisation charges. We start with the identity

$$\nabla' \cdot \left[x' \frac{\varepsilon_r(\mathbf{r}') - \varepsilon_B}{\varepsilon_r(\mathbf{r}') - 1} \mathbf{j}(\mathbf{r}') \right] = x' \nabla' \cdot \left[\frac{\varepsilon_r(\mathbf{r}') - \varepsilon_B}{\varepsilon_r(\mathbf{r}') - 1} \mathbf{j}(\mathbf{r}') \right] + \frac{\varepsilon_r(\mathbf{r}') - \varepsilon_B}{\varepsilon_r(\mathbf{r}') - 1} j_x(\mathbf{r}') . \tag{2.31}$$

Now, let us integrate this identity over a volume which includes the object and its boundary (V^+). That is, unlike the previous case, the bounding surface is the outer boundary (∂V^+) rather than the inner boundary (∂V^-). The LHS of the identity gets converted into a surface integral

by Gauss' theorem, but the integrand on the surface is identically zero because $\varepsilon_r(\mathbf{r}') = \varepsilon_B$ outside. The integral on the second term of the RHS is seen to be $-i\omega p_x$ by comparison with Eq. (2.27). Thus we have

$$
\begin{aligned}
p_x &= -\frac{i}{\omega} \int\limits_{V^+} x' \nabla' \cdot \left[\frac{\varepsilon_r(\mathbf{r}') - \varepsilon_B}{\varepsilon_r(\mathbf{r}') - 1} \mathbf{j}(\mathbf{r}') \right] \mathrm{d}\mathbf{r}' \\
&= -\varepsilon_0 \int\limits_{V^+} x' \nabla' \cdot \left[(\varepsilon_r(\mathbf{r}') - \varepsilon_B) \mathbf{E}(\mathbf{r}') \right] \mathrm{d}\mathbf{r}' \,.
\end{aligned}
\tag{2.32}
$$

The integrand on the RHS vanishes everywhere except at the surface where it has delta function behaviour. Integrating the delta function carefully, we obtain

$$
p_x = \varepsilon_0 (\varepsilon_r - \varepsilon_B) \oint\limits_{\partial V^-} x' \mathbf{E}(\mathbf{r}') \cdot \hat{\mathbf{n}} \, \mathrm{d}\mathbf{r}' \,.
\tag{2.33}
$$

Note that the integral has to be done over the inner surface, since the normal component of the electric field is discontinuous across the interface. Using Eq. (2.2a) for the perpendicular component of electric field,

$$
p_x = -i \frac{\varepsilon_r - \varepsilon_B}{\omega \epsilon_r} \oint x' \nabla' \cdot \mathbf{J}(\mathbf{r}') \, \mathrm{d}S' \,.
\tag{2.34}
$$

This could also have been obtained by integrating Eq. (2.30) by parts. Finally, by comparing with Eq. (2.16), we have

$$
p_x = \varepsilon_B \oint x' \sigma_p(\mathbf{r}') \, \mathrm{d}S' \,.
\tag{2.35}
$$

By repeating similar steps for y and z and combining the results, we obtain the following expression for the dipole moment in terms of the polarisation charges:

$$
\mathbf{p} = \varepsilon_B \oint \mathbf{r}' \sigma_p(\mathbf{r}') \, \mathrm{d}S' \,.
\tag{2.36}
$$

That is, the dipole moment is the position moment of the polarisation charges as we have in electrostatics, but multiplied by a factor of ε_B. The multiplicative factor is not of particular physical significance since it could have been absorbed by putting a different prefactor in Eq. (2.27), but is required for consistency.

We now move on to the $n = 1$ term in the series expansion in Eq. (2.26), $\int\limits_V \mathbf{j}_c(\mathbf{r}')(\hat{\mathbf{r}} \cdot \mathbf{r}') \, \mathrm{d}\mathbf{r}'$. Following [144], we write this as the sum of two quantities which are symmetric and antisymmetric on exchanging $\mathbf{j}_c$ and $\mathbf{r}'$,

$$
(\hat{\mathbf{r}} \cdot \mathbf{r}') \mathbf{j}_c = \frac{1}{2} \left[(\hat{\mathbf{r}} \cdot \mathbf{r}') \mathbf{j}_c + (\hat{\mathbf{r}} \cdot \mathbf{j}_c) \mathbf{r}' \right] + \frac{1}{2} (\mathbf{r}' \times \mathbf{j}_c) \times \hat{\mathbf{r}}.
\tag{2.37}
$$

The two terms correspond to electric quadrupole and magnetic dipole response, respectively.

The magnetic dipole moment is given by

$$\mathbf{m} = \frac{1}{2} \int_V \mathbf{r}' \times \mathbf{j}_c(\mathbf{r}') \, \mathrm{d}\mathbf{r}' . \tag{2.38}$$

We will convert this into a surface integral by first expressing the contrast current in terms of the curl of the magnetic field,

$$\mathbf{m} = \frac{1}{2} \frac{\varepsilon_r - \varepsilon_B}{\varepsilon_r} \int_V \mathbf{r}' \times \left(\nabla' \times \mathbf{H}(\mathbf{r}') \right) \mathrm{d}\mathbf{r}' . \tag{2.39}$$

We now manipulate the integrand using vector calculus identities and Maxwell's equations,

$$\mathbf{r}' \times \left(\nabla' \times \mathbf{H} \right) = \nabla' \left(\mathbf{r}' \cdot \mathbf{H} \right) + \nabla' \times \left(\mathbf{r}' \times \mathbf{H} \right) + \mathbf{H} \left(\nabla' \cdot \mathbf{r}' \right) - 2 \left(\mathbf{H} \cdot \nabla' \right) \mathbf{r}'$$

$$= \nabla' \left(\mathbf{r}' \cdot \mathbf{H} \right) + \nabla' \times \left(\mathbf{r}' \times \mathbf{H} \right) - \frac{i}{\omega \mu_0} \left(\nabla' \times \mathbf{E} \right) . \tag{2.40}$$

Every term on the RHS is a gradient or curl of some quantity, and their volume integrals can be converted into surface integrals,

$$\mathbf{m} = \frac{1}{2} \frac{\varepsilon_r - \varepsilon_B}{\varepsilon_r} \left[\oint \left(\mathbf{r}' \cdot \mathbf{H}(\mathbf{r}') \right) \mathrm{d}\mathbf{S}' + \oint \mathrm{d}\mathbf{S}' \times \left(\mathbf{r}' \times \mathbf{H}(\mathbf{r}') \right) - \frac{i}{\omega \mu_0} \oint \mathrm{d}\mathbf{S}' \times \mathbf{E}(\mathbf{r}') \right] . \tag{2.41}$$

Though the result is cumbersome, the integrals can be expressed in terms of $\mathbf{J}$ and $\mathbf{M}$, and integrated analytically using Eqs. (2.5a) to (2.5d). The power scattered by the magnetic dipole is

$$P = \frac{\mu_0 \omega^4 \varepsilon_B^{3/2}}{12 \pi c^3} |\mathbf{m}|^2. \tag{2.42}$$

We finally turn our attention to the remaining electric quadrupole term. Inside the domain, we have

$$\nabla \cdot \left[x' \left(\mathbf{r}' \cdot \hat{\mathbf{r}} \right) \mathbf{j}_c \right] = \left(\hat{\mathbf{r}} \cdot \mathbf{r}' \right) j_{c,x} + \left(\hat{\mathbf{r}} \cdot \mathbf{j}_c \right) x' . \tag{2.43}$$

Thus,

$$\int_V \left[\left(\hat{\mathbf{r}} \cdot \mathbf{r}' \right) j_{c,x} + \left(\hat{\mathbf{r}} \cdot \mathbf{j}_c \right) x' \right] \mathrm{d}\mathbf{r}' = \oint_{\partial V} x'(\mathbf{r}' \cdot \hat{\mathbf{r}}) \, \mathbf{j}_c \cdot \mathrm{d}\mathbf{S}' . \tag{2.44}$$

Combining the similar results for y and z, and expressing the contrast current in terms of the

electric field, we obtain the complete integral

$$\int_V \frac{1}{2} \left[(\hat{\mathbf{r}} \cdot \mathbf{r}') \mathbf{j}_c + (\hat{\mathbf{r}} \cdot \mathbf{j}_c) \mathbf{r}' \right] \, \mathrm{d}\mathbf{r}' = -\frac{i\omega}{2} \varepsilon_0 (\varepsilon_r - \varepsilon_B) \oint_{\partial V} \mathbf{r}' (\hat{\mathbf{r}} \cdot \mathbf{r}') \, (\mathbf{E} \cdot \mathrm{d}\mathbf{S}')$$

$$= -\frac{i\omega}{2} \varepsilon_B \oint \mathbf{r}' (\hat{\mathbf{r}} \cdot \mathbf{r}') \sigma_p(\mathbf{r}') \, \mathrm{d}S \, . \tag{2.45}$$

We have managed to express the integral in terms of the polarisation charges as well. Based on this, we can define the quadrupole moment tensor $\mathbf{Q}$, with components

$$Q_{ij} = \varepsilon_B \oint (3 x_i' x_j' - r'^2 \delta_{ij}) \sigma_p(\mathbf{r}') \, \mathrm{d}\mathbf{r}' \, . \tag{2.46}$$

The term being subtracted has been introduced to make the tensor traceless by convention [144], and does not affect the fields in the far-field radiation zone. The power radiated by the quadrupole is

$$P = \frac{\mu_0 \omega^6 \varepsilon_B^{3/2}}{1440 \pi c^3} |\mathbf{Q}|^2 \, . \tag{2.47}$$

Electric dipole, magnetic dipole and electric quadrupole moments have thus been expressed as surface integrals using the surface currents. In principle, further higher order moments can also be computed following the same procedure, but it gets more and more cumbersome. Fortunately, the contributions from the higher order moments are expected to be small especially when the structure is subwavelength, according to the series expansion.

2.4.1 Results

We will first look at the moments on the gold dolmen structure in the inset of Fig. 2.9 (a). The dolmen is composed of two vertical bars and a horizontal bar, each of dimensions 100 nm × 40 nm × 40 nm. The vertical bars are separated by a gap of 60 nm. The horizontal bar has been displaced from the centre of the gap between the vertical bars in plane by 20 nm along y and out of plane (along z) by 50 nm so that the gap between the horizontal bar and the vertical bars is 10 nm. The system is simulated with water ($\varepsilon_B = 1.33^2$) as the background medium, and the permittivity data for gold is taken from Ref. [175]. The dolmen is illuminated by a planewave propagating along $-z$ and polarised along x.

The electric dipole, electric quadrupole and magnetic dipole moments for the system are plotted in Fig. 2.9 (a). Since the moments themselves have different units, the radiated power due to the multipoles is plotted instead, to be able to understand their relative magnitudes. The sum of the radiated powers due to the three is also plotted. In addition, the scattering cross section of the dolmen is computed by integrating the Poynting vector in the far field and
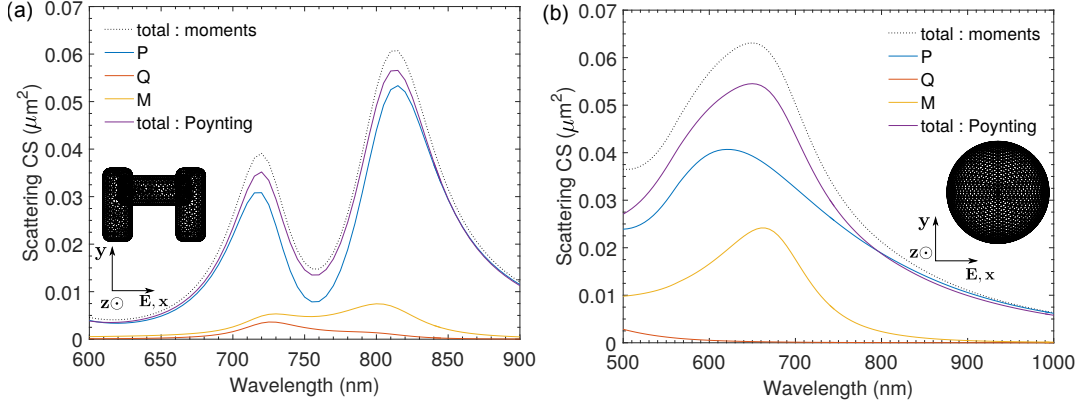
Figure 2.9 – Electric dipole (P), magnetic dipole (M) and electric quadrupole (Q) moments plotted in units of scattering cross section. The sum of the scattering cross sections for the three moments and the scattering cross section found by integrating the Poynting vector in the far field are also shown for comparison. (a) Gold dolmen structure in water with arms of dimensions 100 nm × 40 nm × 40 nm. The horizontal rod is displaced from the centre of the pair of vertical bars by 20 nm along y and by 50 nm along z. The vertical bars have a 60 nm gap between them. The system is illuminated by a planewave in the $-z$ direction polarised along x. (b) Silicon sphere of radius 75 nm placed in silica.

normalising the result to the incident field Poynting vector,

$$C_{sc} = \frac{\oint \frac{1}{2} Re\left[\mathbf{E}_{sc} \times \mathbf{H}_{sc}^*\right] \cdot d\mathbf{S}}{\left|\frac{1}{2} Re\left[\mathbf{E}_{in} \times \mathbf{H}_{in}^*\right]\right|} \; . \tag{2.48}$$

This result is also shown for comparison.

The first spectral feature which is immediately evident is the Fano resonance, which is expected for dolmen structures [206–208]. The scattering cross section and the electric dipole moment show two distinct peaks with the Fano dip between them. The electric dipole gives the bulk of the contribution towards the scattering, except near the Fano dip where the magnetic dipole and electric quadrupole terms become relatively significant as well. The dip in the scattering cross section is shallower than the electric dipole moment alone would indicate, due to the contribution from the magnetic dipole and electric quadrupole terms.

Although the three moments provide a good qualitative description of the spectrum, the quantitative agreement is not so good. In fact, adding up the scattering contributions from the three moments gives a higher result than the far field scattering cross section itself. This is because, unlike the multipole moments defined using vector spherical harmonics, the moments found here do not give orthogonal fields in the radiation zone and directly adding up the scattering cross sections is incorrect in general. We can easily see that this has to be the case by performing a coordinate transformation. Equation (2.27) is independent of the choice of origin of the coordinate system and arbitrary translation of the origin leaves **p** invariant.

However, **m** does change with the choice of the origin as evident from Eq. (2.38). One could in principle perform a translation of the coordinate system origin with a magnitude which is large enough to make the radiated power due to the magnetic dipole itself higher than the scattering cross section. The resolution is thus to accept that the higher order terms which have not been considered here result in radiated fields which are non-orthogonal, and modify the scattering cross section through cross terms. As the size of the nanostructure becomes larger, the contribution of the higher order terms is going to increase as well. Care must thus be taken while evaluating the magnitudes of the moments, especially for large structures. In particular, for asymmetric structures, the choice of origin should be considered carefully to extract useful physical information from the moments.

The next system we look at is a silicon sphere (permittivity data taken from [209]) of radius 75 nm placed in silica ($\varepsilon_B = 1.5^2$). The sphere is illuminated by a planewave propagating along z and polarised along x. The origin of the coordinate system is at the centre of the sphere. Due to symmetry, the induced electric dipole is expected to be along x, the magnetic dipole to be along y, and the electric quadrupole to have only xz- and zx-components. These conditions were verified to be satisfied from the numerical results which are not shown here. The scattering cross sections computed using the different moments are plotted in Fig. 2.9 (b). The magnetic dipole is now quite strong throughout the wavelength range, and results in the scattering peak showing a significant red shift compared to the dipole moment itself. The qualitative features of the scattering spectrum can be explained well using the multipolar moments.

This example illustrates the utility of multipole moments. We will study polarisation charges and electric dipole and quadrupole moments in more detail in Section 8.3.

2.5 Conclusion

We have developed a novel formalism for the calculation of optical forces and torques, polarisation charges and multipole moments utilising the SIE surface currents. The method is straightforward, flexible and bypasses some numerical steps to allow accurate and efficient computation. In particular, all the calculations for arbitrarily shaped objects only require the SIE surface mesh discretisation. We have applied this formalism to compute the optical forces on some simple as well as complicated systems to prove its validity and accuracy by comparing it to existing calculations. We have also shown how polarisation charges and multipole moments provide valuable physical insights into the optical response of plasmonic systems. These tools thus promise utility in improving the efficiency and accuracy as well as the understanding of SIE simulations, and it would be useful to extend the surface current integral method for computing other physical quantities.

3 Optimisation of the SIE integration procedure

In this chapter, we study the convergence of the integrals in the SIE formulation. We analyse how the numerical quadratures used to compute the integrals affect the accuracy of the SIE matrix elements and, in turn, that of the physical quantities calculated using the method. Based on these studies, we propose an optimised algorithm for evaluation of the integrals, which improves the accuracy of the results without significantly increasing the calculation overhead. Parts of this chapter were published in a peer-reviewed journal article [210].

3.1 Introduction

Even though the surface integral equations themselves are completely accurate within the realm of classical electrodynamics, any numerical implementation would only be able to solve them approximately. The various fields and currents are expanded in terms of a finite number of basis functions which can only approximate the actual values. There are multiple approaches to address this problem. One method used to tackle this issue in finite element-based methods in electromagnetics and other fields is to use basis functions which are of higher order than linear [87, 211]. The higher order basis functions can approximate the real fields more closely than constant or linear functions. When used in conjunction with curved isoparametric elements to describe the domain boundaries, very good geometrical and physical agreement can be achieved between the basis functions and the fields [212, 213]. Alternately, one could make the simulation mesh finer and finer so that the variations of the geometry and the field over a mesh element are negligible. Unfortunately, these approaches are complicated and increase computational costs tremendously in three dimensional problems [87]. In addition, the 4-dimensional integrals required in the calculation of the matrix elements involving the Green's tensor have to be done numerically. If the scatterer surface is discretised into N elements, $O(N^2)$ such integrals will have to be computed, and using complicated algorithms to calculate the integrals accurately can be prohibitively expensive. It is therefore desirable to use low-order integration routines as long as it does not compromise the accuracy, and even validity, of the results. These integration problems are magnified by the singular nature of the integrand for some integrals involving overlapping or nearby elements.

In the general context of the method of moments, much work has been dedicated to improving the integral accuracy using schemes of singularity subtraction [98, 140, 214, 215] or improved numerical integration [216, 217].

Here we focus specifically on the relevance of these problems for the modelling of the optical properties of metallic nanostructures. We study the link between numerical quadrature order and integral accuracy, and how it relates to the accuracy of the physical quantities calculated by SIE. Since we are mostly interested in finely meshed sub-wavelength structures in plasmonics, wave effects due to the change of phase of the Green's tensor over a triangular element are not of primary concern. However, the singular behaviour of the Green's tensor at the source causes a large variation in amplitude over triangular elements close to it. It is this latter effect which is numerically more relevant in plasmonics. Hence we will be addressing specifically the geometric singularities rather than wave effects.

3.2   Evaluation of D and K integrals for the SIE matrix

The optical response of nanostructures to arbitrary illuminations is contained in their **D** and **K** matrices. We refer the reader to Section 1.2 for their definition and derivation. The evaluation of **D** and **K** matrix elements require 4D integrals according to Eqs. (1.12a) and (1.12b), which are performed as successive 2D integrals over the source and test triangles. Two types of 2D numerical quadratures for the triangle will be considered to study the effect of the number of integration points on accuracy:

- Symmetrical Gaussian triangular quadratures as derived in Ref. [218], which will be called Dunavant quadrature for short. The quadrature orders used here are $n_O = 1, 2, 3, 4, 5, 6, 7, 10, 13, 17$ and 19, which correspond to $N_q = 1, 3, 4, 6, 7, 12, 13, 25, 37, 61$ and 73 integration points, respectively. The quadrature points for $n_O = 5$ ($N_q = 7$) and $n_O = 17$ ($N_q = 61$) are shown in Fig. 3.1 (a) and (b) respectively. The quadrature points can be seen to follow all the symmetries of the triangle. However, they are not placed on the triangle uniformly. For large n_O, there are more points far from the centre of the triangle, for example. It should be noted that the different quadrature points are assigned different weights during integration.

- Uniform subdivision of the triangle, consisting of subdividing each edge into n elements, resulting in dividing the area into n^2 congruent sub-triangles. The centres of the sub-triangles are the $N_q = n^2$ quadrature points. The quadrature orders used are 21, 30 and 40, corresponding to $N_q = 441, 900$ and 1600 integration points, respectively. The quadrature points for $n_O = 21$ ($N_q = 441$) are shown in Fig. 3.1 (c). The points are distributed symmetrically and uniformly, and are assigned identical weights during integration.

Note that for a given N_q, the total number of quadrature points for the 4D integral is N_q^2.
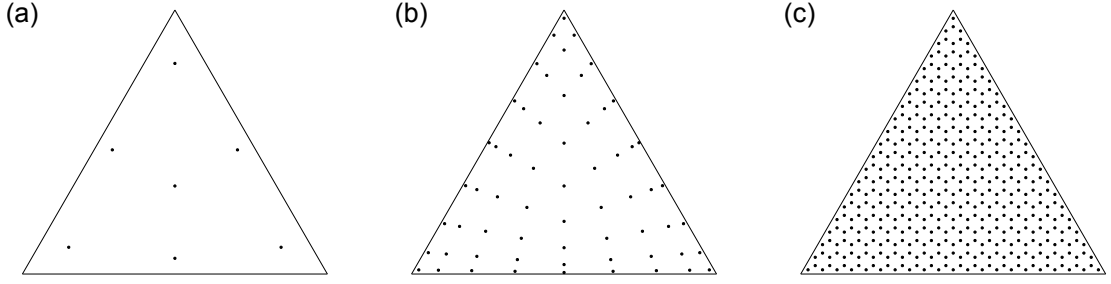
Figure 3.1 – Quadrature points for (a) Dunavant quadrature of order $n_O = 5$ ($N_q = 7$), (b) $n_O = 17$ ($N_q = 61$), and (c) uniform subdivision of order $n_O = 21$ ($N_q = 441$).

The standard singularity subtraction (SSS) scheme is used for both **D** and **K** integrals. Additionally, the following techniques were also implemented to improve the accuracy:

First, within the SSS scheme, the double integrals involving $1/(4\pi R)$ which is the dominant term in the singular Green's function in Eq. (1.14) can be computed entirely analytically for identical triangles in **D**, using the formulae of Ref. [219]. The remaining integral involving $G^i(R) - 1/(4\pi R)$ is then integrated numerically without any singularity issues.

Second, for non-identical triangles, it has been pointed out by Yla-Oijala and Taskinen in Ref. [215] that there also remains a "small" logarithmic singularity for **K** associated with the second term in $G^i_{\text{sing}}(R)$, which may cause problems in the numerical integration over the test triangle. They also proposed to overcome this problem by changing the order of integration and replacing the outer integral (now over the source triangle) by a line integral over its edges (Eq. (22) in Ref. [215]). This approach was implemented and will be referred as the SSL method (singularity subtraction with line integral). In these cases, the line integral is computed using a standard Gauss-Legendre quadrature. The number of quadrature points on the line is chosen to be $N_l = 4n_O$, so that it is approximately equal to the number of points on the triangle for Dunavant quadratures. For example, for $n_O = 17$, we have $N_l = 68$ and $N_q = 61$.

3.3   Accuracy of the matrix elements

We first consider the accuracy of the **D** and **K** matrix elements used to construct the full SIE interaction matrix. We focus on the integrals involving the Green's function of the embedding domain (with relative permittivity chosen as $\epsilon_1 = 1$), as they are not strongly dependent on permittivity. For illustration purposes, we will consider a cuboid, shown in the inset of Fig. 3.2(d), as it provides a variety of configurations between pairs of elements. To avoid wave effects, the structure and thus the triangular elements are made much smaller than the simulation wavelength. The cuboid dimensions are 20 nm × 5 nm × 5 nm whereas the wavelength is 500 nm. The surface of the cuboid is discretised into 160 triangles. To study the accuracy of the reaction integrals, we classify the triangle pairs (T, T') into the following four groups, which we identified as having different convergence properties:

- Identical triangles, i.e. $T = T'$.

- Adjacent triangles, when T and T' share a common edge.

- Touching triangles, when T and T' share only a common vertex.

- Other triangles in all the other cases.

The cuboid example conveniently contains several pairs in each of these groups, including both coplanar, non-coplanar, and orthogonal configurations. The integral accuracy, as estimated from the relative error with respect to the value obtained for the largest quadrature order ($n_O = 19$), is studied as a function of the number of quadrature points N_q. Note however that computing times scale approximately quadratically with N_q for double integrals.

Fig. 3.2 shows the results obtained for the integrals pertaining to the **D** matrix. It is clear that the Dunavant quadratures outperform uniform quadratures significantly. This should not be surprising since the Dunavant quadrature is specifically designed to capture higher order polynomial approximations of the integrand with increasing order of integration [218]. We will therefore only focus on Dunavant quadratures in the rest of this study. Moreover, for all triangle pairs, relative errors of 10% or better are obtained even with a single integration point ($N_q = 1$). If a higher accuracy is required, then this is easily achieved with a small number of points for most triangle pairs, but convergence is slower for pairs with a common edge or vertex. Overall, using $N_q = 61$ (order 17) for these pairs and $N_q = 7$ (order 5) for the others will guarantee a relative error of 10^{-4} or better for the entire **D** matrix. In addition, for identical triangles, we compare in Fig. 3.2(a) the SSS method with the alternative approach with 4D analytical evaluation of the singular part of the integral [219]. The latter provides improved precision and is also marginally faster, so should clearly be preferred.

A similar study can be carried out for the **K** matrix, the results of which are shown in Fig. 3.3. The situation is slightly more complicated here. The integrals are zero for pairs of coplanar triangles [215], which includes identical triangles, so these special cases should not be calculated but enforced to be zero and are therefore excluded from the analysis. In addition, as seen in Fig. 3.3(a), a small number of integrals exhibit an abnormally large relative error. A closer look indicates that these problematic integrals are in fact much smaller in magnitude than the average integrals. This can be attributed to the cross product in Eq. (1.12b) – the magnitude of the **K** matrix integral is strongly dependent on the relative orientation of the two triangles and can become very small if one of the triangles is nearly coplanar to their relative position vector. The errors in these elements are thus not absolutely higher than the errors in the other elements of the matrix, and it is their low values which result in large relative error. We expect that these are unlikely to affect the final results. A fairer estimate of the error in this case is by normalising the absolute error to a typical magnitude of the **K** matrix, which we chose as the root-mean-square average of the modulus of the non-zero matrix elements. As seen in Fig. 3.3(a), this normalised error is of the same order as the relative error in most cases, but
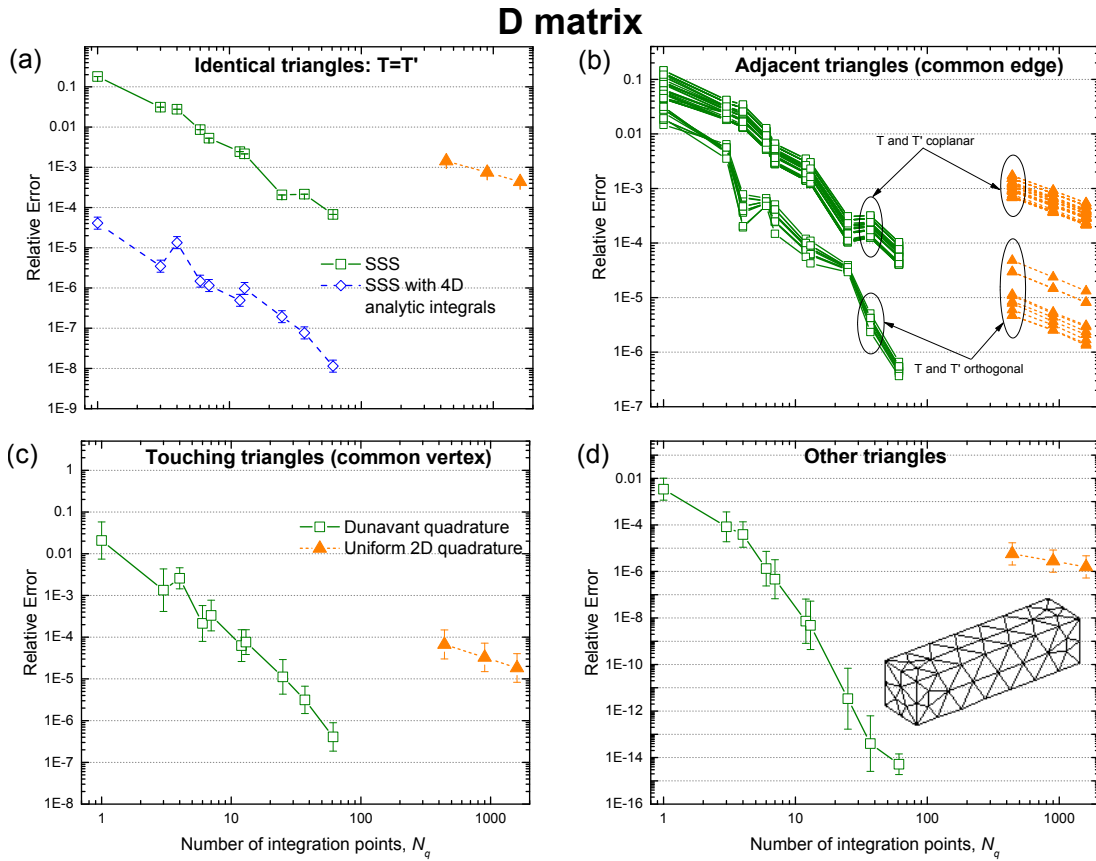
Figure 3.2 – Variation of the relative errors of the **D**-matrix integrals as a function of the number of quadrature points per triangle, for a cuboid mesh of 160 triangles as shown in (d). Four cases are distinguished depending on the pair of source and test triangles. (a) Identical triangles, (b) adjacent triangles sharing an edge, (c) touching triangles sharing a vertex, and (d) other triangles. The Dunavant quadrature (open symbols) is compared to the uniform triangular quadrature (filled triangles), which is clearly much worse. In (b), the data are shown explicitly for 48 individual pairs of triangles out of a total of 480 pairs with a common edge to highlight the two different groups corresponding to coplanar and non-coplanar pairs (the latter are located along sharp edges of the rectangle). In (a,c,d), we show the statistical analysis of the log of the error over 160 (a) or 1400 (c,d) pairs of triangles, i.e. the symbols represent the geometric mean and the error bars the standard deviation of the log of the error.

not affected by the small-magnitude integrals, so it is used in Fig. 3.3 to characterise the errors in the **K**-matrix elements.

It is clear from Fig. 3.3(b) that the integrals for **K** can be highly inaccurate in the case of triangles with a common edge. The normalised error can be of the order of 100% with one integration point and remains as large as $1 - 10\%$ with $N_q = 61$. This slow convergence is in fact associated with a remaining logarithmic singularity in the numerical integral, which can be overcome using the SSL method [215]. Figures 3.3(b,c) also show the errors obtained using this SSL method. It is evident that this method improves the accuracy for adjacent triangles,
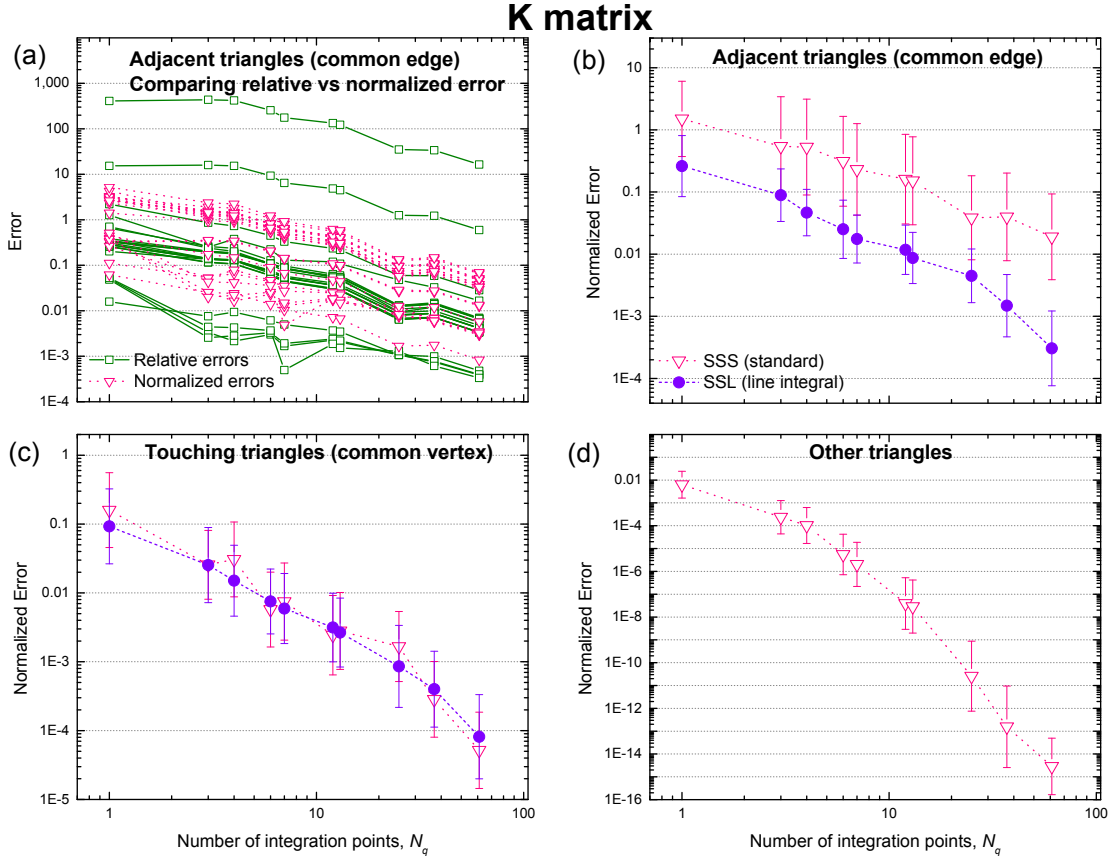
Figure 3.3 – Variation of the errors in the **K**-matrix integrals as a function of the number of integration points using Dunavant quadratures for the same cuboid mesh as in Fig. 3.2. To avoid artificial problems with low-magnitude matrix elements, we compute the normalised error as the absolute error normalised to the root mean square of the K-matrix elements. The two measures are compared in (a) for 21 pairs of adjacent triangles sharing an edge (which are necessary located along sharp edges). The other cases are shown in (b-d) as the statistical analysis of the log of the error, like in Fig. 3.2. In (b,c) the results from the standard singularity subtraction (SSS) and the alternative singularity subtraction with line integral (SSL) [215] are compared.

by a factor as large as 100 when using $N_l = 68$, $N_q = 61$, which results in errors of $0.01 - 0.1\%$ only. Interestingly, as seen in Fig. 3.3(c), for triangles with only a common vertex (and for all non-adjacent triangles), the line integral formulation does not offer any improvement and is therefore not necessary.

Finally, we note that Figs. 3.2 and 3.3 can also be obtained for the matrices/integrals corresponding to the metallic domain (with $\epsilon_2 = -8.5 + 0.4i$). They are not shown here as they are virtually identical to those obtained for the free-space Green's function. This can be understood because the integration problems are primary geometrical and associated with the $1/R$ dependence in the Green's function, not the $\exp(ikR)$ factor, which is anyway almost constant over a given triangle in meshes relevant to plasmonics.

3.4   Proposed algorithm

Based on these results, we propose the following algorithm to compute the SIE matrix elements to reasonable accuracy without making the computation too expensive. Two Dunavant quadratures are used depending on accuracy requirements: $n_O = 5$, $N_q = 7$ for low-precision, and $n_O = 17$, $N_q = 61$ for high-precision. The integrals are computed as follows:

- All the double integrals on identical triangles for **D** are computed from the full analytical formulae [219] for the singular part of the 4D integrals and numerically with $n_O = 17$ for the smooth part. A lowest order would give the same accuracy for small triangles, but would not result in significant speed improvements. For **K**, these integrals are zero.

- All the double integrals on triangles sharing a common edge are computed using the SSS method with high-precision ($n_O = 17$) quadrature for the numerical integration over test triangles. Moreover, for **K**, the SSL line integral formulation proposed in Ref. [215] is used, with a one-dimensional Gauss-Legendre quadrature with $N_l = 4n_O = 68$ integration points.

- All the double integrals on triangles sharing a common vertex are computed using the SSS method and $n_O = 17$. The line integral formulation is not needed for these.

- All other double integrals are computed using the SSS method and low-precision quadrature ($n_O = 5$).

- Finally, as pointed out in Ref. [215], the SSS method is not necessary for triangles that are sufficiently far from each other. No singularity subtraction is therefore applied if the following criterion is met: $d > (p_1 + p_2)/2$, where d is the centre-to-centre distance and p_1 and p_2 are the perimeters of T_1 and T_2. The criterion is geometric rather than wavelength-dependent because it is the fast variation in the Green's function due to the singular term that throttles the accuracy rather than wavelength-dependent phase effects when the nanostructures are finely meshed compared to the wavelength.

This approach, which we will denote for short acc-SIE (accurate SIE), guarantees a relative accuracy of 10^{-4} or better for the vast majority of integrals of the SIE matrix. It could be argued that such a fine accuracy is not needed in most practical cases, but it may be important for some aspects of the problem (such as absorption) and for some geometries (such as those with sharp edges). One could also adjust these choices to specific needs, but it should be noted that the limiting step for realistic calculations with a large number of degrees of freedom in the case of homogeneous domains is not the matrix calculation but its inversion. This is because only $O(N^2)$ matrix elements have to be computed for a structure discretised into N triangular elements whereas inverting the matrix requires $O(N^3)$ operations. Compromising on matrix accuracy may therefore not result in worthwhile gain in computing speed for challenging problems with many degrees of freedom. However, the situation could be different in the case of other media where Green's tensor calculation is itself a costly operation.
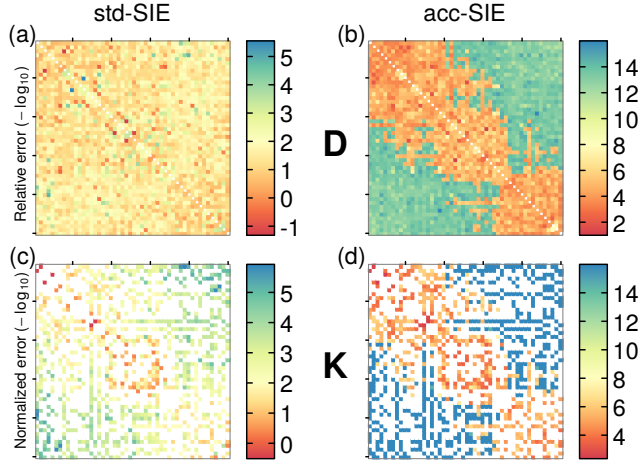
Figure 3.4 – Symmetry of the matrix elements for the cuboid mesh in Fig. 3.2(d) obtained from the coarse (std-SIE, $N_q = 1$, left) and optimised (acc-SIE, $N_q = 7, 61$ with SSL, right) methods presented in this paper. Only a subset of 50×50 elements is shown for clarity. The colour maps represent the number of digits agreement, i.e. $\alpha = -\log 10(\epsilon)$ for a given error ϵ between transposed elements. The relative error is considered for the **D** matrix (a,b), and the normalised error for the **K** matrix (c,d). Note the different scales in each panel, and that the error is larger than 100% ($\alpha < 0$) for some elements in (a,c).

3.5 Validation of the proposed implementation

We will now compare the performance of this proposed optimised algorithm with the approach previously used for plasmonics calculations (and denoted here std-SIE), where the SSL method is not used and numerical integrations are carried out with a single integration point ($N_q = 1$).

3.5.1 Symmetry of matrix elements

One relatively straightforward way to assess the accuracy of the SIE matrix is to check the symmetry properties of the matrix elements. In principle, both **D** and **K** should be symmetric, since the Green's tensor itself is symmetric between source and observation points in the case of homogeneous media. This is a consequence of electromagnetic reciprocity [220]. But numerically, the symmetry is broken when applying the singularity subtraction method, which involves integrating over one triangle analytically and the other numerically. The error in the symmetry of these matrices can therefore indicate their accuracy. Moreover, any significant breakdown of the symmetry could result in unphysical predictions (for example like negative absorption).

The degree of symmetry in the **D** and **K** matrix elements are shown in Fig. 3.4. It is evident that the acc-SIE method shows a much higher degree of symmetry compared to the coarse approach for all types of matrix elements. In particular, std-SIE outputs matrix elements might have a relative difference of more than 100% compared to their symmetric counterparts.

In comparison, all matrix elements found by acc-SIE are symmetric at least to the second decimal, and the bulk of the matrix elements are symmetric up to four digits or more.

3.5.2 Optical properties

We now move on to study the effects of integration quadrature on the accuracy of physical quantities calculated by SIE. We consider two sets of optical properties - optical cross sections and surface fields. The surface fields were obtained directly from the electric and magnetic surface currents using Eqs. (2.3a) and (2.3b). The extinction and absorption cross-sections are then derived by integrating the relevant Poynting vectors on the particle surface [221], namely:

$$\sigma_{\text{ext}} = -\frac{1}{2} \int_S \text{Re} \left[\left(\mathbf{E}_{\text{inc}} \times \mathbf{H}_{\text{surf}}^* + \mathbf{E}_{\text{surf}} \times \mathbf{H}_{\text{inc}}^* \right) \cdot \mathbf{n} \right] \mathrm{d}S, \tag{3.1a}$$

$$\sigma_{\text{abs}} = -\frac{1}{2} \int_S \text{Re} \left[\left(\mathbf{E}_{\text{surf}} \times \mathbf{H}_{\text{surf}}^* \right) \cdot \mathbf{n} \right] \mathrm{d}S, \tag{3.1b}$$

where $\mathbf{E}_{\text{inc}}$, $\mathbf{H}_{\text{inc}}$ are the incident fields. This provides a fast and accurate way of computing those important properties. From the surface fields, we can also derive the average field intensity enhancement factor as : $\langle |\mathbf{E}_{\text{surf}}|^2 / |E_0|^2 \rangle$, where $\langle \rangle$ denotes surface averaging. The parallel and perpendicular components may be considered separately.

We will study two systems relevant to plasmonics, a silver sphere of 30 nm radius and a tetrahedron of side 40 nm both embedded in water. Both systems are illuminated by plane waves incident in the z-direction and polarised along x. The relative permittivity of water is taken to be constant ($\epsilon = 1.77$) throughout the wavelength range, whereas the relative permittivity of silver is taken from the analytical fit to experimental data [36, 222].

The surface of the silver sphere is discretised by meshes of increasing finesse, and the structure is simulated using both the proposed optimised algorithm (acc-SIE) and the standard method (std-SIE). The exact optical response of the sphere on illumination by the plane wave is also calculated using Mie theory [36] and used as a benchmark. For the system under consideration, considering the first ten terms in the Mie expansion guarantees convergence to machine precision.

We first consider the wavelength-dependent far-field and near-field properties, which result from the surface plasmon resonances of the nanostructure. Fig. 3.5 summarises the main results for a representative coarse mesh ($N = 240$) and a finer mesh ($N = 840$). Both the std-SIE and acc-SIE approach predict the main features of the resonance, even with the relatively coarse mesh. We do however observe discrepancies when looking more closely at the details. Notably, the std-SIE approach exhibits significant errors in the quantitative determination of the absorption cross-section and of the perpendicular and parallel components of the average local field intensity enhancement factor (EF). The acc-SIE approach is much better in this respect, although the finer mesh ($N = 848$) is necessary to reproduce closely the exact results.
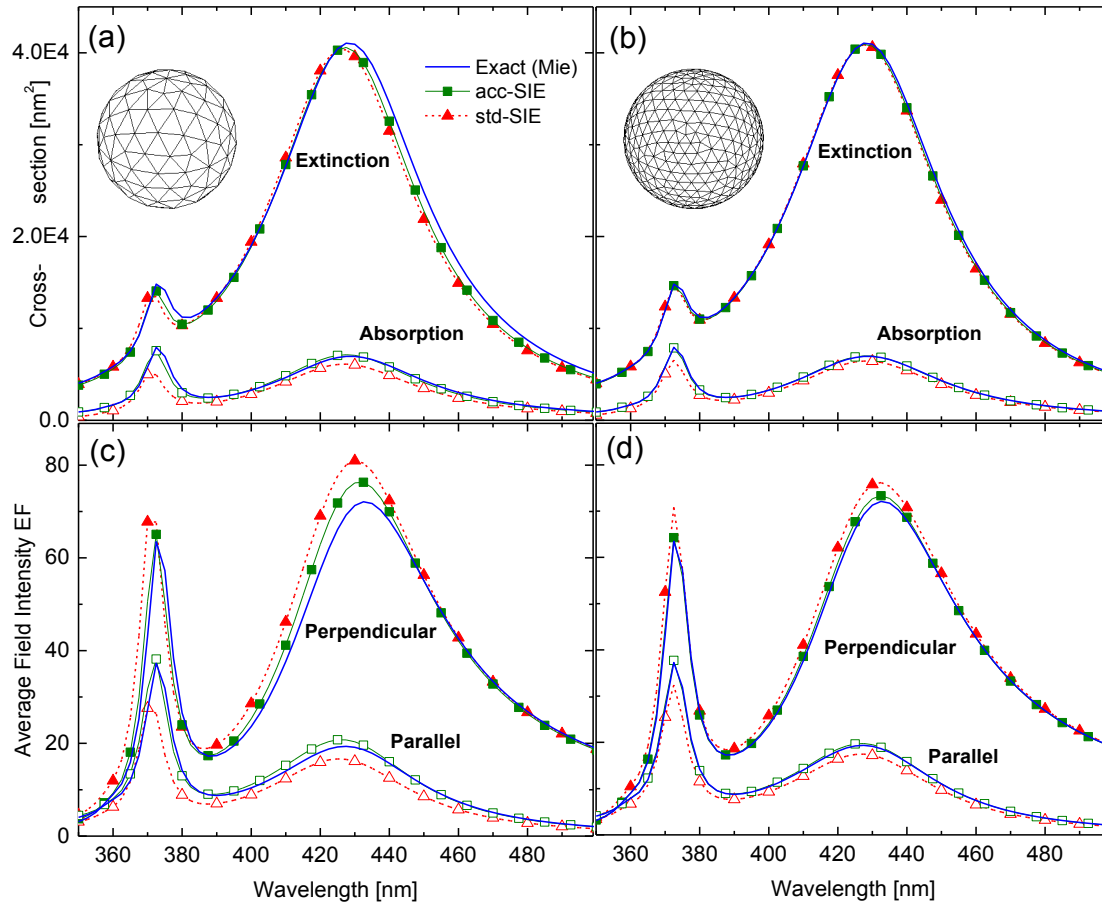
Figure 3.5 – Wavelength-dependence of (a-b) the far-field, and (c-d) near-field optical properties for a 60 nm diameter silver sphere in water modelled with SIE utilising the std-SIE and acc-SIE approaches. Panels (a,c) show the results for a coarse mesh ($N = 240$), whereas panels (b,d) have a finer mesh ($N = 848$).

This can be attributed to the fact that the coarser mesh is not yet an accurate approximation to the spherical geometry.

In order to study the accuracy more quantitatively, we compute the error in the optical properties for various mesh finesses. We focus on a single wavelength, 470 nm, which is close to resonance but not at resonance to avoid placing too much emphasis on errors associated with resonance shifts. The convergence properties of both approaches (std-SIE and acc-SIE) are presented in Fig. 3.6. It can be seen that the std-SIE approach provides an accuracy almost comparable to the acc-SIE approach for both the extinction cross-section and the average field intensity on the surface. However, it is an order of magnitude less accurate in terms of predicting the absorption cross-section and the parallel component of the surface field. Even with a mesh refinement of 2400 triangles, the std-SIE method shows an error of 5% or more whereas the acc-SIE is better by an order of magnitude. Although comparable accuracy could eventually be reached with the std-SIE approach, it would require a much finer mesh
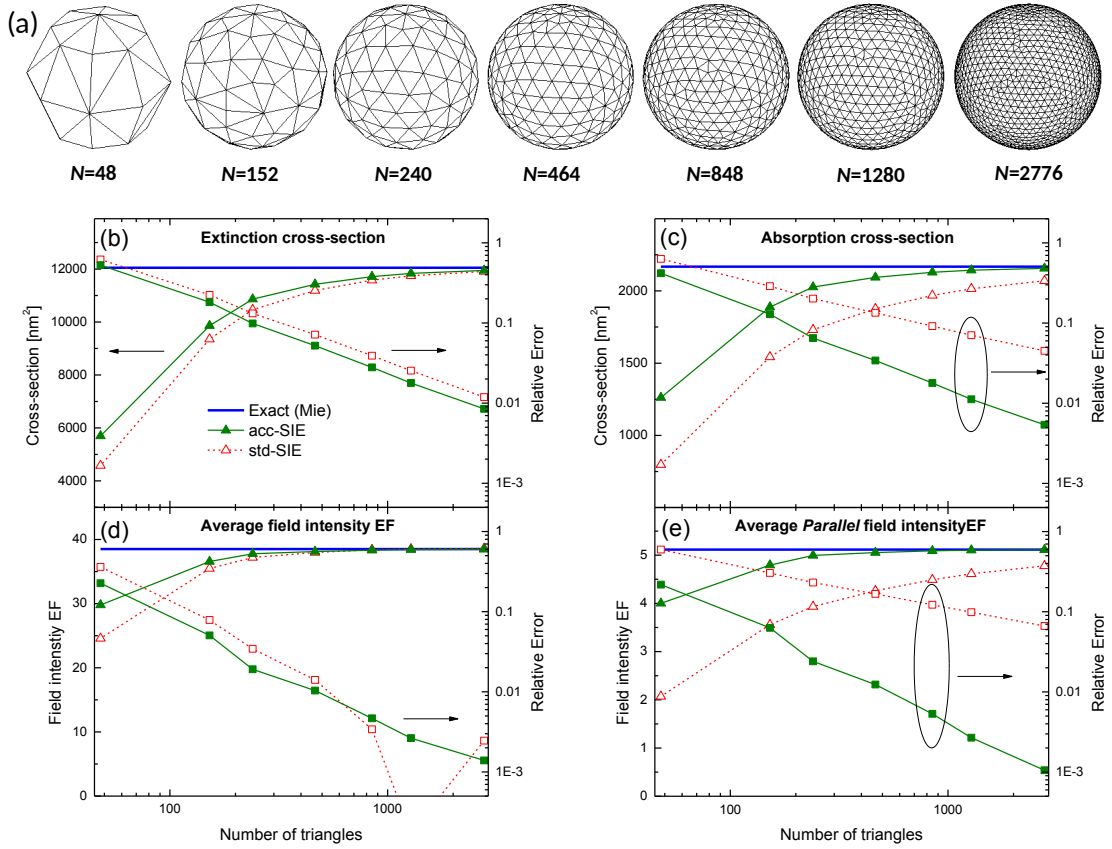
Figure 3.6 – Comparison between the results calculated by SIE utilising the std-SIE and acc-SIE approaches for a 60 nm diameter silver sphere in water at 470 nm, as a function of the number of triangles on the mesh. 7 meshes of increasing finesse are considered (a). The properties studied are the extinction (b) and absorption (c) cross sections, the average electric field intensity (d), and the average parallel electric field intensity (e). The relative error is obtained by comparison with the exact results of Mie theory.

and therefore, more CPU/memory resources. We note that the same conclusions would be obtained by doing the study exactly at resonance (429 nm, not shown here).

In contrast with a sphere, a tetrahedron contains sharp corners and edges around which the fields are expected to vary significantly. One therefore expects numerical predictions to be much more challenging. To capture the field variations reasonably well using linear basis functions, the mesh has to be refined near the edges and corners. The mesh we used to simulate the tetrahedron contains 4680 triangles, and is shown in Fig. 3.7(d). The wavelength dependence of the extinction and absorption cross sections and average surface field intensity as computed by both the std-SIE and acc-SIE approaches are plotted in Fig. 3.7. Despite the finesse of the mesh, the std-SIE approach clearly fails to predict any physical results. In particular, the absorption cross section is found to be negative. This sort of unphysical behaviour arising from the inaccuracy of SIE using coarse quadratures has been reported before [223]. In comparison, the acc-SIE approach shows a smooth behaviour without any such glaring
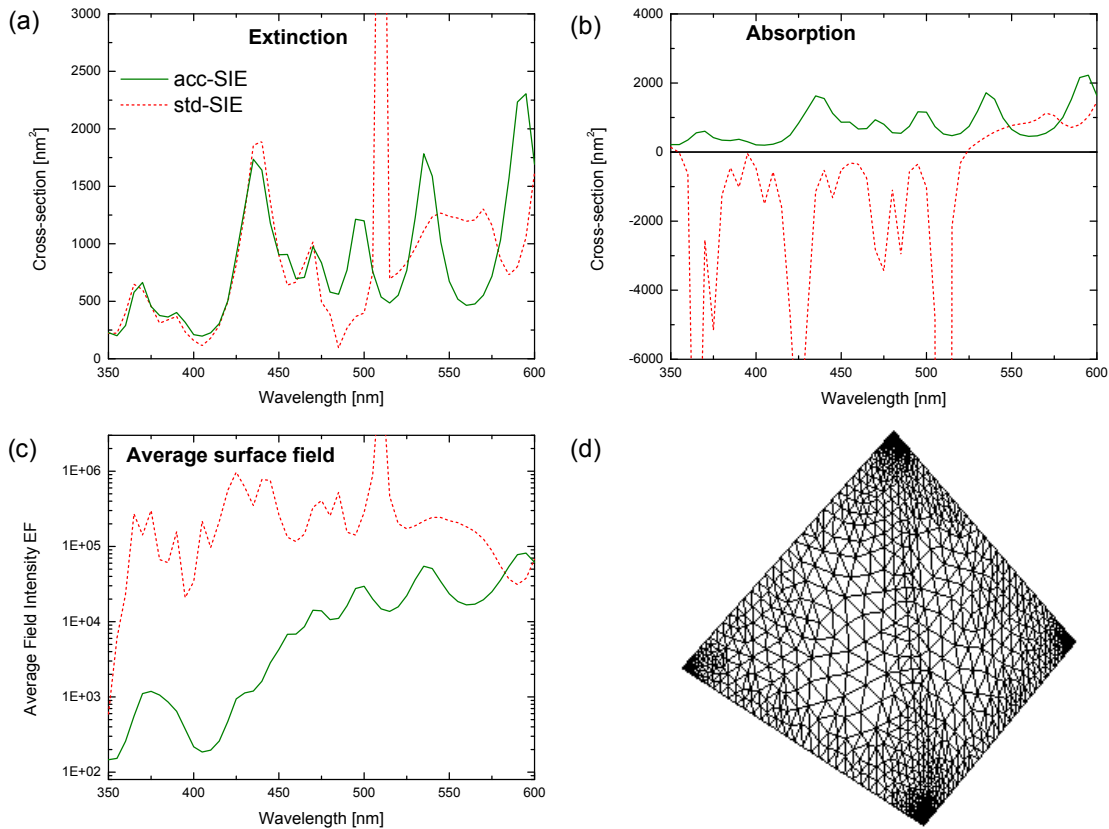
Figure 3.7 – Wavelength-dependence of optical properties for a silver regular tetrahedron of 40 nm side embedded in water, computed using the std-SIE and acc-SIE approaches: (a) Extinction cross section, (b) absorption cross section, and (c) average surface field intensity. The mesh used for the calculation is shown in (d).

unphysical results (the accuracy of the results would nevertheless need to be checked by considering finer meshes, but this is outside the scope of this work). The particularly poor behaviour of the std-SIE approach can be understood from the fact that the optical properties here are likely to be very sensitive to potentially large errors in the integration of nearby elements around the edges and corners, which play a significant role in the optical properties.

We note that sharp edges or corners may be an idealisation of realistic nanostructures, which often exhibit some degree of rounding of the edges and corners. They are nevertheless an important theoretical tool as rounding of the edges introduces additional parameters that are often difficult to measure experimentally. Moreover, the modelling of structures with sharp edges or corners will be necessary to understand the consequences of such rounding on the optical properties.
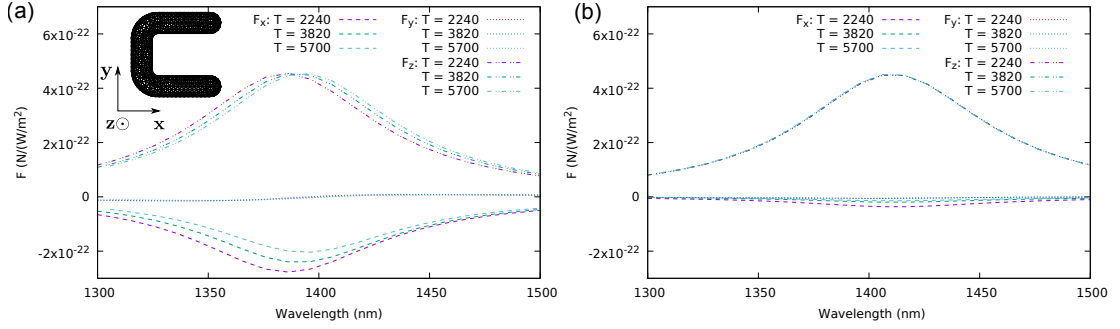
Figure 3.8 – Components of optical force on the c-shaped gold structure found using (a) std-SIE, and (b) acc-SIE for different number of triangles (T) on the mesh. The geometry is illustrated in (a), and the system is illuminated by a planewave along z with circular polarisation L.

3.5.3 Optical forces

Next, we look at the effect of the improved integration recipe on the computation of optical forces on complicated structures. To this end, we study the optical forces on the c-shaped gold structure shown in Fig. 3.8 (a). The structure has dimensions of 170 nm × 160 nm × 40 nm, and the cross section of the arms is circular with a radius of 20 nm. The structure is placed in vacuum and illuminated by an L-polarised wave propagating along z. Three different triangular meshes are considered, with triangle counts of 2240, 3820 and 5700. The forces are computed directly from the surface currents following the method developed in Section 2.2.

The forces on the structure computed by std-SIE are shown in Fig. 3.8 (a). The dominant component of the force F_z retains its shape and magnitude on increasing the triangle count, but the position of the peak seems to continuously shift to higher wavelengths. The lateral force component F_x seems to be quite high – but it keeps reducing in magnitude as the triangle count is increased, without signs of convergence. The F_y component of the force seems negligible.

The forces computed by acc-SIE, plotted in Fig. 3.8 (b), show a very different picture. The F_z component has retained its shape but the peak has moved further to a higher wavelength. There is little difference between the values for the three meshes. The component F_x has drastically reduced in magnitude, which could perhaps have been observed with std-SIE too if the mesh had been further refined. There seems to be some difference in the values for $T = 2240$ and 3820, but we seem to be reaching convergence at 5700. It should be noted that it is physically possible for such a lateral force to exist since the object is asymmetric and could scatter asymmetrically. But the magnitude of the force due to such scattering asymmetry should be quite weak for such small structures. We get the correct prediction from acc-SIE, but the results of std-SIE were completely misleading.

This result shows once again that using the optimised integration recipe gives more accurate results at much lower triangle counts. The associated increased computational cost could thus well be offset by the reduction in the required mesh refinement.

3.6 Extension to periodic backgrounds

The SIE formulation can be extended to periodic structures [109, 224]. The matrix formulation remains the same, with the difference that the Green's function is now modified to incorporate the periodicity in the system:

$$G_{i,\text{per}}(\mathbf{r}, \mathbf{r}') = \sum_{\mathbf{t}} \frac{e^{i k_i |\mathbf{R_t}|}}{4\pi |\mathbf{R_t}|} \exp(i\mathbf{k} \cdot \mathbf{t}) , \qquad (3.2)$$

where the summation is performed over $\mathbf{t}$, the set of translations of all unit cells. $\mathbf{R} = \mathbf{r} - \mathbf{r}'$, and $\mathbf{R_t} = \mathbf{R} - \mathbf{t}$. We will consider only 2D periodicities in this section, following the treatment of Ref. [109].

Unlike the Green's function for a homogeneous background, the above expression does not have a closed form and has to be performed as an infinite sum. The summation can be sped up using Ewald's method [225–228]. We do not go into the details here since they can be found in Ref. [109]. What is important is that the singularity in the periodic Green's function is of the same form as the homogeneous Green's function. This can be understood from Eq. (3.2) – the singularity appears only in that term of the summation where $\mathbf{r}$ and $\mathbf{r}'$ lie on the same unit cell of the lattice after translation, in which case the term reduces to the homogeneous Green's function. The singularity subtraction can thus be performed in the same fashion as for the homogeneous background. It should also be noted that, since the Ewald's method truncates the sums after a finite number of terms in the reciprocal lattice, the Green's function found is still not exact. We use 9 terms in the Ewald sum, following Ref. [109].

We thus implement the optimised integration recipe for periodic backgrounds in an identical fashion. We test the optimised recipe on a system consisting of two media separated by a planar interface. The $z > 0$ region is vacuum, whereas the $z < 0$ region is composed of material with $\varepsilon_r = 4$. A plane wave of 600 nm propagating in the $-z$-direction and polarised along x is incident on the interface. Note that it is not possible to simulate the response of this system using homogeneous SIE since the media are unbounded. However, periodic SIE permits the simulation by considering the space as composed of repeating unit cells. We choose a 400 nm × 400 nm square lying on the xy-plane and centred on the origin as the unit cell. Repeating the unit cell periodically tiles the entire plane.

We compute the reflected fields at various heights using the surface integral equation for the scattered field. To find the dependence of the error on the distance, sets of 100 random points each are chosen chosen in the following four bins of heights : $0 - 10$ nm, $10 - 100$ nm, $100 - 1000$ nm and $1000 - 10000$ nm. The reflected fields are also computed analytically using Fresnel coefficients. The relative error is found as the ratio of the norm of the difference between the computed and analytic fields to the norm of the analytic field (which is a constant). The relative error is averaged over all the 100 points in the height bin and plotted in Fig. 3.9 (a). We see that acc-SIE continues to outperform std-SIE significantly at all heights. When the mesh count is small, fields close to the interface are extremely inaccurate for std-SIE. On the
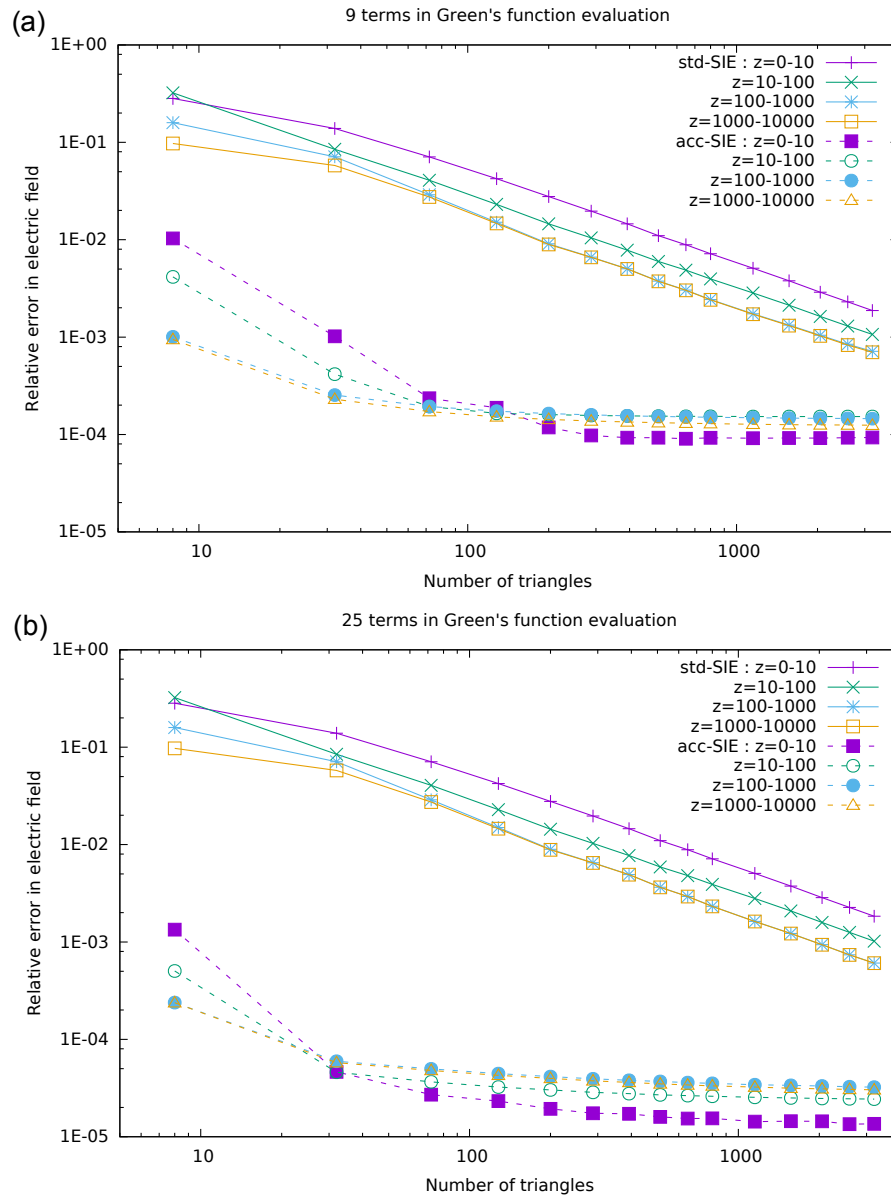
Figure 3.9 – Relative error in the electric fields computed at different heights by std-SIE and acc-SIE using (a) 9 terms, and (b) 25 terms in the Ewald sum for Green's function computation.

other hand, acc-SIE gives very accurate results with errors between 1% and 0.1% from the near zone to the far zone. Increasing the mesh size improves the accuracy for both std-SIE and acc-SIE, but the latter retains its dominance.

However, increasing the number of triangles beyond a point does not seem to improve the accuracy of acc-SIE as the error flattens out. The error in std-SIE is much worse, and the triangle count would have to be increased tremendously for it to reach the flat error region. Though the error itself is quite small, this kind of flattening would seem puzzling. After all,
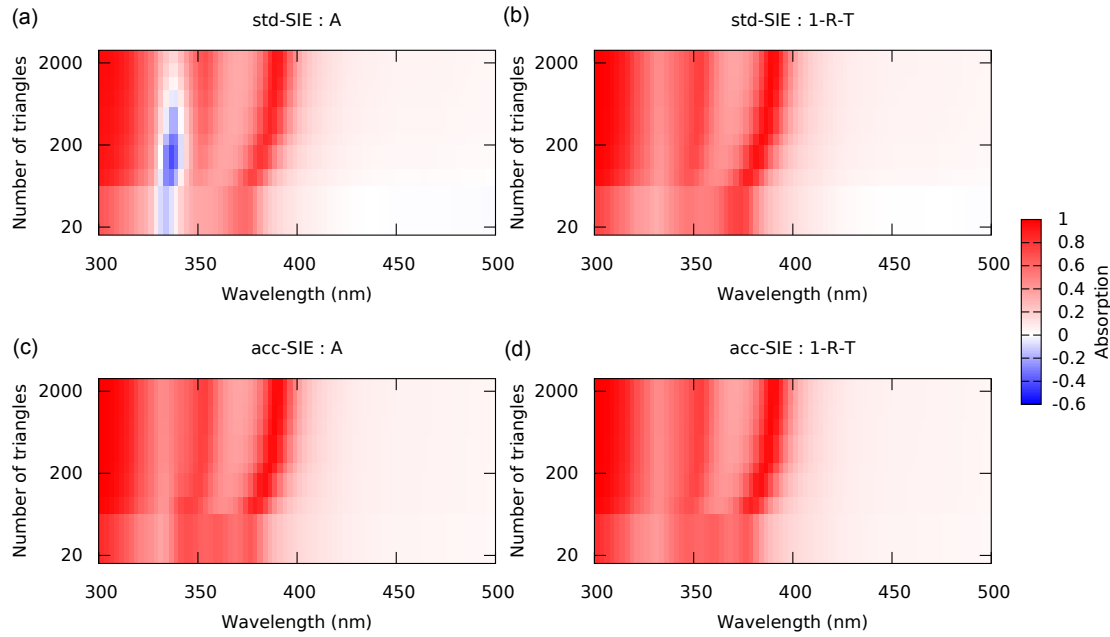
Figure 3.10 – Absorption by 30 nm radius silver spheres in a square array of periodicity 70 nm placed in vacuum 10 nm above an interface with glass, computed using (a,b) std-SIE and (c,d) acc-SIE. The system is illuminated from the glass side by a TM polarised planewave with an angle of incidence of 45°. The absorption by a sphere is normalised to the total incident energy per unit cell, and absorption is computed in two ways : integrating the Poynting vector on the surface from the surface currents (a,c), and taking the compliment of the sum of reflectance and transmittance (b,d).

sufficient refinement of the mesh is supposed to achieve better and better convergence down to machine precision. This does not happen here because, at large mesh sizes, the accuracy of the result is not throttled by the integration routine but by the accuracy of Green's function computation. To see this, we have repeated the computation using 25 terms in the Ewald sum in Fig. 3.9 (b). The error now flattens to a lower value for acc-SIE. The result for std-SIE is nearly identical to the previous case with 9 terms, showing that the error there is limited by the accuracy of the integration routine and finding the Green's function to better accuracy does not help.

Next, we consider the absorption by a square array of silver spheres above a vacuum-glass interface. The radius of the spheres is taken to be 30 nm, and they are placed in a square array with a periodicity of 70 nm along both x- and y-directions. The surface-to-surface separation between adjacent spheres is thus merely 10 nm. The array is placed in vacuum above an interface with glass (which coincides with the xy-plane), such that the sphere surface is 10 nm above the interface. The system is illuminated by a TM polarised planewave incident from the glass side at an incidence angle of 45°. The absorption by a single sphere can be computed using Eq. (3.1b), and is normalised to the total incident power reaching the interface in a unit cell of the lattice. An alternate method to compute the absorption is by integrating
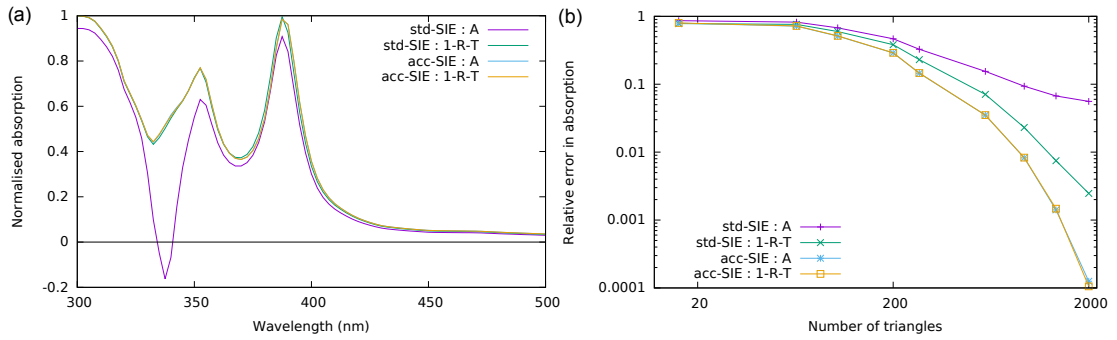
Figure 3.11 – (a) Section of Fig. 3.10 for a mesh consisting of 592 triangles. (b) Relative error in absorption at 390 nm (compared to the absorption calculated using $1 - R - T$ for a mesh consisting of 2848 triangles).

the scattered Poynting vector over the unit cell area in the far field both above and below the interface to obtain the reflectance R and transmittance T. Conservation of energy then requires that the absorption is given by $A = 1 - R - T$. It should be noted that the periodicity is too low to excite higher diffraction orders so that it is enough to compute the Poynting vector at one point in the far field above (below) and multiply it by the area to obtain the transmittance (reflectance). Also, the incidence is above the critical angle for the glass-air interface so that transmittance is zero. Both these points were numerically verified.

The absorption calculated by the two methods using std-SIE and acc-SIE are plotted in Fig. 3.10 as a function of wavelength and number of triangles in the mesh (on the sphere and the interface combined). The first thing we notice is the wavelength regime where the absorption by the sphere calculated by the surface integral using std-SIE is negative and thus unphysical. No such feature exists in the far-field computation or in the results calculated by acc-SIE. Absorption peaks seem to red shift with increasing mesh refinement. Since this effect is qualitatively the same for all the plots, this should be a result of the coarse mesh not capturing the spherical geometry well enough rather than a problem with the integration routine.

To quantify the errors better, the absorption computed by the two methods for a mesh consisting of 592 triangles is plotted in Fig. 3.11 (a). Problems with the surface integral method for computing absorption using std-SIE are once again evident. The remaining three curves are very similar to each other, though the absorption computed by $1 - R - T$ using std-SIE shows slight deviations from the other two. Figure 3.11 (b) shows the relative error in absorption at 390 nm wavelength. Since we do not have an analytic result to compare with, the absorption calculated using $1 - R - T$ for a mesh of 2848 triangles was used as the benchmark. The error curves for absorption computation by the two methods using acc-SIE lie remarkably on top of each other even now. The error in the $1 - R - T$ calculation using std-SIE is an order of magnitude higher, and the surface integral computation even worse. The mismatch between values computed using the two methods for std-SIE can be seen as evidence of consistency problems with std-SIE. By the same token, the remarkable match of the same quantities for acc-SIE shows its superior accuracy.

3.7   Conclusion

We have analysed the effect of the integral quadrature on the accuracy of SIE matrix elements and the physical quantities calculated by SIE. This led us to propose an optimised algorithm to evaluate SIE matrix elements to a high accuracy, which can be applied for SIE in both homogeneous and periodic backgrounds. Even though a coarse integration approach might be sufficient for studying the qualitative behaviour of some systems, quantitatively it performs poorly in comparison to the improved algorithm. The improved algorithm performs significantly better in calculating properties such as absorption, parallel fields and lateral forces on asymmetric structures. It is necessary to use the improved algorithm to obtain any sort of meaningful results in such challenging cases for geometries with sharp corners and edges. The optimised algorithm involves some extra computational overhead, but achieves vastly better accuracy for physical results, enabling the use of coarser mesh discretisation in simulations.

4 Extension of SIE to stratified backgrounds

In this chapter, we attempt to extend the surface integral formulation to treat nanostructures embedded in layers of stratified media. We discuss the theoretical and implementation details of this extension and use it to simulate plasmonic systems. Finally we discuss the shortcomings of this simplified extension and how they can be overcome in future to obtain a more general and efficient simulation tool for stratified backgrounds.

4.1 Introduction

Though homogeneous SIE is a very useful simulation tool, it has the fundamental limitation that it cannot simulate some of the most common plasmonic systems involving nanostructures embedded in the layers of a stratified medium or placed on substrates. Such cases are typically dealt with under the homogeneous SIE formulation by assuming the background to have an effective permittivity corresponding to a weighted mean of the layers [229, 230], or by using periodic SIE with a large enough period that the unit cells are essentially decoupled, and discretising the layer surface within a unit cell. Both these approaches are only approximate and have their own problems. Homogeneous SIE with the weighted layer index approximation cannot deal with the field gradients near an interface properly or take into account experimentally important illuminations that occur at surfaces, such as the evanescent field produced by a large numerical aperture lens. In the periodic SIE approximation, it might be impossible to achieve a periodicity which avoids coupling and higher diffraction orders at the same time. It is also difficult to obtain the far-field radiation pattern without the periodicity effects, and meshing the layered parts of the unit cell causes additional overhead. It is very useful to have a simulation technique which can deal with stratified media explicitly. Volume integral equations had been extended to deal with stratified media by computing the Green's tensor for stratified media [99–101, 231]. Recently, similar extensions have been made for boundary element and surface integral methods as well [110, 111, 117].

Here, we will present a basic extension of the surface integral equation to simulate plasmonic nanostructures embedded in layers of stratified media. It is based on the SIE formulation

in Ref. [105], modified to incorporate the Green's tensor for the stratified media using the computation method in Ref. [99]. We will also show that, unfortunately, this approach is not suitable when the scatterer approaches an interface and analyse the reasons for this failure.

4.2   Theory

We will derive the SIE formulation for stratified backgrounds, closely along the lines of the derivation in Section 1.2. Space is still described as a union of homogeneous isotropic domains, except that the background domain (for which we drop the domain subscript) is stratified and thus inhomogeneous, with spatially varying permittivity $\varepsilon(\mathbf{r})$ and permeability $\mu(\mathbf{r})$. For an inhomogeneous domain, the wave equations for electric and magnetic fields have different forms

$$\nabla \times \left[\frac{\nabla \times \mathbf{E}(\mathbf{r})}{\mu(\mathbf{r})} \right] - \omega^2 \varepsilon(\mathbf{r}) \mathbf{E}(\mathbf{r}) = i\omega \mathbf{j}(\mathbf{r}) \,, \tag{4.1}$$

$$\nabla \times \left[\frac{\nabla \times \mathbf{H}(\mathbf{r})}{\varepsilon(\mathbf{r})} \right] - \omega^2 \mu(\mathbf{r}) \mathbf{H}(\mathbf{r}) = \nabla \times \left[\frac{\mathbf{j}(\mathbf{r})}{\varepsilon(\mathbf{r})} \right] \,. \tag{4.2}$$

As a result, we have separate electric and magnetic dyadic Green's functions $\overline{\mathbf{G}^e}$ and $\overline{\mathbf{G}^h}$ defined by

$$\nabla \times \left[\frac{\nabla \times \overline{\mathbf{G}^e}(\mathbf{r},\mathbf{r}')}{\mu(\mathbf{r})} \right] - \omega^2 \varepsilon(\mathbf{r}) \overline{\mathbf{G}^e}(\mathbf{r},\mathbf{r}') = \overline{\mathbf{1}} \frac{\delta(\mathbf{r}-\mathbf{r}')}{\mu(\mathbf{r})} \,, \tag{4.3}$$

$$\nabla \times \left[\frac{\nabla \times \overline{\mathbf{G}^h}(\mathbf{r},\mathbf{r}')}{\varepsilon(\mathbf{r})} \right] - \omega^2 \mu(\mathbf{r}) \overline{\mathbf{G}^h}(\mathbf{r},\mathbf{r}') = \overline{\mathbf{1}} \frac{\delta(\mathbf{r}-\mathbf{r}')}{\varepsilon(\mathbf{r})} \,. \tag{4.4}$$

Using these, we can find the surface integral equations for electric and magnetic fields EFIE and MFIE [110, 220]

$$\left(i\omega \int_{\partial\Omega} \mathrm{dS}' \mu(\mathbf{r}') \overline{\mathbf{G}^{\mathrm{e}}}(\mathbf{r},\mathbf{r}') \cdot \mathbf{J}(\mathbf{r}') - \frac{1}{\varepsilon(\mathbf{r})} \int_{\partial\Omega} \mathrm{dS}' \varepsilon(\mathbf{r}') [\nabla \times \overline{\mathbf{G}^{\mathrm{h}}}(\mathbf{r},\mathbf{r}')] \cdot \mathbf{M}(\mathbf{r}') \right)_{\mathrm{tan}} = (\mathbf{E}^{\mathrm{inc}}(\mathbf{r}))_{\mathrm{tan}} \,, \tag{4.5}$$

$$\left(\frac{1}{\mu(\mathbf{r})} \int_{\partial\Omega} \mathrm{dS}' \mu(\mathbf{r}') [\nabla \times \overline{\mathbf{G}^{\mathrm{e}}}(\mathbf{r},\mathbf{r}')] \cdot \mathbf{J}(\mathbf{r}') + i\omega \int_{\partial\Omega} \mathrm{dS}' \varepsilon(\mathbf{r}') \overline{\mathbf{G}^{\mathrm{h}}}(\mathbf{r},\mathbf{r}') \cdot \mathbf{M}(\mathbf{r}') \right)_{\mathrm{tan}} = (\mathbf{H}^{\mathrm{inc}}(\mathbf{r}))_{\mathrm{tan}} \,. \tag{4.6}$$

It is easily verified that these equations reduce to those for the homogeneous domain given in Eqs. (1.4) and (1.7) when ε and μ are constants. Expanding the surface currents over RWG

basis functions and applying the Galerkin approach, we obtain the matrix equations

$$\left[i\omega \mathbf{D}^e \quad \mathbf{K}^h \right] \cdot \psi = \mathbf{q}^E , \tag{4.7a}$$

$$\left[-\mathbf{K}^e \quad i\omega \mathbf{D}^h \right] \cdot \psi = \mathbf{q}^H , \tag{4.7b}$$

where the $\mathbf{D}$ and $\mathbf{K}$ matrices for electric and magnetic fields now have different forms

$$\mathbf{D}_{nk}^e = \int\limits_{\partial\Omega_i} \mathrm{d}S \mathbf{f}_n(\mathbf{r}) \cdot \int\limits_{\partial\Omega_i} \mathrm{d}S' \mu(\mathbf{r}') \overline{\mathbf{G}^e}(\mathbf{r},\mathbf{r}') \cdot \mathbf{f}_k(\mathbf{r}') , \tag{4.8a}$$

$$\mathbf{D}_{nk}^h = \int\limits_{\partial\Omega_i} \mathrm{d}S \mathbf{f}_n(\mathbf{r}) \cdot \int\limits_{\partial\Omega_i} \mathrm{d}S' \varepsilon(\mathbf{r}') \overline{\mathbf{G}^h}(\mathbf{r},\mathbf{r}') \cdot \mathbf{f}_k(\mathbf{r}') , \tag{4.8b}$$

$$\mathbf{K}_{nk}^e = - \int\limits_{\partial\Omega_i} \mathrm{d}S \frac{1}{\mu(\mathbf{r})} \mathbf{f}_n(\mathbf{r}) \cdot \int\limits_{\partial\Omega_i} dS' \mu(\mathbf{r}') \left[\nabla \times \overline{\mathbf{G}}^e(\mathbf{r},\mathbf{r}') \right] \cdot \mathbf{f}_k(\mathbf{r}'), \tag{4.8c}$$

$$\mathbf{K}_{nk}^h = - \int\limits_{\partial\Omega_i} \mathrm{d}S \frac{1}{\varepsilon(\mathbf{r})} \mathbf{f}_n(\mathbf{r}) \cdot \int\limits_{\partial\Omega_i} dS' \varepsilon(\mathbf{r}') \left[\nabla \times \overline{\mathbf{G}}^h(\mathbf{r},\mathbf{r}') \right] \cdot \mathbf{f}_k(\mathbf{r}'). \tag{4.8d}$$

We can combine the integral equations for the different domains using the PMCHWT formulation

$$\left\{ \begin{bmatrix} i\omega\mathbf{D}^e & \mathbf{K}^h \\ -\mathbf{K}^e & i\omega\mathbf{D}^h \end{bmatrix} + \sum_i \begin{bmatrix} i\omega\mu_i\mathbf{D}_i & \mathbf{K}_i \\ -\mathbf{K}_i & i\omega\varepsilon_i\mathbf{D}_i \end{bmatrix} \right\} \cdot \psi = \begin{bmatrix} \mathbf{q}^E \\ \mathbf{q}^H \end{bmatrix} + \sum_i \begin{bmatrix} \mathbf{q}_i^E \\ \mathbf{q}_i^H \end{bmatrix} , \tag{4.9}$$

where the matrices and vectors without subscripts refer to the stratified background, and those with subscripts refer to the various homogeneous domains embedded in it. The embedded homogeneous domains are thus treated in an identical fashion as in homogeneous SIE. The matrix equation can be solved similarly, to obtain the coefficients for the surface currents.

4.3   Numerical implementation

Two pieces are missing to be able to implement the above described formulation – the computation of Green's function for the stratified medium and a proper singularity subtraction method to deal with close source and observation points. We will discuss the numerical implementation of these now.

4.3.1   Computation of the Green's tensor

The dyadic Green's functions for stratified media have no closed-form expressions similar to Eq. (1.3). Also, separate electric and magnetic dyadic Green's functions $\overline{\mathbf{G}^e}$ and $\overline{\mathbf{G}^h}$ need to be computed. The values of these functions depend not just on the relative position between the source and the observation points but on the relative distances of the points to the layer interfaces as well.

The electric dyadic Green's function for stratified media has been derived in Ref. [99] for use in the volume integral equation formulation. We follow an identical procedure, and compute the magnetic dyadic Green's function in the same fashion by utilising duality. The approach involves taking the Fourier transform of the homogeneous electric dyadic Green's function to work in the wavevector (**k**) space, and incorporating the parts corresponding to the multiple reflections for each wavevector through generalised Fresnel coefficients. The resultant can be transformed back to the real space (**r**) to obtain the dyadic Green's function. The inverse transform can be simplified with the use of Bessel functions to require only a one-dimensional numerical integration over k_ρ, the magnitude of the parallel component of the wavevector. However, these Sommerfeld integrals are not straightforward to integrate numerically, and require deformation of the integration path in the complex plane to avoid singularities and to obtain fast convergence. We refer the reader to Ref. [99] for the details of the procedure. The required Bessel and Hankel functions for complex arguments are computed using the SLATEC library [232].

In addition to $\overline{\mathbf{G}^e}$, we also require its curl in Eq. (4.8c). The curl can in principle be evaluated using a finite differences scheme, but this would incur additional overhead and has the risk of causing numerical inaccuracies. Hence we take the curl of the integrand of the Sommerfeld integrals in Eq. (16) of Ref. [99] analytically to obtain

$$
\nabla \times \overline{\mathbf{G}^e}(\mathbf{r}, \mathbf{r}') = -\nabla \times \left[\frac{\hat{\mathbf{z}}\hat{\mathbf{z}}}{k_l^2} \delta(\mathbf{R}) \right] + \frac{i}{4\pi} \int_0^\infty \mathrm{dk}_\rho \left[\nabla \times \mathbf{f}^s(k_\rho; \mathbf{r}, \mathbf{r}') + \nabla \times \mathbf{f}^p(k_\rho; \mathbf{r}, \mathbf{r}') \right]
$$

$$
= -\nabla \times \left[\frac{\hat{\mathbf{z}}\hat{\mathbf{z}}}{k_l^2} \delta(\mathbf{R}) \right] + \frac{i}{4\pi} \int_0^\infty \mathrm{dk}_\rho \left[\mathbf{g}^s(k_\rho; \mathbf{r}, \mathbf{r}') + \mathbf{g}^p(k_\rho; \mathbf{r}, \mathbf{r}') \right] . \tag{4.10}
$$

The components of $\mathbf{g}^s$ and $\mathbf{g}^p$ have been listed in Appendix A. The integrals for both the dyadic Green's tensor and its curl are computed simultaneously over the same integration path to make use of the terms which get repeated in both integrals.

Finally, the magnetic dyadic Green's function $\overline{\mathbf{G}^h}$ and its curl can be computed by duality [111, 220]. It suffices to swap the electric permittivity and magnetic permeability of each layer, and repeating the calculation procedure for the electric dyadic Green's function and its curl now give us the magnetic dyadic Green's function and its curl. With this, we have all the dyadic functions required to compute the matrix elements using Eqs. (4.8a) to (4.8d).

4.3.2 Singularity subtraction

Both the electric and magnetic dyadic Green's functions and their curls have a singularity at $\mathbf{r} = \mathbf{r}'$. To be able to deal with this analytically, we perform singularity subtraction in the same manner as performed in volume integral schemes [100, 101]. We assume that the domain boundaries are sufficiently far from interfaces so that the singularity only affects $\mathbf{r}$ and $\mathbf{r}'$ in the same layer. For source and observation points in the same layer, the electric dyadic Green's

function $\overline{\mathbf{G}}^e$ is expressed as the sum of a direct term $\overline{\mathbf{G}}_D^e$ and an indirect term $\overline{\mathbf{G}}_I^e$ which takes care of multiple reflections at the layer interfaces,

$$\overline{\mathbf{G}}^e(\mathbf{r}, \mathbf{r}') = \overline{\mathbf{G}}_D^e(\mathbf{r}, \mathbf{r}') + \overline{\mathbf{G}}_I^e(\mathbf{r}, \mathbf{r}') . \tag{4.11}$$

The direct term $\overline{\mathbf{G}}_D^e$ is simply the homogeneous medium dyadic Green's function for the layer, which has the closed form expression given by Eq. (1.3). Since the scatterers are sufficiently far from the interfaces, the indirect dyadic is composed of reflected waves which have to propagate a finite distance, and does not have singular behaviour. The singularity is thus entirely contained in $\overline{\mathbf{G}}_D^e$. But the singularity in the homogeneous dyadic Green's function and its curl can be dealt with perfectly by the singularity extraction scheme for homogeneous media. Also, the direct term for the magnetic dyadic Green's function has an identical form since there is no difference between electric and magnetic dyadics in homogeneous media.

Based on this, we implement the following singularity subtraction scheme. For $\mathbf{r}$ and $\mathbf{r}'$ in the same layer, the $\mathbf{D}$ and $\mathbf{K}$ matrices in Eqs. (4.8a) to (4.8d) are evaluated without taking the direct term in the dyadic Green's functions into account. This is equivalent to neglecting the $\hat{\mathbf{z}}\hat{\mathbf{z}}$, $\hat{\bar{\mathbf{I}}}$ and $\hat{\mathbf{m}}\hat{\mathbf{m}}$ terms in Eq. (9) of Ref. [99]. To these matrices, we add the matrix elements in Eqs. (1.12a) and (1.12b) taking the current layer as the homogeneous medium and using singularity subtraction. For source and observation points in different layers, this procedure is not performed and Eqs. (4.8a) to (4.8d) are evaluated directly.

This procedure allows to build the simulation matrix without numerical difficulties, and the description of the method is now complete.

4.4 Results

We will now study a couple of systems using the formalism developed here. First, we will look at the optical response of a silver nanosphere of 20 nm radius placed at the centre of a glass film. The permittivity data for silver is taken from Ref. [175]. The glass film has a thickness of 80 nm and is surrounded by vacuum from both sides. The sphere is then illuminated by a planewave from below by a planewave propagating in the xz-plane at an angle of θ from the z-axis. The schematic of the system is shown in Fig. 4.1(c).

The absorption cross section of the sphere is calculated from the surface integral of the Poynting vector according to Eq. (3.1b), and plotted in Fig. 4.1 as a function of wavelength and angle of incidence for TE and TM polarisations. The plasmon resonance of silver results in an absorption peak near 420 nm for both polarisations. However, the angular dependence of absorption is very different for the two polarisations. In particular, the maximum absorption happens for TE polarisation at normal incidence whereas TM polarisation gives a maximum near 45°. This difference is caused by the difference in Fresnel coefficients for TE and TM polarisations. Due to multiple reflections of the incident wave in the glass film, the sphere encounters a pair of waves propagating up and down. The amplitude and phase relationships
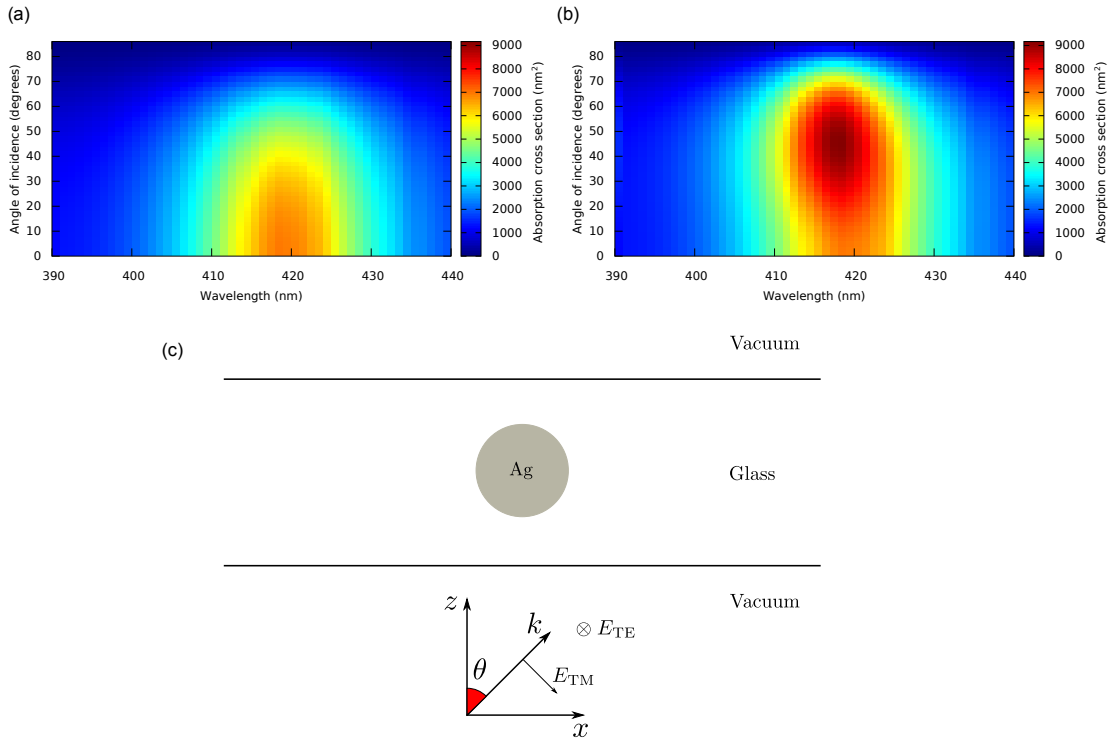
Figure 4.1 – Absorption cross section of a silver sphere of 20 nm radius embedded at the centre of a glass film of 80 nm thickness in vacuum as a function of wavelength and angle of incidence for (a) TE, and (b) TM polarisation. The sphere is illuminated from below by a plane wave with wave vector lying in the xz-plane at an angle θ from the z-axis. The schematic of the system is shown in (c).

of the two waves is different for the two polarisations, and even the total intensity of light at the location of the sphere is different. These differences result in significantly different angular behaviours for absorption.

The real and imaginary parts of electric and magnetic fields in the xz-plane are plotted in Fig. 4.2 for 418 nm wavelength and 46° angle of incidence (corresponding to the absorption peak for TM polarisation, see Fig. 4.1(b)). Since the sphere is placed at the origin and the propagation is also in the xz-plane, this is a symmetry plane for the system and some components of fields vanish. Only E_x, E_z and H_y components are expected to be retained for TE polarisation and only E_y, H_x and H_z for TM polarisations. It was verified that the computed fields show this property and hence only the nonvanishing components of the fields are shown in Fig. 4.2.

The field plots are seen to show the correct continuity behaviour at the different interfaces. All the fields have to be continuous across the surface of the sphere except for the normal component of the electric field in the case of TM polarisation. Similarly, except for E_z for TM polarisation, all the fields should be continuous across the layer boundaries. These features are borne out by the field plots, a consequence of the correct behaviour of the background
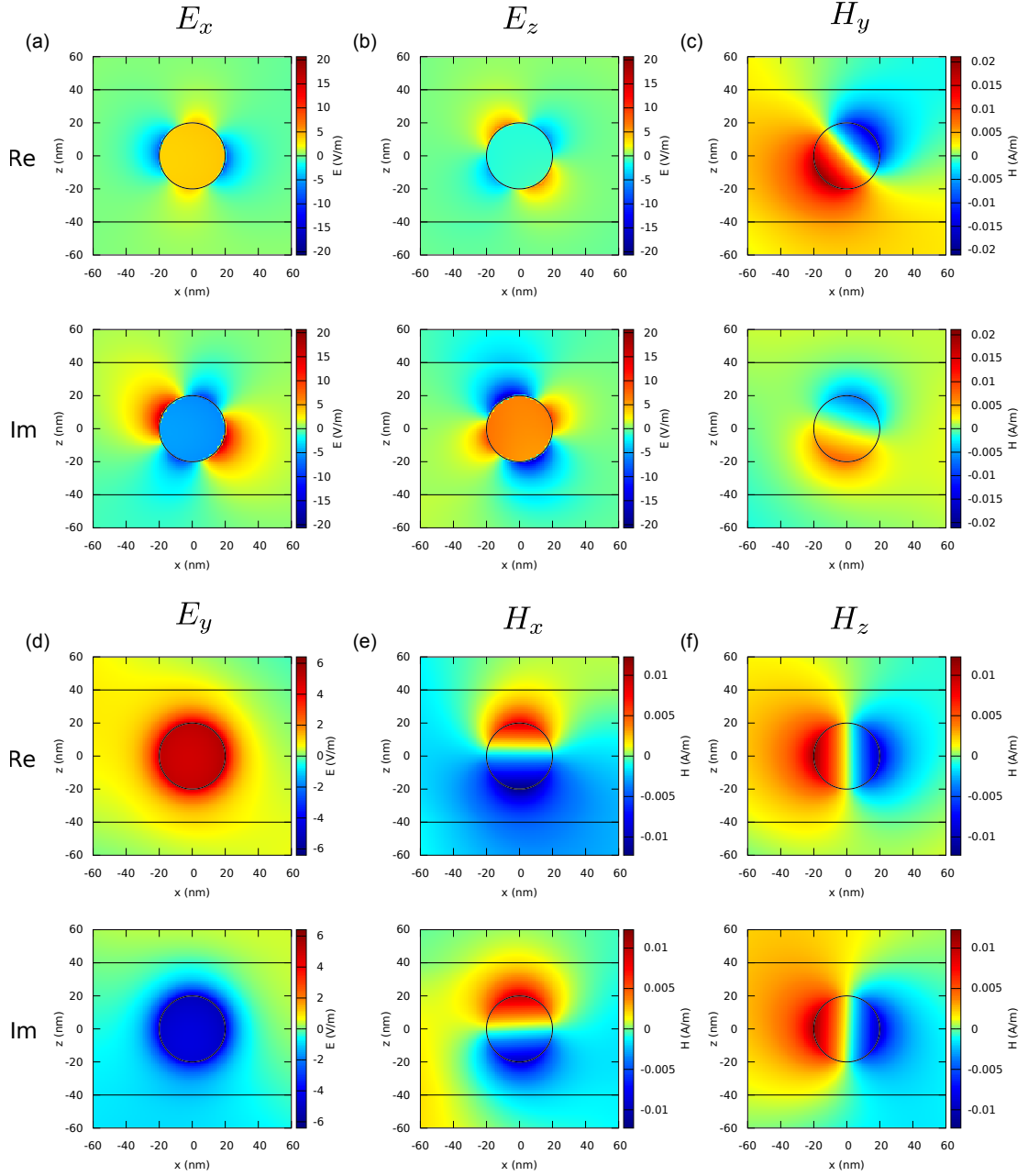
Figure 4.2 – Real (top) and imaginary (bottom) parts of the nonvanishing components of the electric and magnetic fields in the xz-plane for planewave illumination from the lower layer with an incidence angle of 46° at 418 nm. (a-c) E_x, E_z and H_y for TM polarised incidence, and (d-f) E_y, H_x and H_z for TE polarised incidence.

medium Green's function at the layer boundaries. Modification of the scattered fields at layer interfaces is also visible, most evidently in Fig. 4.2(b).

The surface charges on the sphere for the same illumination conditions is computed from the surface currents using Eq. (2.16), and shown in Fig. 4.3. The charge distribution shows that the
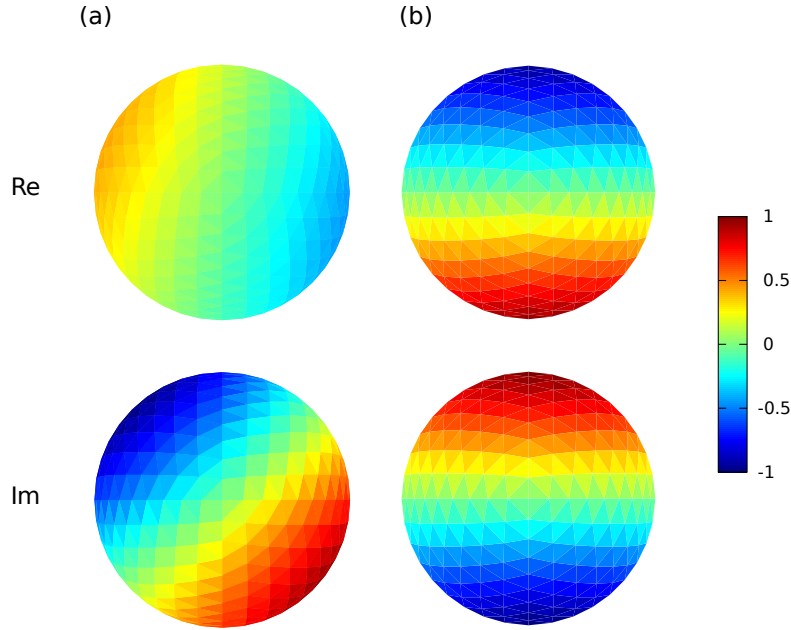
(a) (b)

Re

Im

Figure 4.3 – Real (top) and imaginary (bottom) parts of the polarisation charges on the sphere for planewave illumination from the lower layer with an incidence angle of 46° at 418 nm for (a) TM polarisation, viewed in the y-direction, and (b) TE polarisation, viewed in the $-z$-direction. Note that the charges for the two illuminations have been normalised separately.

two polarisations induce dipole moments in different directions. The charges computed are also seen to be smooth to the level of mesh discretisation, another test of the consistency of the method.

Finally, we use the formalism to compute optical forces on a dielectric sphere near an interface. The sphere has radius $r = 150$ nm and a relative permittivity $\varepsilon_r = 2$. It is placed in vacuum, 30 nm above a substrate with the same permittivity as the sphere. The sphere is illuminated by a plane wave of 633 nm wavelength from the substrate with wave vector lying in the xz-plane at an angle θ from the z-axis. The optical force on the sphere is plotted as a function of angle of incidence in Fig. 4.4.

At normal incidence, the force on the sphere is in the z-direction. The scattering force pushes the sphere away from the interface, as expected. As the angle of incidence is increased, the force increases along x and decreases along z since the transmitted wave now has momentum along x-direction as well. Something very interesting happens near $\theta = 45°$. The z-component of the force changes sign quite abruptly and the sphere is now attracted to the surface instead of being repelled. This happens because the critical angle for the interface is 45°, and the field above the interface is evanescent beyond this angle. At the critical angle, there is no momentum flow across the interface and the sphere gets dragged along the interface [233, 234]. Above this angle, in addition to the lateral dragging force, the sphere experiences a strong field gradient due to the evanescent wave and gets pulled to the surface by the gradient force [167].
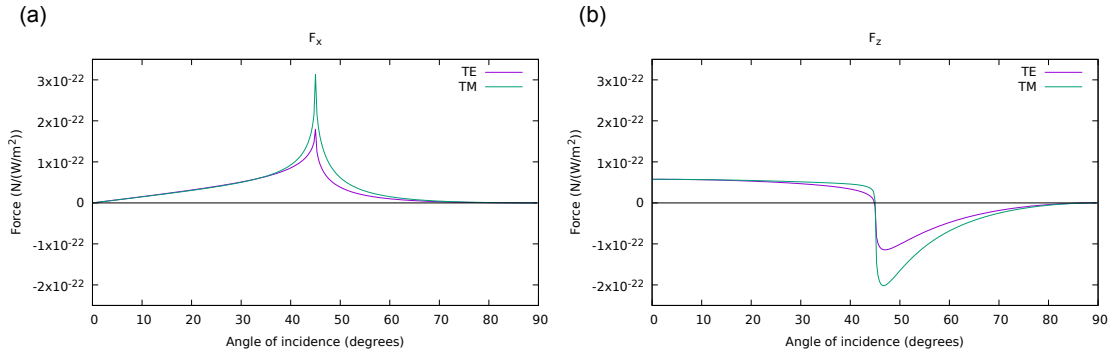
(a)

(b)

Figure 4.4 – (a) x- and (b) z- components of the optical force on a dielectric sphere ($\varepsilon_r = 2$) of 150 nm radius placed in vacuum, 30 nm above a substrate ($\varepsilon_r = 2$). The sphere is illuminated by a plane wave of 633 nm wavelength from the substrate with wave vector lying in the xz-plane at an angle θ from the z-axis.

As the angle is increased, the gradient gets stronger and the pulling force experienced by the sphere increases. However, beyond a certain angle, the field drops too quickly by the time it reaches the location of the sphere, reducing the force. As a result, there is an optimum angle of incidence to achieve maximum pulling force. In contrast, the sideways force along x decreases uniformly beyond the critical angle.

4.5 Shortcomings and possible improvements

Though the formulation is able to obtain useful physical results as seen in the previous section, it suffers from multiple drawbacks which severely limit its applicability. These problems have been overcome recently in Refs. [111, 117]. We will discuss the problems with the current approach and the solutions they have proposed to it.

The first issue we have is that we are restricted to work with domains which are embedded within layers of the stratified medium, sufficiently far from the interfaces. This is because we have applied the singularity subtraction only for the direct term in the stratified medium Green's tensor. When the boundary of the nanostructure moves close to an interface, the reflected Green's tensor shows strong variations when the source point $\mathbf{r}'$ tends to the observation point $\mathbf{r}$. Similarly, if we have two nanostructures in adjacent layers close to the interface separating them, the transmitted Green's tensor has the same problems. In particular, for the most physically useful situation of a nanostructure lying on a substrate, evaluating the reflected Green's function for $\mathbf{r} = \mathbf{r}'$ would result in a delta function singularity. As a result, the formulation is completely unable to simulate this situation.

The solution to this problem is to apply singularity subtraction to the reflected and transmitted parts of the Green's function as well, at least to the first order. That is, the singularity in the Green's function corresponding to one reflection or one transmission from an interface has to be extracted and dealt with analytically. Unless layer thicknesses are extremely small, we do

not expect the multiple reflections to be a problem.

Singularity subtraction can be applied to the reflected and transmitted Green's functions by finding analytically integrable functions with the same asymptotic behaviour, similar to the procedure performed for the homogeneous Green's function [111, 235]. This can be achieved by performing a series expansion of the integrand to extract the singular terms [111]. It should be noted that the singularity subtraction for homogeneous media is typically performed under the method of moments-friendly description of **D** and **K** matrices in terms of the scalar Green's function and its gradient using Eqs. (1.12a) and (1.12b), rather than the forms using the dyadic Green's tensor and its curl in Eqs. (1.10a) and (1.10b). However, our expressions for **D** and **K** matrices for the stratified medium in Eq. (4.8) require the dyadic Green's tensor and its curl. A method of moments-friendly description of stratified medium was proposed by Chew et al. in Ref. [236], and has been used in Ref. [111] to implement singularity subtraction. Modifying the formulation presented here to use the matrix friendly approach and implementing the singularity subtraction procedure should allow the simulation of nanostructures close to the interfaces.

However, additional factors must be taken into account while simulating nanostructures lying on layer interfaces. The stratified medium Green's function has a discontinuity across the interface, and this results in an ambiguity about which limit – upper or lower – should be taken in the integrals. The resolution of this needs a careful treatment of the limiting forms of the surface integral equations near layer boundaries [111, 117]. Properly considering the continuity properties of the surface integral equations across the boundary shows that the results on using the two limits are equivalent [111].

The second issue we face is that the computation is extremely slow compared to the calculation for homogeneous media, by nearly three orders of magnitude. This makes it infeasible to simulate finely meshed structures or to implement an optimised integration routine similar to the one proposed in Chapter 3. We are thus forced to limit ourselves to std-SIE using single point quadrature, and this has the prospect of resulting in serious accuracy problems as described in Chapter 3. Since the singularity is the primary source of inaccuracy, we could implement the optimised integration recipe for the direct Green's function and stick to single point quadrature for reflected and transmitted functions. This could improve the accuracy with negligible overhead, but we will still have problems due to the fast variation of the reflected and transmitted functions near the interfaces as described previously. Thus it is very essential to speed up the computation of matrix elements for the stratified medium.

There are two reasons for the extreme slowness, both arising from the modified form of the stratified medium Green's function. The computation of stratified medium Green's function requires the evaluation of Bessel and Hankel functions. These functions are computed for complex arguments using the SLATEC library [232]. Unlike the homogeneous Green's function which requires only the evaluation of exponentials – which can be performed using extremely optimised algorithms by modern CPUs, the computation of Bessel and Hankel functions

results in significant computational overhead. Having a lookup table for the special functions should thus reduce the computation time significantly. A similar lookup table had been implemented for computing the complementary error functions required for periodic Green's functions in Ref. [109], and resulted in major speedup.

The second source of slowness is the spectral integral required in the computation of the stratified medium Green's function. The integral itself is a source of additional overhead, and the quadrature required for convergence increases significantly when the source and observation points get close to an interface [235]. In this case the integrand decays very slowly. Treating the fast varying singular term analytically and performing the spectral integral only for the remaining part has been shown to speed up the integral evaluation [235]. That is, implementing the singularity subtraction for secondary Green's function offers us speed improvements in addition to accuracy.

Once the singularity has been extracted, computing the remaining part of the Green's function can be performed by interpolation as well [111, 117, 237]. It should be noted that the interpolation table will depend on the layer structure and not be general such as the one used for Bessel and Hankel functions. It will thus have to be computed once for each structure being simulated. The translational invariance and rotational symmetry of the Green's function can be used to reduce the size of the interpolation table required. The discretisation of the interpolation table and the interpolation polynomials have been dealt with in detail in Ref. [111].

To summarise, the primary issues with accuracy and speed of the formulation arise from the behaviour of the stratified medium Green's function close to the interfaces, and is a result of treating the system in a manner which is more suitable for volume integral-based methods. Modifying the matrix elements to a method of moments-friendly form and implementing the singularity subtraction scheme for secondary Green's function and speeding up the calculation by lookup tables should render the formulation more general and practical.

4.6   Conclusion

We have extended the surface integral method to deal with nanostructures embedded in layers of stratified media by computing the electric and magnetic dyadic Green's functions for the background and implementing singularity subtraction. We are able to compute various physical properties such as absorption, near fields, surface charges and optical forces using the method. It is however limited in applicability, primarily due to the simplicity of the singularity subtraction scheme. We have identified the bottlenecks which prevent the method from being more general and suggested possible solutions from recent literature, opening the possibility of overcoming these issues.

Numerical experiments Part II

5 Effects of realistic rounding on optical response of nanostructures

Achieving accurate agreement between numerical simulations and experiments requires, in addition to a robust numerical method, accurate modelling of the geometric and physical parameters of the system being simulated. In this chapter, we utilise SIE to study how rounding effects introduced by fabrication non-idealities affect the scattering from nanostructures. The far-field scattering from nanorod antennae and gap antennae are studied, and polarisation charge shifts are analysed to explain the effects of rounding. Parts of this chapter were published in a peer-reviewed journal article [194].

5.1 Introduction

Nanocuboids are the building blocks of many complicated nanostructures used widely in sensing applications, such as gap antennae [238] and dolmen structures [206, 207, 239]. The existence of a high number of discrete symmetries makes cubes particularly interesting [240, 241], and hence nanocubes and nanocube assemblies have been subject to experimental study as well [242–245].

To achieve accurate agreement with the experimental behaviour of nanostructures, it is not merely enough to have an accurate simulation routine; it is equally important that the object being simulated represents the actual nanostructure accurately. Even though we would like to design ideal nanostructures, fabrication processes introduce various non-idealities [246, 247]. Nanostructure surfaces become rough and geometric edges and corners end up being rounded to various degrees. The simulation needs to incorporate such fabrication induced non-idealities of the geometry. Comparing the behaviour of realistic nanostructures with their ideal counterparts shows significant differences [179].

In particular, the different fabrication techniques [243–245, 248, 249] for cuboidal and cubic nanostructures always introduce rounding effects, as visible in Fig. 5.1. This rounding gives rise to the prospect of changing the optical response of the structures significantly [243, 250–255].
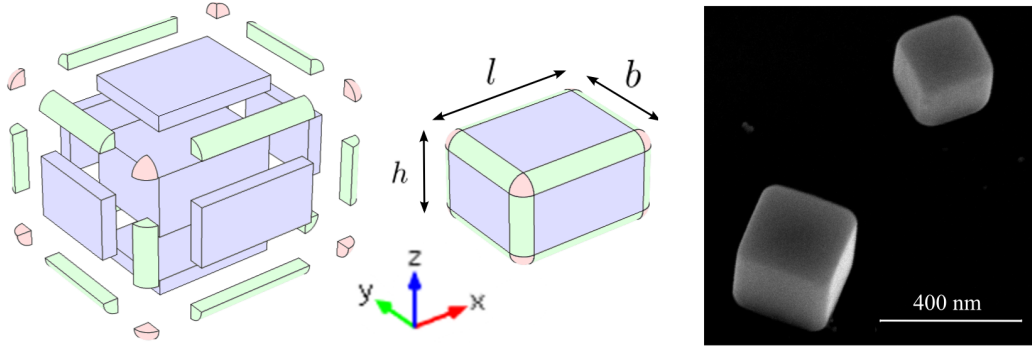
5.2 Formulation of the problem

Figure 5.1 – *(Left)* The individual pieces which can be used to assemble the rounded cuboid. The cuboids, quarter-cylinders and sphere-octants have been coloured blue, green and red, respectively. *(Centre)* The rounded cuboid formed from the constituents. *(Right)* SEM image of silver nanocubes.

In this chapter, the following procedure is used for rounding the corners and edges of cuboids uniformly. Consider a cuboid with dimensions l, b, h. Suppose we need to round the edges and corners with a rounding radius of r such that $2r \leq \min(l, b, h)$. This can be done ensuring continuity and differentiability of the surfaces by making a composite structure consisting of seven cuboids, twelve quarter-cylinders and eight sphere-octants. The assembly of a rounded cuboid from these pieces is shown in Fig. 5.1. It is easy to verify that all boundaries between meeting surfaces are smooth.

In all the structures considered here, the yz-plane cross section of the cuboids is kept constant as $b = h = 40$ nm while the length l along the x-dimension of the structures and the radius of rounding r are varied. In the case of the gap antenna, two such identical cuboids are placed symmetrically such that their yz-plane surfaces face each other. In all the simulations presented here, a plane wave propagating in the z-direction and polarised along x is used for illuminating the structures. The nanostructures being simulated are made out of silver, unless explicitly mentioned otherwise. The dielectric function for silver is taken from Johnson and Christy [175]. The optical response of the nanostructures is simulated using SIE. The surface of each structure is discretised using COMSOL such that the average area of a triangular mesh element is approximately 5 nm^2.

Scattering cross section is calculated by evaluating the flux of scattered Poynting vector on a sphere centred at the structure and having a radius of 50 μm, and normalising the result to the incident field intensity using Eq. (2.48). Bisection method is used to locate peak scattering wavelength with high accuracy. Polarisation charges are calculated at the structure surfaces from the discontinuity in the normal component of electric field using Eq. (2.15). This is performed by subdividing the surface mesh into smaller triangles and evaluating the electric field 1 nm away from the centre of the triangles in either direction of the surface normal.

5.3 Results and discussion

Consider a silver cube with a side length of 40 nm. Figure 5.2 shows the effect of rounding on the scattering cross section of the cube. It can be noted that the scattering plots exhibit a regular trend on increasing rounding radii. As the cube is gradually deformed into a sphere by increasing the rounding radius, two major changes occur: The wavelength at which peak scattering cross section is obtained blue shifts significantly while the peak value of the scattering cross section decreases to about one-fifth of the original value. The continuous shifting of the scattering peaks suggests that there are no numerical problems arising due to the sharpness in the cube geometry. For additional validation, we performed analytical calculations using Mie theory for the case of the sphere and found perfect agreement in the location of the scattering peak. There is no such analytical treatment possible for a cube. However, various numerical methods have been used to calculate the scattering cross sections of cubes of different sizes and they have found the dominant scattering mode of the cube to be corner charge dominated. The value of scattering peak wavelength we calculated for the cube agrees well with those predicted in literature [240, 251, 256].

To understand what happens in the near field at the nanocubes for various radii of rounding, we look at the polarisation charges at the surface. The results are shown in Fig. 5.3. For the nanocube rounded only by 3 nm, the polarisation charges are heavily concentrated at the corners. This is akin to the lightning rod effect [257, 258]. As the rounding radius increases, the size of the "corner" increases as well. As a result, the charges become less localised, and spread to the edges and faces of the rounded nanocube.
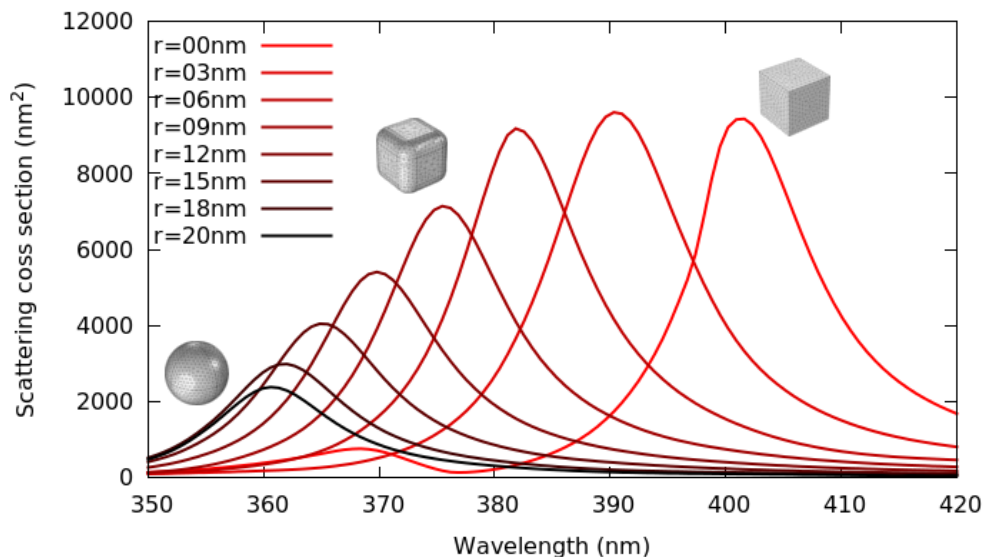

Figure 5.2 – Scattering cross section as a function of wavelength for various rounding radii (r) of the cube.
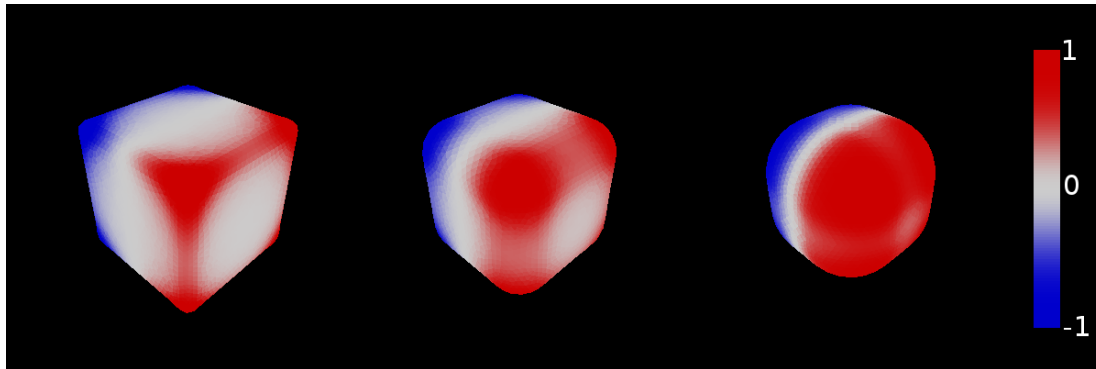
Figure 5.3 – Normalised polarisation charges on the surface of rounded nanocubes. *From left to right:* Rounding radius of 3 nm, 9 nm, 15 nm.

The trend of lower wavelength scattering peaks being associated with more spread-out charge distributions was also noticed in individual structures with multiple scattering peaks. As an example, consider a thin nanocuboid of dimensions 20 nm × 40 nm × 40 nm rounded to a radius of 4 nm. This structure has three prominent scattering cross section peaks occurring with a wavelength separation of about 20 nm, as shown in Fig. 5.4. The polarisation charges corresponding to the three scattering peaks have been shown in Fig. 5.5. There is significant difference between the charge profiles for the three cases. The lowest wavelength peak has polarisation charges distributed all over the square faces whereas the highest wavelength peak has the charges concentrated at the corners. The scattering peak at the intermediate wavelength has charges concentrated primarily at the edges. Once again, the bluer scattering peak is seen to be associated with the more spread-out charge distribution. This correlation
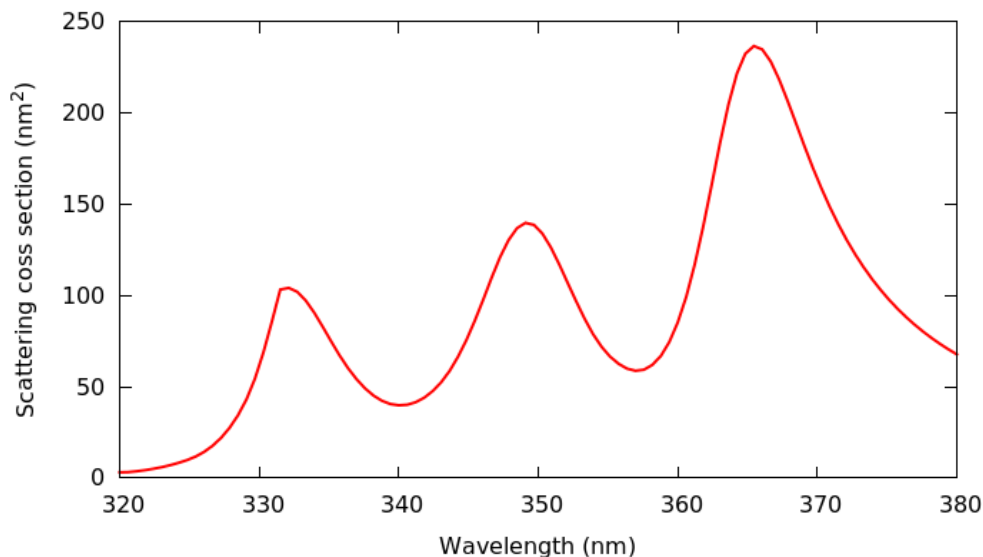

Figure 5.4 – Scattering cross section as a function of wavelength for a silver cuboid of 20 nm length, 40 nm × 40 nm cross section and rounding radius of 4 nm

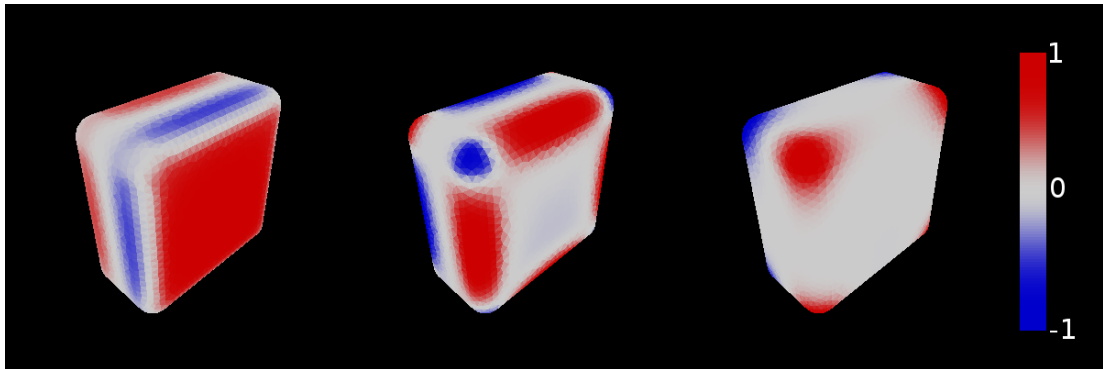Figure 5.5 – Normalised polarisation charges on the surface of the 20 nm × 40 nm × 40 nm antenna for the three scattering peaks in Fig. 5.4. The figures, from left to right, correspond to the peaks from left to right, respectively.

between spreading of charge and blue shifting of scattering peak needs to be studied further. However, we believe that the spreading of charges due to the reduction in the lightning rod effect might be what causes the blue shift of scattering peak on rounding nanostructures.

The peak shifting behaviour for cuboids of various lengths as well as gap antennae was studied in the same fashion. This time, cuboids made of silver as well as gold were considered. Dielectric function for gold was obtained from Johnson and Christy as well [175]. The trend of blue shifting of the scattering peak as a result of rounding was found in all studied structures made of gold and silver. The peak shift (relative to the scattering peak of ideal structures) as a function of rounding radius is presented in Fig. 5.6.

Interestingly, cuboids of different lengths show similar trends of blue shifting of peak wavelength on rounding. However, the gap antenna shows a significantly higher blue shift. The reason for the same can be understood by comparing the polarisation charge distributions for
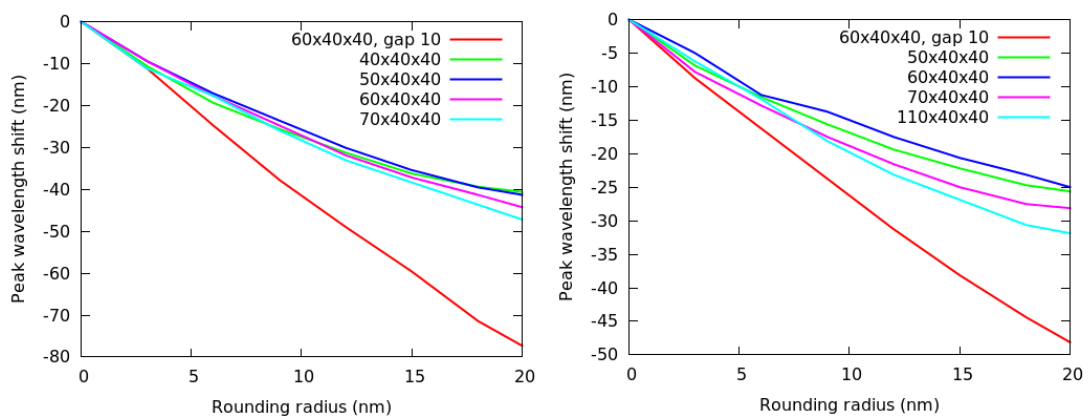

Figure 5.6 – The peak wavelength shift relative to an ideal structure for various values of rounding radii for (*Left*) silver and (*Right*) gold.

the peak scattering wavelengths of a single cuboid and that of a gap antenna. The polarisation charges for a single 60 nm × 40 nm × 40 nm nanorod ($r = 3$ nm) and that for an arm of a gap antenna formed by two such nanorods separated by 10 nm ($r = 3$ nm and $r = 9$ nm) are plotted in Fig. 5.7. As expected, for the single cuboid, the polarisation charges are concentrated at the corners. However, for the gap antenna, the charges are seen to be spread all over the surface facing the gap. This can be explained by the fact that there is an opposite charge at the matching face of the other arm of the gap antenna, attracting charge on this arm towards it. The two oppositely charged faces with charges almost uniformly spread over them acts as a capacitor, providing high field coupling between the faces. However, when the rounding of the cuboids is increased, the situation changes. The polarisation charges are still attracted towards the gap face, but are now more dispersed around the curved edges. It is important to note that the flat part of the face is what is closest to the other antenna arm, thus providing maximum coupling. The presence of charges away from the flat region on the edges reduces the coupling.

This reduction in coupling is what results in a larger blue shift on rounding gap antennae as compared to rounding single cuboids. Consider a cuboid being rounded from an ideal shape to a maximally rounded shape. This would result in a blue shift of peak scattering wavelength by a value as seen earlier, call this shift δ_s. Now consider making a gap antenna out of two such identical ideal cuboids separated by d. Due to the field coupling between the two arms, the peak scattering wavelength for the ideal gap antenna is red shifted with respect to the peak for the ideal rod antenna by a value δ_g^i. Similarly, the peak scattering wavelength for the rounded gap antenna at the same separation d is red shifted with respect to the peak for the rounded rod antenna by a value δ_g^r. Since the coupling in the case of the rounded gap antenna is less than that of the ideal gap antenna, we expect $\delta_g^r < \delta_g^i$. The shift between the peak scattering wavelengths of the rounded gap antenna and the ideal gap antenna is given, as illustrated in Fig. 5.8, by $\delta_g = \left(\delta_s + \delta_g^i - \delta_g^r\right)$. Since $\delta_g^i > \delta_g^r$, we obtain that $\delta_g > \delta_s$. That is, the rounding
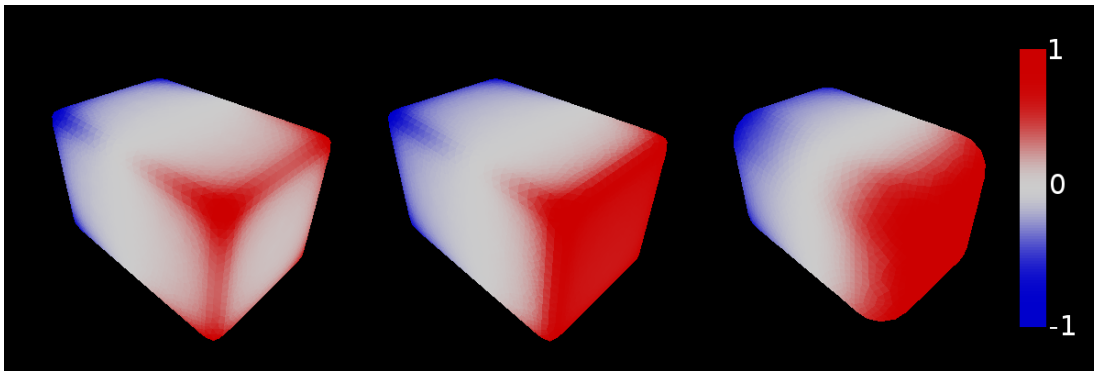
Figure 5.7 – Normalised polarisation charges at the peak scattering wavelength for *(Left)* a single 60 nm × 40 nm × 40 nm cuboid with a rounding radius of 3 nm and the gap-facing surface of a *(Centre)* gap antenna with two such cuboids separated by 10 nm and *(Right)* a similar gap antenna but with a rounding of 9 nm.
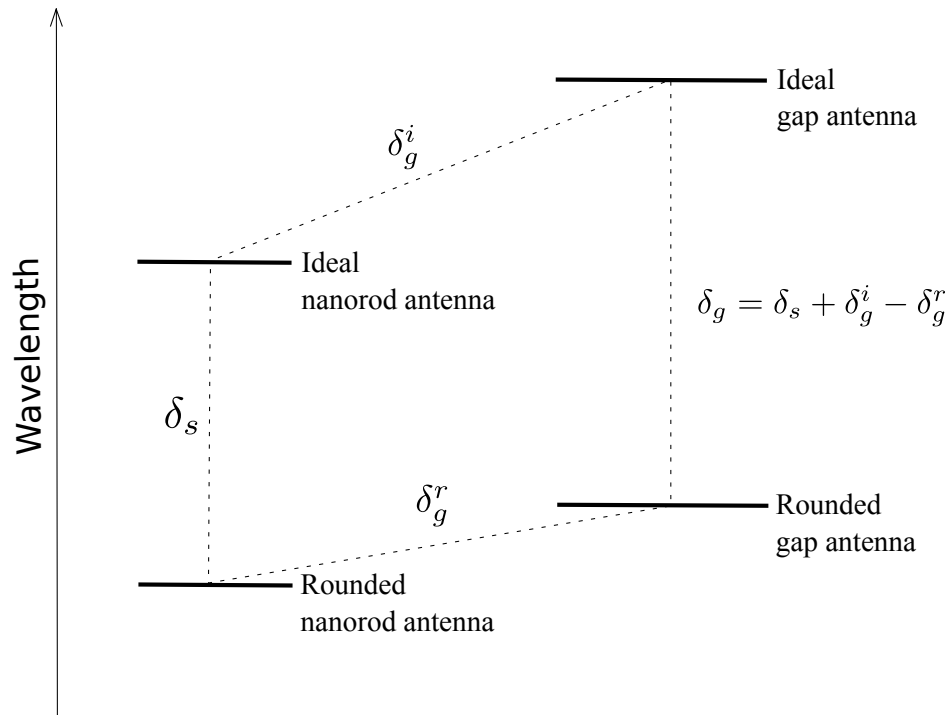
Figure 5.8 – The relationship between various wavelength shifts.

induced blue shift is higher for a gap antenna as compared to a single cuboid antenna.

5.4 Conclusion

It has been shown that rounding affects the scattering from nanoantennae significantly. Since the far field scattering properties change as well, this is not merely a near field effect and will thus change any experimental parameters of the system. The difference is particularly significant for gap antennae, where peak scattering wavelength has been shown to shift by up to 80 nm in the case of silver. This should be taken into consideration while simulating nanostructures to be fabricated to have desired properties. Fabrication always introduces rounding effects into structures, which must be estimated reasonably well and incorporated into the simulations so that the fabricated structures behave as expected. Since peak scattering wavelength is a regularly used quantity for sensing applications, the effect of rounding can be significant in those applications [259, 260]. Rounding effects also need to be considered in other problems where coupling between surfaces plays a significant role, as similar to the case of the gap antenna, coupling can be reduced due to curvature in such cases as well.

6 Internal forces in plasmonic nanostructures

In compound plasmonic nanostructures, the presence of multiple metallic nanoparticles in close proximity results in strong internal forces. In this chapter, we study the internal optical forces arising in three ubiquitous plasmonic systems - the gap antenna, the dolmen, and the split ring resonator. These internal forces show a rich behaviour with varying wavelength, incident polarisation and geometrical parameters. There arise interesting and anomalous features such as lateral force reversal, optical pulling force, and circular polarisation-induced forces and torques along directions symmetry-forbidden for orthogonal linear polarisations. Parts of this chapter were published in a peer-reviewed journal article [195].

6.1 Introduction

Theoretical studies of plasmonic optical tweezers with propagating waves concern themselves primarily with forces in the direction of, or opposite to, the wave propagation. However, the presence of plasmonic nanostructures can lead to the particles experiencing a lateral force perpendicular to the direction of propagation of the incident wave as well, as seen, for example, in nanoparticle dimers [177]. Obviously, internal forces will also arise within a nanostructure upon illumination, especially when this nanostructure is composed of several parts. Such internal forces have been studied only in some dimer systems [143, 177, 261–263]. In this chapter, we computationally investigate the internal forces on the individual parts of three compound systems commonly encountered in plasmonics : the plasmonic gap antenna, the dolmen structure, and the split ring resonator. Gap antennas were one of the first plasmonic structures providing high field enhancement with easy tunability, and have been utilised for optical trapping as well [59, 174, 238, 264–266]. The dolmen system has also been of considerable interest in plasmonics since it supports a Fano resonance due to the coupling between the dipolar mode in the horizontal arm and the quadrupolar mode supported by the vertical arms [206–208]. Split ring resonators have been used as building blocks for metamaterials, and have permitted the creation of effective media with interesting physical properties such as negative refraction [267–269]. Studying the internal forces in these representative and ubiquitous plasmonic systems will help to understand how internal forces

arise generally in plasmonic systems.

The electromagnetic response of the nanostructures is simulated using SIE. The plasmonic structures are modelled with the background medium as vacuum. The optical forces and torques on the particles are computed from the surface electric and magnetic currents using the formalism developed in Section 2.2. Surface polarisation charges are also calculated from the surface currents using Eq. (2.16). The scattering cross section (C_{sc}) of the structures is evaluated by integrating the flux of the scattered Poynting vector over a sphere of radius 50 μm around the structure and normalising it to the incident field intensity using Eq. (2.48).

6.2 Results and discussion

6.2.1 Gap antenna

We first look at the simplest of the three systems, the plasmonic gap antenna. The gap antenna we study is symmetric with arm lengths of 600 nm and has a circular cross section with radius 20 nm. The gap size is 20 nm, and the faces of the antenna are fully rounded. The arms are made of Drude metal with the permittivity defined by [270, 271]:

$$\epsilon(\omega) = \epsilon_\infty - \frac{\omega_p^2}{\omega(\omega + i\gamma)}, \tag{6.1}$$

with the parameters $\epsilon_\infty = 9.1$, $\omega_p = 9.0843$ eV and $\gamma = 0.07078$ eV. The system is illuminated by a plane wave polarised along the axis of the antenna (x-axis) and propagating in the z-direction, as depicted in the schematic in the inset of Fig. 6.1(a).

The scattering cross section C_{sc} of the antenna is shown in Fig. 6.1(a). The dipolar resonance is visible at 2170 nm, with higher order scattering peaks present at 755 nm and 570 nm. The polarisation charges induced on the structure at these three wavelengths are shown in
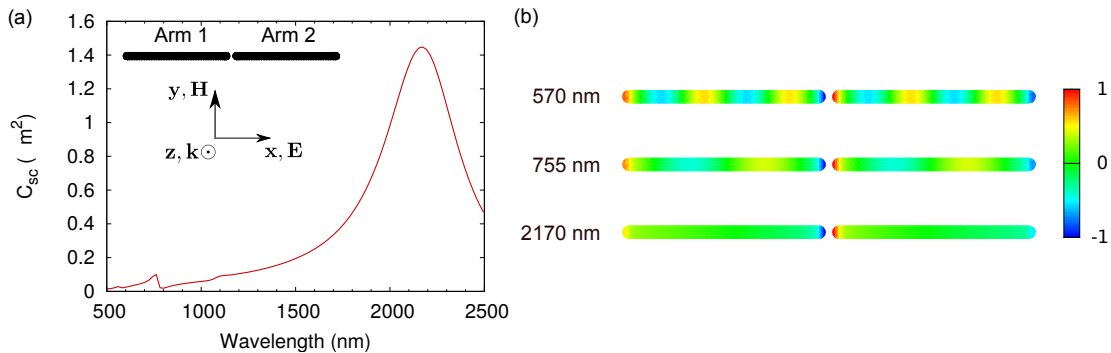

Figure 6.1 – (a) Scattering cross section as a function of wavelength for a symmetric gap antenna with arm lengths of 600 nm and gap size of 20 nm, shown in inset. (b) Normalised polarisation charges induced on the antenna arms at selected wavelengths.
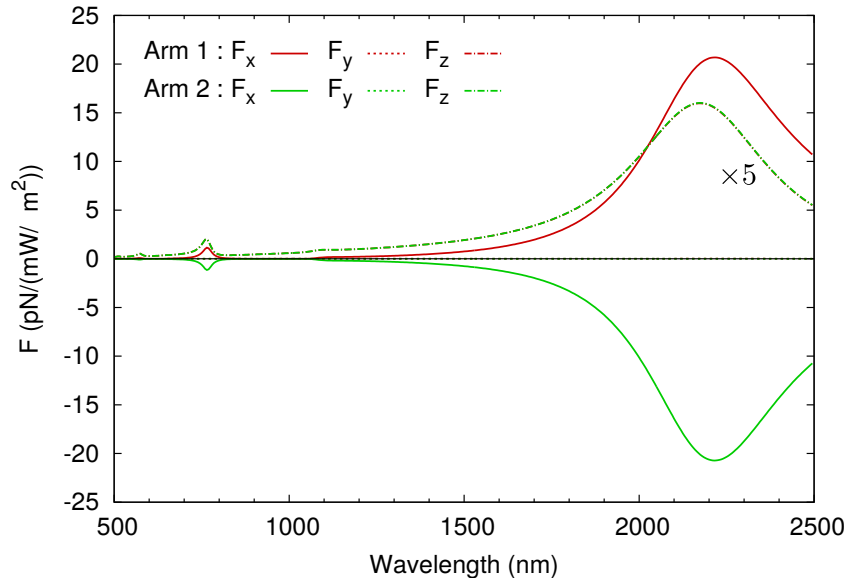
Figure 6.2 – Optical forces on the symmetric antenna arms. Different force components along x-, y- and z-directions are considered (see axes in the inset of Fig. 6.1(a)).

Fig. 6.1(b). The imaginary part of the complex polarisation charges dominates over the real part at the resonances, as we will discuss in more detail in Section 8.3, and is what is plotted in Fig. 6.1(b). The charge distributions are independently normalised to the maximum charge density at each wavelength. The charge plots clearly depict the higher order nature of the low-wavelength peaks. In all cases, the charge concentration is very high at the gap-faces of both arms [61, 194]. The charge distribution shows an odd symmetry about the gap centre, resulting in opposite charges being created at the gap faces of the two arms, suggesting an attractive force between the arms in all cases.

Indeed, the force on the arms plotted in Fig. 6.2 confirms this. The force between the two arms in the x-direction is always attractive, and equal in magnitude as symmetry dictates. Also, the attractive force F_x is very strong due to the large concentration of charges across the small gap, nearly an order of magnitude stronger than the scattering force F_z at the same wavelength. For a wide wavelength range, the lateral force trumps the scattering force in magnitude. Also note that the force along the y-axis is zero, as expected from symmetry considerations. Typical trapping experiments have a laser power of approximately 50 mW, focused to a spot of about 5 μm. The intensity felt by the illuminated plasmonic structure is thus nearly 1 mW/μm^2, resulting in a lateral force as strong as 20 pN, which is very high for a nano-object.

We now repeat the calculations for an asymmetric nanoantenna since symmetry breaking can make the two arms respond differently to light, changing the force properties. The geometry is same as earlier in all respects, except that the right arm is now shorter, measuring 400 nm, as shown in the inset of Fig. 6.3(a). The scattering cross section for this geometry is plotted in Fig. 6.3(a). We note that the dipolar peak has split into two, each peak corresponding to
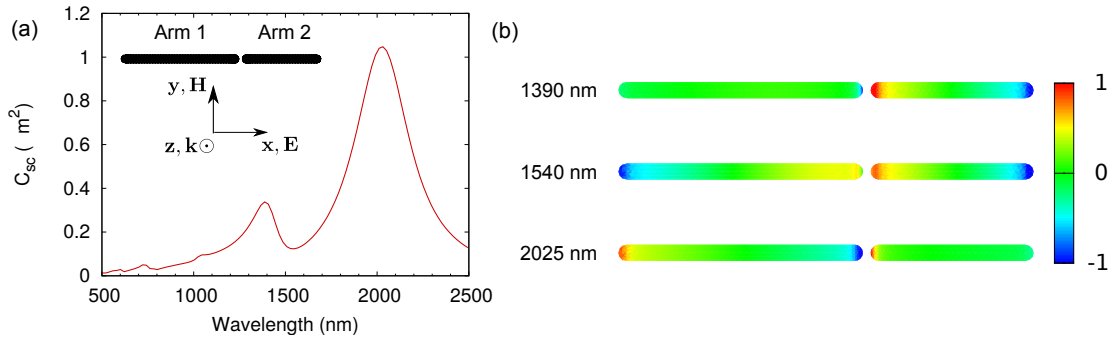
Figure 6.3 – (a) Scattering cross section as a function of wavelength for an asymmetric gap antenna with arm lengths of 600 nm and 400 nm, and gap size of 20 nm, shown in inset. (b) Normalised polarisation charges induced on the antenna arms at selected wavelengths.

the excitation of one of the arms as is evident from the charge distribution at the two peaks plotted in Fig. 6.3(b). Note that the imaginary part of the charges are plotted at the scattering peaks due to the same reason as earlier, whereas real part of the charges are plotted at the dip since it is dominant away from the resonances. The plots for each wavelength are normalised independently to the maximum charge density at the wavelength. At the lower wavelength peak, the shorter arm is excited, which in turn induces opposite charges at the gap face of the longer arm. At the higher wavelength peak, it is the longer arm which is excited and induces opposite charges on the longer arm. At both these wavelengths, we would expect the force between the arms to be attractive.

However, at the scattering dip between the two peaks, we see something different. Both arms are now individually excited by the incident light directly, and since we are at either side of the resonance of the two arms, the dipole moments of the arms are aligned in opposite directions. As a result, the charges on the two sides of the gap now have the same sign, and we expect a repulsive force between the arms, a situation completely unlike the symmetric case.

The forces on the system are plotted in Fig. 6.4. Similar to the case of the symmetric antenna, the lateral force F_x on either arm is higher than the scattering force F_z for much of the wavelength range. It is seen that at both scattering peaks, the arms attract each other strongly. However, at an intermediate range, the force becomes repulsive as expected from the charge distribution. The change of force from attractive to repulsive between the two scattering peaks of an asymmetric nanoantenna has been previously reported by Zhang *et al.* [262].

The behaviour of the scattering force itself is interesting. First of all, the forces on the two arms in the z-direction are no longer equal since the symmetry has been broken. The magnitude of the scattering force on the arm undergoing resonant excitation is higher than that of the other arm at both scattering peaks. More interestingly, at the shorter arm resonance, the longer arm is pulled towards the incident field rather than being pushed away by it, resulting in an optical pulling force.
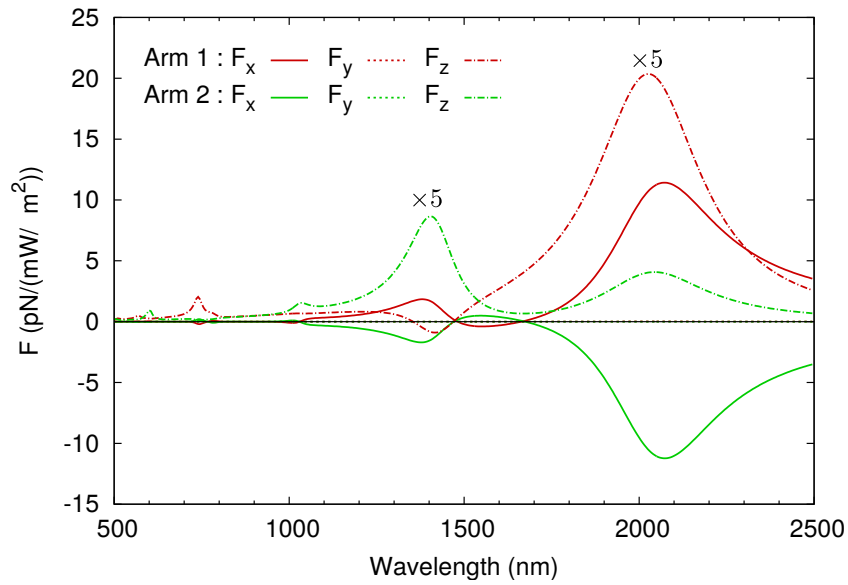
Figure 6.4 – Optical forces on the asymmetric antenna arm.

The torque about the centre of mass of the system in the y-direction is plotted in Fig. 6.5. This figure shows the contrast between the scattering forces acting on both arms more clearly, since the y-component of the torque arises from the variation in the z-component of the force in this case. For the symmetric antenna, there would have been no y-torque. Instead, what we see here is a significant magnitude of torque – that is, the lever arm is comparable to the size of the antenna. The sign of the torque also depends on the wavelength. Had the antenna been
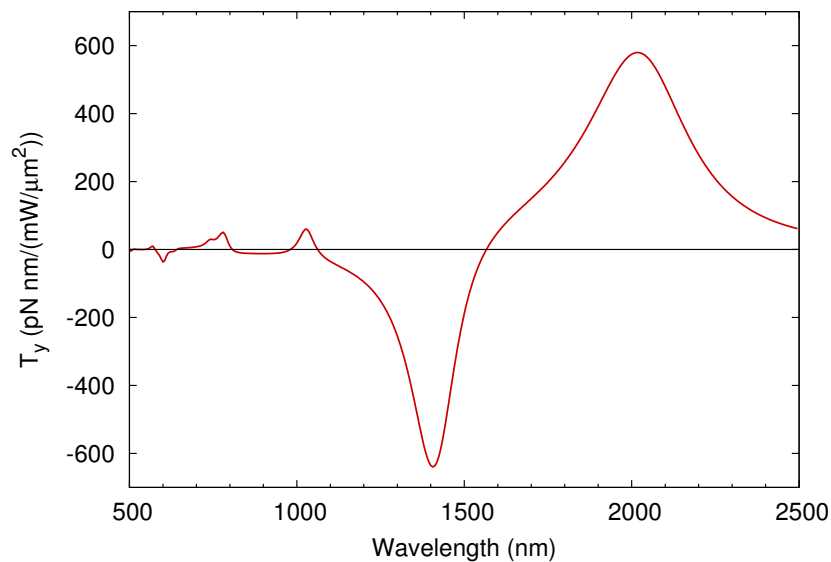
Figure 6.5 – y-component of the optical torque about the centre of mass of the asymmetric antenna.

a rigid system, the shorter arm would have ended up aligning in the direction of the incident field or opposite to it depending on the wavelength of incidence. This behaviour thus offers the possibility of optically orienting nanoparticles. Note that we are talking about wavelength-dependent alignment in the direction of propagation here, as opposed to alignment in the direction of polarisation using polarisation dependent optical forces [272, 273].

Though light can possess both spin and orbital momentum and impart them to particles just as in the case of linear momentum, plane waves do not possess orbital angular momentum, and linearly polarised waves do not possess spin angular momentum either [144, 274–278]. In spite of this, the linearly polarised plane wave is able to transfer angular momentum to the gap antenna under study due to the asymmetry.

Finally, we look at the dependence of the forces and torque on the losses in the system. The asymmetric nanoantenna is simulated with two further values of loss parameter γ in Eq. (6.1), $\gamma = 0.10$ and $\gamma = 0.15$, leaving other material and geometric parameters the same. The change in scattering cross section of the system on varying the loss parameter is plotted in Fig. 6.6(a). The scattering peaks become weaker in intensity and broader in wavelength with increasing values of loss. Apart from this, all the qualitative features of the scattering curve are retained since the imaginary part of the permittivity is still much smaller than the

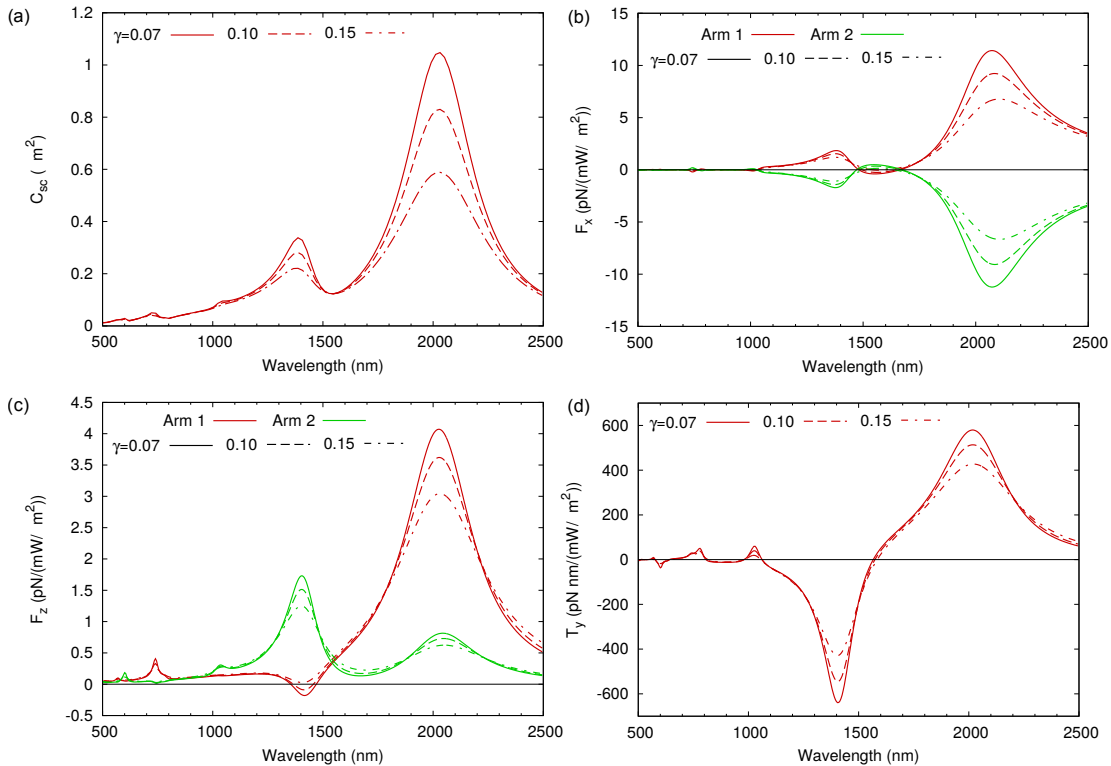Figure 6.6 – (a) Scattering cross section, (b) x-component of force, (c) z-component of force, and (d) y-component of torque on the asymmetric antenna as a function of wavelength for various values of the loss parameter γ in Eq. (6.1).

real part in the wavelength range of interest. The x- and z-components of force on the arms plotted in Figs. 6.6(b) and 6.6(c) and the y-component of torque on the system plotted in Fig. 6.6(d) also show only changes in magnitude with varying loss parameter. The magnitude changes are the highest near the scattering peaks where the scattering cross section shows the highest variation since the forces and torques on the system are directly correlated to the scattering cross section and dipole moment induced on the structure. However, all the qualitative features discussed previously for $\gamma = 0.07078$ eV are retained.

6.2.2 Dolmen structure

We now move on to analyse the internal forces on a more complicated system, the dolmen. The dolmen structure we study here consists of a horizontal arm of length 120 nm and two vertical arms of length 110 nm. All three have cross sections of 40 nm × 40 nm, and the faces are rounded to a radius of 10 nm. The dolmen is made of gold, with permittivity data taken from Johnson and Christy [175]. The dolmen is illuminated by a plane wave propagating in the z-direction and polarised along the x-direction, as depicted in the inset of Fig. 6.7(b).

The scattering cross section as a function of wavelength and the gap between the horizontal
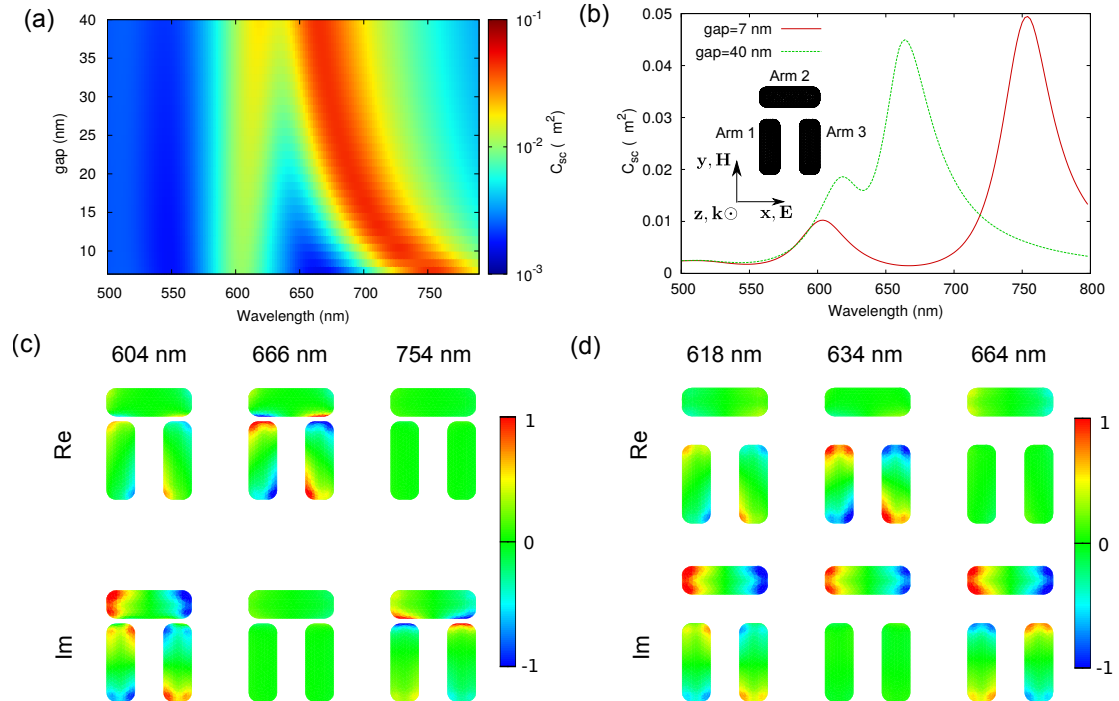
Figure 6.7 – (a) Scattering cross section as a function of wavelength and vertical gap size for the dolmen structure. (b) Scattering cross section of the dolmen for two representative vertical gap sizes, 7 nm and 40 nm. Geometry depicted in inset. (c) Real and imaginary parts of the induced polarisation charges for a dolmen with 7 nm vertical gap at the two scattering peak wavelengths and the scattering dip wavelength. (d) Same as (c) for a vertical gap of 40 nm.

and vertical arms of the dolmen is plotted in Fig. 6.7(a). We see two scattering peaks which increase in separation as the gap is reduced, increasing the coupling between the horizontal and vertical arms [265]. For clarity, the scattering cross sections for two extreme values of the gap (7 nm and 40 nm) are shown in Fig. 6.7(b). The scattering dip is the signature of the Fano resonance [279]. Fano resonances are known to play a crucial role in determining the forces on asymmetric systems and in inhomogeneous fields [262, 263, 280, 281].

The normalised polarisation charge distributions at the two scattering peaks and the dip for 7 nm gap are shown in Fig. 6.7(c), and the same for 40 nm gap in Fig. 6.7(d). Since the polarisation charges induced on the different arms of the dolmen show different phase relationships with the incident field at the relevant wavelengths unlike the case of the gap antenna, both the real and imaginary parts of the polarisation charges have been shown. The physical meaning of the real and imaginary components of charges is discussed in Section 8.2.

For both gaps, the lower wavelength peak corresponds to the anti-bonding mode. The charges induced on the gap-faces of the horizontal and vertical arms are of the same sign, and they clearly repel each other, forcing the charges to move away from the gap. On the other hand, at the higher wavelength peak, we have the bonding mode being excited and the charges on either side of the gap are opposite in sign and attract each other towards the gap. In these scenarios, we expect repulsive and attractive forces, respectively. The charges created on the horizontal arm are weaker at the Fano dip – more so in the case of strong coupling (small gap) than weak coupling (large gap) – whereas the charges on the vertical arms are still significant.

The y-component of the force on the horizontal arm (arm 2) as a function of wavelength and the gap size is shown in Fig. 6.8(a). Note that the colour scale is nonlinear. The major feature is the band where the arm is strongly attracted to the vertical arms (negative force in y-direction). This follows the higher wavelength peak in scattering quite well. In addition, there is a band where it is very weakly repelled (positive force in y-direction), which follows the lower wavelength peak in scattering. Both these features can be well-explained by the charge distributions in the two cases, as described earlier. The relative weakness of the repulsive force
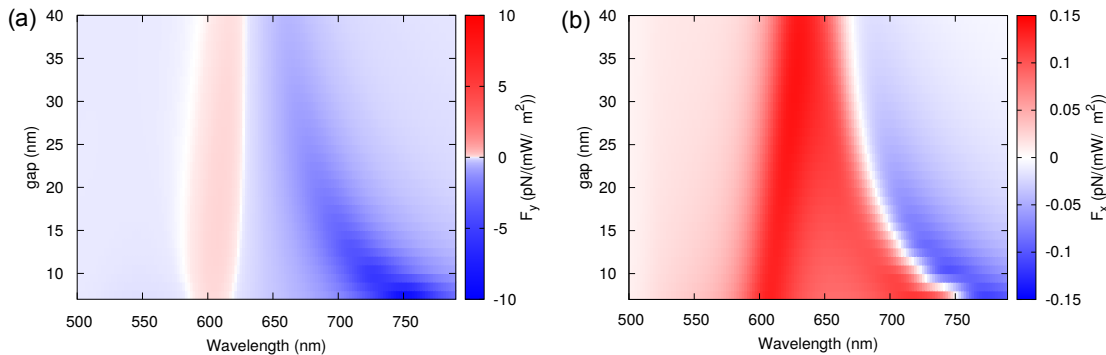

Figure 6.8 – Optical forces on (a) horizontal arm (arm 2) of the dolmen along y-direction, and (b) left vertical arm (arm 1) along x-direction.

compared to the attractive force is a result of the lower dipole moment at the anti-bonding mode, which is also evident from the scattering cross section at the two peaks.

The x-component of the force on the left vertical arm (arm 1) as a function of the same parameters is shown in Fig. 6.8(b). Clearly, this component of the force is much weaker than the y-component. This should not be unexpected since there is no pair of closely separated charges across a gap here unlike in the y-direction. What would seem surprising is that for large wavelengths, the force in the x-direction is repulsive between the vertical arms. If we had considered the x-force to be arising purely from the interaction between anti-parallel dipoles separated by a distance much shorter than the wavelength, we would have expected an attractive force throughout the wavelength range. However, these arms are extended dipoles, and the charges on the horizontal arm play a role in the x-component of the force as well. For short wavelengths, the charges at the gap faces of the horizontal and vertical arms have the same sign. This means that the top part of the vertical arm is subject to attractive forces both from the top part of the other vertical arm and the far end of the horizontal arm. These attractive forces would be stronger than the repulsion from the like charges at the bottom part of the opposite arm due to the higher separation for this pair. As a result, the net force is attractive. However, once we move to the higher wavelength regime, the charge distribution at the far end of the horizontal arm will start to repel the charges at the top of the horizontal arm. This eventually takes over since the dipole moment of the horizontal arm is stronger than that of the vertical arms as it is fed directly by the incident field. As expected, this transition from attractive to repulsive x-force happens around the higher wavelength scattering peak, as can be seen from comparing Fig. 6.7(a) and Fig. 6.8(b).

For clarity, the forces on the arms for a gap of 7 nm are shown in Fig. 6.9(a) and the same for a gap of 40 nm in Fig. 6.9(b). The attractive lateral force in the y-direction is an order of magnitude stronger than the scattering force in the z-direction for the shorter gap. Even the lateral force in the x-direction is comparable to the scattering force for most of the wavelength range. Note that the scattering force is significant only on the horizontal arm for longer
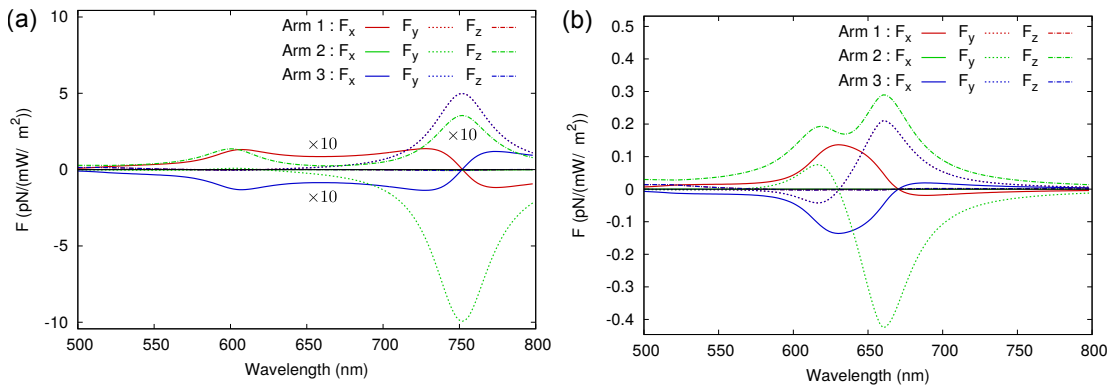

Figure 6.9 – Optical forces on the arms of the dolmen for vertical gap size of (a) 7 nm, and (b) 40 nm.

wavelengths since the horizontal dipole is what is directly excited by the incident field and scatters into the far field. For the larger gap, the y-forces are significantly reduced as a result of the increased charge separation. However, the y-component of the force on the horizontal arm is still the strongest force in the system, being stronger than the scattering force F_z. All the non-zero components of the lateral forces have the same order of magnitude as the scattering force.

6.2.3 Split-ring resonator

Finally, we look at the lateral forces in a split ring resonator. The structure we study here is formed out of two concentric rings lying in the xy-plane with 10 nm gaps on each ring. The outer ring has a radius of 140 nm whereas the inner ring has a radius of 80 nm, with both rings having a cross sectional radius of 20 nm. The rings are aligned such that centres of the gaps on both rings lie on the x-axis. All gap faces are fully rounded. The rings are made of Drude metal with frequency-dependent permittivity following Eq. (6.1), with Drude parameters $\epsilon_\infty = 9.5$, $\omega_p = 8.95$ eV and $\gamma = 0.0691$ eV corresponding to gold [282]. The structure is illuminated by a plane wave propagating in the z-direction.
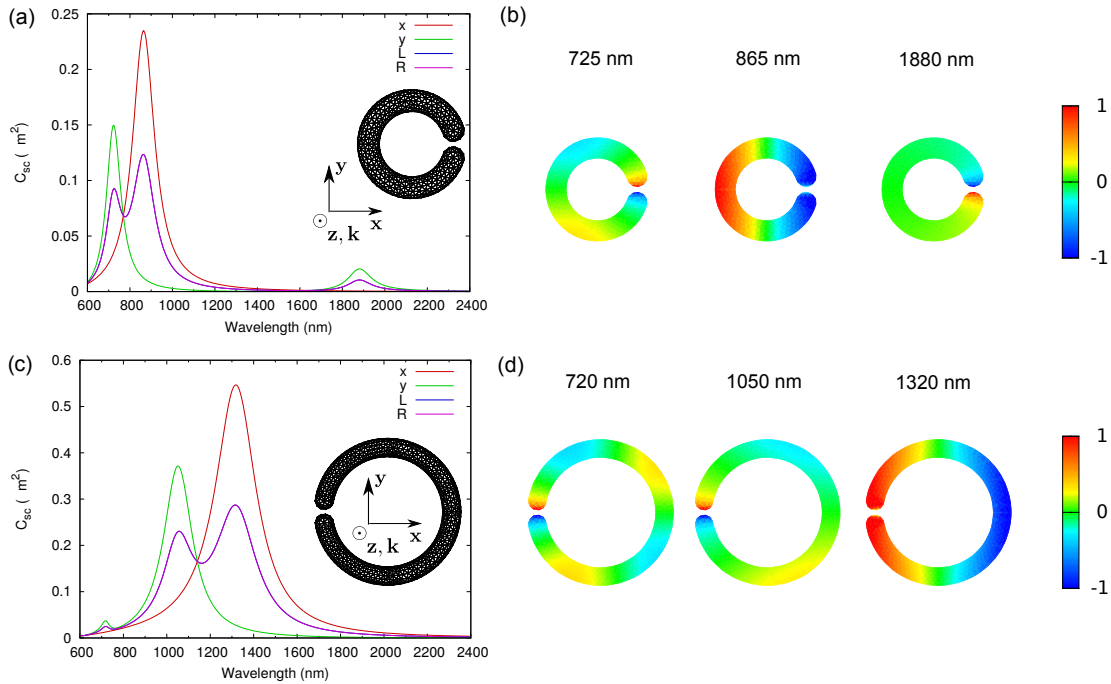
Figure 6.10 – (a) Scattering cross section for different incident polarisations for the inner ring in the split ring structure, as shown in inset. (b) Polarisation charges induced on the inner ring at the scattering peak wavelengths. (c) and (d) show the same results as in (a) and (b), respectively, for the outer ring.

It is instructive to see the response of the two rings individually first, since the optical response of the split ring can be understood in terms of hybridisation of the modes of individual

rings [283]. Figure 6.10(a) shows the scattering response of the inner ring as a function of wavelength for linear polarisations along x- and y-axes, and two circular polarisations L and R with opposite senses of rotation. There is a single scattering peak for polarisation along x-axis, whereas there are two peaks for polarisation along y-axis in the wavelength range considered. The response for the circular polarisations is just a combination of the two linear polarisations. The imaginary parts of the polarisation charges induced for the three peaks is shown in Fig. 6.10(b). The peaks for y-polarisation at 1880 nm and 725 nm are first and second order charge distributions along the circumference of the ring, with strong concentration of charges at the ends of the gap. On the other hand, the charge distribution for the x-polarisation peak at 865 nm is the dipolar charge distribution along x-direction.

In the same vein, Fig. 6.10(c) shows the scattering response of the outer ring. Once again, we have one scattering peak for x-polarisation and two for y-polarisation. However, there is one difference as seen from the charge distribution plots in Fig. 6.10(d). The charge distribution for the x-polarisation peak at 1320 nm is the dipolar distribution along the x- direction. However, the y-polarisation peaks at 1050 nm and 720 nm show second and third order distributions along the circumference of the ring. This should not come as unexpected, since increasing the size of the ring red shifts the scattering spectrum. As a result, the first order peak for the y-polarisation has red shifted outside the wavelength range considered here.

We can now look at the scattering response of the combined split ring system, shown in Fig. 6.11(a). There are two scattering peaks for x-polarised incident light and four for y-polarised incidence. The imaginary parts of the polarisation charge distributions for all six peaks are shown in Fig. 6.11(b). The charge distributions for the x-polarisation peaks at 880 nm and 1500 nm show them to be parallel and anti-parallel hybrids of the x-polarisation peaks of the inner and outer rings. The charge distribution at the isolated y-polarisation peak at 1925 nm essentially follows the inner ring-only charge distribution at 1880 nm whereas the peak at 1090 nm follows the outer ring-only distribution at 1050 nm. The peaks at 695 nm and 800 nm seem to be parallel and anti-parallel hybrids of the inner and outer ring charge
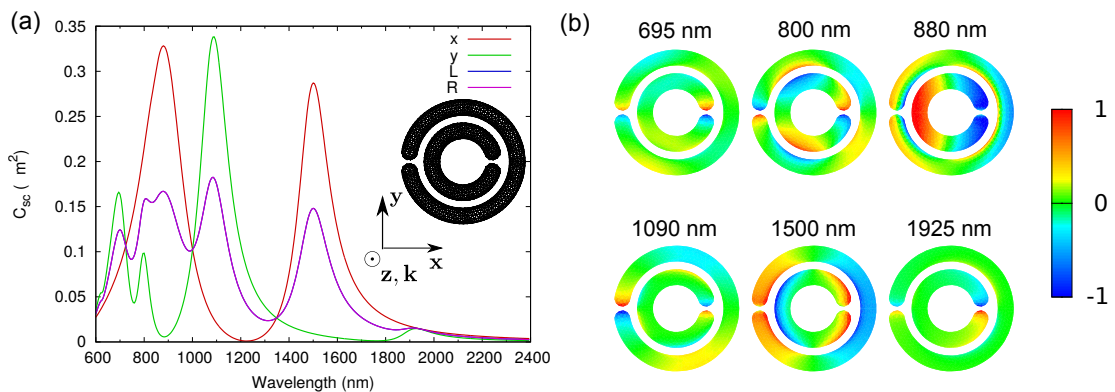

Figure 6.11 – (a) Scattering cross section for different incident polarisations, and (b) polarisation charges at the scattering peak wavelengths for the split ring structure.
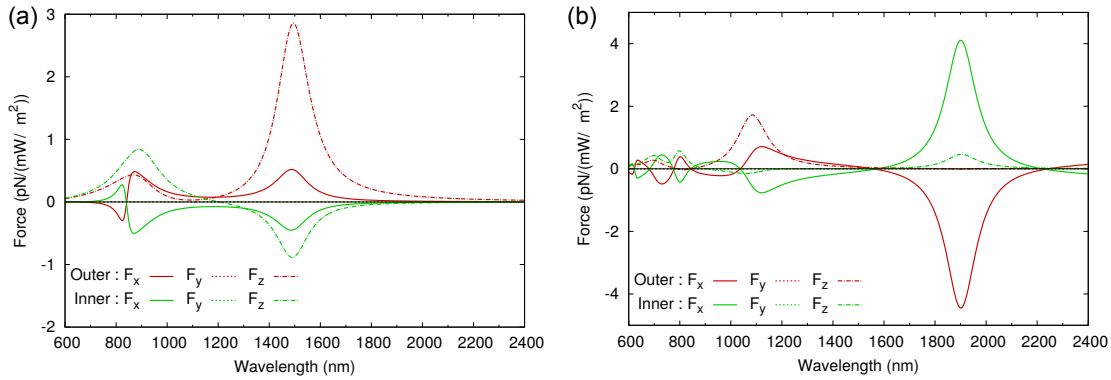
Figure 6.12 – Optical forces on the rings in the split ring structure for (a) x-, and (b) y-polarised incident field.

distributions at 725 nm and 720 nm, respectively. That is, all scattering peaks of the combined system can be understood in terms of the responses of the individual rings.

The forces on the two rings for x-polarised incident light are shown in Fig. 6.12(a). The scattering force in the z-direction is significantly stronger than the lateral force in x-direction. The y-component of the force is zero by symmetry. The direction of the x-component of the lateral force on the outer ring switches from left to right (and vice-versa for the inner ring), similar to the behaviour we had seen in the dolmen structure. Had the rings been gap-free, there would have been no lateral force in the x-direction either. Hence the lateral forces are created by the small charge asymmetry introduced by the gap, which is what makes the lateral forces weak. Due to the near-dipolar nature of the charge distributions for x-polarisation, it is difficult to qualitatively explain the origin of the switch merely using the polarisation charges like we did earlier. Once again, as in the case of the asymmetric antenna, we have a situation where the inner ring is pulled by the incident plane-wave rather than being pushed away from it.

The forces for y-polarised incidence are plotted in Fig. 6.12(b). Unlike the previous case, the lateral forces in the x-direction are comparable or larger than the scattering force in the z-direction. This is because the charge asymmetry is higher since the charges are strongly concentrated at the gaps. At 1925 nm where the inner gap is excited strongly, it induces polarisation charges on the nearby regions of the outer ring, resulting in the inner ring being pushed to the right and the outer ring to the left. At 1090 nm where the outer gap is excited, the situation is reversed. Once again, symmetry ensures that there is no lateral force in the y-direction.

It is interesting to compare the forces observed here with those found in the disk-ring Fano system by Zhang and Xiao [263]. In that system, the authors had uncovered the existence of force reversals and explained them in terms of the hybridization between the dipole modes of the disk and the multipole modes of the ring. There are a few factors which make the two systems very different. First of all, the disk and the ring were placed side-by-side instead of
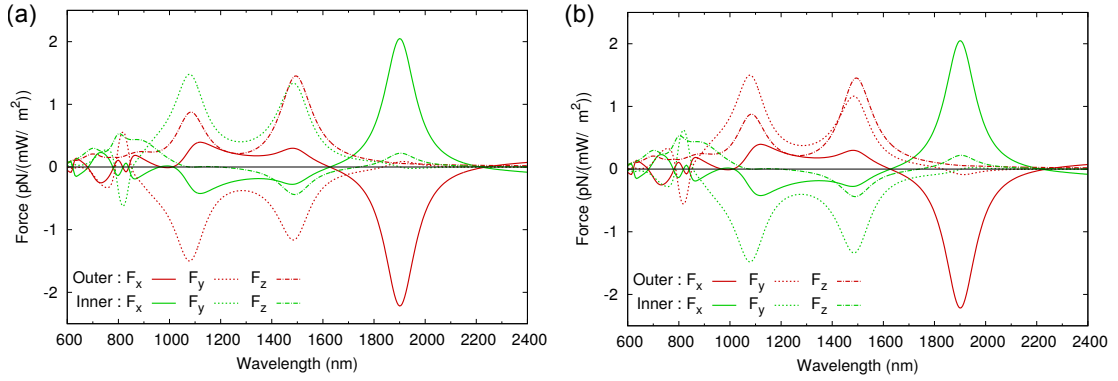
Figure 6.13 – Optical forces on the rings in the split ring structure for (a) L-, and (b) R-polarised incident field.

concentrically as the rings here . As a result, the coupling between the modes of the system happened entirely across the small gap between the disk and the ring - on the contrary, the hybrid modes of the split ring show coupling throughout the length of the rings as is evident from the charge distribution. Also, the charge concentration at the ring gaps and the resulting strong attractive force near the gap were features absent in the disk-ring system. These features make the description of forces in the split ring system more complicated. However, the basic feature that the energy of the hybridised modes dictates the force reversals is retained, which has been observed in systems as simple as a particle in a trap [158].

Figures 6.13(a) and 6.13(b) show the forces for L- and R-polarised incidence, respectively. Surprisingly, we see that the y-component of the force is not zero anymore in spite of the inversion symmetry of the structure about y-axis. In fact, it is the strongest force in the problem for much of the wavelength range. The reason for this apparent geometrical symmetry violation is that the force operator is not linear on the incident fields. Though the incident and scattered fields for circular polarised incidence can be expressed as a linear combination of the fields for x- and y-polarised incidence, the same is not true for the forces as there are cross-terms. It is probably most intuitive to understand the origin of this force component in terms of polarisation charges. When the incident light is x-polarised, the induced charge distribution is even about the x-axis. On the other hand, when the incident light is y-polarised, the charge distribution is odd. Both odd and even symmetries result in a zero net force in the y-direction. However, if we take an arbitrary linear combination of x-and y-polarisations, which is what happens in the case of circular polarisation, the induced charge distribution is neither odd nor even about the x-axis, and we cannot expect zero net force anymore. The importance of circular polarisation in the origin of y-force can be seen from the fact that the sign of the y-force switches on switching the sense of rotation of light, whereas the other components of force do not change. We would like to stress that the y-force is not a result of the chirality of the structure. The split ring structure has both xy- and xz-planes as mirror symmetry planes, so that the chirality of the structure is zero even if we consider two dimensional chirality [284]. Lateral forces arising in such structures without chirality under circular polarised illumination
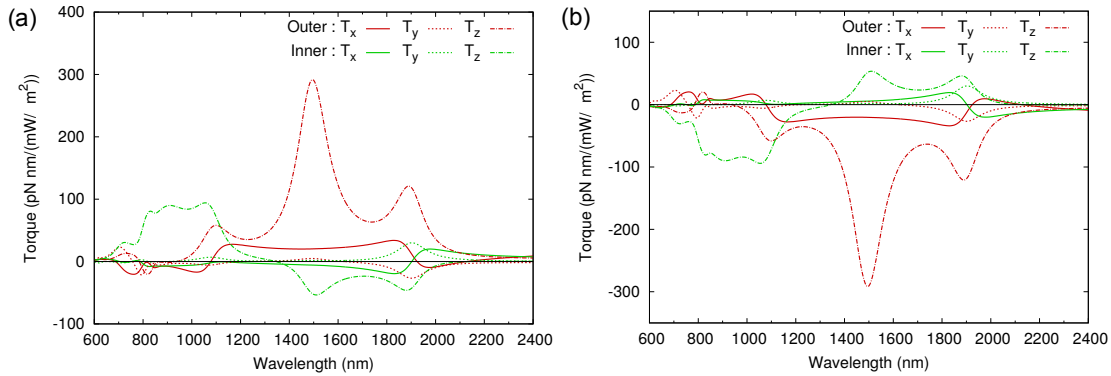
Figure 6.14 – Optical torques on the rings in the split ring structure for (a) L-, and (b) R-polarised incident field.

is a topic with rising recent interest [285, 286].

Finally, we look at the torque on the two rings produced by L- and R-polarised light, as shown in Figs. 6.14(a) and 6.14(b). We see a behaviour exactly opposite to the force in that, on switching the sense of rotation of the light, only y-torque remains unchanged whereas the other components switch sign. This should not be surprising since the y-component of the force affects the x-and z-components of torque. In particular, the x-component of the torque arises in the same fashion as the y-component of force, and would have been symmetry-forbidden for x- and y-polarisations.

What is more interesting is that the sense of rotation imparted to the ring need not be the same as that of the incident light. It is intuitive to understand particles absorbing circularly polarised photons and rotating in the same sense as the incoming light [287]. This can be considered analogous to the scattering forces which push the particle in the direction of wave propagation. However, there exists the phenomenon of negative optical torque, the analogue of optical pulling forces, where the particle ends up rotating in the opposite sense of the angular momentum of incident light [288]. We see such behaviour in the z-component of the torque on the inner ring. We see two distinct wavelength regimes where the z-torque imparted has opposite signs, meaning that the ring can end up rotating in the opposite sense of the angular momentum of the incoming photons.

As a final remark, we would like to add that though the simulations have been performed with vacuum as the background medium, the qualitative behaviour is expected to be retained in other backgrounds. The anomalous features uncovered here such as force reversal and negative optical torques will be present in other media where optical trapping and tweezing experiments are performed in, though there will be associated wavelength shifts and changes in force magnitudes. Fabricating the plasmonic systems on soft substrates which can be deformed by the optical forces should enable the experimental verification of these numerical results [289–291]. Though the presence of substrates can change the optical response of the nanostructures, the differences in optical forces and torques can be minimized by performing

the experiments in a fluid which is index-matched to the substrate. The mechanical stresses induced on the substrate and the material momentum contribution will also have to be taken into account, and the Abraham-Minkowski ambiguity discussed in Section 2.2.2 will come into the picture. Another possibility would be to perform experiments on self-assembled complex nanoplasmonic systems which provide significant freedom of motion [292–294].

6.3   Conclusion

We have shown that in the different plasmonic systems considered here, internal forces are significant, and even become stronger than the scattering force in the system in many cases. Internal forces between particles can be qualitatively understood in terms of the polarisation charges induced by the incident light. These lateral forces show a rich behaviour, switching between regimes of attraction and repulsion, depending on wavelength and inter-particle distance. The nonlinear nature of the force operator results in an interesting dependence on polarisation as well, creating forces in apparently geometrically symmetry-forbidden directions. Keeping all these in mind, lateral forces should be analysed properly along with the scattering/trapping forces while designing trapping experiments since the lateral forces could play a major role in directing the particles to be trapped towards or away from the trapping sites. We have also shown strong optical torques arising in these systems as a result of the lateral forces and also the appearance of negative optical torque, which could be utilised for optical orientation of nanoparticles.

7 Orientation and rotation of plasmonic nanostructures using optical torques

We discussed the presence of strong and varied optical torques in plasmonic systems in the previous chapter. Angular momentum in the incident light can be imparted to nanostructures to align them along desired directions as well as to rotate them continuously. In this chapter we analyse the possibility of utilising optical torques to achieve three dimensional orientation and rotation of plasmonic nanoparticles.

7.1 Introduction

Plasmonic nanoparticles with anisotropic shapes show a highly orientation-dependent optical response. It is thus beneficial to be able to align the nanoparticles in specific directions to achieve desired properties. Since the optical forces and torques exerted on such structures are also a function of their orientation, the optical torques can be used to align the nanoparticles by acting as a feedback mechanism.

Along with the increasing interest in optical trapping and tweezers, many experimental demonstrations of optical alignment of metallic structures were also performed [295–299]. Theoretical and numerical analysis of alignment have confined themselves primarily with two-dimensional manipulation of orientation using the angle the major axis of the nanostructure makes with the polarisation or limit themselves to the dipole limit [272, 273, 300, 301]. We wish to go beyond such limitations and consider three dimensional alignment of plasmonic nanostructures under plane wave incidence. Another field of experimental interest is continuous rotation of nanostructures by transferring the angular momentum in the incident light to the nanostructure [287, 302, 303]. Optical rotation permits achieving high angular frequencies for trapped particles, and it might be of interest to be able to rotate anisotropic nanoparticles about different axes.

Here we use SIE to numerically study the feasibility of achieving three-dimensional alignment and rotation of plasmonic structures. Two simple geometries are considered - a nanorod and a nanotorus. We delve into the direction and the stability of the alignment and its dependence on

wavelength and polarisation. The nanostructures are modelled to be made out of silver, with refractive index data taken from Johnson and Christy [175]. The simulations are performed with vacuum as the background medium.

7.2 Results and discussion

7.2.1 Nanorod

The first structure we study is a silver nanorod of dimension 120 nm × 40 nm × 40 nm. We will first consider the torques on the nanorod when it is displaced from the direction of polarisation of the incident field in the plane perpendicular to the propagation direction. The nanorod is placed on the xy-plane with the long axis along x, and illuminated by a plane wave propagating in the z-direction and linearly polarised in the xy-plane at an angle θ from the long axis of the rod. The schematic of the simulated system is shown in Fig. 7.1.

We obtain restoring torques on the nanorod in the z-direction, corresponding to angular motion in the xy-plane. These torques are plotted as a function of the illumination wavelength and the displacement angle in Fig. 7.1.

The first noticeable feature is the perfect sinusoidal behaviour of the restoring torque as a function of angular displacement. This can be explained using the fact that both the force and torque operators can be thought of as sesquilinear forms in the fields. That is, if the fields are represented by a vector $|\psi\rangle$, the torque operator has the form $\mathrm{Re}\left[\langle\psi|T|\psi\rangle\right]$. If the fields corresponding to the displacements of 0° and 90° at a certain wavelength are represented by $|0\rangle$ and $|90\rangle$ respectively, linearity implies that the field corresponding to a displacement of θ
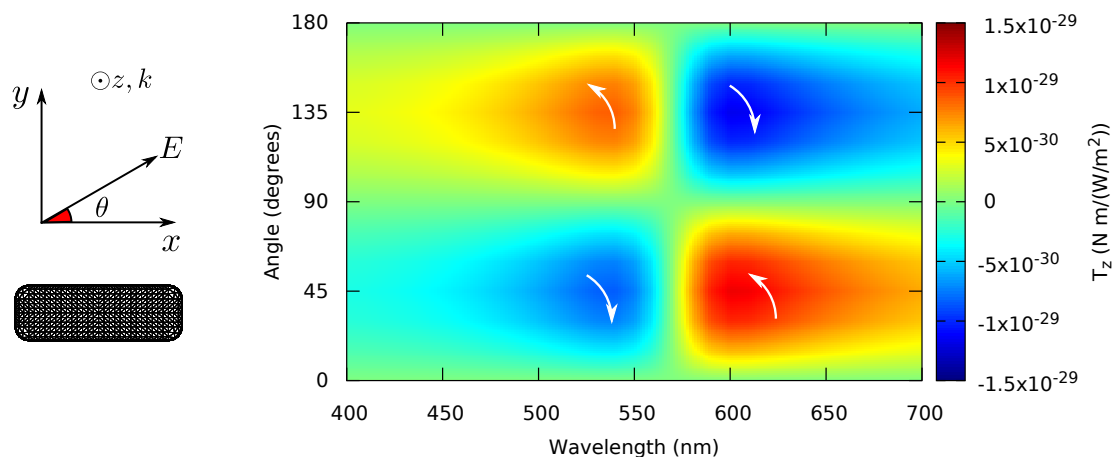

Figure 7.1 – Torque on the nanorod as a function of wavelength and displacement angle for angular displacement in the plane perpendicular to the propagation direction, as shown in the schematic . Arrows in the density plot depict the sense of rotation of the nanorod.

is given by

$$\left|\psi(\theta)\right\rangle = \cos(\theta)\left|0\right\rangle + \sin(\theta)\left|90\right\rangle , \tag{7.1}$$

The restoring torque for an angular displacement of θ is thus given by

$$
\begin{aligned}
T_z(\theta) &= \mathrm{Re}\left[\left\langle\psi(\theta)\right|T_z\left|\psi(\theta)\right\rangle\right] \\
&= \mathrm{Re}\left[(\cos(\theta)\left\langle0\right| + \sin(\theta)\left\langle90\right|)\ T_z\ (\cos(\theta)\left|0\right\rangle + \sin(\theta)\left|90\right\rangle)\right] .
\end{aligned} \tag{7.2}
$$

Now, symmetry dictates that the torque has to vanish for $\theta = 0°$ and $90°$. That is, $\mathrm{Re}\left[\left\langle0\right|T_z\left|0\right\rangle\right] = \mathrm{Re}\left[\left\langle90\right|T_z\left|90\right\rangle\right] = 0$. Using this in Eq. (7.2), we obtain

$$
\begin{aligned}
T_z(\theta) &= \cos(\theta)\sin(\theta)\,\mathrm{Re}\left[\left\langle0\right|T_z\left|90\right\rangle + \left\langle90\right|T_z\left|0\right\rangle\right] \\
&= \sin(2\theta)\,\mathrm{Re}\left[\left\langle0\right|T_z\left|90\right\rangle\right] .
\end{aligned} \tag{7.3}
$$

This perfectly explains the angular symmetry in the torques observed in Fig. 7.1. Note that we have only used symmetry arguments in the above proof, and no approximations (such as approximating the response of the nanorod as dipolar) have been made. The result is thus general and can be extended to explain the behaviour of larger and more complicated systems as long as they satisfy the required symmetry.

We can use this to understand the direction of stable orientation of the nanorod as well. Though both $\theta = 0°$ and $90°$ result in zero torque, only one of those orientations can result in stable equilibrium. If I_z is the moment of inertia of the nanorod about the z-axis, we have

$$
\begin{aligned}
I_z\ddot{\theta} &= -T_z(\theta) \\
&= -\sin(2\theta)\,\mathrm{Re}\left[\left\langle0\right|T_z\left|90\right\rangle\right] ,
\end{aligned} \tag{7.4}
$$

where the negative sign arises from the definition of the angle as the anticlockwise displacement of the polarisation vector from the rod axis rather than the other way round. This means that if $\mathrm{Re}\left[\left\langle0\right|T_z\left|90\right\rangle\right]$ (which has the same sign as the restoring torque at $\theta = 45°$) is positive, $\theta = 0°$ is the stable orientation direction and the nanorod orients itself perpendicular to the polarisation direction; and if it is negative, $\theta = 90°$ is stable and the nanorod orients along the polarisation.

A section of Fig. 7.1 for $\theta = 45°$ is extracted and plotted in Fig. 7.2. The torque is seen to be negative below 570 nm and positive above. Based on the discussion above, this means that the nanorod orients itself perpendicular to the polarisation direction at lower wavelengths and parallel at higher wavelengths. This behaviour has been studied previously and explained based on the nanorod being excited almost entirely along the long axis [272, 273, 304].
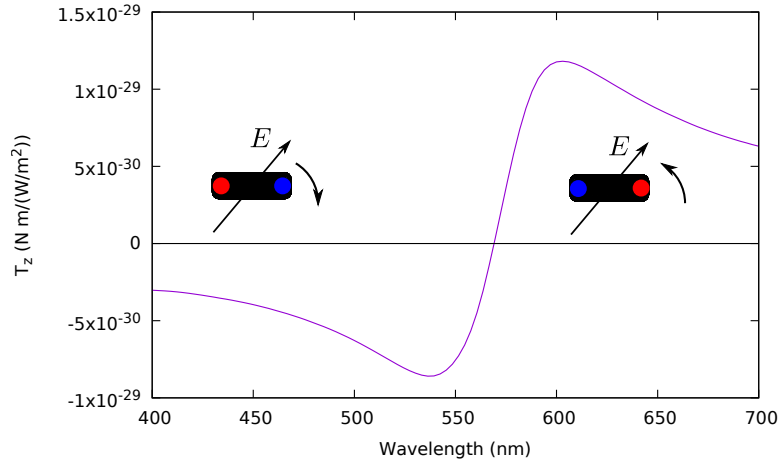
Figure 7.2 – Torque on the nanorod in Fig. 7.1 for a displacement angle of 45°. As we move across the plasmon resonance, the dipole induced on the nanorod changes from being in-phase with the electric field to out-of-phase, resulting in a switch in the sign of the torque.

Since one dimension of the nanorod is much longer than the others, for the wavelength range under consideration, it can be approximated to be polarised only along the long axis with polarisability α. As a result, the parallel component of the electric field is what polarises the nanorod, with the induced dipole moment $\mathbf{p} = \alpha E_x \hat{x}$. Under this approximation, the torque is given by

$$
\begin{aligned}
\mathbf{T} &= \frac{1}{2} \operatorname{Re}\left[\mathbf{p} \times \mathbf{E}\right] \\
&= \frac{1}{4} \operatorname{Re}(\alpha) |\mathbf{E}|^2 \sin(2\theta)\hat{z}.
\end{aligned}
\tag{7.5}
$$

Note how this expression has the same form as the more general one found in Eq. (7.3). Since the real part of the dipole moment switches sign on moving across the plasmon resonance, the sign of the torque switches as well.

It is interesting to estimate how strong this optical torque is. For a typical laser illumination of $1\,\mathrm{mW}/\mu\mathrm{m}^2$, we see that the optical torque is of the order of $10^{-20}\mathrm{N}\,\mathrm{m}$. The moment of inertia of the nanorod is merely of the order of $10^{-36}\mathrm{kg}\,\mathrm{m}^2$. Using these numbers, we can see that the angular frequency of oscillation is extremely high, around $10^8\mathrm{Hz}$. This is much higher than the experimentally achieved rotation frequency of a few kHz [287]. Thus the optical alignment of the nanorod is an extremely quick process, limited by the damping in the fluid rather than the strength of the field itself. It must be noted that the relaxation times are much higher than the time period of the light itself, so that it happens over many cycles and the variation of fields within a cycle does not matter.

We will now consider displacing the nanorod away from the polarisation plane - that is, changing the angle the long axis makes with the propagation direction. The rod is kept with its
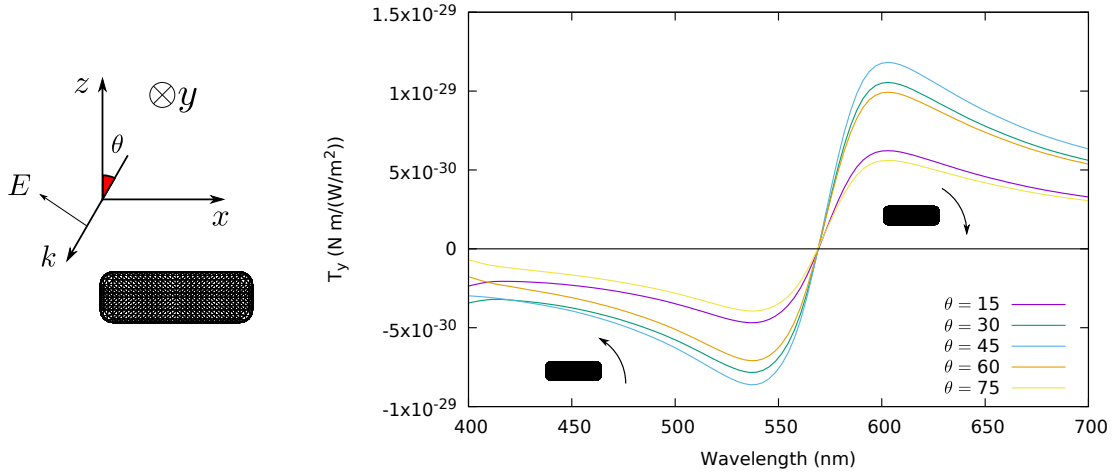
Figure 7.3 – Torque on the nanorod as a function of incident wavelength for different angular displacements from the propagation direction in the TM plane, as shown in the schematic. The torques are similar in both magnitude and features as in the case of displacement in the perpendicular plane.

long axis along x, and the angle of incidence θ is varied in the xz-plane with TM polarisation as depicted in the schematic in Fig. 7.3.

The restoring torques in the y-direction for selected angular displacements is plotted in Fig. 7.3. The torque for $\theta = 45°$ is virtually identical to the one in Fig. 7.2. This should not be surprising since the nanorod is still polarised primarily along the long axis of the rod and the angle between this axis and the polarisation direction is the major source of the torque. As a result, the nanorod orients parallel to the propagation direction (perpendicular to the polarisation) for low wavelengths and perpendicular to the propagation (parallel to the polarisation) at high wavelengths.

In the dipole approximation, according to Eq. (7.5), we have $T_y(\theta) = T_y(90° - \theta)$. The torques found for $\theta = 30°$ and $60°$ (and for $\theta = 15°$ and $75°$) would thus have been identical if the approximation were fully valid. However, there is a noticeable difference between the torques for the pairs of angles. This shows that, though the nanorod-polarisation angle is the primary source of the torque, the higher modes in the system induced due to retardation effects along the nanorod length have already shown their signature. Retardation effects increase as the size of the object increases compared to the wavelength, and the pairwise differences increase for low wavelengths as a result.

We now repeat the calculation for TE polarisation, as shown in Fig. 7.4. The resulting torques are seen to be much weaker, by nearly three orders of magnitude. The nanorod is now being polarised along its short axis, and the resultant dipole is in the same direction as the incident electric field. Thus the torque now arises entirely from retardation effects due to the length of the nanorod, and is doubly weak due to the low polarisability about the short axis.
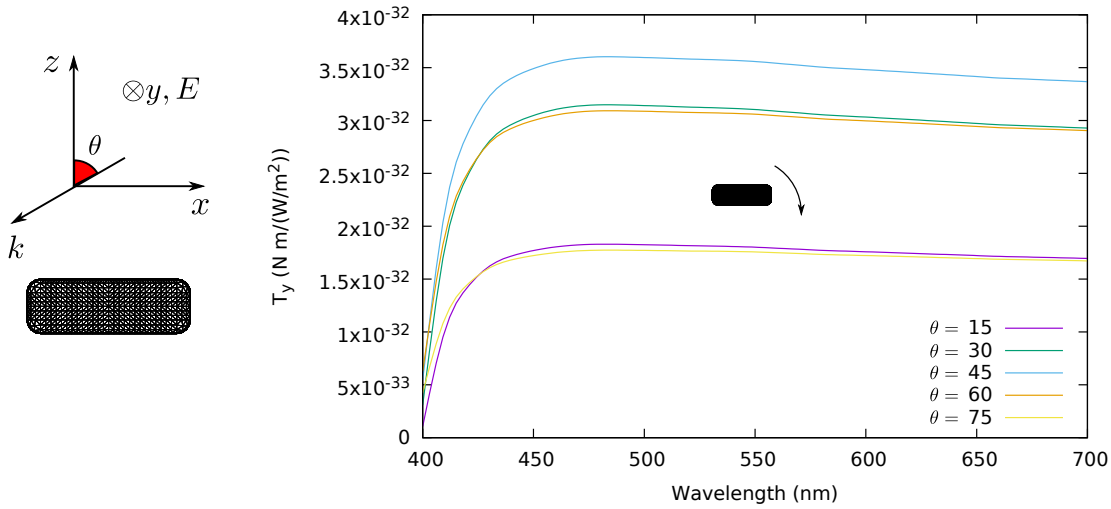
Figure 7.4 – Torque on the nanorod for different angular displacements from the propagation direction in the TE plane. The torques in this case are much weaker than those seen earlier.

This suggests that orienting the nanorod along the propagation direction at low wavelengths is not entirely stable. At high wavelengths, displacements in any direction away from the polarisation direction tend to return the rod to polarisation alignment. However, at low wavelengths, only a displacement away from the propagation direction towards the polarisation direction is guaranteed to bring it back. Displacement in the orthogonal direction results in a very weak torque and the plane perpendicular to the polarisation direction behaves as a plane of neutral equilibrium.

We will now look at the issue of stability more deeply. For this, the angle of incidence will be varied freely in the first octant, as shown in Fig. 7.5. The nanorod is still placed along the x-direction. The resultant torque vector is computed and its x-component is ignored since
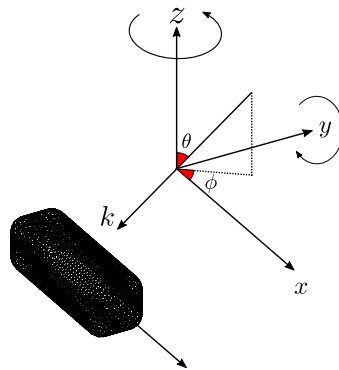
Figure 7.5 – Coordinate system to study the restoring torque on the nanorod for 3D displacements. The nanorod is placed with its long axis along x, and different (θ, ϕ) incidence angles are considered. The torques along y- and z-directions can be used to find the net torque away from the propagation direction.

Figure 7.6 – Restoring torque on the nanorod for different incidence angles for (left) TE and (right) TM polarisations. The restoring torque nearly vanishes when $\phi = 0°$ or $\phi = 90°$ for TE polarisation, and when $\theta = 90°$ or $\phi = 90°$ for TM. Sign of the restoring torque is otherwise independent of angle and polarisation for a given wavelength, and shows the switch around the plasmon resonance.

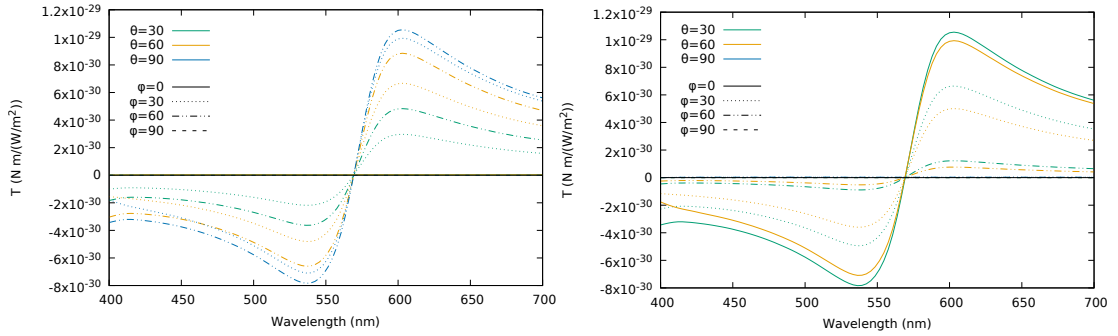that only results in the rod spinning about its own axis. From the remaining components, the component of the torque aligning the rod with respect to the propagation direction is extracted and plotted in Fig. 7.6 for both TE and TM polarisations.

The first observation is that the sign of the torque is the same for all angles of incidence and both polarisations, except for the sign flip at the plasmon resonance. The sign of the restoring torque is thus independent of polarisation. However, the component of torque vanishes (or nearly so) for certain angles. For angles for which the torque vanishes are $\phi = 0°$ and $\phi = 90°$ for TE polarisation, and $\theta = 90°$ and $\phi = 90°$ for TM. Of these, the $\phi = 90°$ cases should not be concerning since those correspond to the nanorod being perpendicular to the propagation direction, and it could still be a stable equilibrium if the nanorod moves towards (or away from) the plane for small displacements. However, different values of θ for $\phi = 0°$ (TE) and different values of ϕ for $\theta = 90°$ (TM) correspond to non-perpendicular orientations of the nanorod with respect to the propagation direction, and low values of torque for those cases shows that the equilibrium is only neutral, as suspected.

The difficulty in this system is that all orientations of the nanorod perpendicular to the polarisation direction are equivalent in terms of optical torques, and it is not possible to pick the propagation direction from it. One possible way to overcome this is by using circular polarisation instead of linear, so that all orientations perpendicular to the propagation direction are now identical and the propagation direction becomes the unique direction. The results for restoring torques for L and R polarisations for the same geometry are shown in Fig. 7.7.

We immediately see that the torques for the two circular polarisations are identical, as would be expected from symmetry. The torques are qualitatively similar to those in the case of linear polarisation, except that torque vanishing now happens only for the three cardinal directions. We thus have stable alignment along propagation direction for low wavelengths and in the polarisation plane for high wavelengths. This means that the nanorod ends up
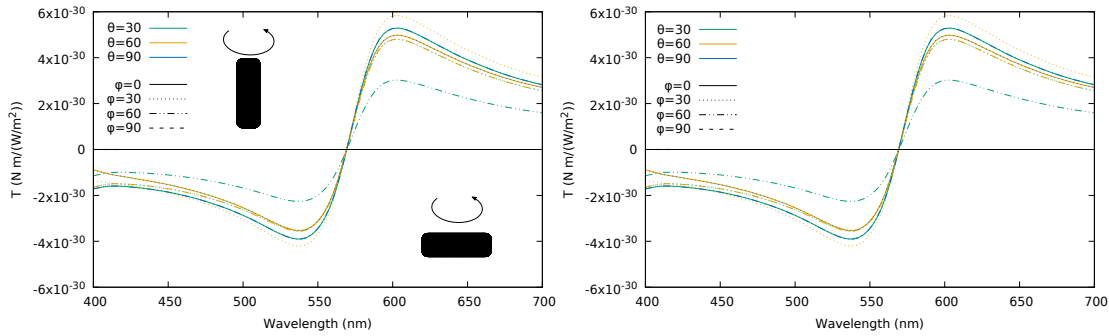
Figure 7.7 – Restoring torque on the nanorod for different incidence angles for (left) L and (right) R polarisations. Both polarisations result in identical restoring torques which vanish only for incidence along one of the coordinate axes. Restoring torques for different angular displacements are now nearly equal in magnitude, and tend to rotate the nanorod about its long axis at short wavelengths and its long axis at higher wavelengths.

rotating continuously due to the angular momentum in the incoming light, about the long axis at short wavelengths and about the short axis at long wavelengths.

7.2.2 Nanotorus
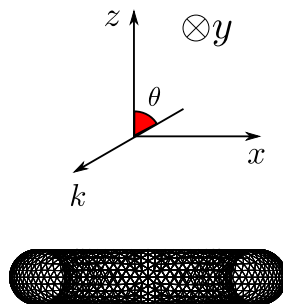
Figure 7.8 – Schematic for studying restoring torques on the nanotorus. The torus is placed on the xy-plane with its axis along z, and direction of incidence in the xz-plane.

Though stable three dimensional alignment has been achieved for the nanorod using circular polarisation, this is accompanied by rotation of the object. To be able to achieve multiple stable trapping directions for linearly polarised incidence, more needs to be done. The results from the previous section suggest that using a nanostructure with higher retardation might do the trick. We attempt this by choosing a more oblate object, a silver nanotorus of major radius $R = 80$ nm and minor radius $r = 20$ nm. The torus is placed on the xy-plane with its axis along z, and the angle of incidence is varied in the xz-plane as shown in Fig. 7.8.

The restoring torque as a function of wavelength and angle of incidence is plotted for TE and TM polarisations in Fig. 7.9. The qualitative features are very similar to what was found in the nanorod. The plasmon resonance has red shifted and the torque switching now happens above 800 nm, with the torus orienting with its axis parallel to the propagation direction at
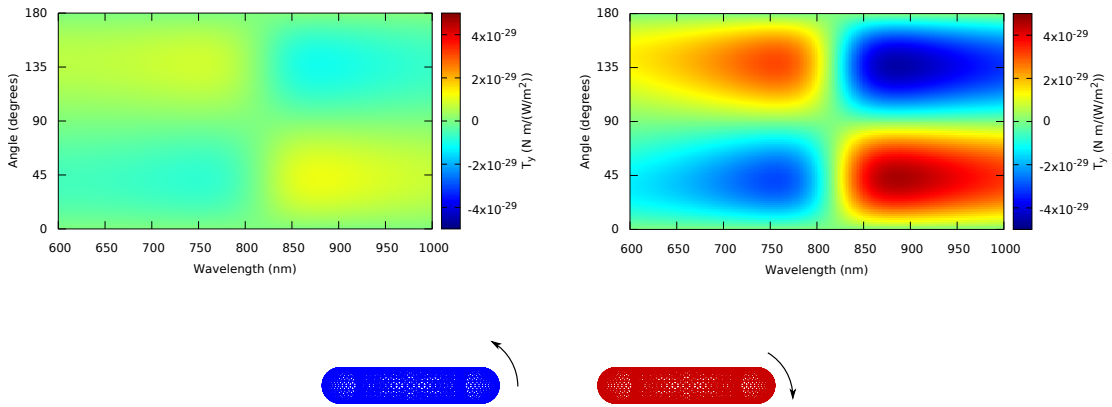
Figure 7.9 – Restoring torque on the torus as a function of incident wavelength and displacement angle for (left) TE and (right) TM polarisations. The torque switching behaviour is very similar to the case of the nanorod.

higher wavelengths, and with the propagation direction passing through the plane of the torus at lower wavelengths.

The restoring torque for TE polarisation is still weaker than in the case of TM, but the relative magnitudes are now better. This can be seen from the section of Fig. 7.9 for $\theta = 45°$, plotted in Fig. 7.10. Unlike the case of the nanorod where the two sets of torques differed by three orders of magnitude, they are of nearly the same order here. Also to be noted is that they show the same qualitative behaviour with wavelength, including the sign flip at the same wavelength. This is because the torus is flat unlike the nanorod which was long, and the high polarisability direction now has a multiplicity of two.

As a result, the nanotorus allows us to achieve stable orientation along two different directions even for linear polarisation.

We finally look at the restoring torques on the nanotorus for circular polarisation, shown in
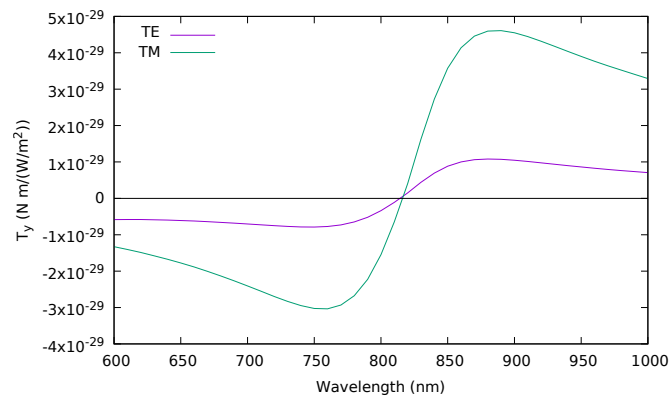
Figure 7.10 – Restoring torque on the torus for $\theta = 45°$. The restoring torque for TE polarisation is now relatively significant.

93
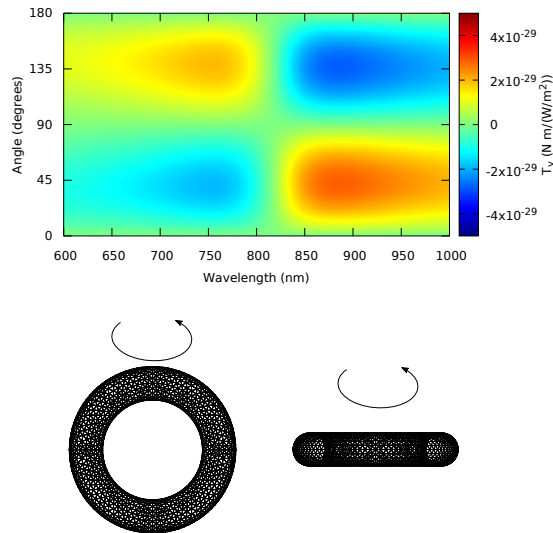
Figure 7.11 – Restoring torque on the torus for circular polarisation (Both L an R polarisations result in the same restoring torque, and thus only one figure is shown). The restoring torques result in the torus rotating about an axis passing through the plane of the torus for low wavelengths, and about the cylindrical symmetry axis for high wavelengths.

Fig. 7.11. Since both L and R polarisations result in the same restoring torques, only one set is shown. The restoring torque retains the qualitative features and remains high in magnitude. Thus we can use circularly polarised light to rotate the nanotorus about an axis that passes through the plane of the torus at low wavelengths, and about the axis of the torus at high wavelengths.

7.3 Conclusion

We have shown that optical torques can be used to align and rotate plasmonic nanostructures about different axes. By tailoring the optical torques suitably, it should be possible to create plasmonic three dimensional orientation switches. Moving from two-dimensional to three-dimensional orientation switching requires the use of retardation effects and thus the multipolar modes in the nanostructure. Designing multimode plasmonic structures thus offers the prospect of providing better control over the orientation using optical torques.

The results of the simulations suggests another important point : when optical experiments are performed with anisotropic nanoparticles suspended in a fluid, for example, it should not be assumed that they are dispersed isotropically. The incident fields can be strong enough to orient the nanoparticles along certain directions, and their optical response would be completely different from that of an isotropically dispersed system, and can result in a seemingly strange wavelength-dependent behaviour. Alignment effects of optical torques must thus be taken into consideration during such optical experiments.

8 Polarisation charges in plasmonic systems

Numerical evaluation of polarisation charges at nanostructure surfaces provides insights into various aspects of the electromagnetic response of the nanostructures such as scattering peak shifts and optical forces [61, 194]. In this chapter, we explore the information contained in the complex polarisation charges produced by electromagnetic simulations in the frequency domain. We discuss how to understand and visualise the complete charge information in systems of increasing complexity. We also touch upon a few pitfalls which should be avoided while dealing with polarisation charges.

8.1 Introduction

Applying an electric field on an object placed in a background of a different dielectric constant induces polarisation charges on the object. If all domains in the system have homogeneous dielectric permittivities, the induced charges lie only on the surfaces where permittivity changes abruptly between two domains. Shining monochromatic light - an electromagnetic wave with a harmonic time dependence - on nanostructures results in the creation of polarisation charges at the nanostructure surfaces having the same harmonic dependence as the incident light, as long as we limit ourselves to the linear regime.

Since we are interested in a fundamental treatment, all the SIE simulations are performed with vacuum as the background medium, and the nanostructures are made of gold. The permittivity of gold as a function of frequency ($\epsilon(\omega)$) is given by the Drude formula Eq. (6.1), with Drude parameters $\epsilon_\infty = 9.5$, $\omega_p = 8.95$ eV and $\gamma = 0.0691$ eV to fit the permittivity data from Johnson and Christy [175, 282]. The scattering cross section is computed by integrating the Poynting vector of the scattered field on a large sphere surrounding the nanostructure, Eq. (2.48). The polarisation charge density at a point on the structure ($\sigma_p(\mathbf{r})$) is evaluated from the divergence of surface currents using Eq. (2.16).

8.2   Physical meaning of complex polarisation charges

Electromagnetic simulations in the frequency domain such as FEM, DDA, VIE and SIE represent the fields by complex vectors. The real and imaginary parts of the complex vectors, combined, contain the complete details of the time evolution of these quantities. The polarisation charges found by these simulations are thus naturally represented as complex scalar quantities.

Let us first discuss the physical meaning of the real and imaginary parts of the complex polarisation charges. The first thing that any mathematical textbook states while using the trick of representing a physical quantity by a complex number is that only the real part of the quantity has physical significance, and should be extracted at the end of the calculation. However, we will show here that we should be cautious while applying this rule to the polarisation charges we obtain from the simulations as complex scalars. The imaginary part of the complex polarisation charge is not an unphysical mathematical tool and should not be discarded.

Why is this? The answer is that we should discard the imaginary component not at the outset but only while computing the charges at a particular instant. When we find $\sigma_p(\mathbf{r}, t)$, the polarisation charges found at a location on the structure at a given moment, we should indeed ensure that it is real. But the output of the simulation $\sigma_p(\mathbf{r})$ is not merely the polarisation charge at $t = 0$; it contains the entire time evolution of the charges at the location. The surface charges found at a time t can be evaluated as

$$\sigma_p(\mathbf{r}, t) = \mathrm{Re}[\sigma_p(\mathbf{r}) \exp(-i\omega t)] . \tag{8.1}$$

As is evident, the physically relevant charge at an instant is only the real part of the product of the surface charge $\sigma_p(\mathbf{r})$ and the harmonic propagation term $\exp(-i\omega t)$. However, if we had used only the real part of the complex charge $\sigma_p(\mathbf{r})$ at the outset in this equation, we would have found the wrong value of charge at time t. In particular, we have

$$\sigma_p(\mathbf{r}, \frac{T}{4}) = \mathrm{Im}[\sigma_p(\mathbf{r})] , \tag{8.2}$$

where T is the time period of the wave. That is, only the imaginary part of $\sigma_p(\mathbf{r})$ contributes to $\sigma_p(\mathbf{r}, t)$ at this instant. Had we discarded the imaginary part of σ_p at the outset, we would have found the incorrect result of zero instead.

This brings us to the next point, what does time t mean in such a system where all fields and charges have a harmonic dependence? The answer is that usually, the zero point of time is implicitly defined by the illumination conditions. For example, suppose that we simulate the response of our structure for plane wave illumination defined by the complex electric polarisation vector $\mathbf{E}(\mathbf{r}) = \mathbf{E_0} \exp(i\mathbf{k} \cdot \mathbf{r})$. This has already defined the zero of time by $\mathbf{E}(\mathbf{0}, t) = \mathrm{Re}[\mathbf{E_0} \exp(-i\omega t)]$. If we added an additional phase factor $\mathbf{E}(\mathbf{r}) = \mathbf{E_0} \exp(i\phi) \exp(i\mathbf{k} \cdot \mathbf{r})$, all the simulation results would be identical except for all fields and charges getting the additional phase factor of ϕ. This is equivalent to redefining the zero of time, and does

not change the physics in any way. Something slightly different happens when we find the modes of the system instead of the response to certain illumination. In this case, there is automatically the freedom to multiply the fields and charges by an arbitrary phase since the incident illumination is zero.

Since the zero of time has been shown to be arbitrary, we have the freedom to redefine it as we see fit to suit our convenience. Though the values of the real and imaginary parts of charge will change with such a shift, Eq. (8.1) will still be valid. Such time shifts can be used to change the phase of the charge distribution and move the imaginary part of the charge to the real part without any loss of information. As will be shown later, using such time shifts can help understand the charge distribution on some systems better. However, care must be taken to ensure that all charges (and fields, if they are being used) are propagated by the same phase/time delay simultaneously. It is incorrect to modify the phase of the charges on one part of the system while leaving another part unchanged. This could result in unphysical results such as net charges on free standing structures.

With this introduction, we hope that the physical meaning of the complex charge is clear. We will now move on to studying the charges on a few systems of increasing complexity to see how best to study the charges on these systems and to understand various nuances.

8.3   Results and discussion

8.3.1   Nanorod

We will start with a simple system consisting of a single nanorod of dimensions 120 nm × 40 nm × 40 nm. The nanorod is illuminated by a plane wave propagating along one of the short axes, and polarised along the long axis.

The scattering cross section of the nanorod is shown in Fig. 8.1(a). There is a single scattering peak in the frequency range considered, corresponding to the dipole resonance of the nanorod. The complex polarisation charges at five different frequencies induced on the surface are also shown. Note that for each wavelength, the real (top) and imaginary (bottom) parts of the complex polarisation charges are normalised together to the highest value of the component over the whole surface. At low frequencies, it is seen that the real part of the charges dominates over the imaginary part. As the frequency is increased, the imaginary part becomes more and more significant, and looks similar to the real part. Near the resonance peak, the imaginary part dominates the real part. Once the scattering peak is crossed, the real part picks up strength again, though it gains a sign flip as well. Far away from the resonance, we have again the situation where the real part dominates the imaginary part. The nanorod at resonance is a good example of a system in which taking only the real part of the charges at the outset would have given a completely incorrect picture – that would have resulted in zero charge but the charges have not vanished, only shifted in phase.
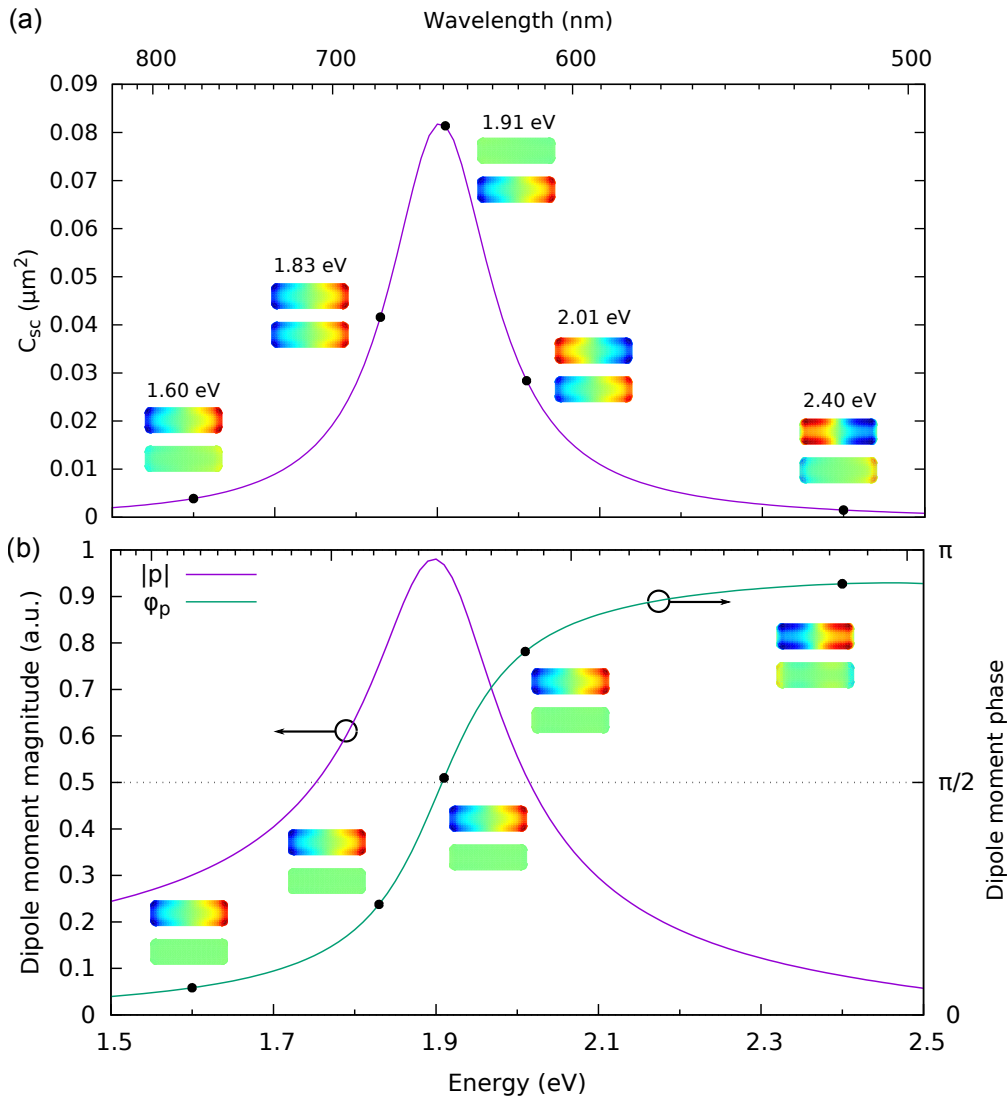
Figure 8.1 – (a) Scattering cross section as a function of frequency for the nanorod for po-larisation along the long axis. The real (top) and imaginary (bottom) parts of the complex polarisation charges at five different frequencies are also shown. (b) The magnitude and phase of the x-component of the dipole moment. The polarisation charges shown previously are corrected to the phase of the dipole moment, and the real and imaginary parts are plotted.

The behaviour of real and imaginary parts of the charge is similar to that seen in simple harmonic motion, since the system is similar to a classical driven oscillator [305–309]. This parallel will become more clear on looking at the dipole moment induced on the rod. The x-component of the dipole moment of the rod was computed from the surface currents using the formalism developed in Section 2.4, and its amplitude and phase are shown in Fig. 8.1(b). The phase of the dipole moment shows a smooth transition from 0 to π, passing through $\pi/2$ near the scattering peak. As explained in the previous section, adding a phase factor to the incident field does not change the physics but adds the same phase factor to the charges. For

each of the five frequencies shown earlier in Fig. 8.1(a), we subtract the phase of the dipole moment at the frequency from the incident field and thus from the charges, and plot the real and imaginary parts of the charges again. With this phase correction, we see that the imaginary component has vanished in almost all cases. This is a signature of the system having a single dominant mode, since the presence of a second mode with a different phase would have resulted in non-vanishing imaginary components. In fact, we do see the emergence of a second mode in the phase-corrected charge plot at the highest frequency (2.40 eV). Here, the imaginary part of the charge has not vanished completely in spite of the phase correction, and shows the signature of a higher order mode. It is interesting to note that this mode is very weak, and its signature was not clear from the real and imaginary charge plots without phase correction since the slight phase difference from π in the charges of the dominant mode results in an imaginary part which dominates the weaker mode charges. The phase-corrected charge plots also show a continuous migration of charges from the face to the centre on increasing frequency, a trend that has been observed before [194].

Having demonstrated the usefulness of phase correction, we now move on to more complicated systems.

8.3.2 Nanosquare

The next system which we consider is a nanosquare of dimensions 120 nm × 120 nm × 40 nm. In Fig. 8.2, the scattering cross section, dipole moment and polarisation charges before and after phase correction are shown in the same manner as in Fig. 8.1 for incident light polarised along x-axis. The same effects described previously can be seen here as well. Due to the symmetry in the system, y-polarised light will result in the same scattering cross section. The charges induced will be identical in magnitude and phase too, except for being rotated by 90°.

The situation becomes more interesting when, instead of x- or y-polarisations, the incident wave polarisation is a linear combination of the two. A general input polarisation can be represented by

$$\mathbf{E_0}(\theta, \psi) = \cos(\theta)\,\hat{x} + \sin(\theta)\exp(i\psi)\,\hat{y} \tag{8.3}$$

It is easy to see that all linear, circular and elliptical polarisations can be described by suitable values of θ and ψ. To study the charges induced by general polarisation states, we fix the input frequency to be 1.95 eV. The real and imaginary components of charges for certain values of θ and ψ are shown in Fig. 8.3(a). Note that these charges are phase-corrected using the phase of the dipole moment as before.

When the relative phase ψ between the x- and y-components of input polarisation is zero, we see that the imaginary component of the phase-corrected charge plots is zero. This should not be surprising since the phase correction sets the imaginary component of charge for both x- and y-polarisations to zero and we are merely looking at a linear combination of both
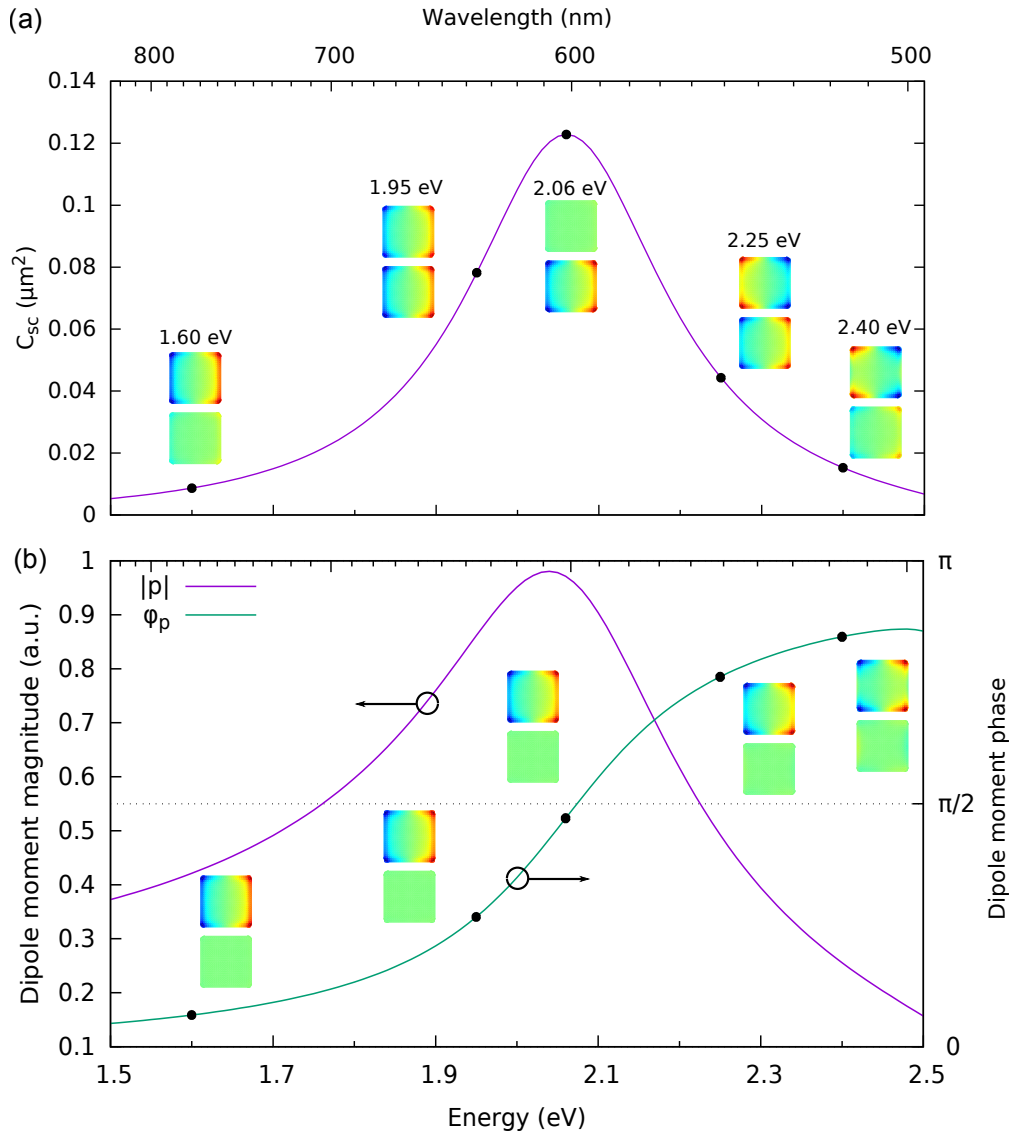
Figure 8.2 – (a) Scattering cross section of the nanosquare for incident light polarised along x-axis, and polarisation charges at five chosen frequencies. (b) Magnitude and phase of the dipole moment, and the polarisation charges in (a) phase corrected to the respective dipole moments.

without additional phase offsets. Changing the value of θ changes the real part of the charge distribution - the charges essentially get rotated by θ. Adding a phase offset of π retains these features since it merely adds a negative sign to one of the components.

However, the situation changes when the phase ψ is nontrivial. When $\theta = \pi/4$ and $\psi = \pi/2$, we see that the real and imaginary plots have equal magnitude. Since they are geometrically rotated by 90°, no phase correction can result in the vanishing of one component, a situation unlike what has been discussed till now. To understand what is going on, we plot the surface

(a)

$\theta = \pi/4$	$\theta = \pi/8$	$\theta = \pi/4$	$\theta = \pi/4$	$\theta = \pi/4$
$\psi = 0$	$\psi = 0$	$\psi = \pi$	$\psi = \pi/2$	$\psi = \pi/4$

$\mathfrak{R}$

$\mathfrak{I}$

(b)

$t = 0$	$t = T/8$	$t = T/4$	$t = 3T/8$	$t = T/2$

(c)

(d) $\mathbf{E}(t)$ $\qquad$ $\mathbf{p}(t)$ $\qquad$ (e) $\mathbf{E}(t)$ $\qquad$ $\mathbf{p}(t)$
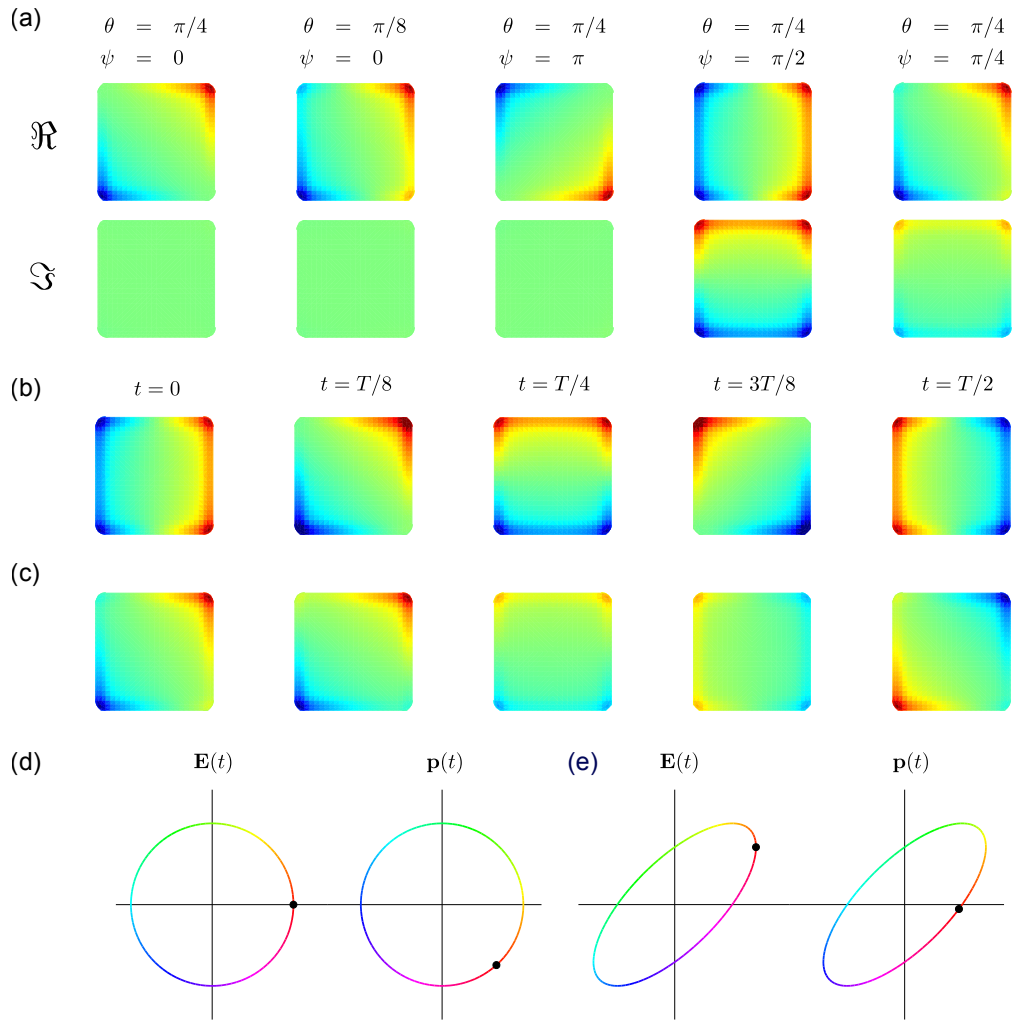
Figure 8.3 – (a) Real (top) and imaginary (bottom) parts of polarisation charges for various linear combinations of x- and y-polarised incidence based on Eq. (8.3). The charge plots have been phase-corrected to the phase of the dipole moment. Instantaneous charge plots at five different times are shown with phase correction for ($\theta = \pi/4, \psi = \pi/2$) in (b), and for ($\theta = \pi/4, \psi = \pi/8$) in (c). The curve traced by the tip of the incident electric field and the dipole moment vectors over a period are plotted without phase correction for the two cases in (d) and (e), respectively. The black dot indicates the time $t = 0$, and the time evolution is colour-coded from red to green to blue to red.

charges $\sigma_p(\mathbf{r}, t)$ at five instants in Fig. 8.3(b). Note that the phase correction to the dipole moment is still applied for clarity. At $t = 0$, the charge distribution is such that the dipole moment is exactly in the x-direction. With increasing time, the charges shift: the positive charges found at the right edge of the square migrate towards the positive y-direction, whereas the negative charges at the left edge do the reverse. This results in a rotation of the dipole moment. At $t = T/4$, the charges have reoriented themselves such that the dipole moment is now in the y-direction. This rotation continues further with time. This should not be

surprising, since $\mathbf{E_0}(\theta = \pi/4, \phi = \pi/2) = (\hat{x} + i\hat{y})/\sqrt{2}$ is circularly polarised illumination. The evolution of the incident electric field and the instantaneous dipole moment as a function of time are plotted in Fig. 8.3(d) without phase correction for the dipole moment. The colours denote the time and $t = 0$ is marked separately. It can be seen that the dipole moment curve is identical to the incident field curve, except for a rotation along the colours. The geometrical similarity is the consequence of the polarisability along x- and y-directions being identical, and the colour rotation is due to the phase shift between incident light and the dipole moment, which has not been corrected for here. The rotation of the dipole moment clearly explains the trends seen in the time evolution of the charges.

When ψ is changed to $\pi/4$, the situation changes tremendously. The instantaneous charges for this case have been plotted in Fig. 8.3(c). The rotation of the dipole moment is no longer uniform. For example, between $t = T/4$ and $t = 3T/8$, the instantaneous dipole moment rotated $90°$ from $+y$ direction to $-x$ in a duration of $T/8$, in contrast with the $\psi = \pi/2$ case which always took $T/4$ time for rotating the dipole moment by $90°$. The reason for this can be understood by looking at the $\mathbf{E}$ and $\mathbf{p}$ curves in Fig. 8.3(e). The incident field is now elliptical, with major axis inclined to the symmetry axes of the square. As a result, so is the dipole moment. Since the colours do not traverse the points on the ellipse at constant angular velocity, the dipole moment rotation is not uniform. The phase difference between incident field and dipole moment also means that their instantaneous rotations have different rates.

This example goes on to show that, though the real and imaginary parts of the charge contain the full information about the evolution of polarisation charges on the structure, visualising the evolution is not straightforward. Additional tools such as movies and snapshots of charges at different times, and dipole moment ellipses as we proposed here, make it easier to grasp the complexity of the charge evolution.

8.3.3 Nanorectangle

Next, we break the symmetry of the nanosquare by turning it into a rectangle. The nanorectangle has dimensions 120 nm × 80 nm × 40 nm. The width of 80 nm ensures that the polarisability along y-direction is comparable to that along x in the frequency range being considered, unlike the nanorod considered previously. As a result, the system has two resonances for the two orthogonal polarisations, but the resonances are sufficiently close in terms of peak intensity and position for them to have significant overlap.

The scattering cross section for x- and y-incident polarisations are plotted in Fig. 8.4(a) along with the real and imaginary polarisation charges for both incidence conditions at six chosen frequencies. It is clear that the relation between real and imaginary parts of charges for each frequency is completely different for the two polarisations. The reason for this can be seen from the dipole moment amplitude and phase for the two different polarisations, plotted in Fig. 8.4(b). Not only is the phase of the two dipole moments different, the phase difference between the two is not a constant either. This is a consequence of the scattering peaks being
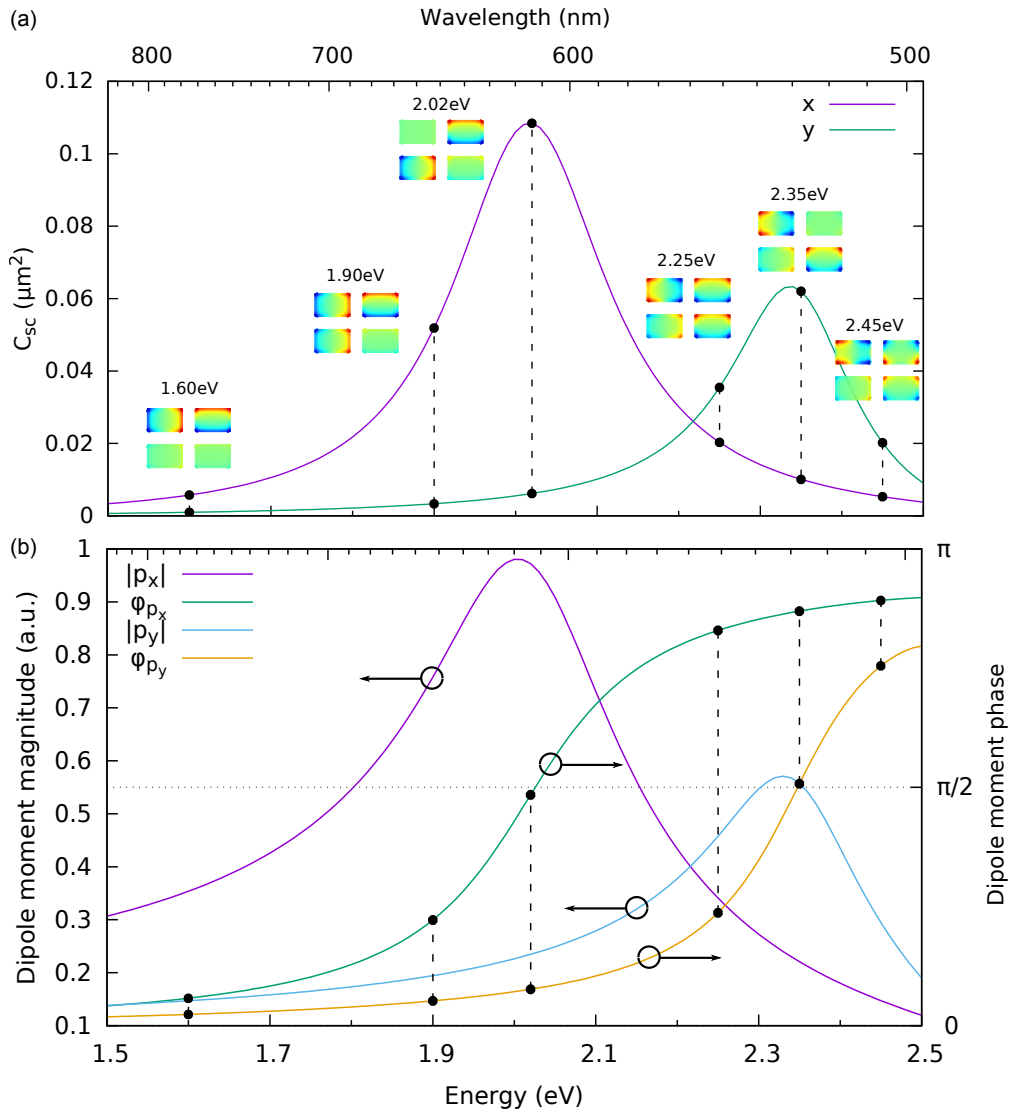
Figure 8.4 – (a) Scattering cross section of the nanorectangle for *x*- and *y*-polarised illuminations. Real (top) and imaginary (bottom) parts of the polarisation charges are also shown for *x*- (left) and *y*- (right) polarised incidence for selected frequencies. (b) Magnitude and phase of the induced dipole moments.

frequency separated. It is hence not possible anymore to simultaneously phase-correct both charge plots to let the imaginary parts of both vanish. We see once again that considering only the real part of the charge distribution would have led us to wrong conclusions especially about the relative magnitudes of the charges (and thus the dipole moments).

Next, as done previously, we will look at the charges on the structure arising from combinations of *x*- and *y*-polarisations. The frequency will be fixed at 2.20 eV since the polarisability along both directions is nearly equal in magnitude. The real and imaginary components of charges for $\theta = \pi/4$ for three different values of ψ are plotted in Fig. 8.5(a). Note that no phase

(a)

$$\theta = \pi/4 \qquad \theta = \pi/4 \qquad \theta = \pi/4$$
$$\psi = 0 \qquad \psi = \pi/2 \qquad \psi = \pi/4$$

(b) $t=0$ $\qquad$ $t=T/8$ $\qquad$ $t=T/4$ $\qquad$ $t=3T/8$ $\qquad$ $t=T/2$

(c)

(d)

(e) $\mathbf{E}(t)$ $\qquad$ $\mathbf{p}(t)$ $\qquad$ (f) $\mathbf{E}(t)$ $\qquad$ $\mathbf{p}(t)$

(g) $\mathbf{E}(t)$ $\qquad$ $\mathbf{p}(t)$
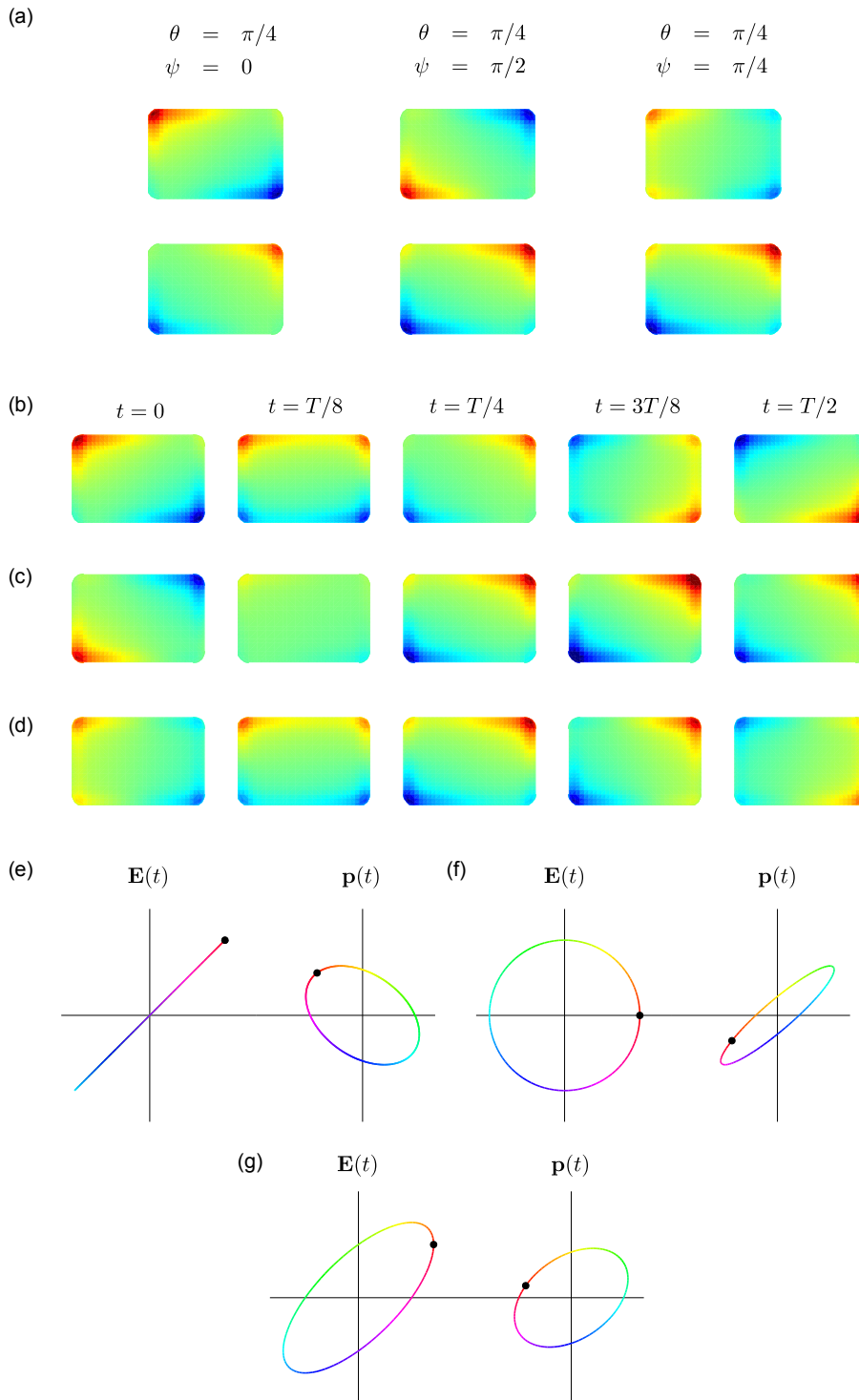
Figure 8.5 – (a) Real and imaginary parts of polarisation charges without phase correction at 2.20 eV for three different incident conditions corresponding to θ and ψ values indicated in the figure. (b-d) Instantaneous charge plots at five different times for the three illuminations in (a). (e-g) Curves traced by the incident electric field and dipole moment vectors over a time period for the three illuminations. The black dot indicates the time $t = 0$, and the time evolution is colour-coded from red to green to blue to red.

correction has been done on any of the images in this set.

The first thing to note is that even when $\psi = 0$, the imaginary part of the charge does not vanish. It is also geometrically different from the real part, implying that no phase correction will fix it, as expected. The time evolution of the charges, plotted in Fig. 8.5(b), shows that the surface charges rotate with time. This is a consequence of the complex polarisability of the rectangle along x and y being different. Fig. 8.5(e) compares the evolution of the incident electric field and dipole moment vectors, and it is evident that the two are not similar anymore unlike the case of the nanosquare. Though the input polarisation curve is a straight line, the dipole moment curve is an ellipse with the minor axis comparable to the major axis. The nanorectangle is thus able to convert linearly polarised incident field into partly circularly polarised scattered field.

For $\psi = \pi/2$, the real and imaginary parts of charges look similar except for a sign flip. This is the signature of the polarisation charges on the structure being linear. This can be observed in the time evolution plotted in Fig. 8.5(c). The charges seem to wax and wane rather than move about the structure. Looking at the incident field and dipole moment plots in Fig. 8.5(f) explains why : though the incident field moves in a circle, the dipole moment is an ellipse with a very short minor axis, so that the dipole moment nearly moves in a line with time. $\psi = \pi/4$ gives an intermediate situation, where both the incident field and the dipole moment are elliptical (Figure 8.5(d,g)). But it is interesting to note that the two ellipses have opposite senses of rotation. The colours on the two ellipses are flipped, and the dipole moment rotates clockwise while the incident polarisation rotation is anticlockwise. This interesting behaviour arises from the large phase difference ($> \frac{\pi}{2}$) between the dipole moments along x and y. Since the magnitudes of the dipole moments along x and y are nearly equal for the frequency under consideration, this means that polarisabilities along the two directions are almost negatives of each other. As a result, the dipole moment ellipse is flipped with respect to the incident field ellipse and the sense of rotation is reversed. It should be noted that rotation of the dipole moment gets transmitted to the far field as circular polarisation in the scattered field. Nanostructures like the nanorectangle which have polarisabilities along the two axes with similar magnitudes but large phase differences can achieve relative rotation between incident field and induced dipole moment as described above, and thus be used as polarisation converters [310, 311].

8.3.4 Dolmen

The next structure we analyse is the dolmen, a system of considerable interest to the plasmonic community due to the Fano resonance shown due to the interaction between the dipole mode supported by the horizontal arm and the quadrupole mode supported by the vertical arms [206–208, 262, 263, 279–281, 312–315]. Both the horizontal arm and the vertical arms of the dolmen have dimensions 120 nm × 40 nm × 40 nm. The scattering cross section for incident polarisation along the horizontal arm and real and imaginary components of the
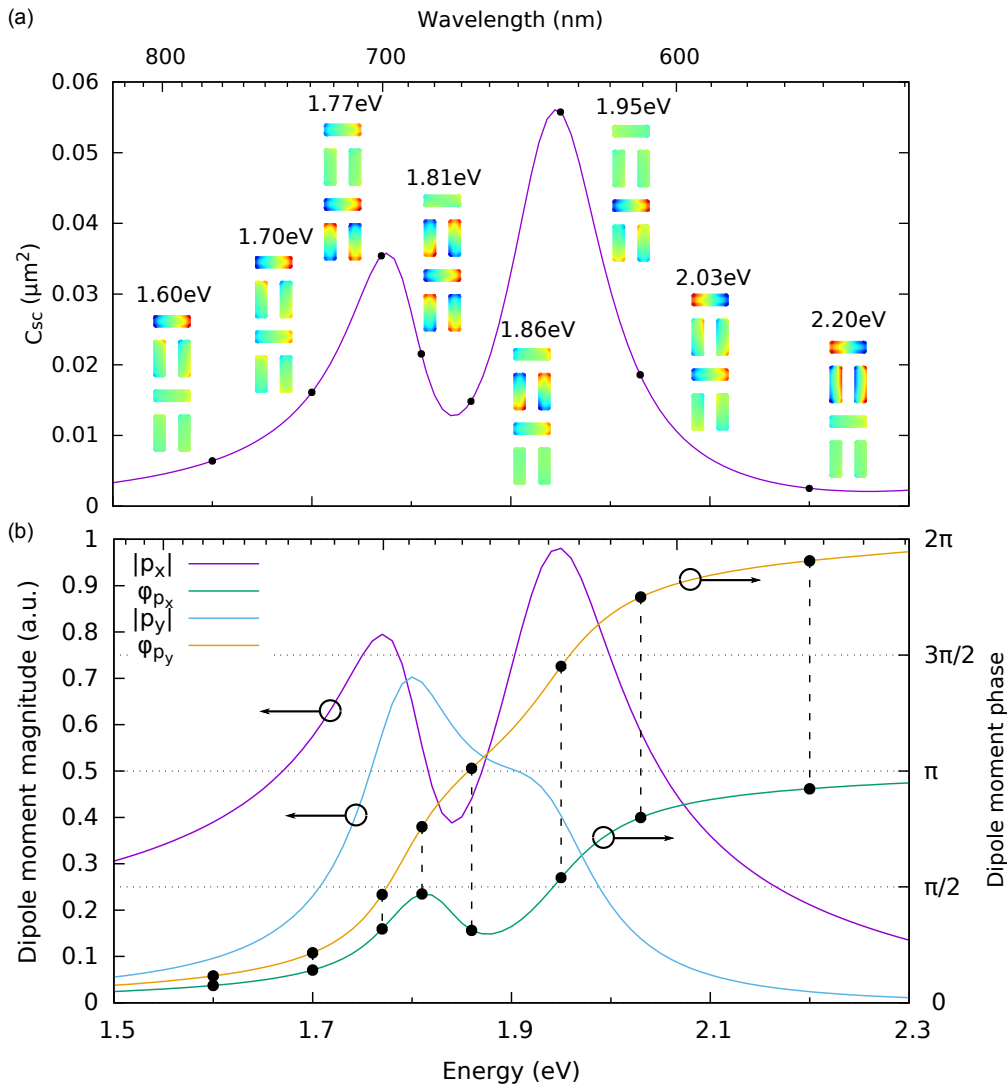
Figure 8.6 – (a) Scattering cross section of the dolmen for x-polarised incidence, and real and imaginary parts of the polarisation charges at eight different frequencies. (b) Magnitude and phase of the x-component of the dipole moment of the horizontal arm and y-component of the dipole moment of the left vertical arm.

polarisation charges for selected frequencies are plotted in Fig. 8.6(a).

The scattering cross section shows the features of a Fano resonance, with two scattering peaks and a scattering dip. As the frequency is increased, the charges on the horizontal arm behave in a similar fashion as the single nanorod shown in Fig. 8.1(a). At low frequencies, the real part of the charges is dominant. With increasing frequency, the imaginary part takes over, after which the real part becomes dominant again. The behaviour of the vertical arm is more interesting. The charges on the vertical arms change from real to imaginary to real twice. This can be seen more clearly in the dipole moment plot in Fig. 8.6(b). The amplitude of the dipole moment along x-direction for the horizontal arm and y-direction for the left vertical arm are
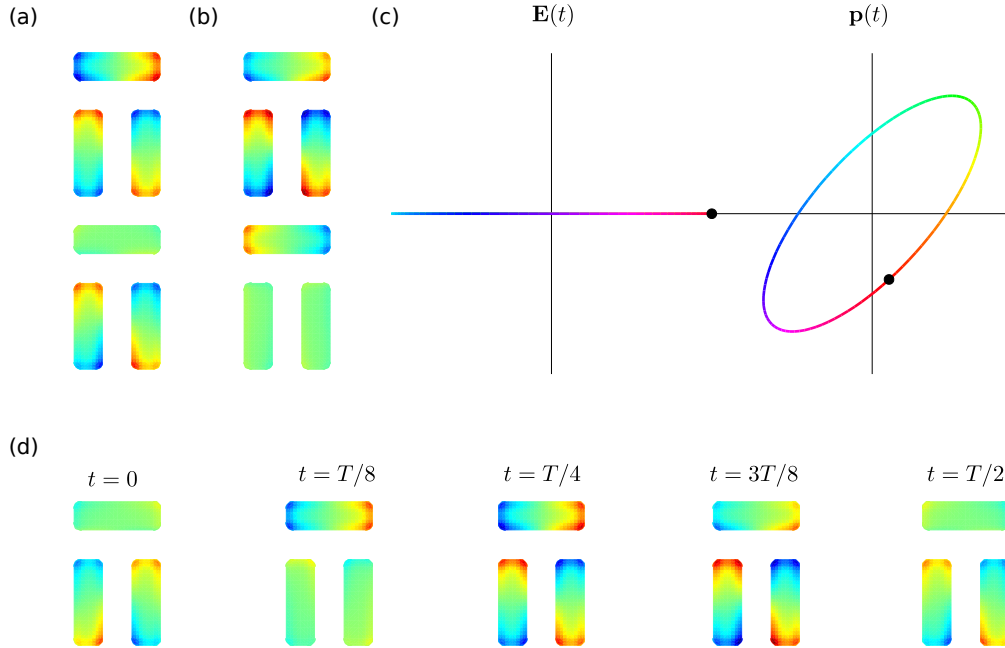
Figure 8.7 – (a) Real and imaginary parts of the charge plots at 1.80 eV after phase correction to the horizontal arm. (b) Same as (a), but phase corrected to the vertical arm. (c) Curves traced by the incident electric field and the combined dipole moment of the horizontal arm and the left vertical arm. (d) Time evolution of the instantaneous charge plots.

shown (the right vertical arm has charges opposite to the left). The phase of the dipole moment of the horizontal arm changes from 0 to π as usual. But the vertical arm phase changes from 0 to 2π. This is due to the fact that the mode of the system changes from bonding to antibonding across the Fano resonance. The charges on the horizontal and vertical bars across the gap are attractive at low frequencies but repulsive at high frequencies. The dipole moment of the vertical bars thus gets an additional sign flip relative to the horizontal bar (which is being fed by the incident field directly and thus gains a phase of π across the resonance), resulting in a total phase change of 2π. The emergence of the resonance of the vertical arms can also be observed at high frequencies.

The phase difference between the charges on the horizontal and vertical arms means that simultaneous phase correction is impossible in this case as well. The real and imaginary parts of the charge plots corrected to the dipole moment phase of the horizontal and vertical arms are shown in Fig. 8.7(a) and (b) respectively for 1.80 eV. Correcting the charge plots by the dipole moment phase of the horizontal arm indeed results in the vanishing of the imaginary component of the charge on the horizontal arm, but the component remains on the vertical arm. On applying phase correction using the dipole moment of the vertical arm, the reverse happens. This shows that in coupled systems, taking a snapshot of charges at any single instant does not give the complete information about the charge evolution, even for simple incidence conditions.

The evolution of charges on the dolmen with time have been shown in Fig. 8.7(d). It is evident that though the charge evolution of both the horizontal arm and the vertical arm are similar to that of a single rod, they do not happen in phase. This phase difference can be visualised better in the incident field and dipole moment evolution curves shown in Fig. 8.7(c). Note that the dipole moments of only the horizontal arm and the left vertical arm are considered since the dipoles in the two vertical arms cancel off each other. The dipole moment ellipse has major axis at nearly 45 degrees, and the aspect ratio is not too high. This is a result of the dipole moments of both arms being nearly equal in magnitude, and the phase difference between them being significant.

8.3.5 Ellipsoid

All the systems considered until now were thin in the direction of propagation, and hence could be considered planar. As a result, propagation of the planewave does not result in retardation and phase variation along the thickness of the structure. To understand what happens when this restriction is removed, we study the polarisation charges on an ellipsoid of dimensions 200 nm × 250 nm × 300 nm. All three dimensions are comparable to the wavelengths under consideration, and retardation effects on the structure should be significant.

The scattering cross sections of the ellipsoid for x- and y-polarised planewaves propagating along z are plotted in Fig. 8.8(a). For x- (y-) polarised incidence, there is a scattering peak at 2.50 eV (2.38 eV). However, the shape of the curve is quite different from that of the individual structures considered until now, with the prominent difference that a shoulder is visible in the scattering curve for x (y) at a higher frequency of 2.64 eV (2.59 eV). The polarisation along the thinner dimension x gives blue shifted scattering peaks, similar to the behaviour seen for the nanorectangle.

Polarisation charges induced on the surface at the four frequencies are shown in Fig. 8.8(a). The real and imaginary parts of the charges are shown from both front (viewing in the direction of y-axis, shown on the left side in each set of charge plots) and side (viewing in the direction of $-x$ axis, shown on the right side). Nodes can be seen in the charge distribution along the propagation direction. The major scattering peak for both polarisations have one node each in the charge distribution along z, whereas the charge distribution at the scattering shoulder have two nodes each. This is a result of retardation due to the large size of the object along the propagation direction.

The presence of the nodes along z means that the charge distribution is no longer dipolar at the scattering peaks. The dipole moments in the top and bottom halves of the structure cancel each other. The dipole moment induced on the structure (p_x for x-polarisation and p_y for y-polarisation) are plotted in Fig. 8.8(b). It can be seen that the dipole moments do not show a maximum near at the scattering peaks, but show only a minor change in strength near the scattering shoulder. Thus the major scattering peaks are not dipolar. The induced quadrupole moments ($Q_{xz} = Q_{zx}$ for x-polarisation and $Q_{yz} = Q_{zy}$ for y-polarisation) shown
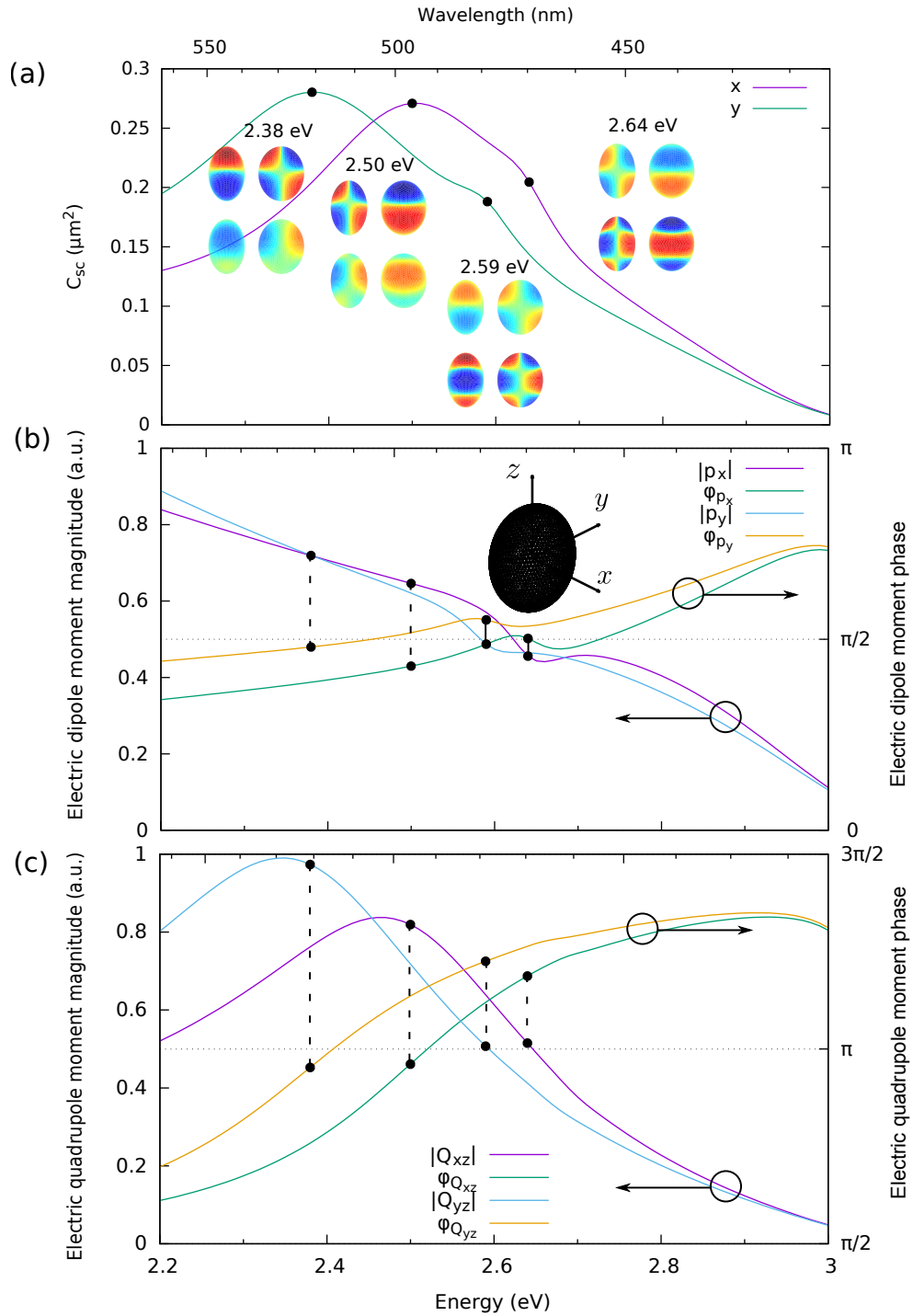
Figure 8.8 – (a) Scattering cross section of the ellipsoid for x- and y-polarised planewaves incident along z, with the coordinate system shown in the inset of (b). Views of the real (top) and imaginary (bottom) parts of polarisation charges on the ellipsoid when viewed from the front (in the $+y$ direction) and from the right side (in the $-x$ direction) are also shown side-by-side, for four different frequencies. (b) Magnitude and phase of the x-component of dipole moment for x-polarisation and y-component for y-polarisation. (c) Magnitude and phase of the xz-component of quadrupole moment for x-polarisation and yz-component for y-polarisation.

109

in Fig. 8.8(c) provide the resolution. They are seen to peak near the scattering peaks, and show the expected relative magnitudes as well.

It should also be noted that the modes here are quite broad and overlap with each other. The dominant charge distribution at the scattering shoulders are hexapolar, according to the imaginary parts of the charges. But the quadrupole has not died down at this frequency, as can be seen from looking at the real parts of the charges at these wavelengths or from the quadrupole moment plot. When modes overlap, it can be fairly difficult to understand the various contributions to the charges. In the case of symmetric structures such as the ellipsoid, we can utilise the fact that different modes have different symmetries to retrieve some information about the modes.

To achieve this, we decompose the polarisation charge distribution as a sum of odd and even functions of the three coordinates,

$$\sigma_p(\mathbf{r}) = \sigma_p^{+++}(\mathbf{r}) + \sigma_p^{++-}(\mathbf{r}) + \sigma_p^{+-+}(\mathbf{r}) + \sigma_p^{+--}(\mathbf{r}) + \sigma_p^{-++}(\mathbf{r}) + \sigma_p^{-+-}(\mathbf{r}) + \sigma_p^{--+}(\mathbf{r}) + \sigma_p^{---}(\mathbf{r}) \, . \quad (8.4)$$

Here, the three signs in the superscript denote the odd/even nature of the function for the three coordinates. For example, $\sigma_p^{-+-}(\mathbf{r})$ is odd in x, even in y and odd in z. The functions themselves can be found by symmetric addition of the charges with the correct signs,

$$\begin{aligned}\sigma_p^{abc}(x,y,z) =& \sigma_p(x,y,z) + c\sigma_p(x,y,-z) + b\sigma_p(x,-y,z) + bc\sigma_p(x,-y,-z) + a\sigma_p(-x,y,z) \\ & + ac\sigma_p(-x,y,-z) + ab\sigma_p(-x,-y,z) + abc\sigma_p(-x,-y,-z) \, . \quad (8.5)\end{aligned}$$

For example,

$$\begin{aligned}\sigma_p^{-+-}(x,y,z) =& \sigma_p(x,y,z) - \sigma_p(x,y,-z) + \sigma_p(x,-y,z) - \sigma_p(x,-y,-z) \\ & - \sigma_p(-x,y,z) + \sigma_p(-x,y,-z) - \sigma_p(-x,-y,z) + \sigma_p(-x,-y,-z) \, . \quad (8.6)\end{aligned}$$

Now, it is easy to see that each multipolar moment vanishes for some of the functions. For example, the only symmetrised function which can provide a nonvanishing x-component of electric dipole (p_x) is σ_p^{-++}. Similarly, only σ_p^{-+-} can result in nonzero Q_{xz}. The list of all non-vanishing components for the various symmetrised functions is provided in Table 8.1. It should be noted that higher order modes and moments with the same symmetry properties as a dipole/quadrupole moment will be nonvanishing for the same functions. For example, a hexapole mode will have the same symmetry as the dipole mode and will be seen in the same symmetrised function. Also, though none of the dipole or quadrupole moments are nonvanishing for σ_p^{---}, there can be charge distributions with octupole moments which result in σ_p^{---}.

By using a symmetric mesh for the SIE simulations, it is straightforward to generate all the symmetrised charge functions – since the charge density is a constant for each triangle, one only needs to add the charge densities over the sets of symmetric triangles with the

Symmetrised function	Nonvanishing components
σ_p^{+++}	$Q_{xx}, Q_{yy}, Q_{zz} = -(Q_{xx} + Q_{yy})$
σ_p^{++-}	p_z
σ_p^{+-+}	p_y
σ_p^{+--}	$Q_{yz} = Q_{zy}$
σ_p^{-++}	p_x
σ_p^{-+-}	$Q_{xz} = Q_{zx}$
σ_p^{--+}	$Q_{xy} = Q_{yx}$
σ_p^{---}	

Table 8.1 – List of components of electric dipole moment and quadrupole moment which do not automatically vanish by symmetry for each of the symmetrised functions.

correct signs. The ellipsoid was simulated using a symmetric mesh, and the symmetrised functions computed for a planewave propagating along z and linearly polarised along y are plotted in Fig. 8.9(a) for an incident frequency of 2.55 eV. We immediately see that only σ_p^{+-+} and σ_p^{+--} are nonvanishing. This should not be surprising since the illumination condition is symmetric about x and antisymmetric about y. Had the object been thin along z and retardation effects been negligible, σ_p^{+-+} would have been dominant because we do not expect nodes in the charge distribution along the z axis. However, both σ_p^{+-+} and σ_p^{+--} are similar in magnitude and it can also be seen that σ_p^{+-+} in fact has a hexapolar charge distribution. The quadrupolar and hexapolar charge distributions which we had found while looking at the charge distributions at the scattering peak and shoulder in Fig. 8.8 have nicely separated into different symmetrised functions.

Next, we vary the direction of incidence in the xz plane to 45° so that the unit vector along the propagation direction is $(\frac{1}{\sqrt{2}}, 0, \frac{1}{\sqrt{2}})$. The direction of polarisation is retained as y, and the frequency is kept at 2.55 eV. The charge distribution and its decomposition into symmetrised functions is shown in Fig. 8.9(b). The quadrupole in σ_p^{+--} retains its shape, and a similar quadrupole corresponding to Q_{xy} has arisen in σ_p^{--+}. In addition to the hexapole in σ_p^{+-+}, we also see a non-vanishing charge distribution arising in σ_p^{---}. This is an analogue of the classic octupole with charges placed at the coordinates of a cuboid with opposite signs for adjacent vertices. We could not have got this term for normal incidence along x-or y-directions due to symmetry, and it is thus a result of symmetry breaking in the geometry of the ellipsoid and the illumination condition.

Finally, we move the direction of incidence out of the xz plane. We now come in the incident direction $(\frac{1}{2}, \frac{1}{2}, \frac{1}{\sqrt{2}})$, with light polarised along $(-\frac{1}{\sqrt{2}}, \frac{1}{\sqrt{2}}, 0)$ at the same frequency. This brings the retardation along all axes into the picture. The charges and the symmetric decomposition are plotted in Fig. 8.9(c). We now see that all functions are nonvanishing, though the relative magnitudes differ. What is most interesting among these is σ_p^{+++}, which gives diagonal components for Q. In fact this is now the strongest among the symmetrised functions, another
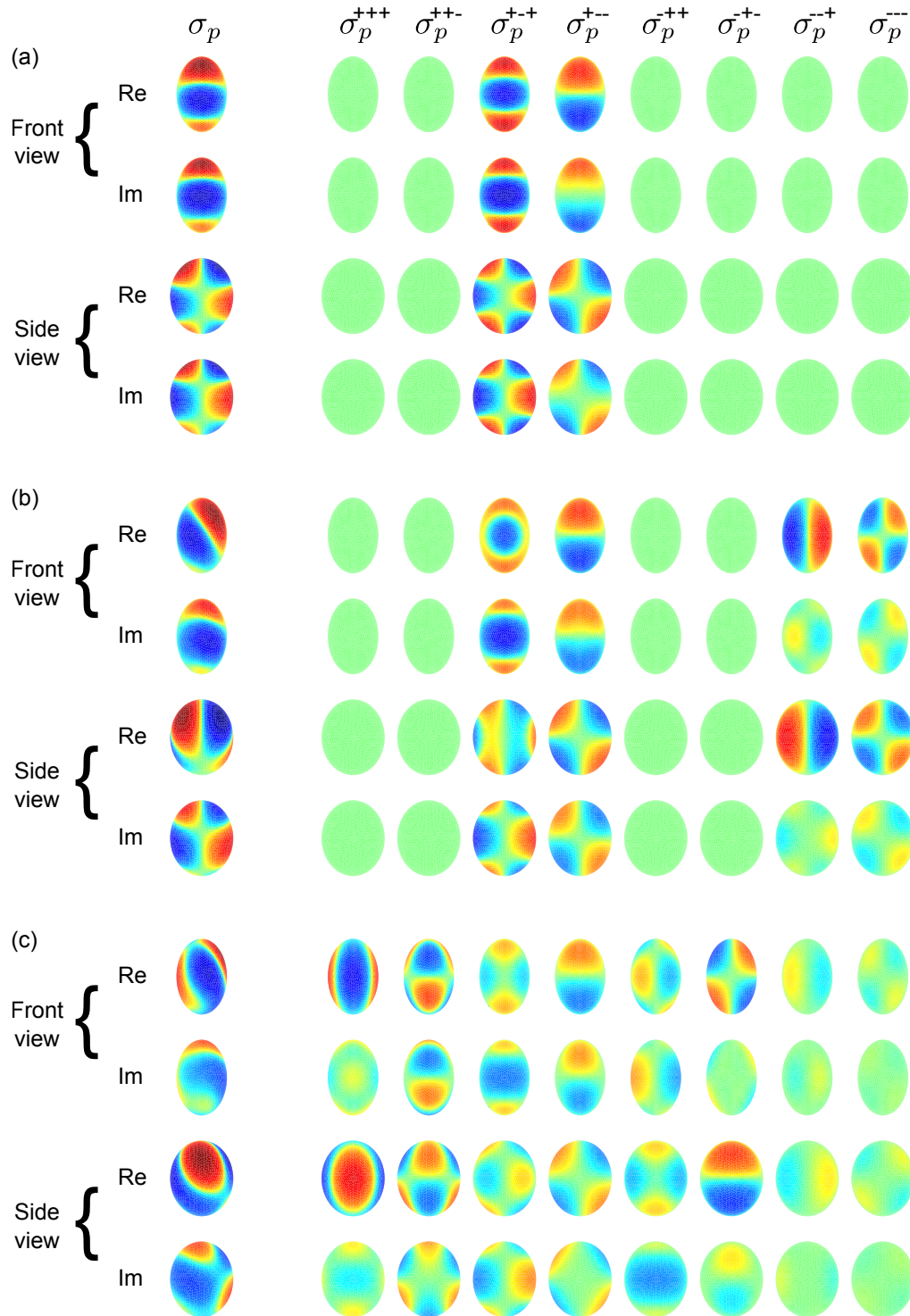
Figure 8.9 – Front ($+y$ direction) and side ($-x$ direction) views of the real and imaginary parts of the polarisation charge distribution and its symmetric decomposition at 2.55 eV on the ellipse in the inset of Fig. 8.8(b) for (a) propagation along $(0,0,1)$, polarisation along $(0,1,0)$, (b) propagation along $(\frac{1}{\sqrt{2}},0,\frac{1}{\sqrt{2}})$, polarisation along $(0,1,0)$, and (c) propagation along $(\frac{1}{2},\frac{1}{2},\frac{1}{\sqrt{2}})$, polarisation along $(-\frac{1}{\sqrt{2}},\frac{1}{\sqrt{2}},0)$.

consequence of symmetry breaking. The various multipolar modes found earlier appear here with different magnitudes, and the decomposition allows to visually compare them very easily. It is impossible to obtain any such insight by looking at the total charge distribution. Symmetric decomposition is thus a very useful tool in understanding and visualising the charges on nanostructures, though its utility is limited to objects with symmetries.

8.4 Conclusion

Polarisation charges are a useful tool in gaining physical insight into the optical response of plasmonic nanostructures. Both the real and imaginary parts of the complex charges are relevant, and taking only the real part results in a misleading interpretation of physical phenomena. The increasingly complicated behaviour of the polarisation charges on systems possessing multiple modes, asymmetry and retardation effects makes it tricky to extract relevant physical information from them. We have studied different plasmonic systems and shown how techniques such as phase correction, polarisation ellipse representation and symmetric decomposition help to visualise the charges and understand the respective structures better. Applying a phase correction on the charges to the phase of the dominant moment in the system permits uncovering relatively weak modes in the system with a different phase. In the case of systems which have two modes with dipole moments in different directions, the coloured ellipse representation for the incident field and the dipole moment can be used to understand the time evolution of the charges on the system. Charges on systems with symmetries can be decomposed into a sum of symmetric functions, separating the modes with different components of electric dipole and quadrupole moments into different functions. It should be possible to apply phase correction to each of the symmetric functions separately and uncover the weaker modes in each of them.

9 Raman scattering from metal-coated multiwalled carbon nanotubes

In this chapter, we study surface-enhanced Raman scattering (SERS) from metal-coated multiwalled carbon nanotubes using SIE. We use a Monte Carlo method to compute the Raman signal and are able to qualitatively explain the Raman enhancement in nanotubes in the presence of a metallic coating, and the corresponding reduction in the Raman signal from the substrate. We also show how computing the fields in such complex systems requires the use of the optimised integration recipe developed in Chapter 3.

9.1   Introduction

Extreme local field enhancement provided by plasmonics makes it very attractive for intensity-dependent phenomena like Raman scattering. Signal intensity boosts provided by plasmonic materials have long been used to study this phenomenon, and plasmonics as a field has advanced hand in hand with surface-enhanced Raman scattering (SERS) [34–40, 316]. Metal coated multiwalled carbon nanotubes have recently been used as a SERS substrate, and were shown to benefit from the plasmonic response of the structure as well as the local hotspots provided by the graininess of the metal on the surface [317–319]. Here, we study the enhancement of the Raman scattering from the nanotubes themselves due to the metallic coating, and contrast it with the suppression of the signal from the silicon substrate.

The nanotubes were fabricated by the group of Prof. William I. Milne, Centre for Applied Photonics and Electronics, University of Cambridge, UK. The fabrication method involved forming "seed" nickel nanoparticles on a silicon substrate by thermal annealing of a nickel thin film, followed by plasma-enhanced chemical vapor deposition to grow the multiwalled nanotubes under the nickel seeds [320–322]. SEM image of the fabricated nanotubes is shown in Fig. 9.1(a). The typical length of the nanotubes fabricated is 500 nm and the diameter is 64 nm, with a nanotube filling fraction of 50%, corresponding to a carbon thickness of 10 nm.

Following this, the nanotubes were coated with silver. Two different kinds of coating were applied. In the first case, the nanotubes were subject to vertical evaporation of silver, to a
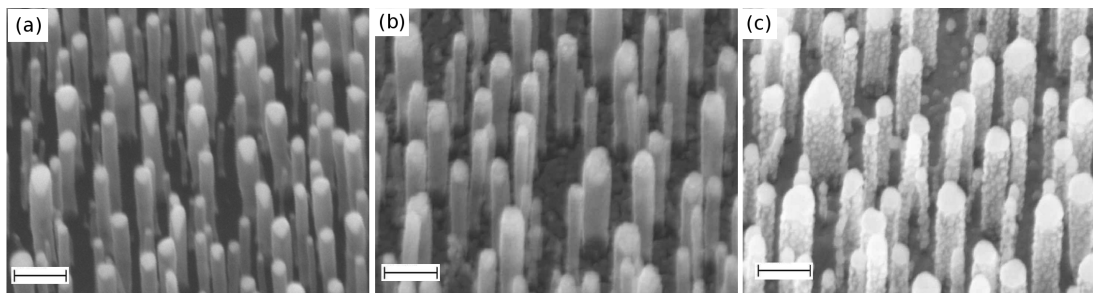
Figure 9.1 – SEM images of (a) bare multiwalled nanotubes grown on a silicon substrate using plasma-enhanced chemical vapor deposition under nickel seed particles, (b) nanotubes with 5.2 nm vertical silver deposition, and (c) nanotubes coated on all sides by depositing silver at an angle of 15° on a spinning substrate, resulting in a thickness of 18.5 nm on the silicon base. The scalebars in all images correspond to 200 nm, and the bare nanotubes have a typical height of 500 nm. SEM images courtesy from the group of Prof. Paul Dawson, Centre for Nanostructured Media, Queen's University, Belfast, UK.

thickness of 5.2 nm. This resulted in silver being deposited at the top of the nanotubes as well as on the substrate. SEM images of the silver capped nanotubes is shown in Fig. 9.1(b). In the second method, the evaporation was performed at an angle of 15° while the substrate was rotated. The nanotubes were thus coated with silver from all sides, as seen from the SEM image in Fig. 9.1(c). The vertical thickness of the silver coating in this case was 18.5 nm.

Raman measurements (not reproduced here) by the group of Prof. Paul Dawson at the Centre for Nanostructured Media, Queen's University, Belfast, UK showed that the 5.2 nm vertical deposition of silver resulted in boosting the Raman signal from the nanotubes at 633 nm by a factor of 4–4.5, and diminishing the signal from the substrate by a factor of 2.3. For the 18.5 nm thick oblique deposition, the enhancement and suppression factors were 15 and 6, respectively. We model the system using SIE to find the source of the metal-induced modification of the signal.

9.2 Model

9.2.1 Geometric modelling

Based on the SEM images, we choose the height of the nanotube as 500 nm and the radius as 32 nm. The multiwalled nanotubes are hollow, and we assign a thickness of 10 nm to them, which corresponds to a filling fraction of just under 50%. The top of the nanotubes is rounded to a hemispherical shape, with the inner hollow region also being rounded in the same fashion so that the nanotube has uniform thickness. Simulations are performed with and without the nickel nanoparticle seeds at the top to understand their effect. In the former case, these nickel nanoparticles are modelled as spheres of the same radius as the inner wall of the nanotube. To take into account the interaction between adjacent nanotubes, we simulate them on a
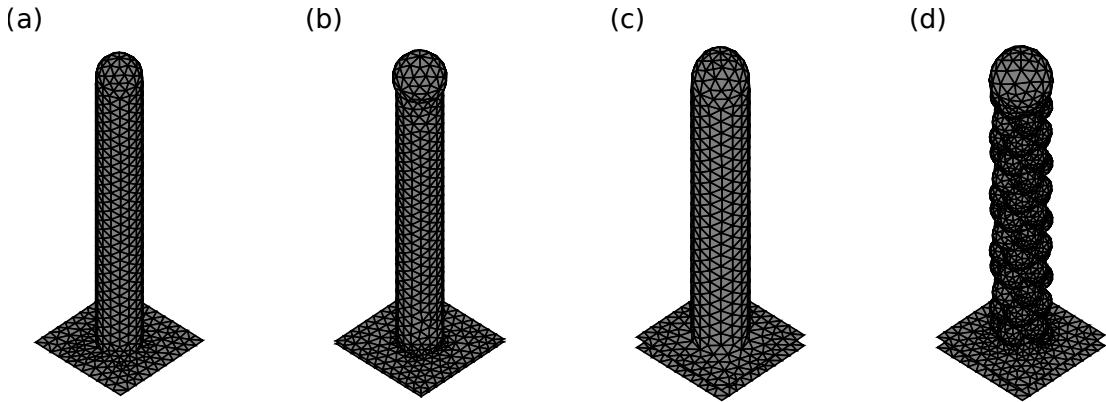
Figure 9.2 – Simulation geometries of the nanotubes with different levels of metallic coating. (a) *Bare*: nanotube of 32 nm radius, 10 nm inner thickness and 500 nm height, standing on a silicon substrate with a unit cell of 160 nm × 160 nm. (b) *Capped*: nanotube with 5 nm silver coating at the cap and on the substrate. (c) *Coated-1*: nanotube with 18.5 nm silver coating at the cap and on the substrate, and 7.5 nm coating on the walls. (d) *Grainy-4*: nanotube with 18.5 nm silver coating at the cap and on the substrate, and a grainy coating on the walls. The grains are modelled as spheres of 19.5 nm radius, distributed with their centres in a helical pattern at a distance of 23.5 nm from the axis.

periodic array of dimensions 160 nm × 160 nm. The simulation mesh corresponding to the bare nanotube geometry (henceforth referred to as *Bare*) without the nickel nanoparticle is shown in Fig. 9.2(a).

We now take into account the effect of deposition of silver. For the case of evaporation at normal incidence, we add a silver layer of thickness 5 nm to the substrate and a cap of the same thickness to the top of the nanotube. The mesh (*Capped*) is shown in Fig. 9.2(b). For deposition at oblique incidence with a rotating substrate, the ideal scenario is that the nanotube walls are covered uniformly by silver. We simulate two different thicknesses of silver on the walls: 7.5 nm (*Coated-1*, shown in Fig. 9.2(c)), and 11.0 nm (*Coated-2*). In both cases, the cap of the nanotube and the substrate are covered with 18.5 nm thick silver.

The silver deposition on the walls is not smooth and uniform in practice, as evident from Fig. 9.1(c). We model the grains as spheres of radius r distributed with their centres in a helical pattern at a distance of R from the nanotube axis. We consider four different levels of graininess, from smoothest to roughest: $r = 27$ nm and $R = 16$ nm (*Grainy-1*); $r = 25$ nm and $R = 18$ nm (*Grainy-2*); $r = 22.3$ nm and $R = 20.7$ nm (*Grainy-3*); and $r = 19.5$ nm and $R = 23.5$ nm (*Grainy-4*, shown in Fig. 9.2(d)).

The simulations are performed at the incidence wavelength of 633 nm. The permittivity of nickel was taken from Ref. [323], that of silicon from Ref. [324] and for silver from Ref. [175]. We use the refractive index formula given by Bruna and Borini, $n_{\mathrm{MWNT}} = 3.0 + i(C/3.0)\lambda$ with $C = 5.445 \ \mu\mathrm{m}^{-1}$ for the permittivity of the carbon nanotube [325]. Both the background and the hollow region inside the nanotube are taken as vacuum. Simulations are performed both

at normal incidence and at 25° with p polarisation to incorporate the effect of wide angle incidence.

9.2.2 SERS computation

Since the Raman signal arises from all parts of the nanotube and the substrate, we require to compute the average Raman signal over each domain. We do this by a Monte Carlo approach. 40,000 points are chosen uniformly randomly in the volume of the Carbon part of the nanotube, and similarly in the substrate. Since the geometry of the nanotube is complicated and the mesh is too discrete to be specified by mathematical formulae, we ensure that the points are inside the correct domain by the implementation in Ref. [105] of binary space partitioning [326]. This is not required for the silicon substrate since the boundary is flat. The substrate is semi-infinite and needs to be truncated to do the averaging. We hence choose the limit for the substrate Monte Carlo point sampling as 10 micron to allow the field sufficient depth to decay. For simulations differing only in the illumination condition where the simulation mesh is identical, the set of points used is also identical.

The Raman signal should ideally be calculated by finding the field intensity enhancement at each point and then computing the radiated far field from it [327, 328]. However, this would require treating each point in the Monte Carlo sampling as a separate illumination for SIE, making this treatment prohibitively expensive. We hence make the approximation that the Raman signal from a point is proportional to $|E_{\text{loc}}|^4$, where E_{loc} is the local electric field at the illumination wavelength [318]. This amounts to neglecting the Stokes shift and working at the illumination wavelength [37].

9.3 Results and discussion

The intensity of the electric field in the xz-plane for structures without the nickel nanosphere at the top is shown in Fig. 9.3. Since silicon is a high index material, most of the light falling on the substrate is reflected, giving rise to a standing wave pattern. Adding the metal coating affects the fields in multiple ways. For the *Capped* structure, there is a slight increase in intensity at the cap of the nanotube as well as near the substrate interface, as seen in Fig. 9.3(b). When a thick coating is applied, the field in the hollow centre of the tube is seen to increase since it behaves as a reflective cavity. The graininess of the silver coating changes the outside field significantly, but is not seen to have such an impact on the field inside the tube (Fig. 9.3(e-h)).

Next, we look at the Raman signal from the nanotubes. The 40,000 points for which $|E_{\text{loc}}|^4$ is computed are split into ten sets of equal sizes. The points in each set were still uniformly distributed within the nanotube – that is, they were not separated by region. Since each set is a Monte Carlo sampling in itself, the results from the sets can be compared among themselves to verify whether convergence has occurred and whether there are large variations due to outliers. The mean value for each set is calculated, and the standard deviation of the means is
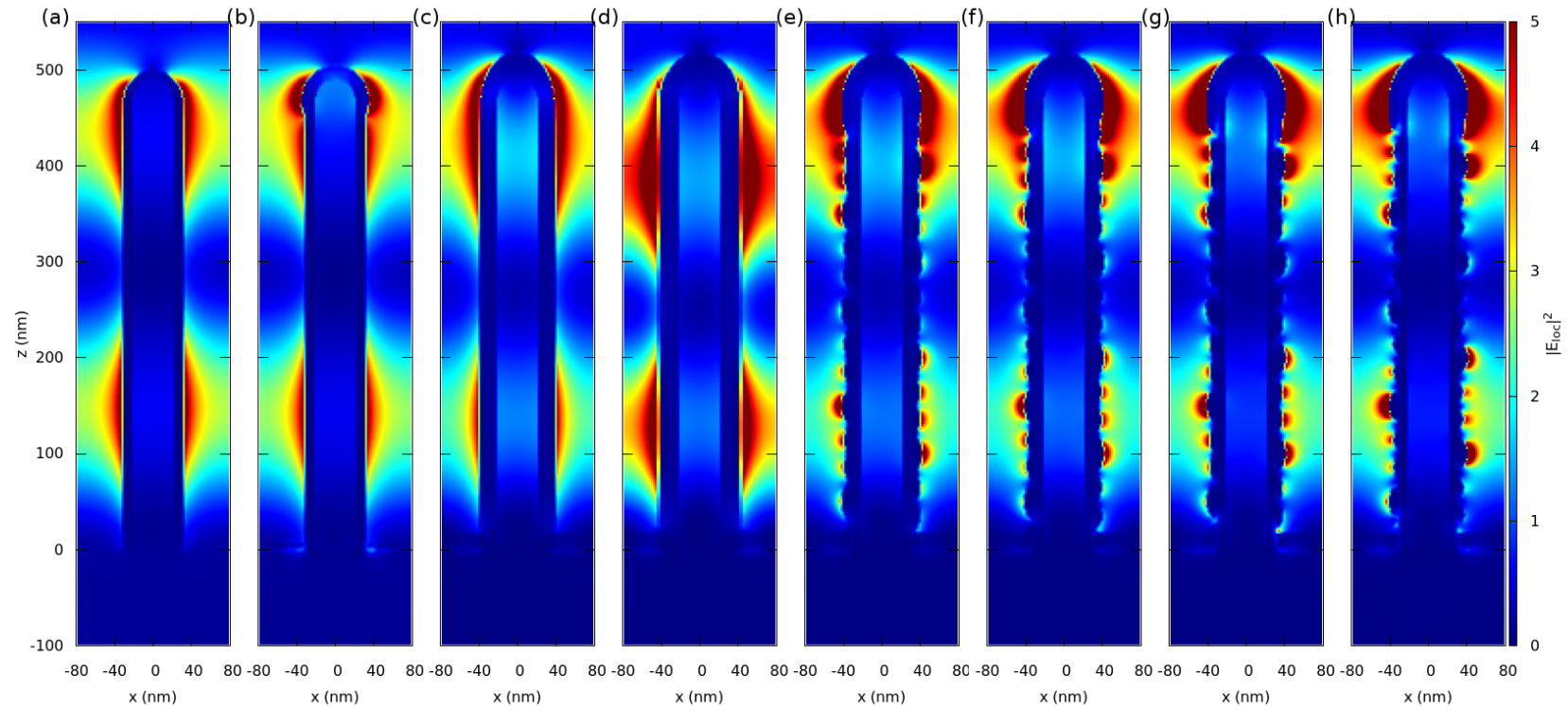
Figure 9.3 – Intensity of the electric field in the xz-plane for normal incidence without the nickel nanosphere for (a) *Bare*, (b) *Capped*, (c) *Coated-1*, (d) *Coated-2*, (e) *Grainy-1*, (f) *Grainy-2*, (g) *Grainy-3*, and (h) *Grainy-4* structures.

also computed to get an estimate of the error. The mean and standard deviation are tabulated for the different structures in Table 9.1, with incident electric field of unit intensity. For normal incidence without nickel, the standard deviations over the ten sets are much smaller than the corresponding means, suggesting that the Monte Carlo method has produced converged results.

All kinds of metal coatings are seen to increase the Raman signal from the nanotube. The *Capped* structure provides the lowest enhancement (a factor of 1.8), and the *Coated-1* structure provides the highest enhancement (a factor of 5.1). Counter to intuition, we see that making the grains rougher reduces the Raman signal instead of enhancing it.

To understand the source of Raman enhancement, we plot the $|E_{loc}|^4$ values for the set of Monte Carlo points inside the nanotube for each structure in Fig. 9.4. For ease of visualisation, all the points have been rotated to the xz-plane. This way of plotting provides better insight into the source of the Raman signal than the cross sectional intensity plots of Fig. 9.3. For the *Bare* structure in Fig. 9.4(a), the Raman intensity is essentially uniform except for the modulation along the length of the tube due to the standing wave pattern. The *Capped* structure in Fig. 9.4(b) shows enhancement at the top region where silver has been deposited. The *Coated-1* structure in Fig. 9.4(c) shows the strongest enhancement throughout the length of the tube, once again modulated by the standing wave pattern outside. Interestingly, points showing higher value of Raman intensity are situated closer to the inside of the tube. This suggests that the nanotube is not passively receiving the intensity enhancement from the silver coating but plays a role in deciding the field distribution. It therefore matters that the tube is hollow and not filled. Also, there seems to be an optimum thickness for achieving the Raman enhancement since increasing the thickness of the coating from 7.5 nm to 11.0 nm reduces the Raman intensity; compare *Coated-1* (Fig. 9.4(c)) and *Coated-2* (Fig. 9.4(d)). As we increase the roughness of the grains from *Grainy-1* to *Grainy-4* in Fig. 9.4(e to h), the hotspots are seen to

	Average value of $|E_{loc}|^4 \times 10^2$			
	Without nickel		With nickel	
	0°	25°	0°	25°
Bare	3.83 ± 0.07	4.43 ± 0.04	3.13 ± 0.08	4.54 ± 1.77
Capped	6.92 ± 0.21	7.40 ± 0.21	3.45 ± 0.10	5.77 ± 4.44
Coated-1	19.6 ± 0.36	19.4 ± 0.25	17.2 ± 0.39	20.9 ± 8.02
Coated-2	14.8 ± 0.29	13.5 ± 0.15	14.1 ± 0.31	15.5 ± 7.85
Grainy-1	18.2 ± 0.41	19.0 ± 0.34	16.5 ± 0.42	20.2 ± 5.30
Grainy-2	17.8 ± 0.44	18.6 ± 0.39	15.8 ± 0.44	19.5 ± 5.48
Grainy-3	15.5 ± 0.16	18.0 ± 0.11	12.7 ± 0.27	18.8 ± 7.15
Grainy-4	13.8 ± 0.23	16.8 ± 0.61	11.0 ± 0.25	17.6 ± 7.16

Table 9.1 – Mean value of $|E_{loc}|^4$ in the nanotube and the standard deviation over ten sets of points in the Monte Carlo method.
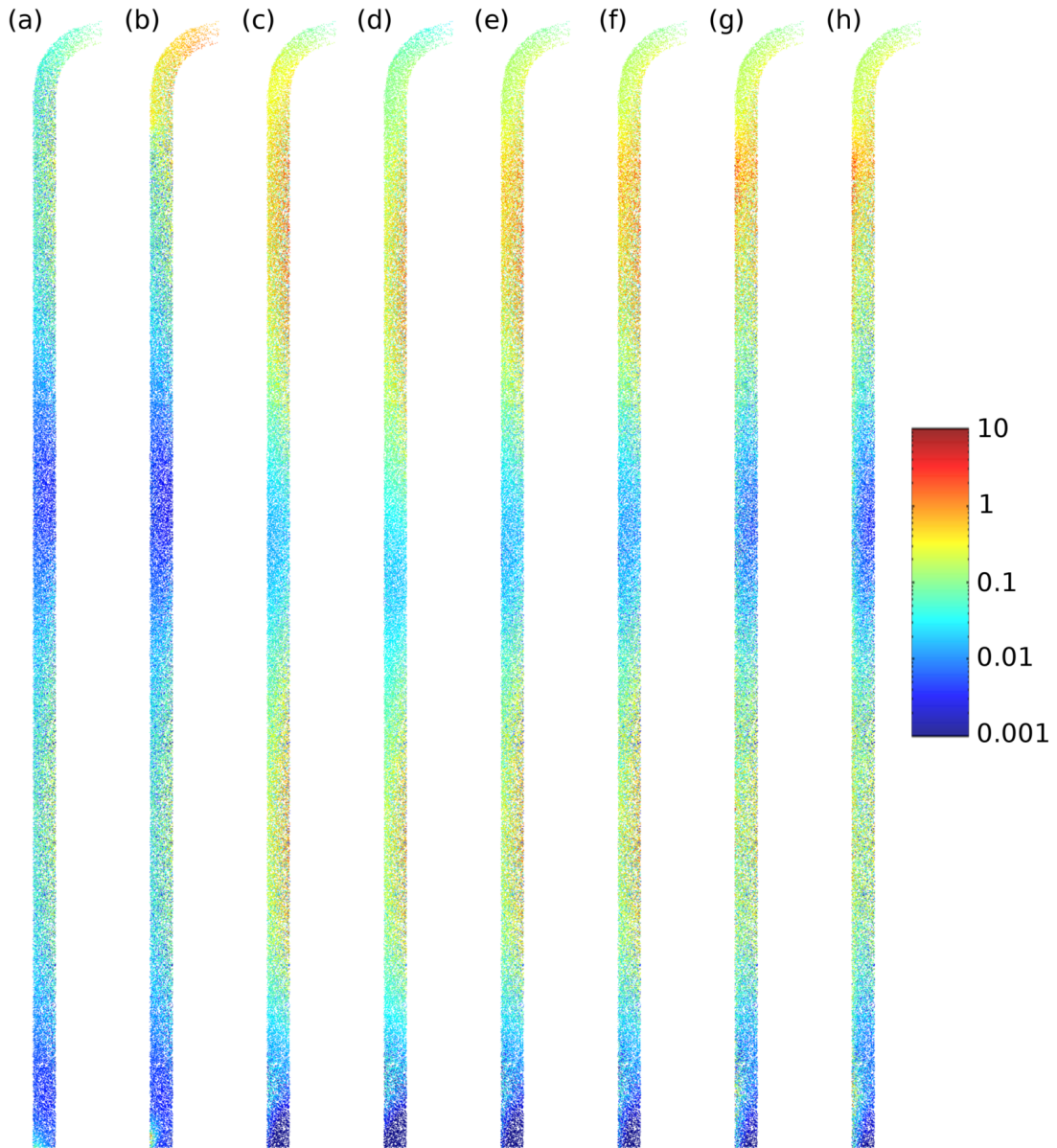
Figure 9.4 – $|E_{\text{loc}}|^4$ values at the 40,000 points selected inside the nanotube in the Monte Carlo approach for normal incidence without the nickel nanosphere for (a) *Bare*, (b) *Capped*, (c) *Coated-1*, (d) *Coated-2*, (e) *Grainy-1*, (f) *Grainy-2*, (g) *Grainy-3*, and (h) *Grainy-4* structures. Note that all the points have been rotated to the xz-plane for ease of visualisation.

move towards the outer region from the inside, but the total intensity decreases. The increase localised fields due to the graininess are offset by the reduction in the intensity due to the change in the shape of the metal coating. From these observations, we can conclude that the entire metal coating takes part in the intensity enhancement rather than just the grains, a result that seems to support the findings of Ref. [318].
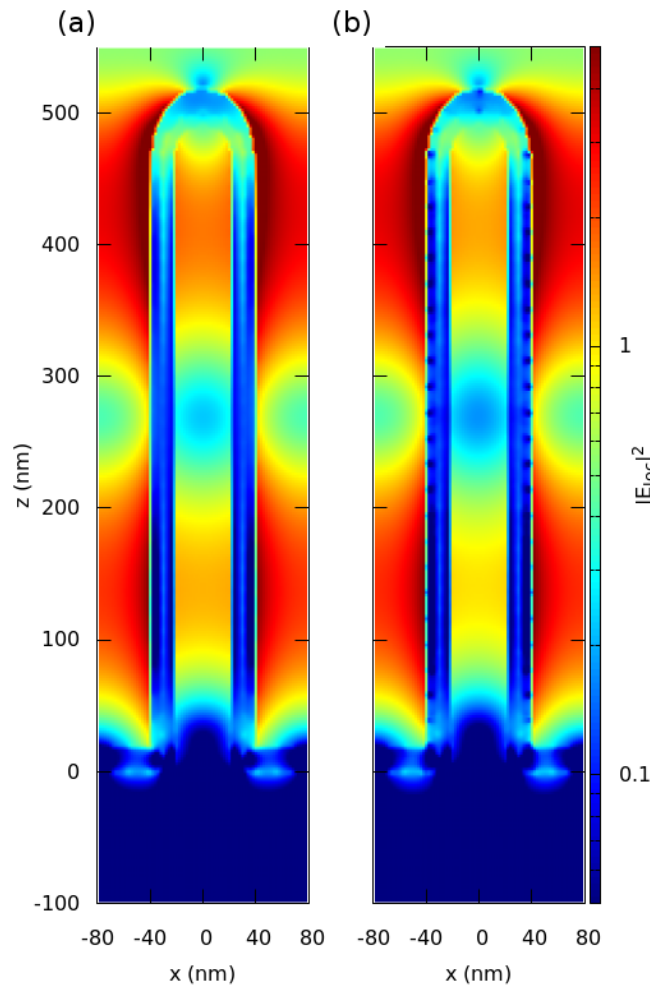
Figure 9.5 – Intensity in the xz-plane for the *Coated-1* structure without the nickel nanosphere at normal incidence computed by (a) the optimised integration recipe, and (b) the standard single-point integration.

Qualitatively, the enhancements are not very different when the incidence angle is increased to 25° and when the nickel sphere is included at the top. Oblique incidence results in a higher intensity. This is because the incident and reflected fields now have a z-component, and continuity of the Maxwell's equations implies that they will penetrate the high-index nanotubes better than the x-component. On the other hand, nickel reduces the field directly entering the nanotube, reducing the Raman signal. One interesting feature in Table 9.1 is the large standard deviations present in the column corresponding to oblique incidence in the presence of nickel. It turns out that these are associated with the sharp boundary where the nickel sphere is joined to the nanotube. Sharp domains result in high field intensities, but in this case it is an artefact of the model and not a real physical effect [258]. However, choosing a large number of sampling points has reduced the effect of the outliers associated with this region, as can be seen from comparing with the other columns in Table 9.1.

	Average value of $\lvert E_{\text{loc}}\rvert^4 \times 10^5$			
	Without nickel		With nickel	
	0°	25°	0°	25°
Bare	214 ± 9	136 ± 6	205 ± 8	132 ± 5
Capped	155 ± 6	100 ± 5	157 ± 6	106 ± 4
Coated-1	8.98 ± 0.34	0.45 ± 0.07	10.8 ± 0.41	0.59 ± 0.09
Coated-2	8.49 ± 0.48	2.83 ± 0.73	9.82 ± 0.56	3.07 ± 0.77
Grainy-1	7.72 ± 0.31	0.62 ± 0.06	9.39 ± 0.37	0.76 ± 0.07
Grainy-2	8.77 ± 0.35	1.35 ± 0.07	10.7 ± 0.42	1.66 ± 0.09
Grainy-3	12.7 ± 0.73	4.69 ± 0.49	15.1 ± 0.88	5.65 ± 0.59
Grainy-4	14.6 ± 0.84	5.42 ± 0.57	17.4 ± 1	6.52 ± 0.68

Table 9.2 – Mean value of $\lvert E_{\text{loc}}\rvert^4$ in the substrate and the standard deviation over ten sets of points in the Monte Carlo method.

Another point to note is that this is a system in which the optimised integration recipe developed in Chapter 3 is absolutely necessary. The large size of the structure forces us to choose a relatively coarse discretisation. Compounded by the fact that there are multiple domains touching and in close proximity, the accuracy of the results depends a lot on the integration routine. All the results reported here have been computed using the optimised recipe. For comparison, we have plotted the intensity in the xz-plane for normal incidence on the structure *Coated-1* without the nickel particle computed using the optimised integration recipe and the standard procedure in Fig. 9.5. The simulation mesh and the points at which the field is plotted are identical for both cases, and a logarithmic intensity scale is used so that low intensity regions are clearer. The fields calculated by the standard integration method, plotted in Fig. 9.5(b), show strange numerical artefacts inside the metal. There seem to be closely spaced nodes and antinodes. These vanish under the computation using the optimised integration procedure in Fig. 9.5(a), and the magnitude of the fields in other regions is also different.

Finally, we look at the Raman signal from the silicon substrate. The means and standard deviations are computed in the same fashion as before, and listed in Table 9.2. The general trend is reversed – that is, the presence of silver quenches rather than enhances the Raman signal from the substrate. This is not surprising since the presence of the metallic layer in the direction of propagation results in reflection and absorption of the incident light. For normal incidence without nickel, the *Capped* structure diminishes the Raman signal from the substrate by a factor of 1.4. For all the other structures, the suppression factor is much higher, ranging from to 14.7 to 27.7. Oblique incidence results in further lowered signal due to the increased reflection. It should also be noted that unlike the results in Table 9.1, the nickel sphere does not result in large variations because we are sufficiently far from the problem region.

For both the nanotubes and the silicon substrate, the results presented here agree qualitatively with the experimental measurements. The enhancement and suppression of the signal due to the thicker coating around the nanotubes are much higher than those for the thin vertical coating. However, the quantitative match of the factors is not very good. Experimentally, the presence of the metallic coating was measured to boost the Raman signal from the nanotubes by upto a factor of 15, whereas the best result we have obtained is 5.5 (for the *Coated-1* structure including the nickel nanoparticle). A similar mismatch had been noticed in the SIE computation for Raman scattering from the outer region in Ref. [318], and was attributed to the neglected hotspots which could arise due to tiny gaps between the silver grains and between adjacent nanotubes. In contrast, the suppression of Raman signal in the substrate that we have calculated is much stronger than experimentally measured.

There are multiple fronts on which the geometrical model for the simulation could be improved. A comparison between the SEM image in Fig. 9.1(c) and the simulation mesh in Fig. 9.2(d) shows that the grains on the nanotube are much smaller than we have simulated. As seen from Fig. 9.4(e-h), reducing the grain size adds more hot spots on the outer wall of the nanotube. It is quite plausible that by using smaller grains than we have considered and in close proximity, we could obtain sufficiently strong hotspots to offset the intensity reduction that has been observed. This might result in a better match with the experimentally measured enhancement. A close look at the SEM images also reveals cracks and bumps on the silver film on the substrate. The uniform film approximation does not capture these details, and hotspots on the film caused by these defects could strongly enhance the Raman signal from the substrate. This is expected to reduce the suppression factor, taking us closer to the experimental values. Unfortunately, implementing these modifications in the model would require a very refined mesh, making the SIE computation very expensive. Incorporating other features such as anisotropic response of the carbon nanotubes and finding a better termination of the nanotube at the top would make the model more physical, improving the quantitative results.

9.4   Conclusion

We have used a Monte Carlo method in combination with SIE to compute Raman scattering from multiwalled carbon nanotubes and silicon substrates. The Raman signal from the nanotubes is boosted whereas that from the substrate is diminished due to silver deposition. We obtain a good qualitative description of the experimental results, and the quantitative agreement can be made better by improving the simulation model. The simulation results show that the optimised integration recipe we developed for periodic SIE in Chapter 3 is necessary to avoid unphysical numerical artefacts.

10 Conclusion and outlook

We are now at the end of the thesis, and this would be a good time to summarise the results of the various chapters and ponder over what the future holds.

In Chapter 2, we developed a formalism to compute optical forces and torques, polarisation charges and dipole moments directly from the surface currents. The method closely followed the SIE scheme itself so that all its advantages would be retained. The power of the technique is immediately obvious – the post-processing cost is significantly reduced, and it spares the user of having to build a Monte Carlo point sampling scheme or an external integration surface to compute each physical quantity. In a way, this turns SIE into a more standalone tool. Though the quantities computed from the surface currents in this thesis are extremely useful, the method is in no way restricted to those. In principle, any domain-specific physical quantity can be integrated in this fashion, provided it can be expressed as a surface integral over the fields. As outlined in the chapter, finding such an expression may not be trivial since one might need to convert complicated volume integral expressions to surface integral forms. However, this one-time theoretical expense is more than rewarded by the results. For instance, being able to replace the Monte Carlo sampling for Raman enhancement by a surface integral which takes care of all the field variations and hot spots in the structure would be extremely useful. One immediate area where work could be done is to find surface integral expressions for higher order multipolar moments which are quite useful in plasmonics, such as the toroidal moments [198, 205].

We developed an optimised integration recipe to compute the SIE matrix elements in Chapter 3. Multiple instances of physical systems were presented where this recipe was required to compute optical cross sections, fields and forces accurately. For simple structures, this method has the prospect of reducing computational expenses by producing the same level of accuracy of results for a coarser mesh. However, the computational overhead due to the refined integrals is a matter of concern and offers scope for improvement. Optimising the program implementation is one way to go about it. Parallelising the matrix building process is another possibility since the matrix elements can be computed independently of each other. Explicitly utilising the symmetry of the structures can also help in reducing the size of the

matrix. Another interesting approach is to use a reduced basis formalism [329]. This essentially involves choosing a correct set of illuminations (the reduced basis) for which the response is computed initially, and the solutions for other wavelengths and angles of incidence can be built in terms of these responses. Speeding up SIE using a fast multipole method is also a possibility [330, 331].

We presented an extension of SIE to deal with scatterers embedded in stratified media in Chapter 4. Though it can simulate free standing structures sufficiently separated from interfaces, it is unable to treat the most useful systems in plasmonics where scatterers lie exactly at the layer boundaries. We thoroughly analysed the present drawbacks and their solutions in Section 4.5, and the natural next step would be to implement these solutions. Once this is done, the optimised integration recipe should be modified to take care of stratified media so that various plasmonic systems can be simulated accurately. Another direction would be to extend SIE to other kinds of backgrounds for which Green's functions can be found, for example graded-index media and waveguides [332, 333].

In Chapter 5, we showed how rounding the edges and corners of nanoantennae changes their far-field and near-field properties significantly. This seems to be a universal effect seen in other kinds of geometries as well [252]. It therefore makes sense to spend some effort on quantifying the kinds of rounding introduced by the various fabrication procedures. Being able to perform SIE simulations with the correct form of rounding for each fabrication method should allow designing systems with desired properties more accurately. Another set of useful numerical experiments to perform in this regard would be to study the effects of rounding on nanostructures placed on substrates, since having a flat base changes the form of rounding.

We analysed the internal forces and torques in compound plasmonic structures in Chapter 6. Many novel phenomena were observed, including reversals and circular polarisation dependence of forces and torques. It will be interesting to experimentally verify these effects. Performing the experiments would require placing the nanostructures on substrates, and an accurate implementation of stratified SIE will be useful to guide these experiments. Also, the force calculation method has to be modified to incorporate the material stresses in the media, making it more general. Based on the results in the chapter, many interesting ideas can be pursued, such as looking for nanostructures which move laterally on circularly polarised incidence. Going beyond these effects, the force computation method is a powerful tool to study plasmonic trapping of realistic structures and can be used to analyse effects beyond the dipole approximation. Once the plasmonics community develops its expertise in optical manipulation further, we can expect assembly line processing at the nanoscale using optical forces to revolutionise nanofabrication [61]. The ability to understand and compute forces accurately will be vital to such an endeavour.

In Chapter 7, we studied the possibility of achieving three dimensional orientation and rotation of nanostructures using optical torques. The numerical results suggest that this should be possible even with plane waves by utilising plasmon resonance, retardation effects and circular

polarisation. Experimental verification of this prediction will open new possibilities for optical manipulation.

We presented a detailed discussion of polarisation charges in plasmonic systems in Chapter 8, describing how to understand and visualise the charges. We showed how symmetrisation and phase correction of charges allow us to see weak modes in the system. It should be possible to use this method to aid the computationally intensive procedure of finding the modes of plasmonic systems, and could even work as an alternative in some situations [334]. It will also be interesting to extend the method of searching for weak modes by combining the charges at different frequencies, similar to the symmetric combination that we performed. This should allow the application of the method to asymmetric systems.

We studied the Raman enhancement from metal-coated multiwalled Carbon nanotubes in Chapter 9. The presence of metal boosts the Raman signal from the nanotubes, suppressing the signal from the substrate at the same time. Our Monte Carlo approach is able to explain the enhancement and suppression factors qualitatively. Obtaining good quantitative agreement requires an improved model which incorporates the geometric features better. Work in this direction should enable more accurate computation of Raman scattering and can be instrumental for the development of other enhanced spectroscopic techniques such as SEIRA [41–48] or fluorescence [24–33] .

The various studies presented here have interesting future prospects in terms of fundamental understanding of plasmonics as well as practical utility. Plasmonics will continue to grow as a field over the coming years, positively affecting the daily lives of non-scientists. Numerical tools will play an important role in developing plasmonic technology, and only time will tell what the future has to offer. We hence end the thesis with the lines from *Calvin and Hobbes* [335]: "It's a magical world, let's go exploring!"

A Sommerfeld integral for the curl of the dyadic Green's function

Using the notation in Appendix B of Ref. [99], we obtain the following expressions for the components of the integrand in the Sommerfeld integral in Eq. (4.10) for the curl of the dyadic Green's function.

$$g_{xx}^s(k_\rho; \rho, \phi) =$$
$$i\left(k_\rho J_0(k_\rho \rho) - \frac{2}{\rho}J_1(k_\rho \rho)\right)\sin\phi\cos\phi\left[A_l^s\exp(ik_{lz}z) - B_l^s\exp(-ik_{lz}z)\right] \tag{A.1}$$

$$g_{xx}^p(k_\rho; \rho, \phi) =$$
$$\pm i\frac{k_{lz}^2}{k_l^2}\left(-k_\rho J_0(k_\rho \rho) + \frac{2}{\rho}J_1(k_\rho \rho)\right)\sin\phi\cos\phi\left[A_{l,xx}^p\exp(ik_{lz}z) + B_{l,xx}^p\exp(-ik_{lz}z)\right]$$
$$\pm i\frac{k_\rho^2}{k_l^2}\left(-k_\rho J_0(k_\rho \rho) + \frac{2}{\rho}J_1(k_\rho \rho)\right)\sin\phi\cos\phi\left[A_{l,zx}^p\exp(ik_{lz}z) + B_{l,zx}^p\exp(-ik_{lz}z)\right]$$
$$\tag{A.2}$$

$$g_{xy}^s(k_\rho; \rho, \phi) =$$
$$i\left(-k_\rho J_0(k_\rho \rho)\cos^2\phi + \frac{1}{\rho}J_1(k_\rho \rho)\cos 2\phi\right)\left[A_l^s\exp(ik_{lz}z) - B_l^s\exp(-ik_{lz}z)\right] \tag{A.3}$$

$$g_{xy}^p(k_\rho; \rho, \phi) =$$
$$\mp i\frac{k_{lz}^2}{k_l^2}\left(k_\rho J_0(k_\rho \rho)\sin^2\phi + \frac{1}{\rho}J_1(k_\rho \rho)\cos 2\phi\right)\left[A_{l,xx}^p\exp(ik_{lz}z) + B_{l,xx}^p\exp(-ik_{lz}z)\right]$$
$$\mp i\frac{k_\rho^2}{k_l^2}\left(+k_\rho J_0(k_\rho \rho)\sin^2\phi + \frac{1}{\rho}J_1(k_\rho \rho)\cos 2\phi\right)\left[A_{l,zx}^p\exp(ik_{lz}z) + B_{l,zx}^p\exp(-ik_{lz}z)\right]$$
$$\tag{A.4}$$

$$g_{xz}^s(k_\rho; \rho, \phi) = 0 \tag{A.5}$$

Appendix A. Sommerfeld integral for the curl of the dyadic Green's function

$$g_{xz}^p(k_\rho;\rho,\phi) =$$
$$-\frac{k_{lz}k_\rho^2}{k_l^2}J_1(k_\rho\rho)\sin\phi\left[A_{l,xz}^p\exp(ik_{lz}z) + B_{l,xz}^p\exp(-ik_{lz}z)\right]$$
$$-\frac{k_\rho^4}{k_l^2 k_{lz}}J_1(k_\rho\rho)\sin\phi\left[A_{l,zz}^p\exp(ik_{lz}z) + B_{l,zz}^p\exp(-ik_{lz}z)\right] \tag{A.6}$$

$$g_{yx}^s(k_\rho;\rho,\phi) =$$
$$i\left(k_\rho J_0(k_\rho\rho)\sin^2\phi + \frac{1}{\rho}J_1(k_\rho\rho)\cos 2\phi\right)\left[A_l^s\exp(ik_{lz}z) - B_l^s\exp(-ik_{lz}z)\right] \tag{A.7}$$

$$g_{yx}^p(k_\rho;\rho,\phi) =$$
$$\pm i\frac{k_{lz}^2}{k_l^2}\left(k_\rho J_0(k_\rho\rho)\cos^2\phi - \frac{1}{\rho}J_1(k_\rho\rho)\cos 2\phi\right)\left[A_{l,xx}^p\exp(ik_{lz}z) + B_{l,xx}^p\exp(-ik_{lz}z)\right]$$
$$\pm i\frac{k_\rho^2}{k_l^2}\left(k_\rho J_0(k_\rho\rho)\cos^2\phi - \frac{1}{\rho}J_1(k_\rho\rho)\cos 2\phi\right)\left[A_{l,zx}^p\exp(ik_{lz}z) + B_{l,zx}^p\exp(-ik_{lz}z)\right]$$
$$\tag{A.8}$$

$$g_{yy}^s(k_\rho;\rho,\phi) = -g_{xx}^s(k_\rho;\rho,\phi) \tag{A.9}$$

$$g_{yy}^p(k_\rho;\rho,\phi) = -g_{xx}^p(k_\rho;\rho,\phi) \tag{A.10}$$

$$g_{yz}^s(k_\rho;\rho,\phi) = 0 \tag{A.11}$$

$$g_{yz}^p(k_\rho;\rho,\phi) =$$
$$\frac{k_{lz}k_\rho^2}{k_l^2}J_1(k_\rho\rho)\cos\phi\left[A_{l,xz}^p\exp(ik_{lz}z) + B_{l,xz}^p\exp(-ik_{lz}z)\right]$$
$$+\frac{k_\rho^4}{k_l^2 k_{lz}}J_1(k_\rho\rho)\cos\phi\left[A_{l,zz}^p\exp(ik_{lz}z) + B_{l,zz}^p\exp(-ik_{lz}z)\right] \tag{A.12}$$

$$g_{zx}^s(k_\rho;\rho,\phi) =$$
$$\frac{k_\rho^2}{k_{lz}}J_1(k_\rho\rho)\sin\phi\left[A_l^s\exp(ik_{lz}z) + B_l^s\exp(-ik_{lz}z)\right] \tag{A.13}$$

$$g_{zx}^p(k_\rho;\rho,\phi) = 0 \tag{A.14}$$

$$g_{zy}^s(k_\rho;\rho,\phi) =$$
$$-\frac{k_\rho^2}{k_{lz}}J_1(k_\rho\rho)\cos\phi\left[A_l^s\exp(ik_{lz}z) + B_l^s\exp(-ik_{lz}z)\right] \tag{A.15}$$

$$g_{zy}^p(k_\rho;\rho,\phi) = 0 \tag{A.16}$$

$$g_{zz}^s(k_\rho;\rho,\phi) = 0 \tag{A.17}$$

$$g_{zz}^p(k_\rho;\rho,\phi) = 0 \tag{A.18}$$

Bibliography

[1] A. V. Zayats and I. I. Smolyaninov, "Near-field photonics: surface plasmon polaritons and localized surface plasmons," J. Opt. A: Pure. Appl. Opt. **5**, S16 (2003).

[2] S. A. Maier, *Plasmonics: Fundamentals and Applications* (Springer, 2007).

[3] M. Faraday, "The bakerian lecture: experimental relations of gold (and other metals) to light," Philos. Trans. R. Soc. Lond. **147**, 145–181 (1857).

[4] W. L. Barnes, A. Dereux, and T. W. Ebbesen, "Surface plasmon subwavelength optics," Nature **424**, 824–830 (2003).

[5] S. A. Maier and H. A. Atwater, "Plasmonics: Localization and guiding of electromagnetic energy in metal/dielectric structures," J. Appl. Phys. **98**, 011101 (2005).

[6] A. V. Zayats, I. I. Smolyaninov, and A. A. Maradudin, "Nano-optics of surface plasmon polaritons," Physics Reports **408**, 131 – 314 (2005).

[7] S. A. Maier, "Plasmonic field enhancement and sers in the effective mode volume picture," Opt. Express **14**, 1957–1964 (2006).

[8] E. Ozbay, "Plasmonics: Merging photonics and electronics at nanoscale dimensions," Science **311**, 189–193 (2006).

[9] D. K. Gramotnev and S. I. Bozhevolnyi, "Plasmonics beyond the diffraction limit," Nat Photon **4**, 83–91 (2010).

[10] J. A. Schuller, E. S. Barnard, W. Cai, Y. C. Jun, J. S. White, and M. L. Brongersma, "Plasmonics for extreme light concentration and manipulation," Nat. Mater. **9**, 193–204 (2010).

[11] M. I. Stockman, "Nanoplasmonics: past, present, and glimpse into future," Opt. Express **19**, 22029–22106 (2011).

[12] A. Haes and R. Van Duyne, "A unified view of propagating and localized surface plasmon resonance biosensors," Anal. Bioanal. Chem. **379**, 920–930 (2004).

[13] J. Homola, *Surface plasmon resonance based sensors*, vol. 4 (Springer Science & Business Media, 2006).

[14] J. Zhao, X. Zhang, C. R. Yonzon, A. J. Haes, and R. P. Van Duyne, "Localized surface plasmon resonance biosensors," Nanomedicine **1**, 219–228 (2006).

[15] K. A. Willets and R. P. V. Duyne, "Localized surface plasmon resonance spectroscopy and sensing," Annu. Rev. Phys. Chem. **58**, 267–297 (2007).

[16] I. Abdulhalim, M. Zourob, and A. Lakhtakia, "Surface plasmon resonance for biosensing: A mini-review," Electromagnetics **28**, 214–242 (2008).

[17] J. N. Anker, W. P. Hall, O. Lyandres, N. C. Shah, J. Zhao, and R. P. Van Duyne, "Biosensing with plasmonic nanosensors," Nat. Mater. **7**, 442–453 (2008).

[18] J. Homola, "Surface plasmon resonance sensors for detection of chemical and biological species," Chem. Rev. **108**, 462–493 (2008).

[19] B. Sepúlveda, P. C. Angelomé, L. M. Lechuga, and L. M. Liz-Marzán, "LSPR-based nanobiosensors," Nano Today **4**, 244 – 251 (2009).

[20] J. Becker, A. Trügler, A. Jakab, U. Hohenester, and C. Sönnichsen, "The optimal aspect ratio of gold nanorods for plasmonic bio-sensing," Plasmonics **5**, 161–167 (2010).

[21] A. A. Yanik, A. E. Cetin, M. Huang, A. Artar, S. H. Mousavi, A. Khanikaev, J. H. Connor, G. Shvets, and H. Altug, "Seeing protein monolayers with naked eye through plasmonic fano resonances," Proc. Natl. Acad. Sci. U.S.A. **108**, 11784–11789 (2011).

[22] C. Wu, A. B. Khanikaev, R. Adato, N. Arju, A. A. Yanik, H. Altug, and G. Shvets, "Fano-resonant asymmetric metamaterials for ultrasensitive spectroscopy and identification of molecular monolayers," Nat. Mater. **11**, 69–75 (2012).

[23] D. Rodrigo, O. Limaj, D. Janner, D. Etezadi, F. J. García de Abajo, V. Pruneri, and H. Altug, "Mid-infrared plasmonic biosensing with graphene," Science **349**, 165–168 (2015).

[24] T. Liebermann and W. Knoll, "Surface-plasmon field-enhanced fluorescence spectroscopy," Colloids Surf. A Physicochem. Eng. Asp. **171**, 115 – 130 (2000).

[25] T. Neumann, M.-L. Johansson, D. Kambhampati, and W. Knoll, "Surface–plasmon fluorescence spectroscopy," Adv. Func. Mater. **12**, 575–586 (2002).

[26] F. Yu, B. Persson, S. Löfås, and W. Knoll, "Attomolar sensitivity in bioassays based on surface plasmon fluorescence spectroscopy," J. Am. Chem. Soc. **126**, 8902–8903 (2004).

[27] J. R. Lakowicz, "Radiative decay engineering 5: metal-enhanced fluorescence and plasmon emission," Anal. Biochem. **337**, 171 – 194 (2005).

[28] F. Tam, G. P. Goodrich, B. R. Johnson, , and N. J. Halas, "Plasmonic enhancement of molecular fluorescence," Nano Lett. **7**, 496–501 (2007).

[29] G. Colas des Francs, A. Bouhelier, E. Finot, J. C. Weeber, A. Dereux, C. Girard, and E. Dujardin, "Fluorescence relaxation in the near-field of a mesoscopic metallic particle: distance dependence and role of plasmon modes," Opt. Express **16**, 17654–17666 (2008).

[30] T. Ming, H. Chen, R. Jiang, Q. Li, and J. Wang, "Plasmon-controlled fluorescence: Beyond the intensity enhancement," J. Phys. Chem. Lett. **3**, 191–202 (2012).

[31] S. Derom, A. Berthelot, A. Pillonnet, O. Benamara, A. M. Jurdyc, C. Girard, and G. Colas des Francs, "Metal enhanced fluorescence in rare earth doped plasmonic core–shell nanoparticles," Nanotechnology **24**, 495704 (2013).

[32] G. Lu, J. Liu, T. Zhang, H. Shen, P. Perriat, M. Martini, O. Tillement, Y. Gu, Y. He, Y. Wang, and Q. Gong, "Enhancing molecule fluorescence with asymmetrical plasmonic antennas," Nanoscale **5**, 6545–6551 (2013).

[33] M. Bauch, K. Toma, M. Toma, Q. Zhang, and J. Dostalek, "Plasmon-enhanced fluorescence biosensors: a review," Plasmonics **9**, 781–799 (2014).

[34] A. Campion and P. Kambhampati, "Surface-enhanced raman scattering," Chem. Soc. Rev. **27**, 241–250 (1998).

[35] N. P. W. Pieczonka and R. F. Aroca, "Single molecule analysis by surfaced-enhanced raman scattering," Chem. Soc. Rev. **37**, 946–954 (2008).

[36] E. C. Le Ru and P. G. Etchegoin, *Principles of Surface-Enhanced Raman Spectroscopy and related plasmonic effects* (Elsevier, Amsterdam, 2009).

[37] W. Zhang, H. Fischer, T. Schmid, R. Zenobi, and O. J. F. Martin, "Mode-selective surface-enhanced raman spectroscopy using nanofabricated plasmonic dipole antennas," J. Phys. Chem. C **113**, 14672–14675 (2009).

[38] J. Margueritat, H. Gehan, J. Grand, G. Lévi, J. Aubard, N. Félidj, A. Bouhelier, G. Colas des Francs, L. Markey, C. M. D. Lucas, A. Dereux, and E. Finot, "Influence of the number of nanoparticles on the enhancement properties of surface-enhanced raman scattering active area: Sensitivity versus repeatability," ACS Nano **5**, 1630–1638 (2011).

[39] R. Chang, *Surface enhanced Raman scattering* (Springer Science & Business Media, 2013).

[40] A. Trügler, J.-C. Tinguely, G. Jakopic, U. Hohenester, J. R. Krenn, and A. Hohenau, "Near-field and sers enhancement from rough plasmonic nanoparticles," Phys. Rev. B **89**, 165409 (2014).

[41] M. Osawa, "Surface-enhanced infrared absorption," in "Near-Field Optics and Surface Plasmon Polaritons," , vol. 81 of *Topics in Applied Physics*, S. Kawata, ed. (Springer Berlin Heidelberg, 2001), pp. 163–187.

Bibliography

[42] F. Le, D. W. Brandl, Y. A. Urzhumov, H. Wang, J. Kundu, N. J. Halas, J. Aizpurua, and P. Nordlander, "Metallic nanoparticle arrays: A common substrate for both surface-enhanced raman scattering and surface-enhanced infrared absorption," ACS Nano **2**, 707–718 (2008).

[43] F. Neubrech, A. Pucci, T. W. Cornelius, S. Karim, A. García Etxarri, and J. Aizpurua, "Resonant Plasmonic and Vibrational Coupling in a Tailored Nanoantenna for Infrared Detection," Phys. Rev. Lett. **101**, 157403 (2008).

[44] A. Pucci, F. Neubrech, D. Weber, S. Hong, T. Toury, and M. L. de la Chapelle, "Surface enhanced infrared spectroscopy using gold nanoantennas," Physica Status Solidi B **247**, 2071–2074 (2010).

[45] V. Liberman, R. Adato, T. H. Jeys, B. G. Saar, S. Erramilli, and H. Altug, "Rational design and optimization of plasmonic nanoarrays for surface enhanced infrared spectroscopy," Opt. Express **20**, 11953–11967 (2012).

[46] K. Chen, R. Adato, and H. Altug, "Dual-band perfect absorber for multispectral plasmon-enhanced infrared spectroscopy," ACS Nano **6**, 7998–8006 (2012).

[47] R. Adato and H. Altug, "In-situ ultra-sensitive infrared absorption spectroscopy of biomolecule interactions in real time with plasmonic nanoantennas," Nat. Commun. **4**, 2154 (2013).

[48] C. D'Andrea, J. Bochterle, A. Toma, C. Huck, F. Neubrech, E. Messina, B. Fazio, O. M. Marago, E. Di Fabrizio, M. Lamy de la Chapelle, P. G. Gucciardi, and A. Pucci, "Optical Nanoantennas for Multiband Surface-Enhanced Infrared and Raman Spectroscopy," ACS Nano **7**, 3522–3531 (2013).

[49] S. Kim, J. Jin, Y.-J. Kim, I.-Y. Park, Y. Kim, and S.-W. Kim, "High-harmonic generation by resonant plasmon field enhancement," Nature **453**, 757–760 (2008).

[50] K. D. Ko, A. Kumar, K. H. Fung, R. Ambekar, G. L. Liu, N. X. Fang, and K. C. Toussaint, Jr., "Nonlinear optical response from arrays of au bowtie nanoantennas," Nano Lett. **11**, 61–65 (2011).

[51] J. Berthelot, G. Bachelier, M. Song, P. Rai, G. Colas des Francs, A. Dereux, and A. Bouhelier, "Silencing and enhancement of second-harmonic generation in optical gap antennas," Opt. Express **20**, 10498–10508 (2012).

[52] M. Kauranen and A. V. Zayats, "Nonlinear plasmonics," Nat. Photon. **6**, 737–748 (2012).

[53] K. Thyagarajan, S. Rivier, A. Lovera, and O. J. Martin, "Enhanced second-harmonic generation from double resonant plasmonic antennae," Opt. Express **20**, 12860–12865 (2012).

[54] K. Thyagarajan, J. Butet, and O. J. F. Martin, "Augmenting second harmonic generation using fano resonances in plasmonic systems," Nano Lett. **13**, 1847–1851 (2013).

[55] S. Viarbitskaya, O. Demichel, B. Cluzel, G. Colas des Francs, and A. Bouhelier, "Delocalization of nonlinear optical responses in plasmonic nanoantennas," Phys. Rev. Lett. **115**, 197401 (2015).

[56] M. Dienerowitz, M. Mazilu, and K. Dholakia, "Optical manipulation of nanoparticles: a review," J. Nanophoton. **2**, 021875–021875–32 (2008).

[57] M. Righini, G. Volpe, C. Girard, D. Petrov, and R. Quidant, "Surface plasmon optical tweezers: Tunable optical manipulation in the femtonewton range," Phys. Rev. Lett. **100**, 186804 (2008).

[58] R. Quidant and C. Girard, "Surface-plasmon-based optical manipulation," Laser Photon. Rev. **2**, 47–57 (2008).

[59] W. Zhang, L. Huang, C. Santschi, and O. J. F. Martin, "Trapping and sensing 10 nm metal nanoparticles using plasmonic dipole antennas," Nano Lett. **10**, 1006–1011 (2010).

[60] M. L. Juan, M. Righini, and R. Quidant, "Plasmon nano-optical tweezers," Nat. Photon. **5**, 349–356 (2011).

[61] T. V. Raziman, R. J. Wolke, and O. J. F. Martin, "Optical forces in nanoplasmonic systems: how do they work, what can they be useful for?" Faraday Discuss. **178**, 421–434 (2015).

[62] S. Pillai, K. R. Catchpole, T. Trupke, and M. A. Green, "Surface plasmon enhanced silicon solar cells," J. Appl. Phys. **101**, 093105 (2007).

[63] K. R. Catchpole and A. Polman, "Plasmonic solar cells," Opt. Express **16**, 21793–21800 (2008).

[64] K. Nakayama, K. Tanabe, and H. A. Atwater, "Plasmonic nanoparticle enhanced light absorption in gaas solar cells," Appl. Phys. Lett. **93**, 121904 (2008).

[65] H. A. Atwater and A. Polman, "Plasmonics for improved photovoltaic devices," Nat. Mater. **9**, 205–213 (2010).

[66] V. E. Ferry, M. A. Verschuuren, H. B. T. Li, E. Verhagen, R. J. Walters, R. E. I. Schropp, H. A. Atwater, and A. Polman, "Light trapping in ultrathin plasmonic solar cells," Opt. Express **18**, A237–A245 (2010).

[67] J. N. Munday and H. A. Atwater, "Large integrated absorption enhancement in plasmonic solar cells by combining metallic gratings and antireflection coatings," Nano Lett. **11**, 2195–2201 (2011).

[68] Z. Yu, G. Veronis, S. Fan, and M. L. Brongersma, "Design of midinfrared photodetectors enhanced by surface plasmons on grating structures," Appl. Phys. Lett. **89**, 151116 (2006).

Bibliography

[69] C.-C. Chang, Y. D. Sharma, Y.-S. Kim, J. A. Bur, R. V. Shenoi, S. Krishna, D. Huang, and S.-Y. Lin, "A surface plasmon enhanced infrared photodetector based on inas quantum dots," Nano Lett. **10**, 1704–1709 (2010).

[70] W. Wu, A. Bonakdar, and H. Mohseni, "Plasmonic enhanced quantum well infrared photodetector with high detectivity," Appl. Phys. Lett. **96**, 161107 (2010).

[71] M. W. Knight, H. Sobhani, P. Nordlander, and N. J. Halas, "Photodetection with active optical antennas," Science **332**, 702–704 (2011).

[72] G. Mie, "Beiträge zur optik trüber medien, speziell kolloidaler metallösungen," Annalen der Physik **330**, 377–445 (1908).

[73] B. Gallinet, J. Butet, and O. J. F. Martin, "Numerical methods for nanophotonics: standard problems and future challenges," Laser Photon. Rev. **9**, 577–603 (2015).

[74] J. C. Maxwell, "A dynamical theory of the electromagnetic field," Philos. Trans. R. Soc. Lond. **155**, 459–512 (1865).

[75] K. Yee, "Numerical solution of initial boundary value problems involving Maxwell's equations in isotropic media," IEEE Trans. Antennas Propag. **14**, 302–307 (1966).

[76] A. Taflove and M. E. Brodwin, "Numerical solution of steady-state electromagnetic scattering problems using the time-dependent Maxwell's equations," IEEE Trans. Microwave Theory Tech. **23**, 623–630 (1975).

[77] F. Kahnert, "Numerical methods in electromagnetic scattering theory," J. Quant. Spectrosc. Radiat. Transfer **79–80**, 775 – 824 (2003).

[78] J. M. Montgomery, T.-W. Lee, and S. K. Gray, "Theory and modeling of light interactions with metallic nanostructures," Journal of Physics: Condensed Matter **20**, 323201 (2008).

[79] R. Luebbers, F. Hunsberger, K. S. Kunz, R. Standler, and M. Schneider, "A frequency-dependent finite-difference time-domain formulation for dispersive materials," IEEE Trans. Electromagn. Compat. **32**, 222–227 (1990).

[80] T. Kashiwa and I. Fukai, "A treatment by the FD-TD method of the dispersive characteristics associated with electronic polarization," Microw. Opt. Technol. Lett. **3**, 203–205 (1990).

[81] D. Kelley and R. Luebbers, "Piecewise linear recursive convolution for dispersive media using FDTD," IEEE Trans. Antennas Propag. **44**, 792–797 (1996).

[82] P. Monk and E. Suli, "Error estimates for Yee's method on non-uniform grids," IEEE Trans. Magn. **30**, 3200–3203 (1994).

[83] S. Gedney, F. Lansing, and D. Rascoe, "Full wave analysis of microwave monolithic circuit devices using a generalized Yee-algorithm based on an unstructured grid," IEEE Trans. Microwave Theory Tech. **44**, 1393–1400 (1996).

[84] J.-P. Berenger, "A perfectly matched layer for the absorption of electromagnetic waves," J. Comput. Phys. **114**, 185–200 (1994).

[85] W. C. Chew and W. H. Weedon, "A 3D perfectly matched medium from modified Maxwell's equations with stretched coordinates," Microw. Opt. Technol. Lett. **7**, 599–604 (1994).

[86] Z. Sacks, D. Kingsland, R. Lee, and J.-F. Lee, "A perfectly matched anisotropic absorber for use as an absorbing boundary condition," IEEE Trans. Antennas Propag. **43**, 1460–1463 (1995).

[87] J. Jin, *The finite element method in electromagnetics* (Wiley, New York, 2002).

[88] P. Monk, *Finite Element Methods for Maxwell's Equations* (Oxford University Press, Newark, 2007).

[89] J. Nedelec, "Mixed finite elements in $\mathbb{R}^3$," Numer. Math. **35**, 315–341 (1980).

[90] G. Warren and W. Scott, "Numerical dispersion of higher order nodal elements in the finite-element method," IEEE Trans. Antennas Propag. **44**, 317–320 (1996).

[91] J. S. Hesthaven and T. Warburton, "High–order nodal discontinuous galerkin methods for the maxwell eigenvalue problem," Phil. Trans. R. Soc. Lond. A **362**, 493–524 (2004).

[92] J. S. Hesthaven and T. Warburton, *Nodal discontinuous Galerkin methods: algorithms, analysis, and applications* (Springer Science & Business Media, 2007).

[93] J. Niegemann, W. Pernice, and K. Busch, "Simulation of optical resonators using DGTD and FDTD," J. Opt. A: Pure. Appl. Opt. **11**, 114015 (2009).

[94] J. Niegemann, M. König, K. Stannigel, and K. Busch, "Higher-order time-domain methods for the analysis of nano-photonic systems," Phot. Nano. Fund. Appl. **7**, 2 – 11 (2009).

[95] K. Busch, M. König, and J. Niegemann, "Discontinuous galerkin methods in nanophotonics," Laser Photon. Rev. **5**, 773–809 (2011).

[96] V. Varadan, A. Lakhtakia, and V. K. Varadan, "Scattering by three-dimensional anisotropic scatterers," IEEE Trans. Antennas Propag. **37**, 800–802 (1989).

[97] O. J. F. Martin and N. B. Piller, "Electromagnetic scattering in polarizable backgrounds," Phys. Rev. E **58**, 3909–3915 (1998).

[98] J. P. Kottmann and O. J. F. Martin, "Accurate solution of the volume integral equation for high-permittivity scatterers," IEEE Trans. Antennas Propag. **48**, 1719–1726 (2000).

[99] M. Paulus, P. Gay-Balmaz, and O. J. F. Martin, "Accurate and efficient computation of the green's tensor for stratified media," Phys. Rev. E **62**, 5797–5807 (2000).

[100] M. Paulus and O. J. F. Martin, "Light propagation and scattering in stratified media: a Green's tensor approach," J. Opt. Soc. Am. A **18**, 854–861 (2001).

[101] M. Paulus and O. J. F. Martin, "Green's tensor technique for scattering in two-dimensional stratified media," Phys. Rev. E **63**, 066615 (2001).

[102] J. J. Goodman, P. J. Flatau, and B. T. Draine, "Application of fast-fourier-transform techniques to the discrete-dipole approximation," Opt. Lett. **16**, 1198–1200 (1991).

[103] B. T. Draine and P. J. Flatau, "Discrete-dipole approximation for scattering calculations," J. Opt. Soc. Am. A **11**, 1491–1499 (1994).

[104] W.-H. Yang, G. C. Schatz, and R. P. Van Duyne, "Discrete dipole approximation for calculating extinction and Raman intensities for small particles with arbitrary shapes," J. Chem. Phys. **103**, 869–875 (1995).

[105] A. M. Kern and O. J. F. Martin, "Surface integral formulation for 3D simulations of plasmonic and high permittivity nanostructures," J. Opt. Soc. Am. A **26**, 732–740 (2009).

[106] J. M. Taboada, J. Rivero, F. Obelleiro, M. G. Araújo, and L. Landesa, "Method-of-moments formulation for the analysis of plasmonic nano-optical antennas," J. Opt. Soc. Am. A **28**, 1341–1348 (2011).

[107] M. G. Araújo, J. M. Taboada, D. M. Solís, J. Rivero, L. Landesa, and F. Obelleiro, "Comparison of surface integral equation formulations for electromagnetic analysis of plasmonic nanoscatterers," Opt. Express **20**, 9161–9171 (2012).

[108] C. Forestiere, G. Iadarola, G. Rubinacci, A. Tamburrino, L. Dal Negro, and G. Miano, "Surface integral formulations for the design of plasmonic nanostructures," J. Opt. Soc. Am. A **29**, 2314–2327 (2012).

[109] B. Gallinet, A. M. Kern, and O. J. F. Martin, "Accurate and versatile modeling of electromagnetic scattering on periodic nanostructures with a surface integral approach," J. Opt. Soc. Am. A **27**, 2261–2271 (2010).

[110] Y. P. Chen, W. E. I. Sha, W. C. H. Choy, L. Jiang, and W. C. Chew, "Study on spontaneous emission in complex multilayered plasmonic system via surface integral equation approach with layered medium Green's function," Opt. Express **20**, 20210–20221 (2012).

[111] S. Pratama and D. van Oosten, "Efficient and versatile surface integral approach to light scattering in stratified media," Opt. Express **23**, 21741–21760 (2015).

[112] F. J. García de Abajo and A. Howie, "Retarded field calculation of electron energy loss in inhomogeneous dielectrics," Phys. Rev. B **65**, 115418 (2002).

[113] U. Hohenester and J. Krenn, "Surface plasmon resonances of single and coupled metallic nanoparticles: A boundary integral method approach," Phys. Rev. B **72**, 195429 (2005).

[114] G. Baffou, R. Quidant, and F. J. G. de Abajo, "Nanoscale control of optical heating in complex plasmonic systems," ACS Nano **4**, 709–716 (2010).

[115] U. Hohenester and A. Trügler, "MNPBEM – a matlab toolbox for the simulation of plasmonic nanoparticles," Comput. Phys. Commun. **183**, 370 – 381 (2012).

[116] U. Hohenester, "Simulating electron energy loss spectroscopy with the MNPBEM toolbox," Comput. Phys. Commun. **185**, 1177 – 1187 (2014).

[117] J. Waxenegger, A. Trügler, and U. Hohenester, "Plasmonics simulations with the MNPBEM toolbox: Consideration of substrates and layer structures," Comput. Phys. Commun. **193**, 138 – 150 (2015).

[118] X.-M. Pan, K.-J. Xu, M.-L. Yang, and X.-Q. Sheng, "Prediction of metallic nano-optical trapping forces by finite element-boundary integral method," Opt. Express **23**, 6130–6144 (2015).

[119] T. Laroche, F. I. Baida, and D. V. Labeke, "Three-dimensional finite-difference time-domain study of enhanced second-harmonic generation at the end of a apertureless scanning near-field optical microscope metal tip," J. Opt. Soc. Am. B **22**, 1045–1051 (2005).

[120] A. Benedetti, M. Centini, M. Bertolotti, and C. Sibilia, "Second harmonic generation from 3d nanoantennas: on the surface and bulk contributions by far-field pattern analysis," Opt. Express **19**, 26752–26767 (2011).

[121] J. Mäkitalo, S. Suuriniemi, and M. Kauranen, "Boundary element method for surface nonlinear optics of nanoparticles," Opt. Express **19**, 23386–23399 (2011).

[122] M. Hentschel, T. Utikal, H. Giessen, and M. Lippitz, "Quantitative modeling of the third harmonic emission spectrum of plasmonic nanoantennas," Nano Lett. **12**, 3778–3782 (2012).

[123] C. Forestiere, A. Capretti, and G. Miano, "Surface integral method for second harmonic generation in metal nanoparticles including both local-surface and nonlocal-bulk sources," J. Opt. Soc. Am. B **30**, 2355–2364 (2013).

[124] J. Butet, B. Gallinet, K. Thyagarajan, and O. J. F. Martin, "Second-harmonic generation from periodic arrays of arbitrary shape plasmonic nanostructures: a surface integral approach," J. Opt. Soc. Am. B **30**, 2970–2979 (2013).

[125] J. M. McMahon, S. K. Gray, and G. C. Schatz, "Optical properties of nanowire dimers with a spatially nonlocal dielectric function," Nano Lett. **10**, 3473–3481 (2010).

[126] A. Wiener, A. I. Fernández-Domínguez, A. P. Horsfield, J. B. Pendry, and S. A. Maier, "Nonlocal effects in the nanofocusing performance of plasmonic tips," Nano Lett. **12**, 3308–3314 (2012).

Bibliography

[127] W. Yan, N. A. Mortensen, and M. Wubs, "Green's function surface-integral method for nonlocal response of plasmonic nanowires in arbitrary dielectric environments," Phys. Rev. B **88**, 155414 (2013).

[128] A. Zangwill and P. Soven, "Density-functional approach to local-field effects in finite systems: Photoabsorption in the rare gases," Phys. Rev. A **21**, 1561–1572 (1980).

[129] W. Ekardt, "Size-dependent photoabsorption and photoemission of small metal particles," Phys. Rev. B **31**, 6360–6370 (1985).

[130] E. Prodan, P. Nordlander, , and N. J. Halas, "Electronic structure and optical properties of gold nanoshells," Nano Lett. **3**, 1411–1415 (2003).

[131] R. Esteban, A. G. Borisov, P. Nordlander, and J. Aizpurua, "Bridging quantum and classical plasmonics with a quantum-corrected model," Nat. Commun. **3**, 825 (2012).

[132] E. Townsend and G. W. Bryant, "Plasmonic properties of metallic nanoparticles: The effects of size quantization," Nano Lett. **12**, 429–434 (2012).

[133] M. S. Tame, K. R. McEnery, S. K. Ozdemir, J. Lee, S. A. Maier, and M. S. Kim, "Quantum plasmonics," Nat Phys **9**, 329–340 (2013).

[134] G. Hajisalem, M. S. Nezami, and R. Gordon, "Probing the quantum tunneling limit of plasmonic enhancement by third harmonic generation," Nano Lett. **14**, 6651–6654 (2014).

[135] S. Rao, D. Wilton, and A. Glisson, "Electromagnetic scattering by surfaces of arbitrary shape," IEEE Trans. Antennas Propag. **30**, 409–418 (1982).

[136] A. J. Poggio and E. K. Miller, "Integral equation solutions of three-dimensional scattering problems," in "Computer techniques for electromagnetics," (Pergamon, Oxford, U.K., 1973).

[137] Y. Chang and R. F. Harrington, "A surface formulation for characteristic modes of material bodies," IEEE Trans. Antennas Propag. **25**, 789–795 (1977).

[138] T.-K. Wu and L. L. Tsai, "Scattering from arbitrarily-shaped lossy dielectric bodies of revolution," Radio Sci. **12**, 709–718 (1977).

[139] C.-T. Tai, *Dyadic Green Functions in Electromagnetic Theory* (IEEE Press, Piscataway, NJ, 1994).

[140] I. Hänninen, M. Taskinen, and J. Sarvas, "Singularity subtraction integral formulae for surface integral equations with RWG, rooftop and hybrid basis functions," Progress in Electromagnetics Research **63**, 243–278 (2006).

[141] Y. L. Yung, "Variational principle for scattering of light by dielectric particles," Appl. Opt. **17**, 3707–3709 (1978).

140

[142] W. H. Press, S. A. Teukolsky, W. T. Vetterling, and B. P. Flannery, "Numerical recipes: The art of scientific computing," (1992).

[143] A. Ji, T. V. Raziman, J. Butet, R. P. Sharma, and O. J. F. Martin, "Optical forces and torques on realistic plasmonic nanostructures: a surface integral approach," Opt. Lett. **39**, 4699–4702 (2014).

[144] J. D. Jackson, *Classical Electrodynamics* (Wiley, 1998), 3rd ed.

[145] M. Mansuripur, "Radiation pressure and the linear momentum of the electromagnetic field," Opt. Express **12**, 5375–5401 (2004).

[146] A. Ashkin, J. M. Dziedzic, J. E. Bjorkholm, and S. Chu, "Observation of a single-beam gradient force optical trap for dielectric particles," Opt. Lett. **11**, 288–290 (1986).

[147] J. Chen, J. Ng, Z. Lin, and C. T. Chan, "Optical pulling force," Nat. Photon. **5**, 531–534 (2011).

[148] A. Ashkin, "Acceleration and trapping of particles by radiation pressure," Phys. Rev. Lett. **24**, 156–159 (1970).

[149] D. G. Grier, "A revolution in optical manipulation," Nature **424**, 810–816 (2003).

[150] K. C. Neuman and S. M. Block, "Optical trapping," Rev. Sci. Instrum. **75**, 2787–2809 (2004).

[151] J. R. Moffitt, Y. R. Chemla, S. B. Smith, and C. Bustamante, "Recent advances in optical tweezers," Annu. Rev. Biochem. **77**, 205–228 (2008).

[152] T. Shoji and Y. Tsuboi, "Plasmonic optical tweezers toward molecular manipulation: Tailoring plasmonic nanostructure, light source, and resonant trapping," J. Phys. Chem. Lett. **5**, 2957–2967 (2014).

[153] L. Novotny, R. X. Bian, and X. S. Xie, "Theory of nanometric optical tweezers," Phys. Rev. Lett. **79**, 645–648 (1997).

[154] H. Xu and M. Käll, "Surface-plasmon-enhanced optical forces in silver nanoaggregates," Phys. Rev. Lett. **89**, 246802 (2002).

[155] M. Righini, A. S. Zelenina, C. Girard, and R. Quidant, "Parallel and selective trapping in a patterned plasmonic landscape," Nat. Phys. **3**, 477–480 (2007).

[156] K. C. Toussaint, M. Liu, M. Pelton, J. Pesic, M. J. Guffey, P. Guyot-Sionnest, and N. F. Scherer, "Plasmon resonance-based optical trapping of single and multiple Au nanoparticles," Opt. Express **15**, 12017–12029 (2007).

[157] A. Grigorenko, N. Roberts, M. Dickinson, and Y. Zhang, "Nanometric optical tweezers based on nanostructured substrates," Nat. Photon. **2**, 365–370 (2008).

Bibliography

[158] L. Huang and O. J. F. Martin, "Reversal of the optical force in a plasmonic trap," Opt. Lett. **33**, 3001–3003 (2008).

[159] L. Huang, S. J. Maerkl, and O. J. F. Martin, "Integration of plasmonic trapping in a microfluidic environment," Opt. Express **17**, 6018–6024 (2009).

[160] K. Wang, E. Schonbrun, and K. B. Crozier, "Propulsion of gold nanoparticles with surface plasmon polaritons: Evidence of enhanced optical force from near-field coupling between gold particle and gold film," Nano Lett. **9**, 2623–2629 (2009).

[161] K. Wang, E. Schonbrun, P. Steinvurzel, and K. B. Crozier, "Trapping and rotating nanoparticles using a plasmonic nano-tweezer with an integrated heat sink," Nat. Commun. **2**, 469 (2011).

[162] K. Wang and K. B. Crozier, "Plasmonic trapping with a gold nanopillar," ChemPhysChem **13**, 2639–2648 (2012).

[163] S. Lin, W. Zhu, Y. Jin, and K. B. Crozier, "Surface-enhanced Raman scattering with Ag nanoparticles optically trapped by a photonic crystal cavity," Nano Lett. **13**, 559–563 (2013).

[164] T. Shoji, J. Saitoh, N. Kitamura, F. Nagasawa, K. Murakoshi, H. Yamauchi, S. Ito, H. Miyasaka, H. Ishihara, and Y. Tsuboi, "Permanent fixing or reversible trapping and release of DNA micropatterns on a gold nanostructure using continuous-wave or femtosecond-pulsed near-infrared laser light," J. Am. Chem. Soc. **135**, 6643–6648 (2013).

[165] C. Girard, A. Dereux, and O. J. F. Martin, "Theoretical analysis of light-inductive forces in scanning probe microscopy," Phys. Rev. B **49**, 13872–13881 (1994).

[166] P. C. Chaumet and M. Nieto-Vesperinas, "Coupled dipole method determination of the electromagnetic force on a particle over a flat dielectric substrate," Phys. Rev. B **61**, 14119–14127 (2000).

[167] M. Nieto-Vesperinas, P. C. Chaumet, and A. Rahmani, "Near-field photonic forces," Phil. Trans. R. Soc. Lond. A **362**, 719–738 (2004).

[168] M. Mazilu, A. Rudhall, E. M. Wright, and K. Dholakia, "An interacting dipole model to explore broadband transverse optical binding," J. Phys.: Condens. Matter **24**, 464117 (2012).

[169] A. J. Hallock, P. L. Redmond, and L. E. Brus, "Optical forces between metallic particles," Proc. Natl. Acad. Sci. U.S.A. **102**, 1280–1284 (2005).

[170] A. Salandrino, S. Fardad, and D. N. Christodoulides, "Generalized mie theory of optical forces," J. Opt. Soc. Am. B **29**, 855–866 (2012).

[171] M. Fujii, "Finite-difference analysis of plasmon-induced forces of metal nano-clusters by the lorentz force formulation," Opt. Express **18**, 27731–27747 (2010).

[172] M. Mansuripur, "Optical manipulation: Momentum exchange effect," Nat. Photon. **7**, 765–766 (2013).

[173] M. Ploschner, M. Mazilu, T. F. Krauss, and K. Dholakia, "Optical forces near a nanoantenna," J. Nanophotonics **4**, 041570 (2010).

[174] A. Lovera and O. J. F. Martin, "Plasmonic trapping with realistic dipole nanoantennas: Analysis of the detection limit," Appl. Phys. Lett. **99**, 151104 (2011).

[175] P. B. Johnson and R. W. Christy, "Optical constants of the noble metals," Phys. Rev. B **6**, 4370–4379 (1972).

[176] Z. Li, M. Käll, and H. Xu, "Optical forces on interacting plasmonic nanoparticles in a focused gaussian beam," Phys. Rev. B **77**, 085412 (2008).

[177] V. D. Miljković, T. Pakizeh, B. Sepulveda, P. Johansson, and M. Käll, "Optical forces in plasmonic nanoparticle dimers," J. Phys. Chem. C **114**, 7472–7479 (2010).

[178] É. Lamothe, G. Lévêque, and O. J. F. Martin, "Optical forces in coupled plasmonic nanosystems: Near field and far field interaction regimes," Opt. Express **15**, 9631–9644 (2007).

[179] A. M. Kern and O. J. F. Martin, "Excitation and reemission of molecules near realistic plasmonic nanostructures," Nano Lett. **11**, 482–487 (2011).

[180] P. C. Chaumet and M. Nieto-Vesperinas, "Time-averaged total force on a dipolar sphere in an electromagnetic field," Opt. Lett. **25**, 1065–1067 (2000).

[181] M. Abraham, "Zur elektrodynamik bewegter körper," Rend. Circ. Mat. Palermo **28**, 1–28 (1909).

[182] M. Abraham, "Sul l'elettrodinamica di minkowski," Rend. Circ. Mat. Palermo **30**, 33–46 (1910).

[183] H. Minkowski, "Die grundgleichungen für die elektromagnetischen vorgänge in bewegten körpern," Math. Ann. **68**, 472–525 (1910).

[184] P. Kinsler, A. Favaro, and M. W. McCall, "Four poynting theorems," Eur. J. Phys. **30**, 983 (2009).

[185] R. N. C. Pfeifer, T. A. Nieminen, N. R. Heckenberg, and H. Rubinsztein-Dunlop, " ***Colloquium*** : Momentum of an electromagnetic wave in dielectric media," Rev. Mod. Phys. **79**, 1197–1216 (2007).

[186] V. V. Datsyuk and O. R. Pavlyniuk, "Maxwell stress on a small dielectric sphere in a dielectric," Phys. Rev. A **91**, 023826 (2015).

Bibliography

[187] S. Stallinga, "Radiation force on a fabry-perot slab immersed in a dielectric," Opt. Express **14**, 1286–1295 (2006).

[188] J. P. Kottmann, O. J. F. Martin, D. R. Smith, and S. Schultz, "Field polarization and polarization charge distributions in plasmon resonant nanoparticles," New J. Phys. **2**, 27 (2000).

[189] J. P. Kottmann and O. J. Martin, "Plasmon resonant coupling in metallic nanowires," Opt. Express **8**, 655–663 (2001).

[190] T. J. Davis, K. C. Vernon, and D. E. Gómez, "Designing plasmonic systems using optical coupling between nanoparticles," Phys. Rev. B **79**, 155423 (2009).

[191] J. Ye, P. V. Dorpe, L. Lagae, G. Maes, and G. Borghs, "Observation of plasmonic dipolar anti-bonding mode in silver nanoring structures," Nanotechnology **20**, 465203 (2009).

[192] J. A. Fan, C. Wu, K. Bao, J. Bao, R. Bardhan, N. J. Halas, V. N. Manoharan, P. Nordlander, G. Shvets, and F. Capasso, "Self-assembled plasmonic nanoparticle clusters," Science **328**, 1135–1138 (2010).

[193] P. Ginzburg, A. Krasavin, Y. Sonnefraud, A. Murphy, R. J. Pollard, S. A. Maier, and A. V. Zayats, "Nonlinearly coupled localized plasmon resonances: Resonant second-harmonic generation," Phys. Rev. B **86**, 085422 (2012).

[194] T. V. Raziman and O. J. F. Martin, "Polarisation charges and scattering behaviour of realistically rounded plasmonic nanostructures," Opt. Express **21**, 21500–21507 (2013).

[195] T. V. Raziman and O. J. F. Martin, "Internal optical forces in plasmonic nanostructures," Opt. Express **23**, 20143–20157 (2015).

[196] R. E. Raab and O. L. de Lange, *Multipole Theory in Electromagnetism: Classical, quantum, and symmetry aspects, with applications* (Oxford University Press, 2005).

[197] A. B. Evlyukhin, C. Reinhardt, E. Evlyukhin, and B. N. Chichkov, "Multipole analysis of light scattering by arbitrary-shaped nanoparticles on a plane surface," J. Opt. Soc. Am. B **30**, 2589–2598 (2013).

[198] Y.-W. Huang, W. T. Chen, P. C. Wu, V. A. Fedotov, N. I. Zheludev, and D. P. Tsai, "Toroidal Lasing Spaser," Sci. Rep. **3**, 1237 (2013).

[199] R. M. Bakker, D. Permyakov, Y. F. Yu, D. Markovich, R. Paniagua-Domínguez, L. Gonzaga, A. Samusev, Y. Kivshar, B. Luk'yanchuk, and A. I. Kuznetsov, "Magnetic and electric hotspots with silicon nanodimers," Nano Lett. **15**, 2137–2142 (2015).

[200] S. Mühlig, C. Menzel, C. Rockstuhl, and F. Lederer, "Multipole analysis of meta-atoms," Metamaterials **5**, 64 – 73 (2011).

[201] A. E. Miroshnichenko, A. B. Evlyukhin, Y. F. Yu, R. M. Bakker, A. Chipouline, A. I. Kuznetsov, B. Luk/'yanchuk, B. N. Chichkov, and Y. S. Kivshar, "Nonradiating anapole modes in dielectric nanoparticles," Nat. Commun. **6** (2015).

[202] F. B. Arango and A. F. Koenderink, "Polarizability tensor retrieval for magnetic and plasmonic antenna design," New J. Phys. **15**, 073023 (2013).

[203] I. Fernandez-Corbaton, S. Nanz, R. Alaee, and C. Rockstuhl, "Exact dipolar moments of a localized electric current distribution," arXiv preprint arXiv:1507.00752 (2015).

[204] A. B. Evlyukhin, C. Reinhardt, and B. N. Chichkov, "Multipole light scattering by non-spherical nanoparticles in the discrete dipole approximation," Phys. Rev. B **84**, 235429 (2011).

[205] Y.-W. Huang, W. T. Chen, P. C. Wu, V. Fedotov, V. Savinov, Y. Z. Ho, Y.-F. Chau, N. I. Zheludev, and D. P. Tsai, "Design of plasmonic toroidal metamaterials at optical frequencies," Opt. Express **20**, 1760–1768 (2012).

[206] S. Zhang, D. A. Genov, Y. Wang, M. Liu, and X. Zhang, "Plasmon-induced transparency in metamaterials," Phys. Rev. Lett. **101**, 047401 (2008).

[207] N. Verellen, Y. Sonnefraud, H. Sobhani, F. Hao, V. V. Moshchalkov, P. V. Dorpe, P. Nordlander, and S. A. Maier, "Fano resonances in individual coherent plasmonic nanocavities," Nano Lett. **9**, 1663–1667 (2009).

[208] B. Luk'yanchuk, N. I. Zheludev, S. A. Maier, N. J. Halas, P. Nordlander, H. Giessen, and C. T. Chong, "The Fano resonance in plasmonic nanostructures and metamaterials," Nat. Mater. **9**, 707–715 (2010).

[209] D. T. Pierce and W. E. Spicer, "Electronic structure of amorphous si from photoemission and optical studies," Phys. Rev. B **5**, 3017–3029 (1972).

[210] T. V. Raziman, W. R. C. Somerville, O. J. F. Martin, and E. C. Le Ru, "Accuracy of surface integral equation matrix elements in plasmonic calculations," J. Opt. Soc. Am. B **32**, 485–492 (2015).

[211] W. L. Roland, P. Nithiarasu, and K. Seetharamu, *Fundamentals of the finite element method for heat and fluid flow* (John Wiley & Sons Ltd, 2004).

[212] I. Ergatoudis, B. Irons, and O. Zienkiewicz, "Curved, isoparametric, "quadrilateral" elements for finite element analysis," Int. J. Solids Struct. **4**, 31 – 42 (1968).

[213] R. Graglia, P. Uslenghi, and R. Zich, "Moment method with isoparametric elements for three-dimensional anisotropic scatterers," Proc. IEEE **77**, 750–760 (1989).

[214] R. Graglia, "On the numerical integration of the linear shape functions times the 3-D Green's function or its gradient on a plane triangle," IEEE Trans. Antennas Propag. **41**, 1448–1455 (1993).

[215] P. Yla-Oijala and M. Taskinen, "Calculation of CFIE impedance matrix elements with RWG and $n\times$RWG functions," IEEE Trans. Antennas Propag. **51**, 1837–1846 (2003).

[216] A. Polimeridis and J. Mosig, "On the direct evaluation of surface integral equation impedance matrix elements involving point singularities," IEEE Trans. Antennas Propag. **10**, 599–602 (2011).

[217] F. Vipiana, D. Wilton, and W. Johnson, "Advanced numerical schemes for the accurate evaluation of 4-D reaction integrals in the method of moments," IEEE Trans. Antennas Propag. **61**, 5559–5566 (2013).

[218] D. A. Dunavant, "High degree efficient symmetrical gaussian quadrature rules for the triangle," Int. J. Numer. Meth. Engng. **21**, 1129–1148 (1985).

[219] P. Arcioni, M. Bressan, and L. Perregrini, "On the evaluation of the double surface integrals arising in the application of the boundary integral method to 3-d problems," IEEE Trans. Microwave Theory Tech. **45**, 436–439 (1997).

[220] W. C. Chew, *Waves and Fields in Inhomogenous Media* (Van Nostrand Reinhold, New York, 1990).

[221] C. F. Bohren and D. R. Huffman, *Absorption and Scattering of Light by Small Particles* (Wiley, New York, 1983), 3rd ed.

[222] P. G. Etchegoin, E. C. Le Ru, and M. Meyer, "An analytic model for the optical properties of gold," J. Chem. Phys. **125**, 164705 (2006).

[223] A. Kern and O. J. F. Martin, "Pitfalls in the determination of optical cross sections from surface integral equation simulations," IEEE Trans. Antennas Propag. **58**, 2158–2161 (2010).

[224] B. Gallinet and O. J. Martin, "Scattering on plasmonic nanostructures arrays modeled with a surface integral formulation," Photonics and Nanostructures - Fundamentals and Applications **8**, 278 – 284 (2010).

[225] A. Rathsfeld, G. Schmidt, and B. H. Kleemann, *On a fast integral equation method for diffraction gratings* (WIAS, 2006).

[226] I. Stevanovic and J. R. Mosig, "Periodic green" s function for skewed 3-d lattices using the ewald transformation," IEEE Trans. Microwave Theory Tech. **49**, 1353–1357 (2007).

[227] F. Capolino, D. R. Wilton, W. Johnson *et al.*, "Efficient computation of the 2-d green's function for 1-d periodic structures using the ewald method," IEEE Trans. Antennas Propag. **53**, 2977–2984 (2005).

[228] F. Capolino, D. R. Wilton, and W. A. Johnson, "Efficient computation of the 3d green's function for the helmholtz operator for a linear array of point sources using the ewald method," J. Comput. Phys. **223**, 250–261 (2007).

[229] Y.-W. Jiang, L. D.-C. Tzuang, Y.-H. Ye, Y.-T. Wu, M.-W. Tsai, C.-Y. Chen, and S.-C. Lee, "Effect of wood's anomalies on the profile of extraordinary transmission spectra through metal periodic arrays of rectangular subwavelength holes with different aspect ratio," Opt. Express **17**, 2631–2637 (2009).

[230] L. B. Whitbourn and R. C. Compton, "Equivalent-circuit formulas for metal grid reflectors at a dielectric boundary," Appl. Opt. **24**, 217–220 (1985).

[231] J. Alegret, P. Johansson, and M. Käll, "Green's tensor calculations of plasmon resonances of single holes and hole pairs in thin gold films," New J. Phys. **10**, 105004 (2008).

[232] W. Vandevender and K. Haskell, "The slatec mathematical subroutine library," ACM SIGNUM Newsletter **17**, 16–21 (1982).

[233] S. Kawata and T. Sugiura, "Movement of micrometer-sized particles in the evanescent field of a laser beam," Opt. Lett. **17**, 772–774 (1992).

[234] S. Kawata and T. Tani, "Optically driven mie particles in an evanescent field along a channeled wave guide," Opt. Lett. **21**, 1768–1770 (1996).

[235] E. Simsek, Q. H. Liu, and B. Wei, "Singularity subtraction for evaluation of green's functions for multilayer media," IEEE Trans. Microwave Theory Tech. **54**, 216–225 (2006).

[236] W. Chew, J. Xiong, and M. Saville, "A matrix-friendly formulation of layered medium green's function," IEEE Antennas Wireless Propag. Lett. **5**, 490–494 (2006).

[237] P. Atkins and W. C. Chew, "Fast computation of the dyadic green's function for layered media via interpolation," IEEE Antennas Wireless Propag. Lett. **9**, 493–496 (2010).

[238] P. Mühlschlegel, H.-J. Eisler, O. J. F. Martin, B. Hecht, and D. W. Pohl, "Resonant optical antennas," Science **308**, 1607–1609 (2005).

[239] N. Liu, L. Langguth, T. Weiss, J. Kastel, M. Fleischhauer, T. Pfau, and H. Giessen, "Plasmonic analogue of electromagnetically induced transparency at the Drude damping limit," Nat. Mater. **8**, 758–762 (2009).

[240] R. Fuchs, "Theory of the optical properties of ionic crystal cubes," Phys. Rev. B **11**, 1732–1740 (1975).

[241] M. A. Yurkin and M. Kahnert, "Light scattering by a cube: Accuracy limits of the discrete dipole approximation and the T-matrix method," J. Quant. Spectrosc. Radiat. Transfer **123**, 176 – 183 (2013).

[242] W. J. Galush, S. A. Shelby, M. J. Mulvihill, A. Tao, P. Yang, and J. T. Groves, "A nanocube plasmonic sensor for molecular binding on membrane surfaces," Nano Lett. **9**, 2077–2082 (2009).

[243] L. J. Sherry, S.-H. Chang, G. C. Schatz, R. P. Van Duyne, B. J. Wiley, and Y. Xia, "Localized surface plasmon resonance spectroscopy of single silver nanocubes," Nano Lett. **5**, 2034–2038 (2005).

[244] M. Rycenga, J. M. McLellan, and Y. Xia, "Controlling the assembly of silver nanocubes through selective functionalization of their faces," Adv. Mater. **20**, 2416–2420 (2008).

[245] H. Chen, Z. Sun, W. Ni, K. C. Woo, H.-Q. Lin, L. Sun, C. Yan, and J. Wang, "Plasmon coupling in clusters composed of two-dimensionally ordered gold nanocubes," Small **5**, 2111–2119 (2009).

[246] M. E. Stewart, C. R. Anderton, L. B. Thompson, J. Maria, S. K. Gray, J. A. Rogers, and R. G. Nuzzo, "Nanostructured plasmonic sensors," Chem. Rev. **108**, 494–521 (2008).

[247] X. Lu, M. Rycenga, S. E. Skrabalak, B. Wiley, and Y. Xia, "Chemical synthesis of novel plasmonic nanoparticles," Annu. Rev. Phys. Chem. **60**, 167–192 (2009).

[248] W. Li, P. H. C. Camargo, X. Lu, and Y. Xia, "Dimers of silver nanospheres: Facile synthesis and their use as hot spots for surface-enhanced raman scattering," Nano Lett. **9**, 485–490 (2009).

[249] M. Rycenga, C. M. Cobley, J. Zeng, W. Li, C. H. Moran, Q. Zhang, D. Qin, and Y. Xia, "Controlling the synthesis and assembly of silver nanostructures for plasmonic applications," Chem. Rev. **111**, 3669–3712 (2011).

[250] N. Grillet, D. Manchon, F. Bertorelle, C. Bonnet, M. Broyer, E. Cottancin, J. Lermé, M. Hillenkamp, and M. Pellarin, "Plasmon coupling in silver nanocube dimers: Resonance splitting induced by edge rounding," ACS Nano **5**, 9450–9462 (2011).

[251] M. B. Cortie, F. Liu, M. D. Arnold, and Y. Niidome, "Multimode resonances in silver nanocuboids," Langmuir **28**, 9103–9112 (2012).

[252] B. Grześkiewicz, K. Ptaszyński, and M. Kotkowiak, "Near and far-field properties of nanoprisms with rounded edges," Plasmonics **9**, 607–614 (2014).

[253] V. Klimov, G.-Y. Guo, and M. Pikhota, "Plasmon resonances in metal nanoparticles with sharp edges and vertices: A material independent approach," J. Phys. Chem. C **118**, 13052–13058 (2014).

[254] A. Portela, T. Yano, C. Santschi, H. Matsui, T. Hayashi, M. Hara, O. J. F. Martin, and H. Tabata, "Spectral tunability of realistic plasmonic nanoantennas," Appl. Phys. Lett. **105**, 091105 (2014).

[255] T. Attanayake, M. Premaratne, and G. Agrawal, "Characterizing the optical response of symmetric hemispherical nano-dimers," Plasmonics **10**, 1453–1466 (2015).

[256] S. Zhang, K. Bao, N. J. Halas, H. Xu, and P. Nordlander, "Substrate-induced Fano resonances of a plasmonic nanocube: A route to increased-sensitivity localized surface plasmon resonance sensors revealed," Nano Lett. **11**, 1657–1663 (2011).

[257] P. F. Liao and A. Wokaun, "Lightning rod effect in surface enhanced raman scattering," J. Chem. Phys. **76**, 751–752 (1982).

[258] A. V. Ermushev, B. V. Mchedlishvili, V. A. Oleinikov, and A. V. Petukhov, "Surface enhancement of local optical fields and the lightning-rod effect," Quantum Electron. **23**, 435 (1993).

[259] A. Unger and M. Kreiter, "Analyzing the performance of plasmonic resonators for dielectric sensing," J. Phys. Chem. C **113**, 12243–12251 (2009).

[260] A. Lovera, B. Gallinet, P. Nordlander, and O. J. Martin, "Mechanisms of Fano resonances in coupled plasmonic systems," ACS Nano **7**, 4527–4536 (2013).

[261] R. Zhao, P. Tassin, T. Koschny, and C. M. Soukoulis, "Optical forces in nanowire pairs and metamaterials," Opt. Express **18**, 25665–25676 (2010).

[262] Q. Zhang, J. J. Xiao, X. M. Zhang, Y. Yao, and H. Liu, "Reversal of optical binding force by Fano resonance in plasmonic nanorod heterodimer," Opt. Express **21**, 6601–6608 (2013).

[263] Q. Zhang and J. J. Xiao, "Multiple reversals of optical binding force in plasmonic disk-ring nanostructures with dipole-multipole Fano resonances," Opt. Lett. **38**, 4240–4243 (2013).

[264] M. Righini, P. Ghenuche, S. Cherukulappurath, V. Myroshnychenko, F. J. García de Abajo, and R. Quidant, "Nano-optical trapping of Rayleigh particles and *Escherichia coli* bacteria with resonant optical antennas," Nano Lett. **9**, 3387–3391 (2009).

[265] B. Gallinet and O. J. F. Martin, "Influence of electromagnetic interactions on the line shape of plasmonic Fano resonances," ACS Nano **5**, 8999–9008 (2011).

[266] J. Butet, A. Lovera, and O. J. F. Martin, "Detecting the trapping of small metal nanoparticles in the gap of nanoantennas with optical second harmonic generation," Opt. Express **21**, 28710–28718 (2013).

[267] J. Pendry, A. Holden, D. Robbins, and W. Stewart, "Magnetism from conductors and enhanced nonlinear phenomena," IEEE Trans. Microwave Theory Tech. **47**, 2075–2084 (1999).

[268] D. R. Smith, W. J. Padilla, D. C. Vier, S. C. Nemat-Nasser, and S. Schultz, "Composite medium with simultaneously negative permeability and permittivity," Phys. Rev. Lett. **84**, 4184–4187 (2000).

Bibliography

[269] P. Gay-Balmaz and O. J. F. Martin, "Efficient isotropic magnetic resonators," Appl. Phys. Lett. **81**, 939–941 (2002).

[270] P. Drude, "Zur Elektronentheorie der Metalle," Annalen Der Physik **306**, 566–613 (1900).

[271] A. Sommerfeld and H. Bethe, *Handbuch der Physik* (Springer Verlag, 1933), vol. 24-2, chap. Elektronentheorie der Metalle, pp. 333–622.

[272] L. Tong, V. D. Miljković, and M. Käll, "Alignment, rotation, and spinning of single plasmonic nanoparticles and nanowires using polarization dependent optical forces," Nano Lett. **10**, 268–273 (2010).

[273] J.-W. Liaw, W.-J. Lo, and M.-K. Kuo, "Wavelength-dependent longitudinal polarizability of gold nanorod on optical torques," Opt. Express **22**, 10858–10867 (2014).

[274] R. A. Beth, "Mechanical detection and measurement of the angular momentum of light," Phys. Rev. **50**, 115–125 (1936).

[275] L. Allen, M. W. Beijersbergen, R. J. C. Spreeuw, and J. P. Woerdman, "Orbital angular momentum of light and the transformation of Laguerre-Gaussian laser modes," Phys. Rev. A **45**, 8185–8189 (1992).

[276] H. He, M. E. J. Friese, N. R. Heckenberg, and H. Rubinsztein-Dunlop, "Direct observation of transfer of angular momentum to absorptive particles from a laser beam with a phase singularity," Phys. Rev. Lett. **75**, 826–829 (1995).

[277] A. T. O'Neil, I. MacVicar, L. Allen, and M. J. Padgett, "Intrinsic and extrinsic nature of the orbital angular momentum of a light beam," Phys. Rev. Lett. **88**, 053601 (2002).

[278] M. P. J. Lavery, F. C. Speirits, S. M. Barnett, and M. J. Padgett, "Detection of a spinning object using light's orbital angular momentum," Science **341**, 537–540 (2013).

[279] B. Gallinet and O. J. F. Martin, "Relation between near–field and far–field properties of plasmonic Fano resonances," Opt. Express **19**, 22167–22175 (2011).

[280] Z. Li, S. Zhang, L. Tong, P. Wang, B. Dong, and H. Xu, "Ultrasensitive size-selection of plasmonic nanoparticles by Fano interference optical force," ACS Nano **8**, 701–708 (2014).

[281] H. Chen, S. Liu, J. Zi, and Z. Lin, "Fano resonance-induced negative optical scattering force on plasmonic nanoparticles," ACS Nano **9**, 1926–1935 (2015).

[282] C. Oubre and P. Nordlander, "Optical properties of metallodielectric nanostructures calculated using the finite difference time domain method," J. Phys. Chem. B **108**, 17740–17747 (2004).

[283] H. Guo, N. Liu, L. Fu, T. P. Meyrath, T. Zentgraf, H. Schweizer, and H. Giessen, "Resonance hybridization in double split-ring resonator metamaterials," Opt. Express **15**, 12095–12101 (2007).

[284] A. Potts, D. M. Bagnall, and N. I. Zheludev, "A new model of geometric chirality for two-dimensional continuous media and planar meta-materials," J. Opt. A: Pure. Appl. Opt. **6**, 193 (2004).

[285] M. H. Alizadeh and B. M. Reinhard, "Plasmonically enhanced chiral optical fields and forces in achiral split ring resonators," ACS Photonics **2**, 361–368 (2015).

[286] F. J. Rodriguez-Fortuno, N. Engheta, A. Martinez, and A. V. Zayats, "Lateral forces on circularly polarizable particles near a surface," Nat. Commun. **6** (2015).

[287] A. Lehmuskero, R. Ogier, T. Gschneidtner, P. Johansson, and M. Käll, "Ultrafast spinning of gold nanoparticles in water using circularly polarized light," Nano Lett. **13**, 3129–3134 (2013).

[288] J. Chen, J. Ng, K. Ding, K. H. Fung, Z. Lin, and C. T. Chan, "Negative optical torque," Sci. Rep. **4**, 6386 (2014).

[289] O. Vazquez-Mena, T. Sannomiya, M. Tosun, L. G. Villanueva, V. Savu, J. Voros, and J. Brugger, "High-resolution resistless nanopatterning on polymer and flexible substrates for plasmonic biosensing using stencil masks," ACS Nano **6**, 5474–5481 (2012).

[290] X. Shen, T. J. Cui, D. Martin-Cano, and F. J. Garcia-Vidal, "Conformal surface plasmons propagating on ultrathin and flexible films," Proc. Natl. Acad. Sci. U.S.A. **110**, 40–45 (2013).

[291] P. Guo, D. Sikdar, X. Huang, K. J. Si, B. Su, Y. Chen, W. Xiong, L. W. Yap, M. Premaratne, and W. Cheng, "Large-scale self-assembly and stretch-induced plasmonic properties of core–shell metal nanoparticle superlattice sheets," J. Phys. Chem. C **118**, 26816–26824 (2014).

[292] S. J. Tan, M. J. Campolongo, D. Luo, and W. Cheng, "Building plasmonic nanostructures with DNA," Nat. Nanotechnol. **6**, 268–276 (2011).

[293] X. Shen, A. Asenjo-Garcia, Q. Liu, Q. Jiang, F. J. García de Abajo, N. Liu, and B. Ding, "Three-dimensional plasmonic chiral tetramers assembled by DNA origami," Nano Lett. **13**, 2128–2133 (2013).

[294] N. Li, A. Tittl, S. Yue, H. Giessen, C. Song, B. Ding, and N. Liu, "DNA-assembled bimetallic plasmonic nanosensors," Light: Sci. Appl. **3**, e226 (2014).

[295] L. Paterson, M. P. MacDonald, J. Arlt, W. Sibbett, P. E. Bryant, and K. Dholakia, "Controlled rotation of optically trapped microscopic particles," Science **292**, 912–914 (2001).

[296] M. Pelton, M. Liu, H. Y. Kim, G. Smith, P. Guyot-Sionnest, and N. F. Scherer, "Optical trapping and alignment of single gold nanorods by using plasmon resonances," Opt. Lett. **31**, 2075–2077 (2006).

[297] L. Ling, H.-L. Guo, X.-L. Zhong, L. Huang, J.-F. Li, L. Gan, and Z.-Y. Li, "Manipulation of gold nanorods with dual-optical tweezers for surface plasmon resonance control," Nanotechnology **23**, 215302 (2012).

[298] Z. Yan, J. E. Jureller, J. Sweet, M. J. Guffey, M. Pelton, and N. F. Scherer, "Three-dimensional optical trapping and manipulation of single silver nanowires," Nano Lett. **12**, 5155–5161 (2012).

[299] J. Do, M. Fedoruk, F. Jäckel, and J. Feldmann, "Two-color laser printing of individual gold nanorods," Nano Lett. **13**, 4164–4168 (2013).

[300] C. Rockstuhl and J. Tominaga, "Calculation of the torque exerted by light fields on silver elliptical nanocylinders," Europhys. Lett. **73**, 313–319 (2006).

[301] J. Trojek, L. Chvátal, and P. Zemánek, "Optical alignment and confinement of an ellipsoidal nanorod in optical tweezers: a theoretical study," J. Opt. Soc. Am. A **29**, 1224–1236 (2012).

[302] L. Ming, Z. Thomas, L. Yongmin, B. Guy, and Z. Xiang, "Light-driven nanoscale plasmonic motors," Nat. Nanotechnol. **5**, 570–573 (2010).

[303] Z. Yan and N. F. Scherer, "Optical vortex induced rotation of silver nanowires," J. Phys. Chem. Lett. **4**, 2937–2942 (2013).

[304] J.-W. Liaw, W.-J. Lo, W.-C. Lin, and M.-K. Kuo, "Theoretical study of optical torques for aligning ag nanorods and nanowires," J. Quant. Spectrosc. Radiat. Transfer **162**, 133 – 142 (2015).

[305] F. Abelès, "Surface electromagnetic waves ellipsometry," Surf. Sci. **56**, 237–251 (1976).

[306] A. N. Grigorenko, P. I. Nikitin, and A. V. Kabashin, "Phase jumps and interferometric surface plasmon resonance imaging," Appl. Phys. Lett. **75**, 3917–3919 (1999).

[307] Y. S. Joe, A. M. Satanin, and C. S. Kim, "Classical analogy of Fano resonances," Phys. Scr. **74**, 259–266 (2006).

[308] M. A. Kats, N. Yu, P. Genevet, Z. Gaburro, and F. Capasso, "Effect of radiation damping on the spectral response of plasmonic components," Opt. Express **19**, 21748–21753 (2011).

[309] J. Zuloaga and P. Nordlander, "On the energy shift between near-field and far-field peak intensities in localized plasmon systems," Nano Lett. **11**, 1280–1283 (2011).

[310] B. Abasahl, S. Dutta-Gupta, C. Santschi, and O. J. F. Martin, "Coupling strength can control the polarization twist of a plasmonic antenna," Nano Lett. **13**, 4575–4579 (2013).

[311] B. Abasahl, C. Santschi, and O. J. F. Martin, "Quantitative extraction of equivalent lumped circuit elements for complex plasmonic nanostructures," ACS Photonics **1**, 403–407 (2014).

[312] B. Gallinet and O. J. F. Martin, "Refractive index sensing with subradiant modes: A framework to reduce losses in plasmonic nanostructures," ACS Nano **7**, 6978–6987 (2013).

[313] J. Butet and O. J. F. Martin, "Refractive index sensing with Fano resonant plasmonic nanostructures: a symmetry based nonlinear approach," Nanoscale **6**, 15262–15270 (2014).

[314] J. Butet and O. J. F. Martin, "Nonlinear plasmonic nanorulers," ACS Nano **8**, 4931–4939 (2014).

[315] C. Yan and O. J. F. Martin, "Periodicity-induced symmetry breaking in a Fano lattice: Hybridization and tight-binding regimes," ACS Nano **8**, 11860–11868 (2014).

[316] M. Fleischmann, P. Hendra, and A. McQuillan, "Raman spectra of pyridine adsorbed at a silver electrode," **26**, 163 – 166 (1974).

[317] Y.-C. Chen, R. J. Young, J. V. Macpherson, , and N. R. Wilson, "Single-walled carbon nanotube networks decorated with silver nanoparticles: A novel graded sers substrate," J. Phys. Chem. C **111**, 16167–16173 (2007).

[318] P. Dawson, J. A. Duenas, M. G. Boyle, M. D. Doherty, S. E. J. Bell, A. M. Kern, O. J. F. Martin, A.-S. Teh, K. B. K. Teo, and W. I. Milne, "Combined antenna and localized plasmon resonance in raman scattering from random arrays of silver-coated, vertically aligned multiwalled carbon nanotubes," Nano Lett. **11**, 365–371 (2011).

[319] S. Lee, M. G. Hahm, R. Vajtai, D. P. Hashim, T. Thurakitseree, A. C. Chipara, P. M. Ajayan, and J. H. Hafner, "Utilizing 3d sers active volumes in aligned carbon nanotube scaffold substrates," Advanced Materials **24**, 5261–5266 (2012).

[320] M. Chhowalla, K. B. K. Teo, C. Ducati, N. L. Rupesinghe, G. A. J. Amaratunga, A. C. Ferrari, D. Roy, J. Robertson, and W. I. Milne, "Growth process conditions of vertically aligned carbon nanotubes using plasma enhanced chemical vapor deposition," J. Appl. Phys. **90**, 5308–5317 (2001).

[321] P. Goldberg-Oppenheimer, T. Hutter, B. Chen, J. Robertson, S. Hofmann, and S. Mahajan, "Optimized vertical carbon nanotube forests for multiplex surface-enhanced raman scattering detection," J. Phys. Chem. Lett. **3**, 3486–3492 (2012).

[322] K. B. K. Teo, M. Chhowalla, G. A. J. Amaratunga, W. I. Milne, D. G. Hasko, G. Pirio, P. Legagneux, F. Wyczisk, and D. Pribat, "Uniform patterned growth of carbon nanotubes without surface carbon," Appl. Phys. Lett. **79**, 1534–1536 (2001).

[323] M. A. Ordal, R. J. Bell, R. W. Alexander, L. L. Long, and M. R. Querry, "Optical properties of au, ni, and pb at submillimeter wavelengths," Appl. Opt. **26**, 744–752 (1987).

[324] E. D. Palik, *Handbook of optical constants of solids*, vol. 3 (Academic press, 1998).

Bibliography

[325] M. Bruna and S. Borini, "Optical constants of graphene layers in the visible range," Appl. Phys. Lett. **94**, 031901 (2009).

[326] M. Paterson and F. Yao, "Efficient binary space partitions for hidden-surface removal and solid modeling," Discrete & Computational Geometry **5**, 485–503 (1990).

[327] D. A. Weitz, S. Garoff, J. I. Gersten, and A. Nitzan, "The enhancement of raman scattering, resonance raman scattering, and fluorescence from molecules adsorbed on a rough silver surface," J. Chem. Phys. **78**, 5324–5338 (1983).

[328] A. M. Kern, A. J. Meixner, and O. J. F. Martin, "Molecule-dependent plasmonic enhancement of fluorescence and raman scattering near realistic nanostructures," ACS Nano **6**, 9828–9836 (2012).

[329] M. Fares, J. Hesthaven, Y. Maday, and B. Stamm, "The reduced basis method for the electric field integral equation," J. Comput. Phys. **230**, 5532 – 5555 (2011).

[330] N. Engheta, W. Murphy, V. Rokhlin, and M. Vassiliou, "The fast multipole method (fmm) for electromagnetic scattering problems," IEEE Trans. Antennas Propag. **40**, 634–641 (1992).

[331] J. Song, C.-C. Lu, and W. C. Chew, "Multilevel fast multipole algorithm for electromagnetic scattering by large complex objects," IEEE Trans. Antennas Propag. **45**, 1488–1493 (1997).

[332] X. Wang, E. Pan, and J. D. Albrecht, "Exact closed-form electromagnetic green's functions for graded uniaxial multiferroic materials," J. Appl. Phys. **103**, 113511 (2008).

[333] D. Fang, F. Ling, and Y. Long, "Rectangular waveguide green's function involving complex images," in "Antennas and Propagation Society International Symposium, 1995. AP-S. Digest," , vol. 2 (1995), vol. 2, pp. 1045–1048 vol.2.

[334] J. Mäkitalo, M. Kauranen, and S. Suuriniemi, "Modes and resonances of plasmonic scatterers," Phys. Rev. B **89**, 165429 (2014).

[335] B. Watterson, *The complete Calvin and Hobbes*, vol. 1 (Andrews McMeel Publishing, 2005).

Acknowledgements

"If I have seen further, it is by standing on the shoulders of giants," said Newton. At the end of my dissertation, I can't but agree. I owe a lot to the many people who guided and helped me through my PhD, and would like to thank them for their support.

First of all, I would like to thank Olivier for supervising my endeavour. It was an honour to have been invited to join the Nanophotonics and Metrology Laboratory, and I will always be grateful for the amount of effort he put in to guide my work and ensure my personal growth as a researcher along multiple facets. He has surprised me and far exceeded my expectations from a supervisor, and I am especially thankful for his help with the thesis preparation.

I was also very fortunate to have my group of coworkers at NAM. The members of the group, past and present, guided me by example with their dedication to research and ensured to maintain the personal atmosphere in the group which complimented the professionalism. I am thankful to them – Christian, Benjamin, Guillaume, Arash, Andrea, Krishnan, Banafhseh, Shourya, Volodymyr, Jeremy, Mohsen, Chen, Xiaolong, Robert, Kuang-Yu, Madasamy, Gabriel and Alejandro – for all the illuminating scientific discussions inside the lab and the good times we had outside it. Special mention to Krishnan and Robert for being my amazing officemates and never letting the mood be too heavy. I am also indebted to David for the all technical help with the computational architecture, and to Beatrice and Cathy for helping me with the official work.

Collaborating with other researchers and bringing the best out of each other is one of the most enjoyable aspects of research. Some of my research on optical forces was done in collaboration with Alok Ji (Indian Institute of Technology, New Delhi, India) and Robert. Prof. Eric Le Ru (MacDiarmid Institute, Wellington, New Zealand) and Chen collaborated on the work on SIE optimisation, and Chen was also my collaborator on the work on multipole moments. The work on Raman scattering from carbon nanotubes was performed in collaboration with Prof. Paul Dawson (Queen's University, Belfast, UK). I am thankful to them for the great experience of working together and for raising my research standards.

I would also like to thank the members of my thesis committee – Prof. Ulrich Hohenester, Prof. Gérard Colas des Francs, Prof. Hatice Altug, and Prof. Cristophe Moser – for taking the time to read the thesis thoroughly and for making my oral presentation and the deep discussion

Curriculum Vitae

Personal information

Name	Raziman Thottungal Valapu
Nationality	Indian
Address	Avenue du 24 Janvier 30, CH-1020, Renens, Switzerland
Email	raziman.thottungalvalapu@epfl.ch
	razimantv@gmail.com

Education

2012 – present	**PhD** in Photonics.
	Nanophotonics and Metrology Laboratory (NAM),
	Swiss Federal Institute of Technology Lausanne (EPFL).
	Thesis advisor: Prof. Olivier. J. F. Martin.
2007 – 2012	**Master of Science (Integrated)** in Physics.
	Indian Institute of Technology Kanpur (IIT Kanpur).
2007	**Higher Secondary Education** completed.
	Kerala State Education Board.

Academic working experience

2015 – present	Peer reviewing activity for the Indian Journal of Physics.
2012 – present	Teaching assistant for "Advanced Optics" and "Ingénieurie Optique" (Engineering Optics), supervision of student projects.
2011 – 2012	Student teacher for "Physics-II" (Electrodynamics).
2008 – 2009, 2012	Coach at the Indian national training camp for the International Olympiad in Informatics

Peer-reviewed publications

- T. V. Raziman and O. J. F. Martin, "Internal optical forces in plasmonic nanostructures," Opt. Express **23**, 20143–20157 (2015).

- T. V. Raziman, R. J. Wolke, and O. J. F. Martin, "Optical forces in nanoplasmonic systems: how do they work, what can they be useful for?" Faraday Discuss. **178**, 421–434 (2015).

- T. V. Raziman, W. R. C. Somerville, O. J. F. Martin, and E. C. Le Ru, "Accuracy of surface integral equation matrix elements in plasmonic calculations," J. Opt. Soc. Am. B **32**, 485–492 (2015).

- A. Ji, T. V. Raziman, J. Butet, R. P. Sharma, and O. J. F. Martin, "Optical forces and torques

on realistic plasmonic nanostructures: a surface integral approach," Opt. Lett. **39**, 4699–4702 (2014). *Was selected to be included in the Virtual Journal of Biomedical Optics Vol. 9 Issue 10.*

- T. V. Raziman and O. J. F. Martin, "Polarisation charges and scattering behaviour of realistically rounded plasmonic nanostructures," Opt. Express **21**, 21500–21507 (2013).

Under preparation

- "An optimised integration procedure for the simulation of periodic systems using the surface integral equation method."

- "Understanding and visualising polarisation charges in plasmonic systems."

- "Enhancement of Raman scattering from Silver coated multiwalled Carbon nanotubes."

- "Phase bifurcation and zero reflection in planar plasmonic surfaces."

- "Dispersion controlled shift of plasmonic spectra."

Conference presentations

- T. V. Raziman, E. C. Le Ru, and O. J. F. Martin, "Surface integral equation for plasmonic media: near-field, scattering and forces," oral presentation (invited), The 36th Progress In Electromagnetics Research Symposium, Prague, Czech Republic, July 2015

- T. V. Raziman and O. J. F. Martin, "Three dimensional orientation and rotation of nanostructures using optical torques," oral presentation, The 36th Progress In Electromagnetics Research Symposium, Prague, Czech Republic, July 2015

- T. V. Raziman, A. Ji, R. P. Sharma, and O. J. F. Martin, "Internal forces in plasmonic metamaterials," oral presentation, The 5th International Conference on Metamaterials, Photonic Crystals and Plasmonics, Singapore, May 2014

Academic achievements

- Secured first rank at the Indian national level in Joint CSIR-UGC NET for Physical Sciences (December 2011) and GATE Physics (2012) examinations.

- Received the annual Academic excellence award in 2007, 2008, 2009 and 2010, and J. N. Kapur prize for excellence in mathematics in 2009 from IIT Kanpur.

- Represented India at the International Olympiad in Informatics (2007, silver medal) and the International Astronomy Olympiad (2006, gold medal and 2004, bronze medal).

- Received the KVPY fellowship from the Government of India in 2006 and NTSE scholarship from NCERT in 2005.

Languages

Malayalam	Mother tongue
English	Fluent
Hindi	Fluent
French	Basic